Tribological Properties and Corrosion Behavior of Coatings for Geothermal Applications

Gifty Oppong Boakye

Faculty of Industrial Engineering, Mechanical Engineering and Computer Science
University of Iceland
2022

Tribological and Corrosion Behavior of Coatings for Geothermal Applications.

Gifty Oppong Boakye

Dissertation submitted in partial fulfillment of a
Philosophiae Doctor degree in Mechanical Engineering

PhD Committee
Dr. Sigrún Nanna Karlsdóttir
Dr. Andri Stefánsson
Dr. Danyil Kovalov

Opponents
Dr. Ralph Bäßler, Department of Safety of Structures, Bundesanstalt für Materialforschung und -prüfung
Dr. Roy Johnsen, Professor, Norwegian University of Science and Technology

Faculty of Industrial Engineering, Mechanical Engineering and Computer Science
School of Engineering and Natural Sciences
University of Iceland
Reykjavik, December 2022

Tribological Properties and Corrosion Behavior of Coatings for Geothermal Applications
Dissertation submitted in partial fulfillment of a *Philosophiae Doctor* degree in
Mechanical Engineering

Abstract

The increasing global demand for renewable energy has resulted in the increased exploration of geothermal energy resources, which presents corrosion and wear challenges. The objective of the PhD project is to investigate the friction, wear and corrosion behavior of available and novel coatings designed to add wear and corrosion resistance to steels currently used in geothermal applications. The coatings include *tungsten carbide (WC) cermet-, nickel alloy based-, amorphous iron based-, graphene oxide based-, electroless nickel-phosphorus duplex-, and high entropy alloy (HEA) based- coatings*. The results demonstrated that the coatings' hardness influenced abrasion and wear resistance, but the surface roughness complicated friction and sliding behavior. Further autoclave testing revealed that, the wear-resistant coatings acted as a physical barrier in the test solution, preventing steel corrosion. However, deviations were dependent on the coating microstructure, physical properties, and the chemistry of the test environment, promoting localized corrosion effects. In the 120 °C water test, all the coatings were protective by resisting substrate corrosion. After liquid/vapor phase exposure in the challenging environment (i.e., 250 °C with H_2S/CO_2), the coatings were subjected to either internal attack, surface deposits or substrate corrosion. This work revealed good corrosion resistance of the wear resistant HVOF developed HEA in all test environments and thus encouraging industrial exploitation of the coating in CO_2/H_2S-containing fluid commonly encountered in geothermal fields. The findings established systems that produce suitable corrosion- and wear- resistant coatings for targeted applications that can be incorporated into early project phases in geothermal energy exploration.

Útdráttur

Aukin eftirspurn á heimsvísu eftir endurnýjanlegri orku hefur leitt til aukinnar nýtingu á jarðvarmaauðlindum, sem hefur í för með sér áskoranir um tæringu og slit efna sem notuð eru í nýtingu jarðvarmans. Markmið doktorsverkefnisins er að rannsaka núning, slit og tæringarhegðun fáanlegra og nýrra húðunarefna sem eru hönnuð til að bæta slit og tæringarþol stáls sem nú er notað í nýtingu jarðhita. Húðunarefnin sem voru rannsökuð eru wolframkarbíð (WC) keramík samsetningar, nikkelmelmi, myndlaust járn-melmi, fjölliðusamsetningur með grafín-oxíð, nikkel-fosfór samsetningar og há óreiðu málmblöndur (e. High Entropy Alloys (HEA)). Niðurstöðurnar sýndu fram á að harka húðunarefnanna hafði mikil áhrif á núning og slitþol, en hrýfi yfirborðsins flækti núning og renni-hegðun. Frekari tilraunir í háhita og þrýsti kúti (e. autoclave) leiddi í ljós að slitþolnu húðunarefnin virkuðu sem hindrun gegn tæringu í tilraunaumhverfinu og komu í veg fyrir tæringu á undirliggjandi stáli. Hins vegar voru frávik háð örbyggingu húðunarefnanna, eðliseiginleikum og efnafræði tilrauna umhverfisins, sem stuðlaði að staðbundnum tæringaráhrifum. Í tilraunum við 120 °C í vatni við 50 bar voru öll húðunarefnin verndandi með því að verja undirliggjandi stálið gegn tæringu. En í tilraunum í vökva-/gufufasa í hærri hita og auknu tærandi umhverfi (250 °C með CO_2/H_2S gasi) urðu meiri hluti húðunarefnanna fyrir annaðhvort tæringarskemmdum í innri lögum, yfirborðsútfellingum eða tæringu á undirliggjandi stáli. Þessi rannsókn leiddi einnig í ljós gott tæringarþol nýlegra þróaðs slitþolins HEA húðunarefnis í öllum tilraunar umhverfum rannsóknarinnar og sem hvetur til mögulegrar nýtingar á húðunarefninu í CO_2/H_2S-innihaldandi jarðhitaumverfi. Niðurstöðurnar gefa góðan grunn sem hægt er að byggja á til þróunar og framleiðslu í framtíðinni á viðeigandi tæringar- og slitþolnum húðunarefnum fyrir notkun í jarðhitaumhverfi við nýtingu jarðhita.

Dedication

This work is dedicated to my family and friends.

Table of Contents

List of Figures

List of Tables

Abbreviations

LC	Laser Cladding		WCA	Water Contact Angle
LMD	Laser metal deposition		2D	Two Dimensional
ENP	Electro-Nickel Plating		3D	Three Dimensional
ESD	Electro Spark deposition		JP	Journal Paper
HVOF	High Velocity Oxy-Fuel		CP	Conference Paper
SOA	State-of-the-Art		RQ	Research Question
GO	Graphene Oxide		RT	Room Temperature
PEO	Polyethylene Oxide		HTHP	High-Temperature High-Pressure
PEEK	Polyether Ether Ketone		RPM	Revolutions Per Minute
PPS	Polyphenylene Sulfide		COF	Coefficient of Friction
PTFE	Polytetrafluoroethylene		PoD	Pin-on-Disk
CRA	Corrosion Resistant Alloy		SD	Standard Deviation
HEA	High Entropy Alloy		ROP	Rate of Penetration
CCA	Compositionally Complex Alloy		KPI	Key Performance Indicators
FMEA	Failure Mode and Effects Analysis		NCG	Non-Condensable Gases
EIC	Environmentally Induced Cracking		O&M	Operation and Maintenance
SEM	Scanning Electron Microscope		BHA	Bottom-hole assembly
EDS	Energy Dispersive X-ray Spectroscope		HWDC	Heavyweight Drill Collars
XRD	X-ray Diffractometer		MWD	Measurement While Drilling
ICP-OES	Inductively Coupled Plasma-Optical Emission Spectrometry		LWD	Logging While Drilling
			ASTM	American Society for Testing and Materials

Symbols list

μ	Coefficient of friction (-)
F_n	Normal/applied load (N)
F_t	Tangential force (N)
V	Volume loss (mm^3)
t	Time (s/ min/ h)
T	Temperature (°C)
L	Sliding distance (m)
W_{sample}	Specific wear rate (mm^3/Nm)
PP	Partial pressure (atm)
at%	Atomic percent
wt%	Weight percent
HV	Vicker hardness
HK	Knoop hardness

Acknowledgments

I would like to thank my instructor, Sigrun N. Karlsdottir, for giving me the opportunity to do this study, as well as for her contribution and support, nice cooperation, and patience throughout this work.

I would like to thank the other members of the PhD committee, Dr. Danyil Kovalov and Dr. Andri Stefansson, for their guidance, review, and time spent on my work.

I would also like to thank all past and present team from the Materials and Corrosion Research group at University of Iceland for the enormous professional support when it was really needed. A special thanks goes to Erlend Straume, TWI – Cambridge, UPB – Bucharest and Graphenea, SA – Spain for preparing the coatings, assisting in the DOE and all the technical support.

1 Introduction

Geothermal energy is obtained by harnessing energy stored in geothermal reservoirs using simple or advanced technologies [1], which offsets the need for fossil fuel combustion with massive efforts to reduce carbon footprint. Boreholes or wells are drilled to discharge naturally heated groundwater surrounding the geothermal reservoirs or by forced convection, primarily for space heating and power generation. The production wells are drilled into the hot reservoir rocks up to 5 km depth to extract medium temperature (100 °C – 180 °C), high temperature (>180 °C) [2,3], or perhaps superheated (>350 °C) [4] fluid for electricity generation. Interestingly, globally geothermal energy production is steadily gaining acceptance, with an estimated 80% reduction in CO_2 emissions for an equal amount of energy supplied by a coal-fired power plant [5].

Most industrial components have a limited lifetime. The main processes involved in the breakdown of geothermal equipment are corrosion, scaling and wear [6,7]. Scaling or fouling precipitates solid particles from the supersaturated test solution as opposed to corrosion, which results in the formation of solid products from the reaction of the metal with the fluid [6]. Frictional heating in moving parts caused by unsteady operations such as structural vibration, scuffing, micro-ploughing, sliding, or skidding causes surface wear and tear (mechanical damage). Although each degradation mechanism have a considerable impact on productivity, their combined impact is equally significant and is common in such complex service environment [7]. These challenges exist throughout the geothermal power generation process, including the downhole, transmission, main-stream operation, and reinjection systems. Here, the temperature of the fluid must not be underestimated. Drilling equipment; consisting of drill pipes and BHA (bottom-hole assembly) components, valves, seals, turbine, shafts, rotor bearings, and blades are examples of specific problem areas [7,8]. Maintenance, repair, part-replacement, downtime, and safety have enormous and widespread economic consequences [7], as a result, methods for increasing the lifetime of the material used in the components are critical.

Environmentally friendly technologies, such as surface protective coatings for process equipment, are currently being researched [9,10]. Coatings have recently received a lot of research attention due to their diverse applications and benefits in extending equipment life. It is possible to increase and extend service life by designing a cost-efficient composite with a multi-structured surface made of an active-cheap base metal and a noble-expensive material. Improving the surface properties, e.g., lubricity, wetting, wear resistance and corrosion resistance increases efficiency, reliability, and sustainability of geothermal systems [10].

In this dissertation, the tribological properties and corrosion behavior of available and newly developed coatings were studied in the laboratory in simulated geothermal environments. The coatings are designed to add high performance to the substrate material. Different coating techniques (HVOF, LMD/LC, ESD, ESD, and ENP) are used to deposit coating materials on metallic substrates that are representatives of geothermal plant components. The selected substrates have application areas in downhole drilling and mainstream geothermal plant equipment. The main goal includes testing conventional and

novel coating systems, selecting application-dependent loads at reasonable sliding speeds during the tribological test, and simulating appropriate geothermal fluid density/chemistry during the autoclave corrosion test. The majority of the tribological experiments, the friction and wear tests were conducted at ambient dry sliding conditions. The corrosion studies were at high temperatures (HT) of 120 °C and 250 °C at pressure set to 50 bar for both liquid and/or vapor conditions.

The contribution of the dissertation is to provide an understanding of the tribological behavior of the coatings in sliding contact and their corrosion behavior under conditions expected in single-phase (liquid) and two-phase (liquid/steam) geothermal systems with or without Cl⁻ions or H_2S/CO_2 gases present as corrosion species. The proposed research if will afford the opportunity of aptly incorporating the outcome (potential candidate / best coating) in the early project stages of geothermal drilling and plant construction. Three key factors for a coating to be successful in increasing the lifetime of the component are: first, physical barrier protection will prevent metal dissolution (corrosion), second, the hydrophobic coatings will minimize solid deposition, and finally, the hardness property of manufactured coatings, will prevent abrasion and wear at contacting surfaces.

1.1 Related Works

The purpose of coatings is generally to provide a base material with a form of protection from its environment. There are numerous elements or alloys that can be used for coatings depending on the industrial demand, i.e., functionalized surface, high hardness, wear, corrosion, erosion, oxidation, and fouling resistance. In this regard, selection of materials must meet desired performance at each estimated condition that could contribute to coating damage. In this chapter, a retrospective review of coating materials relevant to this research for possible use when metallization or deposition on steels is conducted.

1.1.1 Materials used for the fabrication of coatings

Electroless Nickel – Phosphorus – Ni-P

The primary reasons for employing electroless plating are thickness control, coating uniformity, and deposit tolerances of a few micrometers for complex geometries that can be achieved in depositing the Ni-P based PTFE (Polytetrafluoroethylene) coating. The incorporation of PTFE particles into the Ni-P matrix can benefit from the high mechanical properties of the Ni-P alloy and the chemical inertness of PTFE. Another study discovered a good alternative based on the heat treatment of the coatings through an enhanced microstructure of either crystalline, amorphous, or a blend of the two systems. The altered microstructure of the deposit as a result of heat treatment, improved hardness, wear, corrosion and fatigue resistance [11]. In industrial use where conventional lubricants would be harmful to components, it has been reported that the properties of Ni-P/PTFE coatings gave higher dry lubricity, good wear resistance, and high corrosion resistance at room temperature [11,12]. The coatings are reported to have good substrate adherence but Ni-P coated steel in high temperature gas environment had localized sulfide ion degradation at the coating/substrate interface in contrast to uniform coating deterioration [13,14]. The synergistic effects of Cl⁻/CO_2/H_2S corrosive species and the hot steam that are present in the geothermal well environment have not received much attention, despite the

advancements in this field. In a recent study, Chong Sun et al. highlighted the importance of examining the synergistic corrosive effect of CO_2, H_2S, and Cl^- on Ni-P coatings and reported detrimental effects of corrosion at the coating-substrate interface [13] that may be the primary drawbacks of using conventional Ni-P coatings in geothermal environments.

GO-PTFE (graphene oxide-Polytetrafluoroethylene)

The inclusion of additives is a well-accepted method of improving the mechanical strength of a soft coating [10,15]. Graphite, polyetheretherketone (PEEK), polytetrafluoroethylene (PTFE), and polyethylene oxide (PEO) are examples of relatively low shear strength lubricants [9,15]. It has recently been demonstrated that various carbon-based fillers, like ultrafine diamond particles [16] and graphene platelets [17], can reduce the wear rate of PTFE in environmentally friendly solid lubricants containing innovative carbon-based compounds. In addition to graphene, graphene oxide (GO) has attracted a lot of interest for use in a variety of mechanical and electrical applications. GO has previously been investigated as a barrier and self-lubricating material for tribological and corrosion applications [18–21] but there is limited information regarding PTFE/GO composites for high temperature geothermal applications. In studies published by Huang et al. [18] and Nemati et al. [19] GO was added to PTFE coating in varying percentages. The wear rate was reduced from 5.6 x10^{-8} to 1.9 x 10^{-9} mm^3/Nm and the coefficient of friction (COF) was reduced from 0.16 to 0.045 after 15 vol% added GO [19]. According to a recent study, the friction coefficient and wear rate were reduced by more than two orders of magnitude and approximately 60%, respectively, when 1wt.% GO and PTFE were included in polyimide or epoxy [18] base material. However, in bulk form, the composite was restricted in stiffness and strength, suggesting that a steel substrate may improve structural use.

Ceramic/Metal mixtures – CERMETS

Cermets are recognized cladding materials, appreciated in the industrial sector for their hardness rather than their corrosion resistance. The hardness and tribological properties of thermal spray HVOF-based hard metal coatings including carbides, such as WC-CoCr, WC-(CrC)-Ni, and (CrC)-Ni/Cr, make them suitable for use in preventing wear on machine parts. Cr_3C_2-based coatings may function at temperatures up to 800 °C and are frequently employed in high temperature applications where wear and oxidation resistance is needed [22], while WC-based coatings are typically used below 500 °C [23]. According to reports, using a metallic binder made of Ni, Cr and/or Mo increases corrosion resistance allowing for passivation [24], which reduces the reported corrosion of the coating matrix and segregation of carbide particles in harsh conditions. However, such abrasion resistant coatings [25–27] subjected to geothermal steam with corrosive gases from a deep production well showed blowholes, cracks or delaminations and corrosion rates lower than 0.006 mm/year [27]. Despite this information on the corrosion behavior of HVOF-based hard metal coatings in controlled laboratory high temperature (HT) and high pressure (HP) simulated geothermal environment is lacking. From the above findings simulating HTHP steam to establish corrosion behavior of these coatings for the hot geothermal application is needed.

High entropy alloys – HEA

Metals and metal alloys have long been used for structural applications. A large variety of HEAs have also been developed that exhibit precipitation hardenability, lightweight, anti-

oxidation, anti-wear, corrosion resistance and other properties that could broaden their applicability in many industrial sectors. The enhanced and synergistic properties of such alloys are described to be generated by the high entropy effect, severe lattice distortion effect, and cocktail (mixture) effect [28]. Recently, there have been rapid developments in Co, Cr, Fe, Ni, and Mo HEA coatings for geothermal applications [29–33] amongst others. A fabricated equimolar CoCrFeNiMo bulk material possessed high hardness (593 HV) [29] but a lower wear resistance when compared to CoCrFeNiMo$_{0.85}$ coatings [34]. Another study discovered that a CoCrFeNiMo alloy exhibited a corrosion rate of less than 0.1 mm/yr at ambient temperature in a saline environment [29]. When tested electrochemically at 25 °C in 3.5 wt.% NaCl solution, Fanicchia et al. detected localized corrosion damage of the CoCrFeNiMo$_{0.85}$ coating [33]. At 200 °C, the CoCrFeNiMo alloy showed low corrosion rates when evaluated in-situ with two-phase geothermal steam comprising corrosive H$_2$S and CO$_2$ gases [32]. Similarly, after testing in a simulated superheated geothermal steam environment containing HCl at 350 °C, microscopic inspection of the equimolar CoCrNiFeMo alloy revealed minimal corrosion damage [30].

It is possible to conclude from these findings that the wear and corrosion behavior of coating materials designed for various HT geothermal conditions needs further study.

1.2 Motivation of study

The aim of the project is to study the tribological and corrosion properties of the developed coatings by testing in laboratory simulated environments and identify the most potential candidate for different geothermal power plant equipment. Though other research using coating technologies have been deployed successfully in corrosion control for various industries, this approach incorporates investigations on tribological effects on properties of the various coatings developed for geothermal environments. Wear resistant coatings have only been utilized sporadically in the geothermal industry to extend the lifespan of components where wear, erosion, and corrosion are present because there is a general absence of data and information about their performance and suitability in medium and high temperature geothermal environments. Due to the knowledge gaps that exist, this research is necessary to close them for both scientific reasons and for the global geothermal sector.

Furthermore, if properly evaluated and implemented, renewable (green) tribology has the potential to significantly increase the efficiency of geothermal systems by decreasing wear and friction in tribological processes to conserve energy, renewable energy resources, and safeguard the environment. tribology [35] [36]. As operators become increasingly intent on applying coatings on components, this work also focuses on the efficacy of wear resistant coatings on the corrosion protection. For this purpose, specific objectives are set.

1. Assess the effect of microstructure on the tribological properties and corrosion behavior.
2. Determining the tribological properties of the developed coatings with unidirectional sliding test
3. Simulate geothermal drilling and powerplant environment for laboratory test.
4. Test the corrosion behavior of developed coating in simulated geothermal drilling and power plant environment.

1.3 Research Questions and Structure of Dissertation

From the related works and retrospective study in literature, the following questions were defined in this project and answered based on the findings of the PhD research. The research questions (RQs) are set as follows:

> *RQ1: How does the microstructure of the coatings affect the friction and wear properties of the developed coatings?*
> *RQ2: Do the wear resistant coatings resist corrosion in the simulated high temperature geothermal fluid (H_2O or H_2O -based with H_2S/CO_2 gaseous species)?*
> *RQ3: How does temperature and phase density of the simulated geothermal fluid (i.e., liquid/vapor with H_2S/CO_2) influence the corrosion effect on the tested coatings?*

Each of the published papers contributes significantly to the overall project topic while addressing different aspects of the RQs. Figure 1 shows how the individual journal papers (JP) address the different RQs.

To answer the research questions (RQ), the materials were analyzed visually and microscopically to determine the surface conditions, and microstructure of as-received coatings before testing. The structure of the coatings was then examined after tribological laboratory conditions to determine the material's critical response to the selected test parameters (e.g., load, speed), thereby addressing RQ1. In RQ2 and RQ3, only coatings with the best outcomes from the friction and wear test are subjected to pressurized autoclave corrosion test under established simulated HT fluid conditions with/without CO_2 and H_2S gases. However, RQ3 focuses on aligning results to key performance indicators/indices (KPIs), which can have measurable or non-numerical values. Non-numerical KPIs indicate the failure or success of the coatings from the corrosion test, which is sometimes described with yes -Y or no -N from assessable terms (i.e., quantity, quality, frequency). This ensures that the extent of damage can be measured or evaluated with regards to standards or state-of-the-art (SoA) materials. Therefore, the KPIs are specific, understandable, observable, relevant to an application and achievable within the time frame. Results indicators (see Figure 2) for evaluating the overall functionality of each coating in a single or combined testing environment are the performance of the tested coating materials matched to the KPIs presented in Table 1. These KPIs are identified before material testing.

Research Questions (RQ)

RQ1: How does the microstructure of the coatings affect the friction and wear properties of the developed coatings?

RQ2: Do the wear resistant coatings resist corrosion in the simulated high temperature geothermal fluid (H_2O or H_2O -based containing with H_2S/CO_2 gaseous species)?

RQ3: How does temperature or and phase density of the corrosive simulated geothermal fluid (i.e., liquid/vapor with H_2S/CO_2) influence the corrosion effect on the tested coatings?

Link to Journal Papers (JP)

JP1 The Effect of Polytetrafluoroethylene (PTFE) Particles on Microstructural and Tribological Properties of Electroless Ni-P+PTFE Duplex Coatings Developed for Geothermal Applications

JP2 Microstructural properties and Wear resistance of Fe-Cr-Co-Ni-Mo based High Entropy Alloy Coatings Deposited with Different Coating Techniques

JP3 Corrosion Behaviour of HVOF developed Mo-based High Entropy Alloy coating and selected Hard coatings for High Temperature Geothermal Applications

JP4 Wear-reducing Nickel-Phosphorus and Graphene Oxide-based Composite Coatings: Microstructure and Corrosion behavior in High Temperature Geothermal Environment

Figure 1. Research questions and links to journal papers (JP) in the project.

KPI
Key Performance Index (KPI) for evaluating performance.
- RQ1
- RQ2
- RQ3

Performance
Coating testing

Tribological experiment
- Friction and Wear

Corrosion experiment
- High temperature
- CO_2/H_2S

Indicators
Coating Characterization
*Before and after testing
- Morphology
- Microstructure
- Chemical composition
- Crystal structure
- Phase composition
- Coating thickness
- Hardness
- Film-Substrate adhesion
- Defects or Damages

Figure 2. Key performance index linked to laboratory testing, performance assessment and indicators in the project.

Table 1. Definitions of the key performance index (KPI).

Material testing	Material characterization	KPI name	Units
Testing of materials in the simulated environment	Corrosion analysis	Current density	A/cm^2
		Corrosion rate	mm/yr
	Tribological analysis	Hardness	HV or HK
		Contact angle	Degree
		Mean roughness	µm
		Friction coefficient	-*
		Wear rate	mm^3/Nm
	Pre-/Post-wear	Porosity	%

6

and corrosion performance for exposure test in the laboratory	Cracks	Y/N
	Permeability	Y/N
	Delamination	Y/N
	Corrosion products	Y/N
	Localized damage	Y/N
	Substrate corrosion	Y/N

* - dimensionless

There are seven chapters in the dissertation. The first chapter is an introduction to the topic. The second chapter provides the theoretical background, explaining wear-related and common corrosion mechanisms of metals in geothermal environments. The third chapter describes the experimental design and procedures required to obtain the results. The fourth chapter presents the results and links them to previously published papers. The final chapters (five to seven) include discussion of the main findings, the conclusions, and suggestions for future research, followed by references.

1.4 List of publications

The following journal papers and manuscripts (JP) were written as part of this PhD research project and offer a framework for this manuscript/thesis.

JP1: G. Oppong Boakye, A.M. Ormsdóttir, B.G. Gunnarsson, S. Irukuvarghula, R. Khan, S.N. Karlsdóttir, 'The effect of polytetrafluoroethylene (PTFE) particles on microstructural and tribological properties of electroless Ni-P+PTFE duplex coatings developed for geothermal applications', Coatings. 11 (2021) 670. https://doi.org/10.3390/coatings11060670

JP2: G. Oppong Boakye, L.E. Geambazu, A.M. Ormsdottir, B.G. Gunnarsson, I. Csaki, F. Fanicchia, D. Kovalov, S.N. Karlsdottir, 'Microstructural Properties and Wear Resistance of Fe-Cr-Co-Ni-Mo-Based High Entropy Alloy Coatings Deposited with Different Coating Techniques', Appl. Sci. 12 (2022) 3156. https://doi.org/10.3390/app12063156

JP3: G. Oppong Boakye, E.O. Straume, B.G. Gunnarsson, D. Kovalov, S.N. Karlsdóttir, 'Corrosion Behavior of HVOF developed Mo-based High Entropy Alloy coating and selected Hard coatings for High Temperature Geothermal Applications'. Submitted (01/08/2022) to Corrosion Science. https://papers.ssrn.com/sol3/papers.cfm?abstract_id=4216512

JP4: G. Oppong Boakye, E.O. Straume, D. Kovalov, S.N. Karlsdóttir, Wear-reducing nickel-phosphorus and graphene oxide-based composite coatings: Microstructure and corrosion behavior in high temperature geothermal environment. Corrosion science 209 (2022), 110809. https://doi.org/10.1016/j.corsci.2022.110809

Other disseminations (oral lectures, virtual presentations, posters, bi-annual reports, etc.) emerged from the project. The results contributed to tunning of test equipment, design of

experiment and down-selection of coatings in relation to chemistry and deposition techniques, which were published in the conference proceeding *(CP)*.

Poster 1: <u>G. Oppong Boakye</u>, D. Kovalov, A.Í. Thórhallsson, S. Irukuvarghula, R. Khan, S.N. Karlsdóttir, 'Microstructural Characterization and Tribological Properties of Electroless Nickel PTFE Coatings for Geothermal Applications'. The Ni-P duplex coatings were introduced with detailed description to the effect of phosphorus (P) and PTFE on the tribological behavior of the coatings. Presented at the VIRTUAL EUROCORR 2020 – European Corrosion Congress, September 07-11, Submission ID: 271811.

Lecture/Presentation 1 -CPI: <u>G. Oppong Boakye,</u> D. Kovalov, A.Í. Thórhallsson, S.N. Karlsdóttir, V. Motoiu, 'Friction and Wear Behavior of Surface Coatings for Geothermal Applications'. This paper includes detailed description of the pin-on-disk set-up and measurements used for dry sliding test in this work. For the test, two stainless steels (304L, Type 630) and three carbide coatings (WC-CoCr, Cr_3C_2–NiCr, NiCrFeSiBC alloy) wear evaluated for their friction and wear behavior. PROCEEDINGS in WORLD GEOTHERMAL CONGRESS (WGC) 2020+1, April 26 – May 2, 2021, Reykjavik, Iceland, Paper no. 27094

Lecture/Presentation 2: <u>G. Oppong Boakye</u>, B.A. Rodriguez, E.O. Straume, S.N. Karlsdóttir, 'The impact of corrosion on sliding wear performance of Graphene Oxide Modified Polymer Coatings for Drilling Applications'. Samples were subjected to step corrosion and sliding wear modes in dry and 3.5wt% NaCl solution. This work reported the microstructural, tribological and tribocorrosion properties for polymer (PPS-PTFE) coating as a function of the GO content. Presented at the VIRTUAL EUROCORR 2021 – European Corrosion Congress, September 20-24, 2021, Budapest, Hungary, Submission ID: 337450

Lecture/Presentation 3: <u>G. Oppong Boakye</u>, B.A. Rodriguez, S.N. Karlsdóttir, 'Graphene oxide-based anti-wear materials for drilling tools. The research proposed new bit tooth material to be integrated into drilling hammer technology increasing penetration rate (ROP) and service life. The work identified the best processing route for GO-enhanced WC-CoCr tailored for high wear and abrasion performance. Presented at the VIRTUAL ICDCM 2021 – 31st International Conference on Diamond and Carbon Materials September 06-09, Submission ID. 349.

Lecture/Presentation 4 -CPII: <u>G. Oppong Boakye</u>, E.O. Straume, B.A. Rodriguez, D. Kovalov, S.N. Karlsdóttir, 'Microstructural Characterization, Corrosion and Wear Properties of Graphene Oxide Modified Polymer Coatings for Geothermal Drilling Applications'. This study introduced the concept of added GO (0wt% - 5wt%) into polymeric coatings. The paper discussed not only the features and tribological behavior of the coatings (i.e., 0, 1.0, 2.5 wt.% GO) but also the electrochemical corrosion behavior (OCP and tafel plots). PROCEEDINGS in CORROSION 2021, April 19-30, Conference and Expo June 14-18, 2020, Houston, Texas, USA, Paper Number: NACE-2021-16474.

Lecture/Presentation 5 -CPIII: <u>G. Oppong Boakye</u>, A.M. Ormsdottir, B.G. Gunnarsson, A. Tabecki, F. Zhang, S.N. Karlsdóttir, 'Development of High Velocity Oxygen Fuel (HVOF) corrosion resistant coatings; A comparison between novel high entropy alloy (HEA) and conventional cermets for geothermal application'. Autoclave and electrochemical (OCP and Polarization) techniques were applied to evaluate the corrosion

of WC-CoCr, Cr$_3$C$_2$–NiCr, HEA coatings. The report includes SEM analyses on pre- and post-exposed surfaces to 3.5wt%NaCl and simulated geothermal water. PROCEEDINGS in CORROSION 2022 Conference and Expo, March 6-10, 2022, San Antonio, Texas, USA, Paper Number: AMPP-2022-17675.

Lecture/Presentation 6 -CPIV: <u>G. Oppong Boakye</u>, E.O. Straume, A.M. Ormsdóttir, B.G. Gunnarsson, S. Irukuvarghula, R. Khan, S.N. Karlsdóttir, 'Corrosion and Wear properties of Electroless Ni-P+PTFE Hydrophobic Coating Developed for Geothermal Environment'. This paper detailed the main features and testing of the duplex coatings of high phosphorus bond coat and PTFE— low/high phosphorus topcoat. The experiments include dry sliding, 80 C water sliding, tribocorrosion (OCP with/without sliding), tafel and autoclave test. PROCEEDINGS in European Corrosion Congress – EUROCORR 2022, August 28-01, 2022, Berlin, Germany, Paper no. 37224.

1.5 Author Contribution

Author's name	Affiliation
Gifty Oppong Boakye; G.O.B.	1
Erlend Oddvin Straume; E.O.S.	1
Baldur Geir Gunnarsson; B.G.G.	1
Danyil Kovalov; D.K.	1
Sigrun Nanna Karlsdóttir; S.N.K.	1
Francesco Fanicchia; F.F.	2
Sandeep Irukuvarghula; S.I.	2
Raja Khan; R.K.	2
Ioana Csaki; I.C.	3
Laura E. Geambazu; L.E.G.	3

[1]University of Iceland, Faculty of Industrial Eng., Mechanical Eng., and Computer Science, Hjarðarhagi 2-6, Reykjavík, Iceland
[2]TWI Ltd., Granta Park, Cambridge CB21 6AL, UK
[3]Material Science and Engineering Faculty, University Politehnica Bucharest, Splaiul Independentei 313, 060042 Bucharest, Romania

All authors have read and agreed to the published versions of JP1 – JP4 manuscripts.

G.O.B; Conceptualization, Visualization, Investigation, Data curation, Formal analysis, Validation, Writing—original draft preparation, review, and editing.

A.M.O., B.G.G., E.O.S.; Investigation, Data curation.

F.F., S.I., R.K., I.C., and L.E.G.; Coating fabrication, Writing—review and editing

D.K., S.N.K.; Supervision, Conceptualization, Validation, Formal analysis, Writing—review and editing.

2 Background and challenges

In this study, cost-effective wear and corrosion resistant materials are investigated for geothermal application. This chapter reviews the common failure modes, causes, and effects on materials used in geothermal environments. Well drilling and casing expenses comprise 30-70 % of a geothermal project's overall cost [37,38], which can increase due to deeper drilling lengths, longer trip times, harsher environmental conditions (such as higher temperatures and pressures), and less information (such as drilling blind) [39]. The cost of operation and maintenance (O&M) is another issue with this development. According to a cost sensitivity study, O&M costs for a geothermal plant may be higher than capital costs or investment costs for a longer service [38] usually estimated over 30 years. Therefore, if wear and corrosion resistant coatings could increase the rate of penetration (ROP), minimize the need for tripping when drilling, and limit O&M costs associated with running the power plant would result in significant cost savings.

2.1 Conventional geothermal well and power plant

Conventional wells for power production are predominantly liquid-dominated, drilled to 2-3 km depth and discharged with fluid (liquid or steam) of medium enthalpy (T>100 °C), or high enthalpy (T>150 °C or 200 °C [40]) [2,3]. The high temperature liquid-dominated fields are flashed systems under pre-exploitation conditions [41]. A brine with a pH near to neutral and a Cl level of 1000–10,000 mg/kg [3] that may also contain NCGs, primarily CO_2 and H_2S, is the most typical form of water or fluid encountered at production well depth [3,42]. The fluid may exist at the surface as a liquid, a vapor, or a combination of the two depending on the characteristics of the reservoir; although, the terms "steam," "gas," and "vapor" are all used in the geothermal literature. Non-condensable gas (NCG) concentrations in the steam from major geothermal fields range from 2.5 - 47 g/kg of steam [3]. Such fluid chemistry is believed to have formed at deeper depths, flowing meteoric water and absorbing magmatic volatiles (e.g., HCl, CO_2, SO_2, and H_2S) [3,43]. Power generation with geothermal resources requires multiple components to generate power. A schematic of a two-phase flow system from a downhole to a midstream geothermal powerplant is illustrated in Figure 1. Hot fluid from the well is separated (15-20%) [3,43], and the steam portion drives a turbine attached to a generator to produce electricity. The condensed steam and the remaining wastewater are usually discharged back into reinjection wells.

Drilling is therefore site-specific, where drilling equipment is upgraded according to the challenging conditions observed in the geothermal formations: hard formations, corrosive environments, high temperatures and high pressures (HTHP). The BHA normally consists of the drill bit, a downhole motor, drill collars, measurement while drilling (MWD) / logging while drilling (LWD) equipment, and stabilizers. Heavyweight drill collars (HWDC) are components situated over the drill bit that generate force on the drill bit, allowing it to break the rock formation. A rotary/percussive drill typically strikes the rock

50 times per second while rotating at 75–200 rpm, with hydraulic impact pressure of around 170–200 bar and feed pressure of about 90–100 bar [44]. The well trajectory is maintained by rotating the string 60% of the time to drill straight while sliding (rotation is locked) 45% of the time to build up angle in the rock breaking mechanism illustrated in (Figure 1).
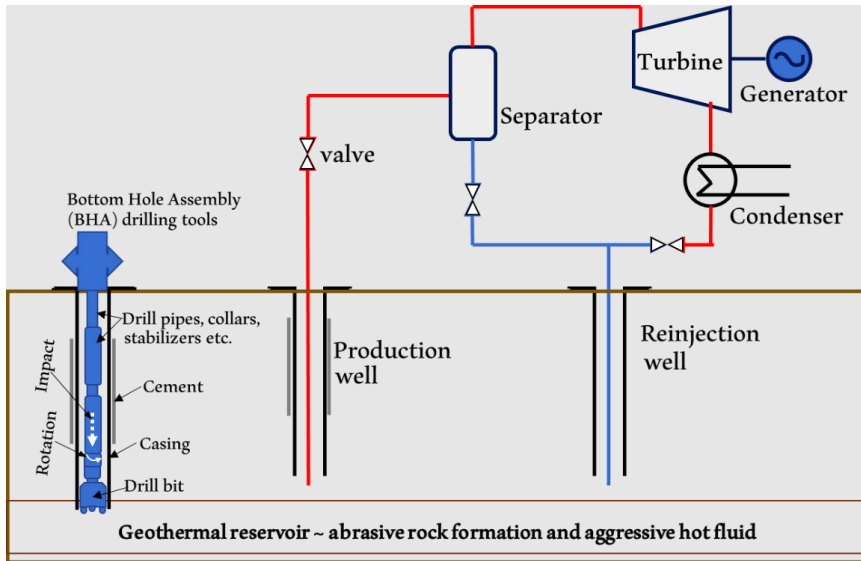
Figure 3. Work principle of impact rotary drill and simplified representation of a "liquid-dominated" geothermal reservoir and power generation system.

For a simplified high temperature power plant, units such as BHA drill components, well casings, pumps, valves, separators/heat exchangers, turbines, and condensers are needed from the exploration, operation, and maintenance (O&M) to reinjection stages. Therefore, numerous components within the geothermal system require protection from the environment created during the harnessing of geothermal energy. The possibility of material degradation caused by the chemistry of geothermal hot fluid in direct contact with components during production must be emphasized [42,45]. Not to mention the drilling-related degradation mechanisms, such as hard formations and high temperatures, as well as deterioration from sliding/rotating of BHA parts and process equipment [46]. If the excessive wear, erosion, and corrosion of the key components are not addressed, it results in service failure.

2.2 Wear in drilling tools and operation equipment

Failures due to corrosion, erosion and wear have been discovered in components used for drilling and down-hole (such as stabilizers, casing, and drill strings) and/or surface equipment (e.g., wellhead, turbine, and its auxiliary unit). Geothermal drilling occurs in tougher rock aggregates, as do the operating conditions for materials used to make downhole drilling tools reducing their mechanical properties [46]. The unfavorable

geological conditions as well as the repeated impact of breaking the rock generate severe bit bouncing and strong vibration. Realistic failure modes include tooth loss, fracture, wear, and microcracks in addition to drilling pipe fatigue from bending force due to buckling load [37]. BHA tools used in geothermal drilling must withstand compressive force from repetitive impact and rotation, as well as abrasive and erosive wear from rock cracking, cuttings, and other debris, resulting in a shorter tool lifetime. Tripping is the process of manually drawing the drill string out of the wellbore to replace worn or damaged tools and then running it back in [47]. The most serious damage is insert wear, fracture, failure of the striking/anvil face, shank failure and drill body/matrix failures that occur when compressive stress on the joint surfaces between the insert and the abrasive particle exceeds the breaking strength of the abrasive particle. During the drilling process, increased temperature exaggerates the tool wear. Wear is unavoidable in real-world situations where objects/surfaces are in contact and moving relative to one another. Rotating, sliding and vibrational effects on components are found in entire regions of the geothermal power generation plant; i.e. in geothermal well casings, transmission, and reinjection systems which affect the wear of metals considerably [7,47]. The main damage were documented in a technical report by Geo-Coat and Ge-Drill project (summarized in Table B.1 in Appendix B) [47] from a survey on 12 power plants around the world, which produced a similar result to the analysis by Feili [7]. Failure Mode and Effects Analysis (FMEA) technique identified common mechanical failures as overheating, stress fractures, thread breakage, and excessive wear due to erosion, abrasion, adhesion/galling, contact/rubbing and corrosion. The research showed that the combined effect of these failures often occurs and depends on the operational parameters and the geothermal brine chemistry.

The primary source of wear is the friction incited by the surface finish and mechanical properties of the process equipment. However, for a sliding couple, the two phenomena may be recursive since high friction promotes wear, and wear advancement influences friction due to contact zone alteration during the wear process [48]. The friction of contact surfaces occurs during unsteady operations such as structural vibration, scuffing, and sliding. The interactions at the rubbing interface during operation are prone to surface damage in certain areas, displayed as sliding, pitting, or fretting wear, which frequently reduces component life. This is owing to high axial, reciprocating, and rotating motions, cyclic thermal stresses, and mechanical loads of operation in the geothermal power plants. Some typical surface damage were rubbing wear of labyrinth seals, abrasive wear of valves, pump shaft, impellers, and wear of turbine rotor due to vibration and imbalances. Valve, seal, turbine shafts, rotor bearings, and blades are examples of specific problem areas. Furthermore, the harsh quality of geothermal steam, including its high temperature and chemical composition, can cause degradation of materials after extended use compromising the structural integrity of the component. For example, steam turbines run at supersonic speeds (1800–3600 rpm) to generate electrical current at a specified frequency [8,49]. This increases mechanical stress, leading to the production of micro pits, cracks, or wear and tear on the component or near metal-assembly surfaces [49].

2.3 Corrosion in geothermal fluid

The corrosion phenomenon generally refers to the degradation of metals or metal alloys caused by the surrounding environment [42]. One of the primary challenges that are

addressed for metal performance is the degradation mechanism in a specific environment. The corrosion forms experienced by a metal depend on the conditions in the environment, chemical composition, and corrosion resistant properties of the metal. The different forms of corrosion experienced, and the main species present in the geothermal environment are reviewed in this section and summarized in Tables presented in Appendix B. The corrosion process is driven by anodic dissolution of the metal (Equations 1 and 2) and cathodic reactions through the environment (Equations 3 - 5).

$$M \rightarrow M^{n+} + ne^- \qquad (1)$$

In geothermal energy exploration, the drill and process equipment are generally constructed with ferrous materials such as different carbon steel grades, low alloy, and highly alloyed steels that are susceptible to corrosion (see Table B.2 and B.3 in Appendix B) in the HT corrosive environment [37,42,46]. The relevant reactions are dissolution of iron (Fe) (see Equation 2) and cathodic reactions such as oxygen reduction (Equation 3), water reduction (Equation 4), or hydrogen evolution (Equation 5; which often occur in acidic conditions) [50]. It is worth noting oxygen reduction may not be present in deep wells or most of the process equipment but other areas of the power plant such as the condensing units.

$$Fe \rightarrow Fe^{2+} + 2e^- \qquad (2)$$

$$O_2 + 2H_2O + 4e^- \rightarrow 4OH^- \qquad (3)$$

$$2H_2O + 4e^- \rightarrow 2OH^- + H_2 \qquad (4)$$

$$2H^+ + 2e^- \rightarrow H_2 \qquad (5)$$

The geophysical and geochemical properties of geothermal fluid vary greatly depending on the location of the geothermal field. A geothermal fluid [43] has water as its bulk phase, but the main corrosion species are from dissolved hydrogen sulfide (H_2S) and carbon dioxide (CO_2) gases, and chloride ions (Cl^-) from the brine environment. HCl can be present in the fluid whereas other corrosive agents include ammonium (NH_4), methane gas (CH_4), nitrogen gas (N_2), sulfate ions (SO_4^{2-}), and dissolved hydrogen gas (H_2). The evolution of hydrogen is expected in HT geothermal wells with NCGs (i.e, H_2S, CO_2) [51] which lowers the fluid pH (increased acidity). This suggests a combination of H_2S, and CO_2 can aggravate corrosion when the gaseous species of both gases are present in an environment.

Hydrogen sulfide reacts with water according to the following reactions.

$$H_2S_{(g)} + H_2O_{(l)} \quad \leftrightarrow \quad H_2S_{(aq)} \qquad (6)$$

$$H_2S_{(aq)} \quad \leftrightarrow \quad H^+_{(aq)} + HS^-_{(aq)} \qquad (7)$$

Similarly, CO_2 reacts with water producing carbonic acids and bi-carbonate products:

$$CO_{2(g)} + H_2O_{(l)} \quad \leftrightarrow \quad H_2CO_{3(aq)} \qquad (8)$$

$$H_2CO_{3(aq)} \quad \leftrightarrow \quad H^+ + HCO_3^-_{(aq)} \quad \leftrightarrow \quad H^+_{(aq)} + CO_3^{2-}_{(aq)} \qquad (9)$$

2.4 Formation of oxide-and sulfide-based corrosion products

When a metal corrodes, the chemical reaction between dissolved ionic compounds from the metal and the environment leads to the formation of irreversible bonds which are identical to the original state of the metal (i.e., its mineral or natural state). The products from the corrosion are often either uniformly precipitated forming a protective layer on the surface or soluble causing further reactions on the surface or at/close to the reaction sites. The corrosion products can be identified d in terms of the structure by microscopic techniques and X-ray diffraction (XRD) analysis. The type of product depends on the surroundings environment exposed to the metal. Steels are mostly referred to in this study as Fe, shows three soluble species and two dry forms of corrosion products in an aqueous environment from the Pourbaix $H_2O/H_2/O_2$ system at 25 °C [50]. The so-called Schikorr reaction describes the transformation process of the three corrosion products: iron (II) hydroxide ($Fe(OH)_2$), magnetite (Fe_3O_4) and hematite (Fe_2O_3) [52]. The first product state to discuss is $Fe(OH)_2$ which exists in both oxygen-deficient and rich environments from Fe reaction in water systems. This slow reaction process leads to the formation of Fe_3O_4 in oxygen-deprived environments (anaerobic conditions) which could be protective for the underlying steel. Here, the oxide is Fe-rich containing both Fe^{2+} and Fe^{3+} ions and composed of mixed Fe_2O_3 and FeO.

$$2Fe_{(s)} + 2H_2O_{(l)} \rightarrow Fe(OH)_2 + 2H^+_{(aq)} + 2e^- \tag{10}$$

$$3Fe^{2+}_{(aq)} + 4H_2O_{(l)} \rightarrow Fe_3O_{4(s)} + 8H^+_{(aq)} + 2e^- \tag{11}$$

$$3Fe(OH)_{2(s)} \rightarrow 2Fe_3O_{4(s)} + H_{2(g)} + 2H_2O_{(l)} \tag{12}$$
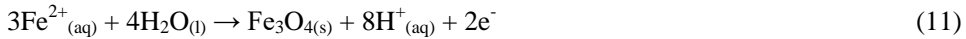
Hematite (Fe_2O_3) also called rust, is formed from oxidized magnetite in an oxygen-rich environment according to the following reactions:

$$2Fe^{2+}_{(aq)} + 3H_2O_{(l)} \rightarrow Fe_2O_{3(s)} + 6H^+_{(aq)} + 2e^- \tag{13}$$

$$2Fe^{3+}_{(aq)} + 3H_2O_{(l)} \rightarrow Fe_2O_{3(s)} + 6H^+_{(aq)} + 2e^- \tag{14}$$

$$3Fe_3O_{4(s)} + H_2O_{(l)} \rightarrow 3Fe_2O_{3(s)} + 2H^+_{(aq)} + 2e^- \tag{15}$$
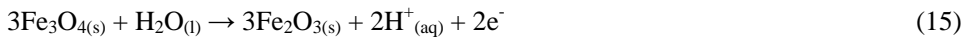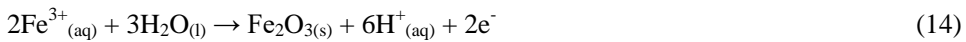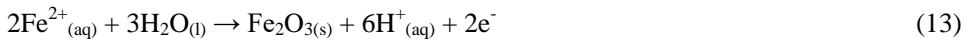
In a CO_2 environment, the dissolution of the metal for instance Fe in Equation 2 produces the corrosion sediment siderite/iron carbonate ($FeCO_3$) as follows:

$$Fe^{2+}_{(aq)} + CO_3^{2-}_{(aq)} \leftrightarrow FeCO_{3(s)} \tag{16}$$

The presence of H_2S is very aggressive which generates several cations (Equation 7) promoting other catalytic processes. The cathodic reaction forms iron sulfides. However, atomic hydrogen diffuses into the steel lattice causing embrittlement, whereas the sulfide present in the material exacerbates the problem by slowing the formation of molecular hydrogen, and therefore amplifying the negative effect.

$$Fe^{2+}_{(aq)} + H_2S_{(aq)} \rightarrow FeS_{m(s)} + 2H^+_{(aq)} \tag{17}$$

Furthermore, depending on the physical state, CO_2 and H_2S gas both dissolve in water (from Equations 6 and 8). As a result, in a mixed CO_2 and H_2S-containing environment, further oxidation of Fe^{2+} to Fe^{3+} can occur through cathodic processes involving the formation and consumption of the various intermediate products (from Equations 7 and 9) [51]. The corrosion behavior becomes dependent on the corrosion product that forms on the surface, even if conditions for $FeCO_3$ and FeS formation are not met. According to reports, a first amorphous Fe_xS_y layer develops on the surface, which subsequently transforms into mackinawite ($Fe_{1+x}S$) and becomes the main corrosion product. Mackinawite eventually acts as a precursor for the corrosion scale that forms under H_2S conditions, including troilite (FeS), pyrrhotite ($Fe_{1-x}S$), and pyrite (FeS_2) [53].

2.4.1 Corrosion types found in geothermal systems

The uniform dissolution of the metal equally throughout the entire metal surface leads to thinning of the exposed surface. This is also called *uniform corrosion* which is quantified as mm/yr. Previously, it was mentioned that $FeCO_3$ (Equation 16) and FeS_m (Equation 17) corrosion products can form on carbon steel exposed to H_2S and CO_2 [51]. If the corrosion product/film is uniform on the surface the metal is protected, if not there is a possibility of establishing anodic and cathodic regions (i.e., galvanic cell) in the unprotected surface accelerating corrosion. It has been reported the corrosion rates increase with increased acidity from the dissolution of the H_2S and CO_2 gases in water and in some cases the presence of chlorides which breaks stable protective corrosion films [42].

The most severe corrosion forms occur after the galvanic cell is established when the passive layer breaks causing pitting or cracking of materials. Underneath the unprotective corrosion product, accelerated local attack occurs in small areas forming filled-up cavities which penetrate or grow into the material until leakage is observed by forming a macro-pit or hole. *Pitting and crevice* corrosion occurs in metals or alloys that passivate; however, the latter can be present in non-passive materials. Crevice corrosion, for instance, can happen to metals in geothermal conditions because of deposits, mill scale, and mechanical fissures. Contrary to most other forms of corrosion, it is dependent on geometry. Stagnant environments promote pitting and crevice corrosion and the susceptibility of the materials is influenced by pH, chloride content and temperature [42,54,55].

Another form of localized corrosion damage is manifested as cracking. These catastrophic failures are environmentally induced cracking (EIC) caused by the simultaneous presence of applied tensile stress or internal stresses in the material and a corrosive environment [42]. The EIC is a broad term that represents the involvement of the environment in the cracking process and includes *stress corrosion cracking, sulfide stress corrosion cracking, hydrogen blistering, hydrogen embrittlement and hydrogen induced cracking*. The corrosion phenomenon predicts or determines the type of corrosion or defined term, which are mostly caused by corrosion fatigue, stresses and high-temperature hydrogen/ sulfur attack of stainless and duplex steels [56–59]. Dissolved H_2S can be aggressive and incite carbon and low alloy steels attack, forming sulfide corrosion products while releasing hydrogen. The effect of absorption/diffusion of atomic hydrogen from the cathodic reactions into the steel lattice induces hydrogen damage. The hydrogen uptake (recombining atomic H^+ to H_2 gas) contributes both in cracking of the materials and hydrogen embrittlement [58]. The microstructure of the stressed material must be

susceptible to these type of cracking, according to the results of a wealth of study undertaken and reported on diverse corrosion conditions.

Additionally, fluid flow and the presence of foreign materials during flow can induce or aggravate corrosive effects. *Erosion-corrosion* is associated with high-velocity fluids carrying solid particles that damage or destroy the surface coating of a material, which would otherwise serve as the material's protective film [42,60]. Fluid turbulence commonly occurs along pipe bends, nozzles, and turbine blades, which causes the material's surface to become more undercut. *Cavitation corrosion* is one form of corrosion connected to fluid flow*,* in which gas bubbles from the moving fluid implode the surface, is the supply of aggressive phases to the active or film/deposit-buried surface by fluid flow-induced corrosion [42]. Furthermore, water droplets transported in the steam phase can cause erosive corrosive effects on steels.

Corrosion-resistant alloys (CRAs) play a crucial role in harsh geothermal brine/ gas environments [46,61,62]. A list of commonly used CRAs in geothermal application and additional information is presented in Appendix B. CRAs consist of metals such as chromium, cobalt, nickel, titanium, or molybdenum. When combined with other metals, they can increase corrosion resistance and generate alloys that provide reliable corrosion protection, reducing the need for costly maintenance and repair. The stability of the surface protective corrosion layer has been demonstrated to improve by the passive alloying elements, with nickel and nickel alloys often recommended for high-temperature environment [42,63].

Recent articles have expanded the definition of elemental alloying to include compositionally complex alloys (CCAs), which show promise for use in a range of industrial applications. Contrary to conventional alloys, which typically contain one or two base elements, CCAs contain a large number of principal elements, and there are considerably more potential high-entropy alloy (HEA) compositions than there are for conventional alloys [28]. In materials science and engineering, HEAs in the form of bulk or coatings are currently a focus of extensive scientific attention. HEAs are defined as "those formed of five major elements mixed in equimolar or near-equimolar ratios" in one of the earliest publications [64]. A critical review of recent studies aimed at addressing fundamental issues related to phase formation in HEAs established that HEAs are promising candidates for new applications, warranting further research due to their significant structural and functional potential as well as design techniques [65].

3 Materials and Methods

3.1 Test materials

Specialized coatings were developed to improve resistance to geothermal wear, corrosion, erosion, and scaling, to increase the service life of drilling tools or plant components. The research focused on coatings from air spray, electroless nickel plating (ENP), high-velocity oxygen fuel (HVOF), electro-spark deposition (ESD), and laser cladding (LC)/ laser metal deposition (LMD) techniques. An extensive test program was outlined for adaptive DoE (design of experiment) to determine the optimum coating materials, coating process and parameters. Among the various process parameters varied for coating fabrication within the Geo-Coat and Geo-Drill projects for the testing in this project were:

- Powder chemistry, metallurgy, and feed rate
- voltage, pulse rate, current intensity, laser power, capacitance, spraying distance and gas feed rate
- temperature, speed, duration, and post-treatment
- feasibility of incorporating second phase nanoparticles, surfactant concentrations, agitation.

Tables 2 and 3 present the coating nomenclature within this research project. Tables 2, 3 and 4 list the various received materials, powder compositions chosen, manufacturing processes, and other descriptive terms used in the project. Substrates used in the project were fabricated to fit the test equipment (see Table 2) and often used as reference material to evaluate the performance and determine the candidacy of the newly developed materials for use in geothermal applications.

Table 2. Summary of main coating materials tested in JP1 -JP4 and the sample geometry.

Coating type	Deposition technique	Composition	Test ID	Geometry -autoclave test
Cermet	Laser cladding (LC) / laser metal deposition (LMD)	WC-CoCr	WC	
		CrC-NiCr	CrC	
		WC-CrC-Ni	WC-CrCNi	
Amorphous/nano-crystalline		FeCCrBMoSiW	Amor	
High entropy alloy (HEA)	High-velocity oxygen fuel (HVOF)	$CoCrFeNiMo_x$	$HEA_{0.85}$/HEA_{27}	
		CoCrFeNiMo	HEA/HEA_{20}	
Self-fluxing	Electro-spark deposition (ESD)	NiCrFeBSi	Flux	Geometry - tribology test
GO modified PPS/PTFE	Air spray	PPS-PTFE	0wt.% GO	
		PPS-PTFE/GO	0.5wt.% GO	
Duplex Electroless Ni-P+PTFE	Electroless nickel-phosphorus plating (ENP)	high P^a/low P^b+PTFE	hp/LPptfe	
		high P^a/high P^b+PTFE	hp/HPptfe	
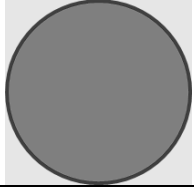
[a]Phosphorus (P) = Ni-P undercoat　　　　[b]Phosphorus (P) = Ni-P topcoat

Table 3. Summary of main coating materials tested in the project.

Polymer coatings: GO modified PPS/PTFE		HVOF coatings		ENP coatings - Duplex	
	0wt% GO		$WC_{10}Co_4Cr$		HP-HP-PTFE_ht[a] 300°C
	0.5wt% GO		Cr_3C_2-NiCr		HP-HP-PTFE_ht[b] 250°C
	1wt% GO		WC-Cr_3C_2-Ni		HP-HP-PTFE_as_plated
	2.5wt% GO		FLUX ($NiCr_{17}Fe_4B_{3.5}C_1Si_4$)		HP-LP-PTFE_ht[a] 300°C
	5wt% GO		AMOR ($FeC_3Cr_{25}B_5Mo_{20}Mn_5Si_2W_{10}$)		HP-LP-PTFE_ht[b] 250°C
					HP-LP-PTFE_as plated
			HEA (CoCrFeNiMo)	ENP coatings - Single layer (PTFE: 5-10g/l)	HP-PTFE_as plated
			$HEA_{0.85}$ ($CoCrFeNiMo_{0.85}$)		MP-PTFE[c]_as plated
			$HEA_{1.3}$ ($CoCrFeNiMo_{1.3}$)		LP-PTFE_as plated

[a]High Phosphorus (HP);　　　Low Phosphorus (LP);　　　Heat treated (ht) -300 °C, 2 hours
[b]High Phosphorus (MP);　　　Low Phosphorus (LP);　　　Heat treated (ht) -250 °C, 4 hours
[c]Medium Phosphorus (MP)

Table 4. Summary of powder composition for tested high entropy alloy coatings (HEACs) in the project.

Coating type	ID n*	Test ID	Nominal composition					
			Element	Co	Cr	Fe	Ni	Mo
CoCrFeNi-Mo_X	1	HEA_{20}[a]	at%	20.0	20.0	20.0	20.0	20.0
	2	HEA_{27}	at%	19.2	19.2	19.2	19.2	26.6
	3	HEA_{18}	at%	20.6	20.6	20.6	20.6	17.6
	1	HEA[b]	wt%	18.3	16.2	17.4	18.3	29.9
	2	$HEA_{1.3}$	wt%	16.7	13.2	15.8	15.7	38.6
	3	$HEA_{0.85}$	wt%	19.2	16.9	18.2	19.1	26.6

[a]HEA represented in atomic ratio　　　　[b]HEA represented in mol ratio

Down-selection was required for the best-performing coating materials to satisfy the project's objectives (Table 1) for the many coatings evaluated (Tables 2, 3) in the project. The materials were down-selected through systematic and fine-tuned laboratory testing. The testing included dry sliding, 80 °C water sliding and selected corrosion tests. The results of pin-on-disk (PoD) tests were employed as the first stage in down-selection (JP1 and JP2), and these coatings were subsequently evaluated in the autoclave for evaluating the corrosion behavior and resistance at elevated temperature in simulated geothermal environment. (JP3 and JP4). The chemical composition of the coatings is reported in Tables 4 to 8.

Table 5. Chemical composition of the surface (topcoat) of the Ni-P + PTFE duplex coatings reported in JP1.

Surface analysis Ni-P+PTFE	Ni		P		C		F	
	wt.%	at. %	wt.%	at%	wt.%	at. %	wt.%	at. %
ENP1*	81.8	54.9	5.3	6.7	9.8	32.0	3.1	6.4
ENP2	76.7	46.6	3.2	3.7	10.9	32.5	9.2	17.2
ENP3	72.3	38.8	3.0	3.0	17.8	46.7	6.9	11.5

ENP1 – ENP3 shows an increasing amount of added PTFE

Table 6. Surface chemical composition of HEA coatings from the different deposition techniques reported in JP2

Test ID	Elemental concentration (wt.%)					
	Co	Cr	Fe	Ni	Mo	O
HVOF-HEA_Mo_{27}	15.8	11.2	13.2	9.7	32.7	17.4
ESD-HEA_Mo_{27}	8.4	18.4	25.4	9.5	19.8	18.0
LC-HEA_Mo_{27}	13.1	20.2	17.2	20.5	10.5	15.6
HVOF-HEA_Mo_{20}	13.0	17.2	15.3	18.7	24.0	11.8
ESD-HEA_Mo_{20}	10.2	11.7	23.0	5.0	9.0	37.0
LC-HEA_Mo_{20}	23.3	9.8	29.1	7.4	9.8	19.5

Table 7. Chemical composition of the HVOF-deposited coatings in JP3

Test ID	Powder composition	Elemental composition (wt.%)											
		Al	Mn	Si	B	Mo	Co	Fe	Ni	C	W	Cr	O
WC	$WC_{10}Co_4Cr$	1.6	-	-	-	-	9.5	-	-	9.2	75.1	3.8	0.8
CrC	$75Cr_3C_2$-25NiCr	0.5	-	-	-	-	-	-	23.1	11.2	-	61.7	3.6
WC-CrCNi	WC-$20Cr_3C_2$-7Ni	-	-	-	-	-	-	-	8.0	-	68.4	22.1	1.5
Flux	$Cr_{14}Fe_5Si_5B_3Ni_{bal}$	-	-	3.7	4.3	-	-	3.5	65.1	8.9	-	14.2	0.3
Amor	$Cr_3C_2Mo_{20}W_{10}Mn_5B_5Si_2Febal$	-	1.8	1.0	0.2	13.5	-	51.1	-	6.8	5.9	18.8	0.9
HEA$_{0.85}$	$CoCrFeNi$-$Mo_{0.85}$	6.1				21.6	18.0	17.2	17.7	0.7		15.1	3.6

Table 8. Chemical composition of the surfaces of the different composite coatings tested in the JP4

Material	Test ID	Nominal composition (wt.%)						
		F	C	Si	S	P	Ni	O
PPS-PTFE	PTFE	11.1	57.0	5.3	17.2	-	-	9.4
PPS-PTFE + 0.5wt.%GO	PPS-PTFE/GO	12.4	57.4	2.9	20.3	-	-	6.2
ENP/PTFE	hp/LPptfe	3.4	7.6	-	-	2.9	86.1	-
	hp/HPptfe	6.9	10.5	-	-	10.3	72.4	-

Table 9. Chemical composition of the low alloy substrate steel type: 817M40 in JP3

Element	C	Cr	Ni	Mo	Mn	Si	B	O
(wt%)	0.4	1.2	1.4	0.2	0.3	0.6	0.01	0.03
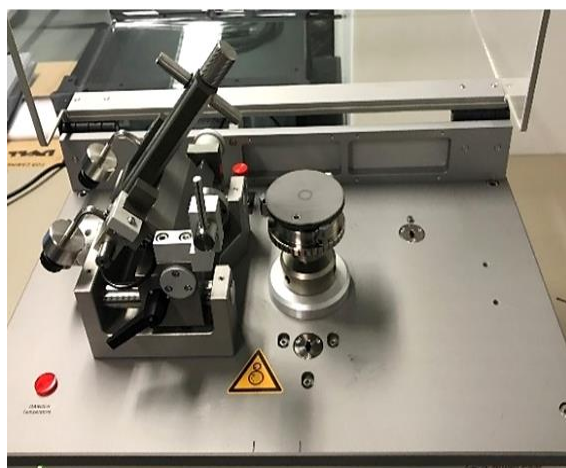
(a)*: The pin-on-disk tribometer showing a mounted test sample.*

(b): The autoclave with the lid opened shows 8 mounted test samples.

Figure 4. Mounted 40 mm diameter coated sample for wear test (left) and 50x25x3 mm coated samples with PTFE separators mounted for corrosion test (right).

3.2 Test Equipment and test conditions

3.2.1 Pin-on-Disk (PoD) Equipment

The Anton Paar® TRB[3] tribometer (Figure 4a) was used to conduct pin-on-disk (PoD) tribological studies on coatings and state-of-the-art (SoA) substrates. The configuration and measurements conformed to the ASTM G99 standard [66]. The pin or ball was

positioned in a stationary holder in the tribometer setup, and the sample stage rotated around the disk's center. The pin holder was mounted with the test load (F_n). As seen in Figure 5, the study involved a ball pressed against a coated or uncoated metallic surface during unidirectional sliding to generate friction (F_t).
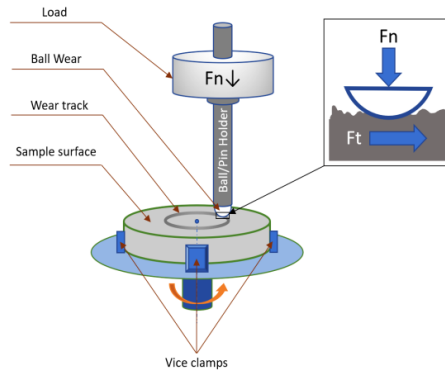
Figure 5. Schematic of friction and wear test using a Pin-on-disk tribometer

3.2.2 Test conditions for tribological performance

The tests were performed using the equipment shown in Figure 5. The stage in the tribometer configuration rotated around the disc's axis while the ball was fixed in a fixed holder. The sliding tests were carried out in a dry, ambient laboratory environment with loads ranging from 2 N to 30 N. Chromium steel (100Cr6) and a hard tungsten (WC) ball with a 6 mm diameter served as the rubbing counterparts. The roughness parameter (Ra) was obtained from the surfaces using a Taylor Hobson Ametek stylus profilometer. The microhardness of the coatings was determined by the Vickers and Knoop method considering the thickness of the coatings using a Buehler (VH1202 Wilson®) tester. Test forces of approximately 50 gf or 100gf were used for indentation in the cross-section of the coatings recording hardness values in $HK_{0.05}$ and $HV_{0.1}$ scale. All tests were repeated and the averages with corresponding standard deviations (SD) were reported. Three Parallel tests were taken from the PoD experiments at the same loads for repeatability. The radius of the wear track was adjusted between 5 mm and 20 mm for each sample during the testing due to the disk size and with the relevant linear velocity variations dependent on the total distance covered. The test period and motor speed were held constant at 3600 seconds and 200 revolutions per minute, respectively. As a result, all experiments at varying velocities produced the same number of cycles.

Table 10. Parameters used in wear testing of in JP1 and JP2.

Journal paper	Temperature [°C]	Sliding time [min]	Counter Ball [6mm]	Load [N]	Sliding radius [mm]	Sliding speed [cm/s]	Sliding distance [m]	Cycles [-]
JP2	RT*	60	WC	5	5-11	10.47-20.3	377-830	12000
JP1		30 / 60	100Cr6	2-10	7-19	14.7-39.8	528-1433	12000

Testing at ambient/room temperature (RT)

Table 11. Parameters used in wear testing of in JP4.

	Temperature	Sliding time	Counter	Load	Radius	Sliding speed	Sliding distance	Cycles
	[°C]	[min]	Ball	[N]	[mm]	[cm/s]	[m]	[-]
JP4	RT	60	100Cr6	5/10	7	10.47	528	12000

3.2.3 Autoclave Equipment

The experiments were conducted in the University of Iceland's HPHT laboratory, which can conduct high-temperature and high-pressure (HTHP) studies with geothermal fluids. Gas detection and warning systems are placed in the laboratory to assure the safety of H_2S and CO_2 gas research. The equipment in this laboratory is a 3-liter autoclave (Figure 6a) manufactured of C276 Hastelloy and rated for temperatures up to 500 °C and pressures up to 300 bar, with a magnetic stirrer built into the lid. The custom-made sample holder is fixed to the reactor lid, and the test samples installed between the vertical sample holder supports illustrated in Figure 4(b) during the experiment. A lifting mechanism controls the lid, which is lowered and sealed to the autoclave vessel (reaction chamber) by nine bolts and covered with an insulation jacket during tests. Heating components around the autoclave vessel control the temperature, and the autoclave cover is insulated during experiments. In the vessel, the temperature is detected using a Pt100 temperature sensor, and pressure measured using a Keller pressure transmitter. The gas components are fed from the gas filling panel (Figure 6a, right side of the image), with the filling rate determined by Brooks mass flow controllers to the autoclave through inlet lines in the bottom (Figure 6b). After each test, the autoclave is depressurized through gas draining line at the top whiles the test solution is drained from the bottom. Figure 6(b) depicts the flow of components through the autoclave equipment.

| (a) | (b) |
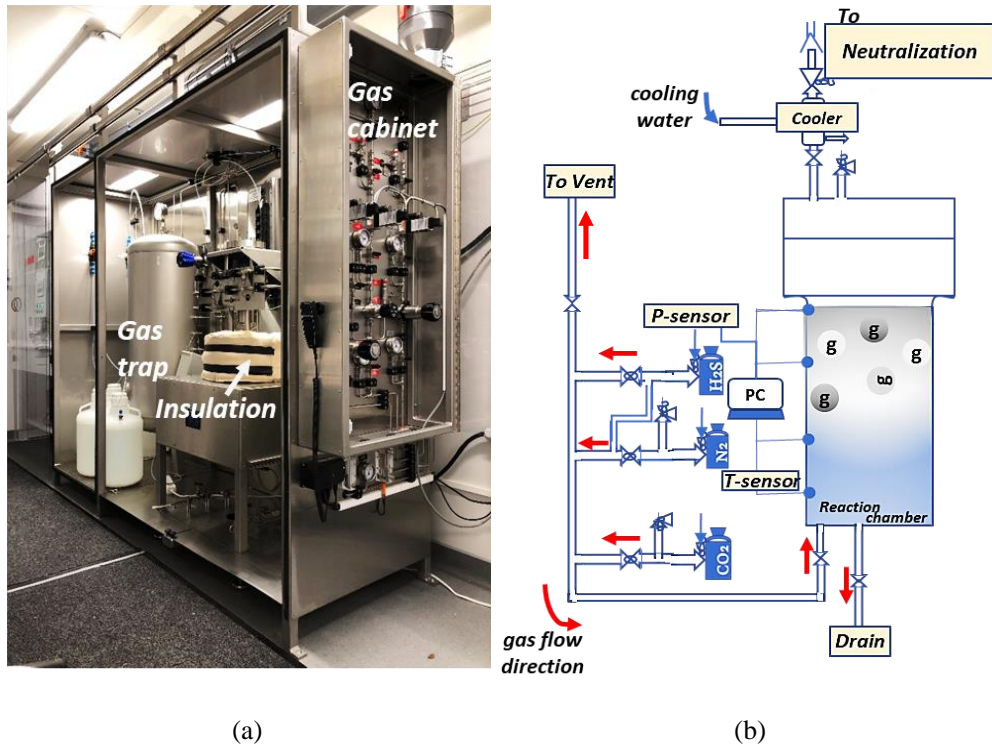
Figure 6. Simplified (a) process flow diagram of the test setup and (b) the autoclave equipment for the HTHP test

3.2.4 Fluid calculation and preparation for corrosion performance

The experiments were performed in two different environments and three different test conditions in Table 11, (A) normal drilling conditions, and (B, C) gas leakage of high temperature corrosive geothermal fluid into the well. The findings were reported in JP3 and JP4.

The water in Iceland has a pH of about 9 at ambient temperature because it flows over basaltic rocks, which are more basic with lower SiO_2 concentration and higher MgO and CaO content [67]. Water in continental Europe, on the other hand, runs through more developed rocks with higher SiO_2 content. As a result, the pH of the ground water is close to neutral, and it is frequently treated with chlorine to reduce undesired biological activity. The cooling fluid used in geothermal drilling is often water-based with a high pH (9) to minimize corrosion [68] and sometimes with supplemental polymers to enable easier transport of cuttings due to lower viscosity. Icelandic tap water is most frequently utilized as a drilling fluid due to its high pH level. Thus, it was agreed based on suggestions from the drilling experts involved in the research that Icelandic tap water should be used to simulate a geothermal drilling fluid for the typical drilling conditions in the corrosion testing. The composition of the tap water is presented in Table 12. In simulating the HTHP conditions of HT geothermal well with H_2S and CO_2 ingress, the autoclave can be pressurized from the bottom with N_2, H_2S, and CO_2 through the gas inlet lines. As shown

in the example of the pressure and temperature plot given in Figure 7, the closed volume autoclave was pressurized to lower pressures at room temperature and attained the experimental pressure while heating to experimental temperature. The Peng-Robinson chemical models in Phreeqc® software were used in calculating the physiochemical parameters and solution chemistry for autoclave corrosion experiments in Table 12. In HT geothermal locations, particularly in Iceland, the chosen test parameters (120 °C/250 °C at 50 bar) are typical (see Appendix B). These HT geothermal wells frequently have bottom hole fluid temperatures between 250 and 280 °C and well head temperatures up to 200 °C. The ideal wellhead pressures for the HT geothermal wells are typically in the 40–70 bar range. An additional set of calculations presented in Tables 13 and 14 show the results of the vapor and water phase compositions at experimental pressure and temperature for conditions B and C.
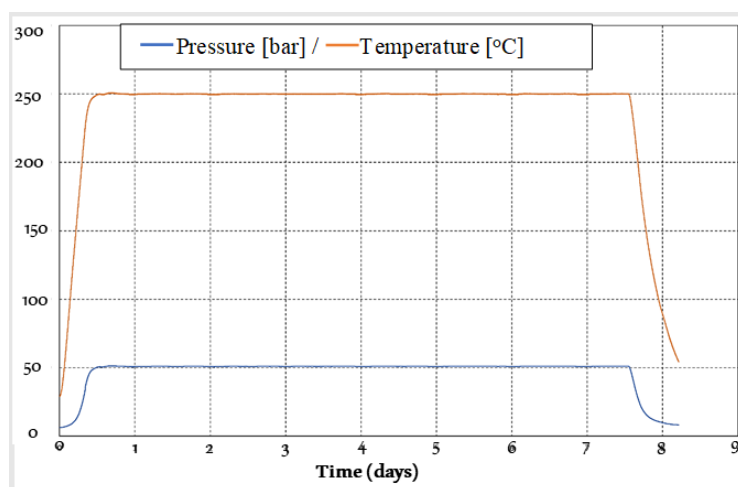
Figure 7. Example of pressure and temperature plot from a 7 day test at 50 bar and 250 °C.

Table 12. Summary of test conditions for HTHP corrosion experiments.

Test type	T (°C)	P (bar)	Phases	Time	pH*	Fluid Chemistry
A	120		Water	14 days	9	N_2 and tap water
B	250	50	Vapor - Water	7 days	7	DI water with added NaCl, NaOH, H_2S, CO_2, and N_2
C			Vapor – Water	7 days	9	N_2 and tap water

pH at ambient/room temperature (RT)

Table 13. The composition of elements dissolved in the tap water from ICP-OES (Inductively coupled plasma - optical emission spectrometry) analysis.

Content	Si	Na	Ca	Mg	K	Fe	Al	B	S
ppm*	13.296	11.048	4.920	0.886	0.3185	0.0005	0.01825	0.0105	2.517

Concentrations in ppm (parts per million by weight)

Table 14. Physiochemical parameters and solution chemistry for autoclave corrosion experiments in JP3 and JP4.

Test parameters	Drilling condition in HT well (14 days test)		gas conditions in two-phase geothermal fluid at HT (7 days test)	
	tap water		DI water with 10 mmol NaOH and 5 mmol NaCl	
Pressure	50 bar		50 bar	
Temp	25 °C	120 °C	25 °C	250 °C
Gas	PP* (atm)	PP (atm)	PP* (atm)	PP (atm)
CO_2	-	-	4.5	3.8
H_2S	-	-	1	0.2
H_2O	-	--	-	41.6
N_2	ca. 35	ca. 50	5	7
Solution	-	-	2 kg	2 kg
CO_2	-	-	2199 ppm	1698 ppm
H_2S	-	-	417 ppm	514 ppm
pH	8.9	7.2*	5.7	6.8*

* - Partial pressure of gas component before it reacted with the solution and predicted pH values.

Table 15. Principle chemical components dissolved in the water phase at 250°C and 50 bar used in JP3 and JP4.

CO_2 [mg/kg]	HCO_3^- [mg/kg]	H_2S [mg/kg]	HS^- [mg/kg]	N_2 [mg/kg]	Na^+ [mg/kg]	Cl^- [mg/kg]
1981	393	472	99	292	350	181

Table 16. Chemical composition of vapor phase at 250°C and 50 bar used in JP3 and JP4.

H_2O [mol%]	CO_2 [mol%]	H_2S [mol%]	N_2 [mol%]
79.8	8.5	0.3	11.4

3.3 Experimental procedure

3.3.1 Tribological: friction and wear testing

The tribological wear tests of the as-sprayed coatings were carried out at room temperature using a tribometer (TRB[3], Anton Paar® Graz, Austria). The setup, procedures and measurements were all done per the ASTM G99 standard [66]. At applied loads ranging from 2 N to 30 N, the ball was pressed against a 30 mm or 50 mm coated disc in a unidirectional dry sliding test. Based on the Archard elastic model [69] (i.e., *H₀/H value should be high*)[1] and the known properties of WC (tungsten carbide) coatings on bearings, seals and turbine blades [70], WC balls were considered as a counter body to the sprayed harder coatings in the laboratory accelerated-wear test to produce an appreciable and

reliable wear assessment. The test time and motor speed were held constant at 3600 seconds and 200 revolutions per minute, respectively (linear speed: 10.47 cm/s). The speeds selected for this study are similar to bottom-hole percussive drilling activity (rotating at 75–200 rpm) [44] but slower than the actual rotational speeds of process equipment such as steam turbines. For instance, geothermal turbines (with targeted units such as bearings, valve stem, shaft, rotor, and blades). Here, we model startup and shutdown scenarios in power industries with periodic slower-speed runs (100–600 rpm for an hour) to allow for troubleshooting before reaching typical operational speeds [71]. Moreover, steam turbines work smoothly at input pressures ranging from 400 to 4000 kPa and vibration levels under 2.54 mm/s [72] when there is no shaft/rotor imbalance. On the contrary, for low load but high wear applications such as coatings in pins, valve seats, sleeves, sliding cases, heat exchanger units etc., the proposed coatings were tested with a lower hardness 6 mm chromium steel (100Cr6) ball. The steel ball is described as having a hardness of 60–66 HRC and a density of 7.83 g/cm^3 by the manufacturer. The WC ball has manufacturing specifications of 6 mm in diameter, 14.95 g/cm^3 in density, and 1640 HV in hardness.

The friction coefficient (CoF) was continuously observed while sliding with the applied load (F_n). Version 8.1.5 of the Instrument X® software from Anton Paar® was used to process the tribometer's data. The average values of regions and entire stable stages of the acquired tangential friction (Ft) curve were calculated using the dimensionless COF (μ) Equation 18. The standard deviation (SD) was used to determine how much fluctuation occurred throughout the acquisition of F_t process. The SD values obtained primarily explain the degree of fluctuation of COF (μ) and geometric contact changes during the test that could reflect the contact interface properties.

$$\mu_{sample} = Ft/Fn \; (-)$$
18

The wear rate, w_{sample} [mm^3/Nm], was evaluated according to Equation 19 by measuring the volume of the removed material, V (mm^3), and using the applied load, F_n (N), and the distance covered during testing, L (m). Three parallel tests were run for each coating and SoA materials and the average findings were presented.

$$w_{sample} = V/F_n L \; (mm^3/Nm)$$
19

3.3.2 Autoclave corrosion testing

The test coupon's shape is designed to be mounted onto the sample holder with 6 mm diameter PTFE insulators to decrease the gap size (μm) while minimizing crevice effects and galvanic in corrosion testing (Figures 8a). The test samples are sandwiched between the vertical sample holder supports shown in Figure 8a and the custom sample holder mounted inside the vessel's lid. The vessel is then filled with the reaction/test solution and the lid is sealed. The coatings were exposed for 14 days at 120 °C in tap water pressured to 50 bar with N_2, simulating standard geothermal well drilling conditions. The second experiment subjected coatings to HTHP corrosion testing for 7 days in a simulated geothermal fluid at 250 °C in liquid/vapor phase conditions compressed to 50 bar with corrosive gases N_2 and CO_2/H_2S. The autoclave, which held 2 liters of liquid, is purged with N_2, H_2S, and CO_2 through the bottom gas inlet pipes. The gas filling panel collects the gas components, and the rate of filling is controlled by Brooks mass flow controls. During

the autoclave test, the top row (A) of the sample holder is in the vapor phase, above the waterline (B), and the bottom row (C), which is in the liquid phase, is completely submerged in water (Figure 8b). In the simulated liquid and vapor phase test conditions, a preliminary 7-day HTHP corrosion test was successfully carried out at 250 °C and 50 bar to establish positions A, B, and C (in Figure 8b) for each sample. Four parallel samples and two sets of test procedures were created to simulate geothermal drilling and aggressive conditions. After each experiment, the autoclave is depressurized using a gas draining line on the top. The drained gas is trapped in plastic containers holding a 13.5 pH water-based solution comprising dissolved zinc acetate and NaOH. The H_2S gas from the autoclave reacts with the zinc acetate to form solid ZnS, which separates from the solution and settles in a container (Figure 6a).

(a)   (b)
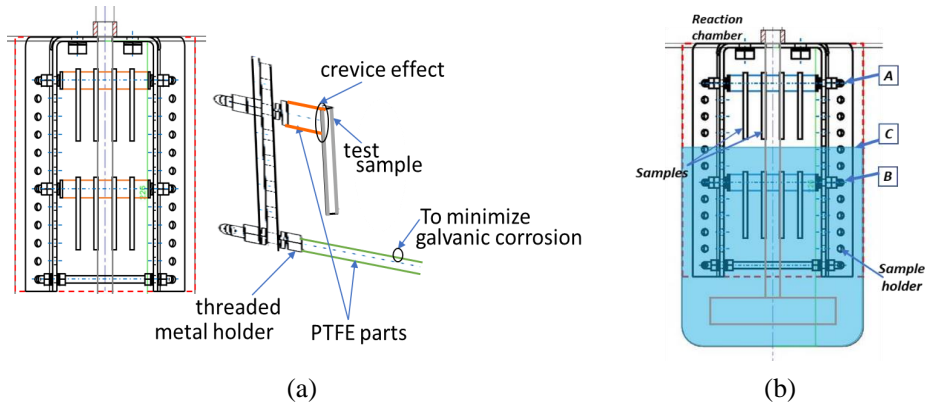
Figure 8. cross-section of the reaction chamber (a) showing the sample holder and PTFE separators and (b) the 3/4 liters-filled reaction vessel with sample positions for A - vapor phase, B – interface/waterline, and C - liquid phase.

3.4 Coatings and Fluid Characterization

3.4.1 Pre-exposure analysis

The received coatings were representative of the materials intended for exploitation on the geothermal industrial component. Therefore, all testing was conducted on the as-received conditions since the surface finish was taken into consideration in the preparation stages. Following solvent cleaning with either ethanol or acetone, the surface conditions and microstructure were investigated before wear and corrosion testing. The analytical technique was dependent on the physical (e.g., thickness) and chemical properties (e.g., composition) of the coating.

3.4.2 Microstructure and chemical composition analysis

Microstructural and elemental composition analysis was carried out with a Zeiss Supra 25® scanning electron microscope (SEM) fitted with an Energy Dispersive X-ray Spectroscopy Detector (EDX/EDS). The Oxford® EDS instrument had a Si(Li) X-ray detector and INCA Energy® 300 expanded with AzTec® software. The materials analyzed with SEM and EDS equipment were performed on the surface and in the microstructure before and after testing to examine wear and corrosion (damage) as well as wear debris and corrosion products present. The hardness of the microstructure was obtained from surfaces and in the cross-section of the samples using either Vickers (HV) or Knoop (HK) method

depending on the thickness of the coatings. The latter has a diamond indenter forming a square indent suitable for relatively thicker and harder alloy compositions. The depth of indentation at an applied load on the material gives the value of hardness for the sample. The samples for microstructural and compositional analysis were sectioned using diamond wafering blades and mounted in thermosetting phenol-formaldehyde resin (i.e., bakelite), and cast under pressure. The equipment used for hardness investigation was Buehlers® VH1202 Wilson micro-hardness tester.

3.4.3 Crystal structure analysis

Structures, phases, crystal orientations, and other structural parameters such as average grain size, crystallinity, and defects were evaluated using the X-ray diffraction (XRD) technique. The test samples were studied using Empyrean, Panalytical® Malvern-UK XRD instrument with Cu Kα radiation ($\lambda = 1.54056$ Å), 45 kV, 40 mA. The data were collected in the standard θ - 2θ range and the patterns were analyzed with HighScore® software. The tested samples were also analyzed with the XRD equipment to evaluate the corrosion products present after the exposure period. Carbon nanomaterials in the form of graphene oxide (GO), is a material of interest in this project. The structural analysis of GO was not well-suited to the SEM/EDS or XRD techniques and therefore differentiated from the coating matrix using Raman spectroscopy which is sensitive to symmetric covalent bonds with little or no natural dipole moment. The data acquisition was in the range of 10 min using 785 nm / 532 nm laser power. The equipment used for the characterization of the samples was a Horiba Scientific® LabRAM HR Evolution – Raman Spectrometer equipment.

3.4.4 Surface roughness and volume loss analysis

The Kruss® Drop Shape Analysis system was used to calculate contact angles using the sessile drop method. The DSA 100® equipment determined a surface's wettability by water to predict hydrophobic properties before testing. Roughness measurements were conducted with a Taylor Hobson® Ametek stylus profilometer to determine the topological surface parameters. Ra is the arithmetic mean deviation which was frequently the roughness parameter of interest. A non-contact optical profilometer generated 2D and 3D topographic profiles to investigate the unworn and worn morphological surface features. Following the wear test, the optical profilometer was used to extract cross-sectional profiles and photographs from the worn areas. Final averages were used to quantify the wear volume and wear rate from the retrieved profiles, which came from at least three representative sites on the wear tracks. The instrument used was Solarius® equipment expanded with the Mountains® software.

3.4.5 Inductively coupled plasma-optical emission spectrometry (ICP-OES)

This method of analysis uses a spectrometer and plasma to identify the elements present in liquid (mostly water-dissolved) samples. The test solutions were quantified before and after the corrosion experiment. The sample is dissolved, atomized, and ionized in the ICP-OES, which also generates plasma and emits electromagnetic radiation. A concentration is computed using calibration after the light intensity at each wavelength is measured. The equipment used in this work is a Thermo Scientific® iCAP 7400 Duo MFC with a CETAC® ASX-560 autosampler.

3.5 Limitation

The main limitations of this study are related to the materials and experimental conditions used to assess the wear and corrosion behavior of the developed coatings. Numerous components in the geothermal energy production process require protection from the discharged hot fluid, but a limited number of representative areas and coating compositions studied in this work. The type of protection varies according to the geophysical characteristics and geochemical fluid properties, which differ depending on location. This means that the coatings were subjected to low loads and speeds during the tribological test rather than high-speed cycles like those found in turbines or drilling. This is not the case in low-load or low-speed applications such as valves and other casings. As a result, the selected conditions were designed to obtain measurable values to determine critical performance parameters.

Likewise in simulating the test environment, the operating conditions vary greatly, and acquiring information for a wide range of geothermal systems is challenging. The test pressures are low for drilling environments but may be high on other surface equipment while the temperature and aggressive gases compared to 2–3 km conventional wells are typical of volcanic areas and therefore not globally representative. However, the tested aqueous solution's physical and chemical characteristics are determined by averaging the chemical compositions of geothermal fluids reported in publications, which contain data from numerous sample locations in wells with high temperatures. However, the temperatures fall within the specified medium to high enthalpy ranges needed for power production while CO_2/H_2S are encountered frequently in drilled gas wells. The pH of the fluid is not monitored during the HT autoclave corrosion test. However, geochemical modeling was carried out in the early stages of fluid calculation inculcating the effect of pH on the chemical composition at increasing temperature test. No corrosion rate estimation was carried out, however no proposed testing standards are developed for coatings since the thickness of each coated sample varies even for the same deposition technique. Key performance indicators were used in this study to evaluate the corrosion behavior of the coatings after exposure.

4 Results

4.1 Summary of results of Journal papers

4.1.1 Journal paper 1 (JP1)

G. Oppong Boakye, A.M. Ormsdóttir, B.G. Gunnarsson, S. Irukuvarghula, R. Khan, S.N. Karlsdóttir, The effect of polytetrafluoroethylene (PTFE) particles on microstructural and tribological properties of electroless Ni-P+PTFE duplex coatings developed for geothermal applications, Coatings. 11 (2021) 670. https://doi.org/10.3390/coatings11060670. This paper contributes to answering RQ1.

Summary of results journal paper 1:

Ni-P thin adhesive layer and Ni-P+PTFE top functional layer form a functionalized duplex structure of the coating. The objective of this study was to test the mechanical and tribological properties of the developed Ni-P-PTFE duplex coatings with varying P, PTFE content and different loads (N). The addition of P reduces the crystallinity of the coating as well as the possibility of internal stresses being introduced due to microstructural changes observed in the XRD analysis. When PTFE is uniformly dispersed in the matrix, dry sliding tests of medium P (moderate stress state); Ni-P+PTFE coating demonstrated excellent friction and wear behavior. Worn or damaged coatings showed the presence of spalls, increased Fe content and oxides. The results showed maximum wear protection of the substrates at the lowest load; however, increasing load and sliding cycles increased the wear rates, and 79% increased lubrication was recorded for the duplex coating with 10g/L PTFE.

4.1.2 Journal paper 2 (JP2)

G. Oppong Boakye, L.E. Geambazu, A.M. Ormsdottir, B.G. Gunnarsson, I. Csaki, F. Fanicchia, D. Kovalov, S.N. Karlsdottir, Microstructural Properties and Wear Resistance of Fe-Cr-Co-Ni-Mo-Based High Entropy Alloy Coatings Deposited with Different Coating Techniques, Appl. Sci. 12 (2022) 3156. This paper contributes to answering RQ1.

Summary of results journal paper 2:

HEAs containing two compositions of Co, Cr, Fe, Ni, Mo with different molar ratios were deposited by three deposition techniques (i.e., HVOF, LC, ESD) and tested with the same loads and sliding speeds. The LC and HVOF techniques were the most efficient in depositing the coatings compared to the ESD method. The ESD is a manual deposition method that uses an electrode feedstock therefore, adhesion of the coatings to the substrate was poor. In addition, high amount of porosity and cracks was observed in the coating. The HVOF method produced a lamella structured coating and highly oxygenated along the splat boundaries. The LC produced coatings which mechanically adhered to the substrate. These coatings were rougher, thicker, and denser (over 1 mm) compared to HVOF and

ESD techniques. However, the wear rates were lower for the HVOF coatings compared to LC- and ESD- produced coatings. The $Co_{19}Cr_{17}Fe_{19}Ni_{18}Mo_{27}$ coating had better friction and wear resistance results than $Co_{20}Cr_{20}Fe_{20}Ni_{20}Mo_{20}$. The variation in microstructure and hardness of each coating was explained by the difference in Mo content in the coatings which contributed to improved resistance to deformation through the formation of BCC, σ and presumably the μ phases.

4.1.3 Journal paper 3 (JP3)

G. Oppong Boakye, E.O. Straume, B.G. Gunnarsson, D. Kovalov, S.N. Karlsdottir, Corrosion Behavior of HVOF developed Mo-based High Entropy Alloy coating and selected Hard coatings for High Temperature Geothermal Applications. Submitted (01/08/2022) to Corrosion Science. This paper contributes to answering RQ2 and RQ3.

Summary of results journal paper 3:

The objective of this work focuses on testing the corrosion resistance of a $CoCrFeNiMo_{0.85}$ high entropy alloy (HEA) and five hard coatings fabricated by the HVOF technique. The coatings were immersed in a simulated alkaline geothermal drilling environment at 50 bar pressure and either 120 °C water or 250 °C with H_2S/CO_2. The coatings showed good general corrosion resistance in water at 120 °C. The 250 °C H_2S/CO_2 experiment maintained both liquid and vapor (saturated steam) phases. The hard coatings experienced localized damage due to temperature and H_2S/CO_2 effects where the extent of corrosion was severe during vapor phase exposure. A noticeable result was subsurface pitting of the amorphous coating exposed to liquid phase, but after the vapor phase test, oxidation and sulfidation of phases were found filling the pores and splat boundaries. The HVOF developed $CoCrFeNiMo_{0.85}$ outperformed selected hard coatings showing more structural integrity and no localized corrosion damage.

4.1.4 Journal paper 4 (JP4)

G. Oppong Boakye, E.O. Straume, D. Kovalov, S.N. Karlsdottir,

Wear-reducing nickel-phosphorus and graphene oxide-based composite coatings: Microstructure and corrosion behavior in high temperature geothermal environment. Corrosion science 209 (2022), 110809. This paper contributes to answering RQ1 to RQ3.

Summary of results journal paper 4:

The fairly thin electroless Ni-P-PTFE duplex and air-sprayed polymer-based coatings were tested in the same test environment as reported in JP3 to investigate their corrosion behavior. The polymer-based coating was modified with graphene oxide (GO) and the electroless Ni-P was heat-treated at 300 °C for 2 hours after deposition to improve its microstructural properties and performance. The results showed that the added nanoparticles improved wetting and friction properties as well as wear resistance of the coatings. The heat treatment of high P, Ni-P+PTFE coating increased the hardness attributed to the formation of Ni_3P structures, thereby improving wear resistance of the coating. In general, GO-modified coating performed better in the 120 °C test compared to the reference material. The Ni-P/PTFE duplex with the lowest P content was suitable in

oxidizing (i.e., H_2O) environment at 120 °C. This is because a crystalline Ni-O corrosion scale was observed as a protective layer after corrosion. The high P was more promising for CO_2/H_2S environment, where a thick, adherent Ni-S surface scale was observed in microscopic images. All the coatings were unprotective and prone to substrate corrosion at 250 °C in H_2S/CO_2 environment.

4.2 Summary of results of conference papers

4.2.1 Conference paper I (CPI)

G. Oppong Boakye, D. Kovalov, A.Í. Thórhallsson, S.N. Karlsdóttir, V. Motoiu, Friction and Wear Behaviour of Surface Coatings for Geothermal Applications, PROCEEDINGS in WORLD GEOTHERMAL CONGRESS 2020+1, April 26–May 22021, Reykjavik, Iceland, Paper no. 27069

Summary of results conference paper 1:

A pin-on-disk test was performed on substrates that are representatives of geothermal plant components and HVOF cermet-coated steels. This study aims to investigate the tribological properties of coatings deposited on steel substrates. The cermets had a lower coefficient of friction and wear volume compared to the bulk 304 and 630 stainless steel substrates. Microscopic examinations of the wear tracks identified abrasive wear mechanisms and showed thin material removal in the coating. The results led to a better selection of test parameters, for instance load, speed, and sliding cycles.

4.2.2 Conference paper II (CPII)

G. Oppong Boakye, E.O. Straume, B.A. Rodriguez, D. Kovalov, S.N. Karlsdóttir, Microstructural Characterization, Corrosion and Wear Properties of Graphene Oxide Modified Polymer Coatings for Geothermal Drilling Applications, PROCEEDINGS in CORROSION 2020 June 14-18, 2020, Conference and Expo, Houston, Texas, USA.

Summary of results conference paper 2:

An electrochemical test in a 3.5wt% NaCl solution and a pin-on-disc sliding test was performed to determine the corrosion and wear resistance of the polymer coatings. In this work, the polyphenylene sulfide-polytetrafluoroethylene (PPS-PTFE) matrix was modified with graphene oxide (PPS-PTFE/GO) to improve the mechanical properties, corrosion, and wear resistance, to provide coatings for drilling components for HT geothermal well environment. The results show that low GO content positively impacted the morphology, WCA, lubricity, corrosion, and wear resistance of the composite coating. The 1wt% GO polymer coating is the most promising; based on the reduction of corrosion current density and 72% reduction in friction compared to carbon steel. The results led to the improvement in coating preparation, chemistry, and ranking of the GO-modified composites. Here, a new formulation with 0.5wt% GO was included in the design and testing matrix and contributed partly to the results presented in conference lecture 2 and JP4.

4.2.3 Conference paper III (CPIII)

G. Oppong Boakye, A.M. Ormsdottir, B.G. Gunnarsson, A. Tabecki, F. Zhang, S.N. Karlsdóttir, Development of High Velocity Oxygen Fuel Corrosion Resistant Coatings; A Comparison between Novel High Entropy Alloy and Conventional Cermet Coatings for Geothermal Applications, PROCEEDINGS in CORROSION 2022 Conference and Expo, March 6-10, 2022, San Antonio, Texas, USA.

Summary of results conference paper III:

Autoclave corrosion testing of $CoCrFeNiMo_{0.85}$ - HEA and Cermet coatings was conducted for 14 days, fully immersed in a simulated alkaline geothermal drilling environment at 120 °C and 50 bar. After surface SEM/EDS examination, good corrosion resistance was observed which affords the use of these coatings in the said environment. In addition, an electrochemical-accelerated corrosion test in a 3.5 wt.% NaCl was carried out at ambient temperature to investigate the behavior of the coatings in the presence of Cl^- ions. The $CoCrFeNiMo_{0.85}$ outperformed Cr_2C_3-NiCr and WC-$Co_{10}Cr_4$ coatings showing more positive corrosion potential (E_{corr}) measured and the lowest corrosion current density (i_{corr}) in the presence of chlorides. The surface oxide film was observed with high Mo and Cr content. The results of this study led to further improvement in test conditions by including HT autoclave test with corrosive species (i.e., 250 °C with H_2S/CO_2 in liquid/vapor phase).

4.2.4 Conference paper IV (CPIV)

G. Oppong Boakye, E.O. Straume, A.M. Ormsdóttir, B.G. Gunnarsson, S. Irukuvarghula, R. Khan, S.N. Karlsdóttir, Corrosion and Wear properties of Electroless Ni-P+PTFE Hydrophobic Coating Developed for Geothermal Environment, PROCEEDINGS in European Corrosion Congress – EUROCORR 2022, August 28–Sept. 01, 2022, Berlin, Germany.

Summary of results conference paper IV:

The corrosion and wear resistance of as-plated and heat-treated ENP/PTFE duplex coatings were tested using an autoclave, electrochemical methods, dry sliding, and HT-wet sliding tests. The results show that the duplex coating on metallic materials provided good performance under both dry and HT-wet conditions. The heat-treated low P containing - duplex had high wear resistance at room temperature, at 80 °C, in saline fluid compared to low alloy steel. The duplex showed no localized damage but experience uniform dissolution of Ni to form a corrosion layer in the alkaline H_2O environment at 120 °C in the autoclave. In the polarization test, no significant difference was observed in the measured corrosion potential (E_{corr}), however, the high P coatings showed larger passive region and passive current density (i_{pass}). This study contributed significantly to the results published in JP4. The results in JP4 included an additional duplex composition and HT autoclave test with corrosive species (i.e., 250 °C with H_2S/CO_2 in the liquid/vapor phase).

4.3 Answers to research questions – Study results

The main goals of the PhD study were to investigate the tribological (friction, wear) and corrosion behavior of coatings under simulated test conditions for geothermal applications. Three questions were set as the primary points of attention to address the research topic.

RQ1: how does the microstructure of the coatings affect the friction and wear properties of the developed coatings?

Answer to RQ1:

The observed effect of fabrication method, coating morphology, thickness and phase structures on friction and wear is attributed to differences in the microstructure. These effects significantly influenced the mechanical and tribological behaviors. The results of the friction and wear tests showed that the carbon-based materials (PTFE, GO and Cermets) compared to the alloys can significantly lower the friction coefficient but not necessarily the overall wear rates. BCC metals are typically more brittle in the alloys. The primary cause is that they have larger dislocation lattice friction stresses than FCC metals. As a result, BCC lattices exhibit less dislocation mobility, which results in less plasticity as compared to FCC metals. The results in HEA showed that the formation of intermetallic compounds can significantly lower the coating's friction coefficient and wear rate when transition elements are added in molar ratio.

A steady friction and wear behavior was observed for the Cermets, 0.5wt% GO-based coating, and ENP/PTFE (10g/L) duplex from the dry sliding test conditions. The mildly scratched surfaces typically of abrasive wear mechanism from SEM analysis signified low material loss influencing high stability during the evolution of friction coefficient. The stable friction and wear characteristics observed are outlined in JP1 for ENP coatings attributed to the structure of the added PTFE nanoparticles which contributed to shear reduction from carbon film formed on the surfaces during sliding. In the alloyed materials, for instance the HEAs, the running-in was severe and the steady-state was harder to achieve during the evolution of friction coefficient. The large average roughness (Ra) of the coatings contributed to a high volume of material removed attributed to pronounced elastic shakedown from the and/or the gradual accumulation of debris. This observation is important for selecting the coatings for practical applications. Deposition by the three different techniques (HVOF, LC, and ESD) did not significantly change this phenomenon because of the powder metallurgy process and high average roughness values (Ra) compared to the other hard coatings. However, the wear rate estimated from measurable material loss showed high wear resistance for the HVOF-developed HEA alloys - $CoCrFeNiMo_x$ which were sensitive to hardness, mixed internal structure and the dislocation impedance by grain boundaries identified and described in JP2. The HVOF-sprayed $CoCrFeNiMo_{0.85}$ showed the best wear resistance among the HEACs.

RQ2: Do the wear resistant coatings resist corrosion in the simulated high temperature geothermal fluid (H_2O or H_2O -based with H_2S/CO_2 gaseous species)?

Answer to RQ2:

Yes, the wear resistant coatings are resistant to corrosion in H_2O at 120 °C, however, the cermet coatings were prone to microcracks.

No, the corrosion behavior in hot geothermal fluid (250 °C) with H_2S/CO_2 gaseous species is distinct for each wear resistant coating material.

The PPS-PTFE/GO, heat treated ENP/PTFE duplexes, $CoCrFeNiMo_{0.85}$, and 'hard' coatings showed the best wear resistance after the tribological testing. Oxygen-based and sulfur-based corrosion products described in JP3 and JP4 were present on the surface of the coatings in all the test environments occurring from coating/fluid reactions. The autoclave testing in the simulated standard drilling geothermal water (i.e., 120 °C water) showed good results for all the coatings except the high phosphorus-containing - ENP/PTFE duplex. However, in the higher temperature fluid (i.e., 250 °C) containing CO_2/H_2S gases, the coatings were prone to general and localized corrosion damage from reaction with corrosive anion species and aqueous gases. For instance, the added GO nanosheets demonstrated low wetting ability preventing surface contamination while suppressing corrosion effects in the polymer matrix at 120 °C outlined in JP3. Additionally, the duplex of high phosphorus content showed poor corrosion resistance in the oxidizing (H_2O) environment at 120 °C. On the other hand, a protective corrosion layer formed on the coatings from the H_2S reaction with N in the 250 °C test with CO_2 and H_2S gases. The results for the conventional hard coatings had high corrosion resistance in the 120°C water test with no corrosive gases. However, the coatings' corrosion resistance decreased, and this significantly depended on the composition, microstructure, interfacial defects, and fluid chemistry when CO_2 and H_2S gases were introduced (at 250 °C). The HVOF- sprayed $CoCrFeNiMo_{0.85}$ showed the highest corrosion resistance. Although, internal oxidation was observed in the coatings usually within phases and along grain boundaries, the research established and discussed the presence of the oxides from the HVOF method in JP2 and JP3. In summary, no localized damage was observed in both 120 °C and 250 °C test with CO_2 and H_2S gases.

RQ3: How does temperature and phase density of the simulated geothermal fluid (i.e., liquid/vapor with H_2S/CO_2) influence the corrosion effect on the tested coatings?

Answer to RQ3:

Yes, the temperature and phase density of the corrosive fluid (liquid/vapor) influenced the corrosion behavior in the test environments as reported in JP3 and JP4. Temperature and phase density of the geothermal fluid accelerated the corrosion behavior and promoted localized corrosion of the wear resistant coatings in this study.

The temperature effect was clearly seen in the polymer-based coatings where morphological changes were observed with pore formation and SiO_2 deposition after testing at 250° C in the higher temperature test. Microcracking was also observed in the

cermets from inherent microstructural and temperature effects. Although the 120° C water test showed little to no corrosion in the liquid phase, significant cracking was found in the coatings described in JP3 after reporting in CPIII. All of the tested coatings experienced an increase in corrosion when exposed to saturated steam (vapor phase) that contained CO_2/H_2S gases. The distinct corrosion behavior with CO_2 and H_2S species in the liquid and vapor phase was easily discernible by the reaction products, as revealed in Fe-based amorphous and Ni-based coatings as described in JP3. The FeCrMoWMnBCSi was prone to subsurface pitting in the liquid phase through the dissolution of Fe, however, the localized damage observed after vapor phase exposure was oxidation/sulfidation of the passive metals in pits, intersplats, and around nano amorphous phases. On the surfaces of the two Ni-based coating systems (self-fluxing -NiCrBSiFe and ENP/PTFE duplex), a thick and adherent NiS corrosion scale was seen after the liquid phase test, but a porous, thin scale was observed after exposure to the vapor phase.

Based on the findings in this work, it can be concluded that the fairly thin GO modified polymer and ENP/PTFE duplex coatings experience substantial localized damage in the coating layers, as well as substrate corrosion due to galvanic effects. The hard coatings were susceptible to both general and localized corrosion damage but the HEA alloys – CoCrFeNiMo$_{0.85}$ showed the best corrosion performance in all test environments.

5 Discussion

The corrosion and wear studies of coatings were conducted in test conditions and simulated laboratory environments in this PhD project. Corrosion studies in sour or H_2S/CO_2 environments have been studied on materials, but a comprehensive tribological and corrosion studies targeted for the physical and chemical properties of hot fluids from geothermal fields are uncommon, thus the accelerated laboratory test on such materials is needed. The findings from this study have improved knowledge on the wear and corrosion behavior of already available and new coating compositions in relevance to geothermal environments and can be aptly incorporated into the different decision-making and project stages of geothermal energy development.

According to the studies, the wear resistance of the coatings in dry sliding of the customary or already available coatings from older publications was established. The developed duplex or GO-modified polymer coatings also provided good wear resistance and a drastic reduction in friction. The PTFE and GO nanoparticles in the coatings promoted a functionalized surface of the steel increasing stability during friction evolution and steady wear behaviors. Similarly, from the corrosion results, the large surface area of the particles served as obstructions to the electrolyte penetrating the coating matrix preventing corrosion of the substrate. However, coatings and underlying substrate were rather susceptible to localized damage at a higher temperature with H_2S/CO_2 gases from galvanic effects outlined in JP4.

In the wear-resistant cermets, the localized corrosion in the H_2S/CO_2 environment is concluded to be driven by microcracking of the hard and brittle coatings during exposure. Notwithstanding, the test solution with no added gases also caused microcracking in the coating layers suggesting temperature contribution to the coating damage. Less damage was observed for CrC-NiCr compared to WC-based coatings (i.e., WC-CoCr and WC-CrC-Ni) due to oxidation of the WC matrix. Segregation in Cr and Ni was found to be the prevalent damaging phenomenon in the CrC-NiCr coating. These results match those from earlier studies [73,74], but in this study, we also observed sulfidation of the Co binder and oxidation of the W in the WC matrix following exposure to vapor or the saturated steam phase. Therefore, the combination of both microcracking from temperature effects and localized corrosion of W in WC-CrC-Ni showed it was more prone to localized corrosion where corrosion of the underlying substrate was reported. Contrary to the wear results, a reverse behavior was observed where resistance was attributed to film forming abilities of the WC matrix during sliding. Thus, the best wear resistance was observed in the harder WC-CoCr and WC-CrC-Ni coatings compared to CrC-NiCr.

Comparatively, the Ni-based self-fluxing alloy (NiCrFeBSi) coatings were susceptible to general corrosion. No localized damage was observed in the coatings or at the coating/substrate interface. The synergistic effects of H_2S and CO_2 caused the dissolution of Ni at the highest test temperature producing a bilayer corrosion product mainly of Ni, and Fe, Cr in the alloy. A distinction between the protective bilayer was seen in the thickness and uniformity from cross-section analysis which was dependent on the fluid properties. The densest and most stable form of the bilayer was observed after liquid phase

exposure. Despite this, a clean surface was seen on the amorphous Fe-based alloy coatings. The negligible amount of corrosion products suggested little-to-no general corrosion behavior. This was established from cross section analysis where localized corrosion damage were seen subsurface. The coatings experienced peeling and spalling of coating layers near-surface and below the surface, corrosion around splat boundaries and substantial pitting in the matrix. The subsurface porosity was apparent in the liquid phase exposure whereas, void enrichment (pores filling) was observed in the cross section in the vapor phase test. In JP3, it was concluded that the pitting mechanism aroused from the dissolution and diffusion of Fe near original porosities in the matrix was supported by the inward influx of vacancies explained by the Kirkendall effect [75].

The HEA coatings are relatively new and have not been actively adopted for industrial applications yet. In this study, two HEA coatings (i.e., $CoCrFeNiMo_{0.85}$ and $CoCrFeNiMo$) were developed by three deposition techniques investigated for potential application in the geothermal environment. The results indicated deposition techniques produced coatings of hard nanophases and a mixed internal microstructure. These structures translated to unsteady friction but a better wear performance except the ESD -HEA coatings where coating/coating and coating/substrate adhesion issues were encountered (JP2). Further autoclave corrosion testing of the best wear resistant HVOF-developed HEA indicated $CoCrFeNiMo_{0.85}$ could be applicable as a coating material on components used in both liquid and steam/vapor conditions withstanding temperatures up to 250 °C. This is because $CoCrFeNiMo_{0.85}$ coating was not prone to localized corrosion damage, however, there is a possibility of forming a thin oxide/sulfide scale from general corrosion mechanisms from the studies with and without H_2S/CO_2 gases. The HVOF spray and impact process produced multi-phase or grain boundaries that enhanced wear resistance in JP2 but identified as a potential site for internal oxidation in JP3. The research conclusively found no internal deterioration in either the 120 °C or 250 °C simulated geothermal environments. Moreover, the LC-HEAs that demonstrated acceptable resistance (10^{-5}) may be evaluated further in comparable corrosion conditions for possible use in applications with higher corrosion or lower wear demands. A continuously layered structure (i.e., without clearly defined grain boundaries) was found in the microstructural analysis of LC-HEA produced by the laser cladding method of deposition in JP2. The findings showed a continuous or uniform layered structure (no obvious grain boundaries) from deposition with the laser cladding method in JP2. Therefore, the LC-HEA which showed acceptable wear could be further evaluated in similar corrosion environments for potential use in higher-corrosion or lower-wear demanding applications. The HEAs could be a feasible candidate for future wear and/or corrosion resistant materials in geothermal drilling and equipment operation environments where high wear is encountered.

The overall goal of the research, which was guided by four (4) working principles and three (3) sub questions, was to identify wear and corrosion resistant materials for use in various geothermal drill tools and plant equipment. The following is a summary of the main findings for the corrosion testing of Ni-P, PTFE/GO, CERMETS, and HEA coatings, which the down-selected coatings from tribological tests (high wear resistance). The study identifies the most promising candidate and potential application for different geothermal power plant equipment in Appendix B -Table list.

- For the *high temperature (250 °C) corrosion test in the simulated geothermal environment in the Autoclave with H_2S and CO_2:*

  - The HVOF sprayed **HEA -CoCrFeNiMo$_{0.85}$** outperformed the other evaluated coatings regarding the corrosion resistance showing no evidence of corrosion damage (corrosion cracks, pits, crevices) and no visible corrosion penetration through the coating.

  - The performance of the **CERMETS** was poor; cracks and the penetration of corrosion species into the coatings was observed, indicated by sulphur and oxide corrosion products that were detected in the cross-section of the coatings.

  - The **ENP (Low P/ High P)** and **PTFE/GO** coatings both showed poor corrosion resistance, i.e., cracks and corrosion penetration into the coating were observed. The corrosion penetration was throughout the thickness of both coatings. The higher phosphorus duplex, **hp/HPptfe** had slightly less penetration, adherent protective scale and thus would be preferred for in applications.

- For the *lower temperature (120 °C) corrosion test in the simulated geothermal environment in the Autoclave with no gases:*

  - The **HEA -CoCrFeNiMo$_{0.85}$** coating demonstrated the highest corrosion resistance to the test conditions over the other tested coatings. No cracks or corrosion penetration in the coating were found.

  - Contrary to the high temperature corrosion test, the developed **CERMETS**, **PTFE/GO** and the **ENP (Low P/ High P)** coatings were successful in hindering corrosion of the substrate, thus performing better than for the 250°C test. However, corrosion penetration into the substrate materials were found in the microstructural analysis to more extent for **WC - type cermet** and **hp/HPptfe** coatings, likely due to the effects of considerably micro-cracks and micro-porosity, respectively. The corrosion effects were only pronounced for the **WC-CrCNi**, regarding the depth of corrosion penetration. Thus, the **hp/LPptfe** is recommended over **hp/HPptfe**. Moreover, **PTFE/GO, WC-CoCr, CrC-NiCr, FLUX, and AMOR** coatings showed better corrosion resistance in this environment.

6 Conclusions

The right selection of corrosion resistant metallic materials has been the focus of numerous prior articles on the topic, but the results presented in this dissertation provide information on the efficacy of friction and wear-resistant coatings in HT corrosive geothermal environments. Coatings are one method for protecting less corrosion resistant but mechanically suitable materials because the use of highly alloyed or nonmetallic materials is always mechanically or economically impractical. Commercial abrasion resistant coatings were compared to the newly developed/ modified coatings during corrosion studies to develop a benchmark on performance in the selected environments up to 250 °C. This dissertation emphasized a thorough examination of four types of coating materials: Ni-P, GO-PTFE, CERMETS, and HEA, with four specific objectives that led to three research questions. The four journal papers show how the coatings studied contribute to increased equipment durability in geothermal applications. The findings summarized in response to the three main research questions point to newly developed HEA-coatings as an alternative resistant alloy with improved corrosion and wear resistance suitable for parts in geothermal applications. The HEA ($CoCrFeNiMo_{0.85}$) material metalized with the HVOF method demonstrated a protective barrier effect on the steel substrate in both wear and corrosion testing conditions. The better compatibility can only be inferred from the findings of the dry sliding wear resistance because tribological studies on HEA-coatings are lacking compared to the selected commercial coatings. High temperature and synergistic tribological tests such as tribocorrosion analyses is the next step to expand on current knowledge and state. However, a deeper understanding of wear and corrosion mechanisms and the effect of gases (H_2S/CO_2) was established in this dissertation which can influence future design, selection, and engineering of corrosion and wear resistant materials for geothermal systems, thereby maximizing the operational life of components.

This dissertation makes a contribution by evaluating numerous coating systems on low alloyed and stainless steels for friction and wear resistance in corrosive environments up to 250 °C relevant to geothermal conditions. A deeper understanding of mechanisms was developed, establishing the foundation for future geothermal powerplant design. Furthermore, it increases the knowledge in the field of corrosion behavior of conventional and novel coating materials at high temperatures and pressure in geothermal environment where there is lacking publication and knowledge, which is increasingly important in promoting the utilization of geothermal energy most efficiently.

7 Future work

Future study is proposed by recommending more experiments that could be performed to acquire 1) quantitative measurements and 2) obtain a better understanding of the effect of temperature and fluid chemistry on the tribological properties and corrosion behavior of steel coatings. The microstructure and chemical composition as-deposited and tested samples as well as corrosion films on the coatings can be evaluated with other high-end techniques such as TEM, EPMA (equipped with EDS and WDS), and XPS. Friction and wear testing at temperatures higher than ambient conditions would be an interesting area for further study and hence provide information on wear in the 'wet corrosive' environment. Based on the findings of this thesis it would be interesting to perform tests in similar fluid density and chemistry as tested in this dissertation, but with higher Cl^- species as well as evaluating individual effects of each gas phase (i.e., H_2S, CO_2) on the corrosion behavior of the coatings. Furthermore, quantitative laboratory methods (such as electrochemical impedance spectroscopy, tafel polarization and/or linear polarization resistance) could be used to evaluate the anti-corrosion performance of protective coatings. Also, the potential to perform electrochemical test in the HTHP autoclave would be of value for further studies. Such electrochemical processes offer parameters that can be used to calculate corrosion rates, usually at ambient temperature, and to define the corrosion process, such as the start of pitting corrosion, the breakdown of protective layer, or the precipitation of corrosion products. Finally, a synergistic evaluation of corrosion and wear (tribocorrosion) properties of specific coatings, such as the novel high entropy alloy coatings, is required to bridge knowledge gaps between tribological and electrochemical behavior in the presence of a corrosive media. The interaction between mechanical and chemical factors governing tribocorrosion can be evaluated through a comparative analysis of triboelectrochemical (such as corrosion potential, galvanic cells, potentiostatic, and potentiodynamic) techniques and interpretation methods with an emphasis on sliding and fretting situations. These techniques will provide better insight on how wear can affect the kinetics of corrosion reactions of the coatings.

Bibliography

[1] D.L. Gallup, Production engineering in geothermal technology: A review, Geothermics. 38 (2009) 326–334. https://doi.org/10.1016/j.geothermics.2009.03.001.

[2] R. Dipippo, Small Geothermal Power Plants: Design, Performance and Economics, GHC Bull. (1999) 1–8. http://www.geothermalcommunities.eu/assets/elearning/7.10.art1.pdf.

[3] E. Barbier, Geothermal energy technology and current status: an overview, Renew. Sustain. Energy Rev. 6 (2002) 3–65. https://doi.org/10.1016/S1364-0321(02)00002-3.

[4] A.I. Thorhallsson, A. Stefansson, D. Kovalov, S.N. Karlsdottir, Corrosion testing of materials in simulated superheated geothermal environment, Corros. Sci. 168 (2020). https://doi.org/10.1016/j.corsci.2020.108584.

[5] E. Huenges, Geothermal Energy Systems: Exploration, Development, and Utilization, 2010. https://doi.org/10.1002/9783527630479.

[6] J.D.D. Ocampo, B. Valdez-salaz, M. Shorr, I. Sauceda, N. Rosas-gonzález, Review of Corrosion and Scaling Problems in Cerro Prieto Geothermal Field over 31 Years of Commercial Operations, in: Proc. World Geotherm. Congr., 2005: pp. 1–5.

[7] H.R. Feili, N. Akar, H. Lotfizadeh, M. Bairampour, S. Nasiri, Risk analysis of geothermal power plants using Failure Modes and Effects Analysis (FMEA) technique, Energy Convers. Manag. 72 (2013) 69–76. https://doi.org/10.1016/j.enconman.2012.10.027.

[8] L.D. Nottingham, Turbine Condition Monitoring, in: Energy Power Gener. Handb., 2005: pp. 1–65. http://asmedigitalcollection.asme.org.

[9] R.R. Reeber, Coatings in Geothermal Energy Production, Thin Solid Films. 72 (1980) 33–47. https://doi.org/10.1016/0040-6090(80)90555-6.

[10] B.G. Mellor, Surface coatings for protection against wear, Woodhead Publishing Limited, 2006. https://doi.org/10.1533/9781845691561.

[11] A. Ramalho, J.C. Miranda, Friction and wear of electroless NiP and NiP + PTFE coatings, Wear. 259 (2005) 828–834. https://doi.org/10.1016/j.wear.2005.02.052.

[12] W. Jiang, L. Shen, Z. Wang, K. Wang, M. Xu, Z. Tian, Wear resistance of a Ni-PTFE composite coating strengthened with nano-SiC particles, Mater. Res. Express. 6 (2019). https://doi.org/10.1088/2053-1591/ab320b.

[13]   C. Sun, H. Zeng, J.-L. Luo, Unraveling the effects of CO2 and H2S on the corrosion behavior of electroless Ni-P coating in CO2/H2S/Cl– environments at high temperature and high pressure, Corros. Sci. 148 (2019) 317–330. https://doi.org/10.1016/j.corsci.2018.12.022.

[14]   Y. Sui, C. Sun, J. Sun, B. Pu, W. Ren, W. Zhao, Stability of an electrodeposited nanocrystalline Ni-based alloy coating in oil and gaswells with the coexistence of H2S and CO2, Materials (Basel). 10 (2017). https://doi.org/10.3390/ma10060632.

[15]   Y. Tong, S. Bohm, M. Song, Graphene based materials and their composites as coatings, Austin J. Nanomedicine Nanotechnol. 1 (2013) 1003. https://www.researchgate.net/publication/350276510 (accessed August 14, 2022).

[16]   S.Q. Lai, L. Yue, T.S. Li, Z.M. Hu, The friction and wear properties of polytetrafluoroethylene filled with ultrafine diamond, Wear. 260 (2006) 462–468. https://doi.org/10.1016/j.wear.2005.03.010.

[17]   S. Bhargava, N. Koratkar, T.A. Blanchet, Effect of platelet thickness on wear of graphene-polytetrafluoroethylene (ptfe) composites, Tribol. Lett. 59 (2015). https://doi.org/10.1007/s11249-015-0533-2.

[18]   T. Huang, T. Li, Y. Xin, B. Jin, Z. Chen, C. Su, H. Chen, S. Nutt, Preparation and utility of a self-lubricating & anti-wear graphene oxide/nano-polytetrafluoroethylene hybrid, RSC Adv. 4 (2014) 19814–19823. https://doi.org/10.1039/c4ra01964d.

[19]   N. Nemati, M. Emamy, S. Yau, J. Kim, D. Kim, High temperature friction and wear properties of graphene oxide/polytetrafluoroethylene composite coatings deposited on stainless steel, RSC Adv. 6 (2016) 5977–5987. https://doi.org/10.1039/C5RA23509J.

[20]   A. Jabbar, G. Yasin, W.Q. Khan, M.Y. Anwar, R.M. Korai, M.N. Nizam, G. Muhyodin, Electrochemical deposition of nickel graphene composite coatings effect of deposition temperature on its surface morphology and corrosion resistance, RSC Adv. 7 (2017) 31100–31109. https://doi.org/10.1039/c6ra28755g.

[21]   R. Ding, W. Li, X. Wang, T. Gui, B. Li, P. Han, H. Tian, A. Liu, X. Wang, X. Liu, X. Gao, W. Wang, L. Song, A brief review of corrosion protective films and coatings based on graphene and graphene oxide, J. Alloys Compd. 764 (2018) 1039–1055. https://doi.org/10.1016/j.jallcom.2018.06.133.

[22]   M.A. Zavareh, A.A.D.M. Sarhan, B.B. Razak, W.J. Basirun, The tribological and electrochemical behavior of HVOF-sprayed Cr3C2-NiCr ceramic coating on carbon steel, Ceram. Int. 41 (2015) 5387–5396. https://doi.org/10.1016/j.ceramint.2014.12.102.

[23]   A.K. Maiti, N. Mukhopadhyay, R. Raman, Effect of adding WC powder to the feedstock of WC-Co-Cr based HVOF coating and its impact on erosion and abrasion resistance, Surf. Coatings Technol. 201 (2007) 7781–7788. https://doi.org/10.1016/J.SURFCOAT.2007.03.014.

[24] V.A.D. Souza, A. Neville, Mechanisms and kinetics of WC-Co-Cr high velocity oxy-fuel thermal spray coating degradation in corrosive environments, J. Therm. Spray Technol. 15 (2006) 106–117. https://doi.org/10.1361/105996306X92677.

[25] K.R. Ragnarsdottir, S.N. Karlsdottir, K. Leosson, A. Arnbjornsson, S. Gudlaugsson, H.O. Haraldsdottir, A. Buzaianu, I. Csaki, G. Popescu, Corrosion testing of coating materials for geothermal turbine application, NACE - Int. Corros. Conf. Ser. 4 (2017) 2949–2962.

[26] Y. Sakai, K. Shiokawa, N. Kunio, Recent Technologies for Geothermal Steam Turbine, in: FUJI Electr. Rev., 2005: pp. 90–95.

[27] H. Kato, K. Furuya, M. Yamashita, Exposure tests of turbine materials in geothermal steam from a deep production well, in: Proc. World Geotherm. Congr. 2000, 2000: pp. 3193–3198.

[28] D.B. Miracle, O.N. Senkov, A critical review of high entropy alloys and related concepts, Acta Mater. 122 (2017) 448–511. https://doi.org/10.1016/j.actamat.2016.08.081.

[29] S.N. Karlsdottir, L.E. Geambazu, I. Csaki, A.I. Thorhallsson, R. Stefanoiu, F. Magnus, C. Cotrut, Phase Evolution and Microstructure Analysis of CoCrFeNiMo High-Entropy Alloy for Electro-Spark-Deposited Coatings for Geothermal Environment, Coatings 2019, Vol. 9, Page 406. 9 (2019) 406. https://doi.org/10.3390/COATINGS9060406.

[30] A.I. Thorhallsson, I. Csáki, L.E. Geambazu, F. Magnus, S.N. Karlsdottir, Effect of alloying ratios and Cu-addition on corrosion behaviour of CoCrFeNiMo high-entropy alloys in superheated steam containing CO2, H2S and HCl, Corros. Sci. 178 (2021) 109083. https://doi.org/10.1016/j.corsci.2020.109083.

[31] A.I. Thorhallsson, F. Fanicchia, E. Davison, S. Paul, S. Davidsdottir, D.I. Olafsson, Erosion and corrosion resistance performance of laser metal deposited high-entropy alloy coatings at hellisheidi geothermal site, Materials (Basel). 14 (2021). https://doi.org/10.3390/ma14113071.

[32] I. Csáki, R. Stefanoiu, S.N. Karlsdottir, L.E. Geambazu, Corrosion behavior in geothermal steam of CoCrFeNiMo high entropy alloy, in: NACE - Int. Corros. Conf. Ser., 2018: pp. 1–8.

[33] F. Fanicchia, I. Csaki, L.E. Geambazu, H. Begg, S. Paul, Effect of microstructural modifications on the corrosion resistance of CoCrFeMo0.85Ni compositionally complex alloy coatings, Coatings. 9 (2019). https://doi.org/10.3390/coatings9110695.

[34] G. Oppong Boakye, L.E. Geambazu, A.M. Ormsdottir, B.G. Gunnarsson, I. Csaki, F. Fanicchia, D. Kovalov, S.N. Karlsdottir, Microstructural Properties and Wear Resistance of Fe-Cr-Co-Ni-Mo-Based High Entropy Alloy Coatings Deposited with Different Coating Techniques, Appl. Sci. 12 (2022) 3156. https://doi.org/10.3390/app12063156.

[35] M. Nosonovsky, B. Bhushan, Toward the "Green Tribology": Biomemitic Surfaces, Biodegradable Lubrication, and Renewable Energy, in: Proc. STLE/ASME 2010 Int. Jt. Tribol. Conf., San Francisco, California, USA, 2010: pp. 1–3.

[36] K. Holmberg, A. Erdemir, Influence of tribology on global energy consumption, costs and emissions, Friction. 5 (2017) 263–284. https://doi.org/10.1007/s40544-017-0183-5.

[37] P. Dumas, M. Antics, P. Ungemach, Report on Geothermal Drilling, 2013. http://www.geoelec.eu/wp-content/uploads/2011/09/D-3.3-GEOELEC-report-on-drilling.pdf (accessed August 16, 2022).

[38] K.P. Ngugi, What Does Geothermal Cost? – The Kenya Experience, 2012. http://www.os.is/gogn/unu-gtp-sc/UNU-GTP-SC-14-13.pdf.

[39] R.A. Parker, R. Graves, S.I. Batarseh, C.B. Reed, Z. Xu, H. Figueroa, N. Skinner, B.C. Gahan, Laser Drilling – Drilling with the Power of Light, Pittsburgh, PA, and Morgantown, WV, 2006. https://doi.org/10.2172/894903.

[40] D. Aravena, M. Muñoz, D. Morata, A. Lahsen, M.Á. Parada, P. Dobson, Assessment of high enthalpy geothermal resources and promising areas of Chile, Geothermics. 59 (2016) 1–13. https://doi.org/10.1016/j.geothermics.2015.09.001.

[41] C. Rubio-Maya, V.M. Ambríz Díaz, E. Pastor Martínez, J.M. Belman-Flores, Cascade utilization of low and medium enthalpy geothermal resources - A review, Renew. Sustain. Energy Rev. 52 (2015) 689–716. https://doi.org/10.1016/j.rser.2015.07.162.

[42] S.N. Karlsdóttir, Corrosion, Scaling and Material Selection in Geothermal Power Production, in: Compr. Renew. Energy, Elsevier Ltd, 2012: pp. 241–259. https://doi.org/10.1016/B978-0-08-087872-0.00706-X.

[43] P.M. Wright, Geochemistry, in: P.J. Lienau, B.C. Lunis (Eds.), Direct Use Eng. Des. Guideb., 2nd ed., United State Department of Energy, Oregon, 1991: pp. 8–12.

[44] A. Gupta, S. Chattopadhyaya, S. Hloch, Critical investigation of wear behaviour of WC drill bit buttons, Rock Mech. Rock Eng. 46 (2013) 169–177. https://doi.org/10.1007/s00603-012-0255-9.

[45] P.F.I. Ellis, M.F. Conover, Materials selection guidelines for geothermal energy utilization systems, 1981. https://doi.org/10.2172/6664808.

[46] H.S. Klapper, J. Stevens, Challenges for metallic materials facing HTHP geothermal drilling, in: NACE - Int. Corros. Conf. Ser., 2013.

[47] F. Zhang, H. Begg, N. Kale, S. Irukuvarghula, K. Franklin, K. Mallin, V. Wittig, S. Hahn, B.A. Rodriguez, F. Chowdhury, M.A. Hoque, S. Nanna, F. Ieg, D. Sebastian, Geo-Drill : Development of novel and cost-effective drilling technology for geothermal systems, in: World Geotherm. Congr. 2020+1, Reykjavik, 2020: pp. 1–8.

[48]   P.J. Blau, Effects of Tribosystem Variables on Friction, in: Frict. Sci. Technol. from Concept to Appl., Second edi, Taylor & Francis Group, London, New York, 2009: pp. 269–310.

[49]   J. Latcovich, T. Astrom, P. Frankhuizen, S. Fukushima, H. HAmberg, S. Keller, Maintenance and Overhaul of Steam Turbines HMN, Int. Assoc. Eng. Insur. 38th Annu. Conf. 42 (2005) 46. http://www.steamforum.com/pictures/wgp4205 Turbine.pdf.

[50]   M. Pourbaix, R.W. Staehle, Lectures on Electrochemical Corrosion, 1973. https://doi.org/10.1007/978-1-4684-1806-4.

[51]   J. Banaś, U. Lelek-Borkowska, B. Mazurkiewicz, W. Solarski, Effect of CO2 and H2S on the composition and stability of passive film on iron alloys in geothermal water, Electrochim. Acta. 52 (2007) 5704–5714. https://doi.org/10.1016/j.electacta.2007.01.086.

[52]   M. de K. Thompson, The Reaction Between Iron and Water in the Absence of Oxygen, Trans. Electrochem. Soc. 78 (1940) 251. https://doi.org/10.1149/1.3071303.

[53]   M. Singer, B. Brown, A. Camacho, S. Nesic, Combined effect of CO2, H2S and acetic acid on bottom of the line corrosion, in: NACE - Int. Corros. Conf. Ser., 2007: pp. 1–25.

[54]   W.F. Bogaerts, I. Winstons, Geothermal corrosion: High-temperature pitting of stainless steels and Ni-alloys, in: NACE - Int. Corros. Conf. Ser., 2017: pp. 2973–2987.

[55]   Y. Wang, G. Cheng, W. Wu, Q. Qiao, Y. Li, X. Li, Effect of pH and chloride on the micro-mechanism of pitting corrosion for high strength pipeline steel in aerated NaCl solutions, Appl. Surf. Sci. 349 (2015) 746–756. https://doi.org/10.1016/j.apsusc.2015.05.053.

[56]   L.K. Zhu, Y. Yan, L.J. Qiao, A.A. Volinsky, Stainless steel pitting and early-stage stress corrosion cracking under ultra-low elastic load, Corros. Sci. 77 (2013) 360–368. https://doi.org/10.1016/j.corsci.2013.08.028.

[57]   S.N. Karlsdóttir, S.M. Hjaltason, K.R. Ragnarsdottir, Corrosion testing in H2S abatement system at hellisheidi geothermal power plant in Iceland, in: NACE - Int. Corros. Conf. Ser., 2016: pp. 3009–3022.

[58]   W. Wu, Z. Liu, S. Hu, X. Li, C. Du, Effect of pH and hydrogen on the stress corrosion cracking behavior of duplex stainless steel in marine atmosphere environment, Ocean Eng. 146 (2017) 311–323. https://doi.org/10.1016/j.oceaneng.2017.10.002.

[59]   S.N. Karlsdóttir, S.M. Hjaltason, K.R. Ragnarsdóttir, Corrosion behavior of materials in hydrogen sulfide abatement system at Hellisheiði geothermal power plant, Geothermics. 70 (2017) 222–229. https://doi.org/10.1016/j.geothermics.2017.06.010.

[60] F. Brownlie, T. Hodgkiess, A. Pearson, A.M. Galloway, A study on the erosion-corrosion behaviour of engineering materials used in the geothermal industry, Wear. 477 (2021) 203821. https://doi.org/10.1016/j.wear.2021.203821.

[61] K.R. Ragnarsdottir, A. Arnbjornsson, S.N. Karlsdottir, H.O. Haraldsdottir, Preliminary corrosion testing of explosive clad materials in geothermal environment, in: NACE - Int. Corros. Conf. Ser., 2018: pp. 1–8.

[62] W.D. MacDonald, J.S. Grauman, Exposure testing of UNS R53400, R56404 and N06625 in simulated salton sea geothermal brine, in: NACE - Int. Corros. Conf. Ser., 2018: pp. 1–9.

[63] S.N. Karlsdóttir, T. Jonsson, A. Stefánsson, Corrosion Behavior of High Alloy Austenitic Stainless Steel in Simulated High Temperature Geothermal Environment, in: Corros. 2017/NACE Int. Pap. No. 9280, 2017: pp. 1–12. https://doi.org/10.1016/j.anpedi.2011.02.007.

[64] J.W. Yeh, S.K. Chen, S.J. Lin, J.Y. Gan, T.S. Chin, T.T. Shun, C.H. Tsau, S.Y. Chang, Nanostructured high-entropy alloys with multiple principal elements: Novel alloy design concepts and outcomes, Adv. Eng. Mater. 6 (2004) 299–303. https://doi.org/10.1002/adem.200300567.

[65] Y.F. Ye, Q. Wang, J. Lu, C.T. Liu, Y. Yang, High-entropy alloy: challenges and prospects, Mater. Today. 19 (2016) 349–362. https://doi.org/10.1016/j.mattod.2015.11.026.

[66] ASTM G99, Standard Test Method for Wear Testing with a Pin-on-Disk Apparatus, Annu. B. ASTM Stand. 05 (2011) 1–5. https://doi.org/10.1520/G0099-05R10.2.

[67] M.J. Gunnarsdottir, S.M. Gardarsson, G.S. Jonsson, J. Bartram, Chemical quality and regulatory compliance of drinking water in Iceland, Int. J. Hyg. Environ. Health. 219 (2016) 724–733. https://doi.org/10.1016/j.ijheh.2016.09.011.

[68] NACE MR0175/ ISO 15156-1, Petroleum and natural gas industries. Materials for use in H2S-containing Environments in oil and gas production., 2009. www.iso.org (accessed May 1, 2022).

[69] J.F. Archard, Contact and Rubbing of Flat Surfaces, J. Appl. Phys. 24 (1953) 981–988. https://doi.org/10.1063/1.1721448.

[70] U.D. Mannem, K. Anand, D.M. Gray, F. Ghasripoor, Protective coatings which provide wear resistance and low friction characteristics, and related articles and methods, 11/610,826, 2008. https://patents.google.com/patent/US20080145649A1/en (accessed July 16, 2019).

[71] R.X. Perez, D.W. Lawhon, Installation, Commissioning and First Solo Run, in: Oper. Guid. to Gen. Purp. Steam Turbines An Overv. Oper. Princ. Constr. Best Pract. Troubl., 1st ed., John Wiley & Sons, Inc, Salem, Massachusetts, 2016: pp. 147–186.

[72] R.X. Perez, D.W. Lawhon, Operator's Guide to General Purpose Steam Turbines: An Overview of Operating Principles, Construction, Best Practices, and Troubleshooting, 1st ed., John Wiley & Sons, Inc, Salem, Massachusetts, 2016. https://doi.org/10.1002/9781119294474.

[73] M.R. Thakare, J.A. Wharton, R.J.K. Wood, C. Menger, Exposure effects of strong alkaline conditions on the microscale abrasion-corrosion of D-gun sprayed WC-10Co-4Cr coating, Tribol. Int. 41 (2008) 629–639. https://doi.org/10.1016/j.triboint.2007.07.012.

[74] J.E. Cho, S.Y. Hwang, K.Y. Kim, Corrosion behavior of thermal sprayed WC cermet coatings having various metallic binders in strong acidic environment, Surf. Coatings Technol. 200 (2006) 2653–2662. https://doi.org/10.1016/j.surfcoat.2004.10.142.

[75] A.D. Smigelskas, E.O. Kirkendall, Zinc Diffusion in Alpha Brass, Trans. AIME. 171 (1947) 130–142.

Appendix A

Journal Paper 1

G. Oppong Boakye, A.M. Ormsdóttir, B.G. Gunnarsson, S. Irukuvarghula, R. Khan, S.N. Karlsdóttir,

The effect of polytetrafluoroethylene (PTFE) particles on microstructural and tribological properties of electroless Ni-P+PTFE duplex coatings developed for geothermal applications,

The Effect of Polytetrafluoroethylene (PTFE) Particles on Microstructural and Tribological Properties of Electroless Ni-P+PTFE Duplex Coatings Developed for Geothermal Applications

Gifty Oppong Boakye [1], Arna María Ormsdóttir [1], Baldur Geir Gunnarsson [1], Sandeep Irukuvarghula [2], Raja Khan [2] and Sigrún Nanna Karlsdóttir [1,*

[1] Mechanical Eng. and Computer Science, Faculty of Industrial Eng., University of Iceland, Hjardarhagi 2-6, Reykjavík, Iceland; gob13@hi.is (G.O.B.); arnamaria@hi.is (A.M.O.); bgg8@hi.is (B.G.G.)
[2] TWI Ltd., Granta Park, Cambridge CB21 6AL, UK; sandeep.irukuvarghula@twi.co.uk (S.I.); raja.khan@twi.co.uk (R.K.)
*   Correspondence: snk@hi.is

Abstract: The selection of electroless nickel-phosphorus plating (ENP) has been inclined towards their properties and advantages with complex geometry applications. These properties include coating uniformity, low surface roughness, low wettability, high hardness, lubricity, and corrosion- and wear-resistance. Materials used in geothermal environments are exposed to harsh conditions such as high loads, temperature, and corrosive fluids, causing corrosion, scaling, erosion and wear of components. To improve the corrosion- and wear-resistance and anti-scaling properties of materials for geothermal environment, a ENP duplex coating with PTFE nanoparticles was developed and deposited on mild steel within the H2020 EU Geo-Coat project. ENP thin adhesive layer and ENP+PTFE top functional layer form the duplex structure of the coating. The objective of this study was to test the mechanical and tribological properties of the developed ENP-PTFE coatings with varying PTFE content. The microstructural, mechanical and tribological properties of the as-deposited coating with increasing PTFE content in the top functional layer in the order: ENP1, ENP2 and ENP3 were evaluated. The results showed maximum wear protection of the substrates at the lowest load; however, increasing load and sliding cycles increased the wear rates, and 79% increased lubrication was recorded for the ENP2 duplex coating. The wear performance of ENP3 greatly improved with a wear resistance of 8.3×10^4 m/mm^3 compared to 6.9×10^4 m/mm^3 for ENP2 and 2.1×10^4 m/mm^3 for ENP1. The results are applicable in developing low friction, hydrophobic or wear-resistive surfaces for geothermal application.

Keywords: composite coating; electroless-nickel plating; friction; geothermal; geo-coat; wear

1. Introduction

Electroless nickel plating (ENP) is a conventional deposition method that involves a chemical reduction of Ni^{2+} from an aqueous solution onto metallic substrates. Placing a coating of a nickel-phosphorus alloy (Ni-P) on a surface is the commonest form of ENP plating. The low-to-high phosphorous material, which typically ranges from 3 to 14 wt% [1], has a significant effect on the deposited electroless nickel-phosphorous layer properties. ENP offers a broad application spectrum via its inherent high coating uniformity, good adhesion, low roughness, high hardness, and corrosion- and wear-resistant properties. Furthermore, it is possible to enhance the mechanical and tribological properties by adding particles as reinforcements to optimize their industrial efficiency [1–4].

The concept of reinforcement is to adjust the wide-range performance of the ENP coatings to achieve specific desired properties. In literature, the common co-deposition processes with either or both soft and hard particles developed over time include: SiO_2, Al_2O_3,

ZrO_2, TiO_2, Mo, MoS_2, PTFE, Diamond, CNT, SiC, CNT-SiC, Si_3N_4, WC, ZnO, B_4C, BN, TiN [3,5–12]. The target application areas include microelectromechanical systems (MEMS), textile, foundry tools, automotive, aerospace, membrane reactors, and heat exchanger units [3]. In tribology, the addition of hard particles creates a hard and wear-resistant composite coating, whereas soft, solid lubricants result in a film with self-lubricating and excellent anti-stick properties [5].

Fluoropolymers (CFx) such as PTFE have low-temperature curability, hydrophobic properties, chemical inertness and thermal stability of up to 350 °C, and are often used for oil and gas coating applications [13,14]. The feasibility of incorporating the PTFE second-phase particles within the ENP matrix at relatively low temperatures and low curing time produces a synergistic advantage of the different properties of the Ni-P alloy and PTFE polymer. The surface energy range of 22 to 28 mN/m can be achieved through the Ni metal properties with the low surface energy of PTFE [15]. The material becomes hydrophobic (as low surface energy limits wettability), offering minimal microbial and anti-scaling properties, decreasing the likelihood of scaling [14] and corrosion [16]. Since PTFE has cryogenic properties and a relatively high melting point compared to the other polymers, ENP+PTFE composite coatings were applied and used in heating and cooling systems up to 290 °C [3]. Besides improved thermal conductivity [17], it also has a lower friction and energy wear rate [16,18], therefore, it could be used in areas of wear from high speeds but low contact loads or in the presence of abrasive materials such as silica scales. This indicates the composite coating could potentially provide protection in boilers, separators, condensers, and safety and pumping systems in geothermal plants.

Few studies have reported a negative impact on film quality because of the dynamic relationship between surface and mass transport during the plating processes for the ENP+PTFE compared to ENP [19]. Several researchers studying ENP technology with particle inclusion found that the ability to achieve (1) uniform particle dispersion (herein PTFE) and (2) good composite adhesion to the substrate is crucial for the coating durability, corrosion and wear performance [20–23]. Therefore, for this study, a duplex coating was fabricated considering the reviewed merits and demerits of the plating process and properties of ENP deposits. An ENP undercoat is deposited to boost coating adhesion onto a steel substrate. PTFE is embedded into the top functional layer of the same composition ENP to form a composite coating of ENP+PTFE. This study aims to improve adhesion to mild steel and assess the tribological properties as a function of different PTFE content in the top coating layer to establish potential application in geothermal power generation systems. For instance, seals, valves, and impellers are subject to friction and wear in the steam production, transmission, and reinjection systems, resulting in leaks due to poor sealing and diameter reduction from material loss. Meanwhile, in addition to avoiding delamination during high-temperature operations, the top functional layer of the duplex coating on a heat exchanger unit will mitigate challenges with drag, pressure drop, heat transfer, and abrasive wear from entrapped particles/periodic mechanical washing.

The focus of this research is to characterize the ENP duplex coatings with varying amounts of PTFE, and test the mechanical and tribological properties in an effort to develop ENP coatings where the duplex (top + undercoat) provides good protection against wear. The functionalized topcoat is expected to influence surface properties by improving friction and wear-resistance. The critical performance of the coating was evaluated against the resultant microstructural, wettability, and mechanical and tribological properties for coatings with different PTFE material content to optimize the required PTFE concentration in the duplex coatings.

2. Materials and Methods

2.1. Sample Surface Preparation

Mild steel discs (50 mm diameter) were degreased in hot alkaline solution (~50 °C) for 15 min followed by rinsing in de-ionized (DI) water. They were then etched in hot (~50 °C) H_2SO_4 solution to remove the surface oxide layer. Once the oxide layer was removed and

acid traces were removed by dipping into de-ionized water, the specimens were quickly transferred into an ENP bath.

2.2. Bath Preparation and Electroless Ni-P+PTFE Composite Coating

All chemicals were of analytical grade and purchased from Sigma Aldrich and Fisher Scientific. PTFE particles, due to their hydrophobic nature, cannot be dispersed homogeneously in water. PTFE particles and F-C4 cationic surfactant portions were mixed in DI water by mechanical stirring for 2–3 h. After that, the solution was subjected to ultrasonic treatment for 3 h. This step de-agglomerated the PTFE particles and produced a homogeneous aqueous dispersion. This was verified using the dynamic light scattering approach to measure their particle size distribution (PSD) (instrument: Malvern ZetaSizer Nano-S, Waltham, MA, USA). The average size of PTFE particles was about 307 nm, yielding a unimodal distribution. Furthermore, efforts were made to minimize defects by optimizing the amount of surfactant (0.1–0.5 g/L) to create aqueous dispersion of PTFE. All ENP were performed in a fume hood. A nickel ion source ($NiSO_4 \times 6H_2O$ (g/L)), reducing agent ($NaH_2PO_2 \times H_2O$ (g/L)), complexing agent ($C_6H_5Na_3O_7 \times 2H_2O$ (g/L)), accelerator (NH_4CH_3COO (g/L)), stabilizer (CH_4N_2S (ppm)), and pH regulator (NH_4OH/CH_3COOH (%)) was employed to streamline the operating conditions of the ENP bath. The amount of chemicals used in the bath was determined by the amount of phosphorus targeted in the Ni-P layer. Since the objective was to produce duplex coatings (i.e., Ni-P undercoat followed by Ni-P+PTFE top coat), the etched specimens were first transferred into Ni-P bath for producing undercoat. After 15 min, the samples were removed and quickly transferred into another Ni-P bath that contained dispersion of PTFE particles within the solution. The samples were immersed in the bath for 60 min after which they were removed and thoroughly cleaned using DI water and dried using a hot air gun. Both undercoat and topcoat depositions were performed at 85–90 °C, with pH being maintained around 5.5. Three types of ENP duplex coated samples were prepared to contain low, medium, and high PTFE content and referred to herein as ENP1, ENP2 and ENP3. The undercoat contained no PTFE while the Ni-P deposits contained medium P content in all cases. Tables 1 and 2 summarize the PTFE content used in the preparation of the coatings and the concentrations of major chemicals used in the plating process.

Table 1. A Summary of The Plating Characteristics Used in ENP Duplex Layer Development.

Plating Method	Undercoat Ni-P *	Topcoat Ni-P+PTFE *		Sample ID
	P Content (wt%)	P (wt%)	PTFE (g/L)	
Bath 1	medium	Medium	5	ENP1
Bath 2	Medium	Medium	10	ENP2
Bath 3	Medium	Medium	15	ENP3

* The amount of PTFE and P content (i.e., 6–8 wt%) used in the fabrication of the duplex coating.

Table 2. Key Chemicals and Their Quantity (per liter) Used for Preparing ENP Baths.

Chemical	Range
Nickel sulphate ($NiSO_4 \times 6H_2O$)	0.1–0.11 M
Sodium hypophosphite ($NaH_2PO_2 \times H_2O$)	0.19–0.28 M
Sodium citrate ($C_6H_5Na_3O_7 \times 2H_2O$)	0.035 M
Acetic acid/ammonium hydroxide (NH_4OH/CH_3COOH)	pH~5.5–6.2

2.3. Testing and Characterisation of Coatings

The microstructure, surface morphology and coating thickness were conducted by scanning electron microscopy (FE-SEM, Zeiss Supra 25® Oberkochen, Germany). The SEM was equipped with an energy dispersive X-ray spectrometer (EDS, Oxford Instruments®, Oxford, UK) used for the elemental and compositional analysis of the selected regions of the coatings. The X-ray diffraction (XRD) was performed in an X-Pert Pro with Cu Kα Radiation (λ = 1.5406 Å). The Kruss Drop Shape Analysis system (DSA 100® Hamburg, Germany) was used to calculate contact angles using the sessile drop method. This equipment determines a surface's wettability by water to predict hydrophobic properties or fouling potential. The contact angle was calculated using the DSA software from 10 different locations. Roughness measurements were carried out with a Taylor Hobson Ametek stylus profilometer to determine the topological surface parameters such as Ra. The steps and measurements were in line with the standard DIN/ISO 4287. Profilometry images of the surfaces after the test were obtained using an optical profiler (Solarius® SD-V100-3219, San Jose, CA, USA). The hardness of the coatings was obtained from 12 different locations along the cross-section with Vickers micro-hardness tester (VH1202 Wilson®, Esslingen, Germany) using 0.05 kg-f load for 15 s. The friction and wear setup, procedure and measurements followed the ASTM G99 standard [24]. The tribological sliding test was done with a ball-on-disc configuration using pin-on-disk tribometer (Anton Paar® TRB³, Graz, Austria). The stationary counterpart was a chromium steel (100Cr6) ball of 6 mm diameter. The applied load was in the range of 2 to 10 N and the test duration was for 1 h. During the tests, the radius of the wear track was varied between 5 mm and 20 mm for each sample, with the corresponding linear velocity (cm/s) variations depending on the total number of tests and distance (m) covered. The coefficient of friction was determined by monitoring the evolution of the tangential force at dry sliding contact and dividing it by the applied load. The specific wear rate, w_{sample} (mm^3/Nm), was evaluated according to Equation (1) by measuring the volume of the removed material, V (mm^3), and using the applied load, F_n (N), and the distance covered during testing, L (m):

$$w_{sample} \ = \ V/F_n \times L \ \left[mm^3/Nm\right] \tag{1}$$

The mild steel substrate and the 304 L stainless steels were also tested and analyzed for comparison according to the previously explained procedure. The study uses 304 L SS as the reference material because it is one of the most widely used materials in plant construction, especially for heat exchangers. The objective is to show that 304 L can be replaced by ENP coated mild steel to save money and extend service life in geothermal applications.

3. Results

3.1. Morphology and Structure of the Duplex Coatings

Figure 1 shows the surface morphology and cross-sectional micrographs of the different ENP+PTFE duplex coatings. The coatings were observed with globular particles, similar to the conventional morphology for ENP coatings [17]. The distribution of F, indicative of PTFE (C_2F_4), was homogeneous on the outer surfaces and entrapped in the interior and between grains in the coatings. From Figure 1a, a finer multiple grain structure was obtained for high Ni-to-low PTFE content coatings at a microscopic level. With increasing PTFE, the grains enlarged, yielding a less rugged morphology but visible nano-holes/pores in the top surface seen in Figure 2b,c. This morphology is explained by the decreasing Ni and P concentration (Table 3) and growth kinetics with PTFE addition to the coating. This is evident in Figure 1b,c, where the nano-pores are visible, introduced due to PTFE incorporation and the hydrogen gas evolution and escape during coating processes.
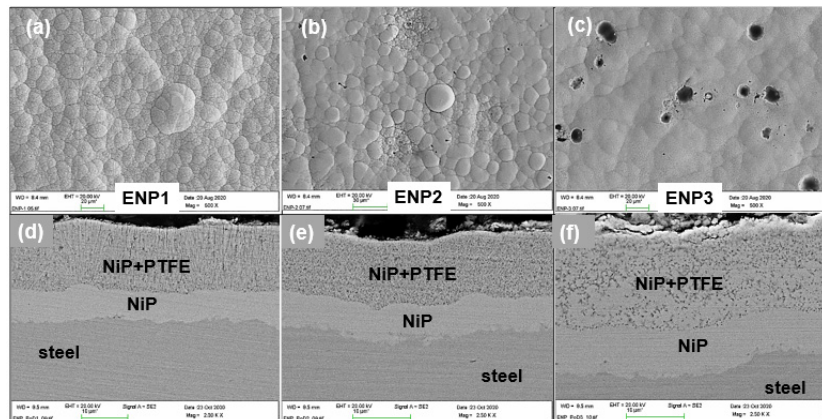
Figure 1. SEM micrographs showing morphology (**a**–**c**) and cross-sectional microstructure (**d**–**f**) of the deposited ENP1, ENP2 and ENP3 duplex coatings.
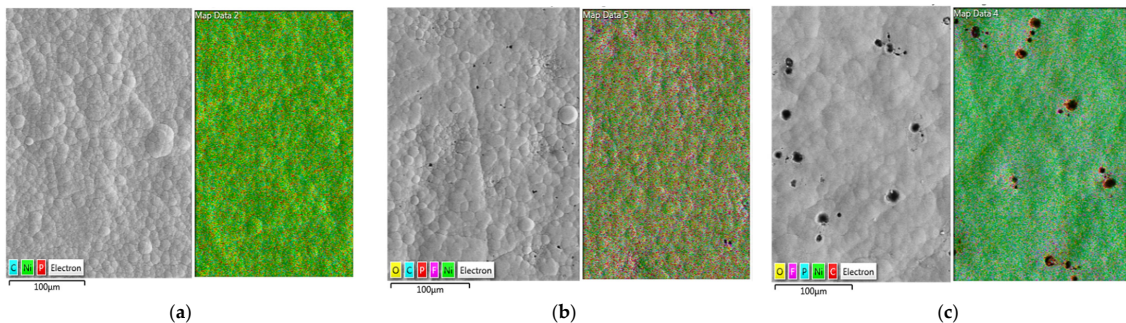
Figure 2. SEM micrographs showing surface morphology and the corresponding elemental maps of (**a**) ENP1, (**b**) ENP2 and (**c**) ENP3.

Table 3. The Elemental Composition of the Surface Maps in Figure 2 of the Ni-P with Embedded PTFE Duplex Coating.

Surface Analysis Ni-P+PTFE	Ni		P		C		F	
	wt%	**at%**	**wt%**	**at%**	**wt%**	**at%**	**wt%**	**at%**
ENP1	81.8	54.9	5.3	6.7	9.8	32.0	3.1	6.4
ENP2	76.7	46.6	3.2	3.7	10.9	32.5	9.2	17.2
ENP3	72.3	38.8	3.0	3.0	17.8	46.7	6.9	11.5

The cross-section micrographs in Figure 1d,e,f reveal the microstructure of the duplex coatings. All the coatings appear dense, continuous and with no obvious pores, but the Ni-P+PTFE layer had dark spots indicative of the nano-PTFE reinforcing phase. The ENP3 had non-uniform dispersion of the PTFE (areas free of dark spots in Figure 1f) in the layers nearer to the substrate. This indicates that depositing 15 g/L of PTFE did not increase PTFE incorporation in the matrix concurrently during plating. Moreover, Table 3 reports a lower wt% F for the ENP3 from the elemental maps of the surfaces of the different coatings given in Figure 2. According to the electroplating theory [25,26], the decrease in F could be clarified by an insufficient cationic surfactant (g/L) to promote the dispersion of the PTFE particles. On the other hand, using PTFE > 10 g/L (ENP3) resulted in a supersaturated plating solution, which accumulated PTFE in areas near the substrate and suppressed the

effective diffusion of PTFE particles to the interface, hence the free spots in the matrix. All the coatings had a thickness of approximately 5 ± 1 μm for Ni-P undercoat and 20 ± 5 μm for Ni-P+PTFE topcoat. A good adhesion was observed between the coating-substrate and the coating-coating interface due to the Ni-P interlayer. No defects or damages were visible at the interfaces.

3.2. Phase Composition of the Coatings

In Figure 3a, the XRD graph shows the phase composition of the ENP+PTFE duplex coatings in the as-plated condition whereas Figure 3b shows the XRD patterns of medium P electroless Ni-P undercoat deposits (i.e., without any PTFE particle dispersion) with low P and high P to complement the results in order to understand the microstructural changes occurring in the layers of the duplex. The results are consistent with the SEM and EDS analyses, where the peaks identified to represent the same elements as detected in the coating. The microstructure of as-plated ENP coatings has similarly been reported by Fayyad et al. [27] as crystalline for low Ni-P (1–5 wt%) and amorphous for high Ni-P (10–12 wt%). The peaks of the duplex coatings in Figure 3a showed crystalline structures and amorphous structures to a certain extent, as well as peaks from the substrate (Fe). In the ENP1 duplex coating, the Ni peak at 44.5° was comparatively highly amorphous. However, the crystalline structure in ENP2 and ENP3 revealed additional amorphous Ni structures. The amorphous Ni was limited to coatings with PTFE $\geq$ 10 g/L, with the peak broadening observed for the reflections around 52° and 76°.

Further examination of Table 3 shows that the elemental surface analysis of the ENP1, ENP2 and ENP3 topcoat contained approximately 5.3, 3.2 and 3.0 wt% phosphorus, respectively. Thus, in the pattern, the medium P content in both the undercoat and topcoat (with PTFE in the Ni-P matrix) accounted for the mixed amorphous-crystalline structures of ENP2 and ENP3 duplex coatings. The refined grains confirmed from the calculated crystallite size from Scherrer's equation [23] caused broader peak diffraction in ENP1, indicative of an amorphous Ni-P coating. The crystallite size of the Ni-P increased with increased PTFE dispersion of the order 43.6 nm, 58.2 nm, 69.8 nm for ENP1, ENP2 and ENP3, respectively. The crystallization peak of PTFE was observed at a diffraction angle of 18. The PTFE peak was prominent in both ENP2 and ENP3. Although there is no chemical interaction of the PTFE with the Ni-P alloy since the nanoparticles are only embedded in the matrix, the plating conditions influenced crystallization. This is evident in the Ni ((111) – FCC) peak at 44.5° in ENP2 and ENP3, which turned microcrystalline with the increased PTFE content used in the fabrication. Therefore, the microstructure of the ENP1 is amorphous, whereas that of the ENP1 and ENP2 coating tends to be a mixed crystalline-amorphous structure (see Figure 3).
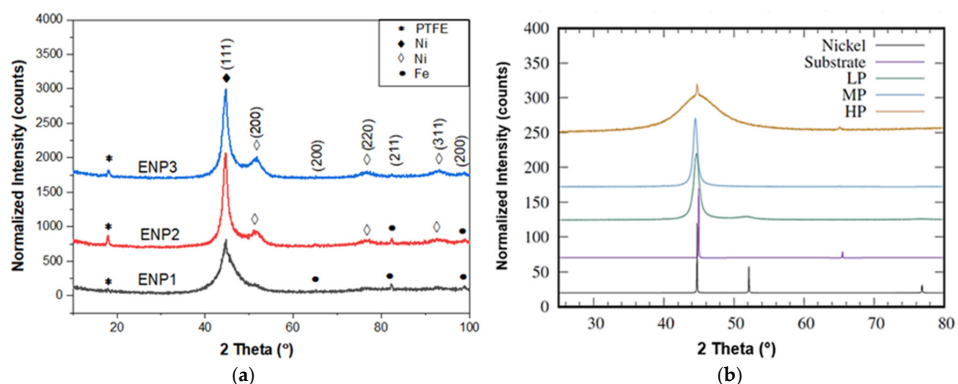
Figure 3. X-ray diffraction patterns of the deposited electroless (**a**) Ni-P matrix (i.e., MP) with embedded PTFE from the top surface (**b**) Ni-P undercoat (i.e., MP) of the ENP duplex coatings compared to LP and HP, along with the simulated patterns of nickel and the substrate. LP is low phosphorus, MP is medium phosphorus, and HP is high phosphorus.

3.3. Surface Roughness and Water Contact Angle (WCA) Analysis of the Coatings

The surface structures, morphology and topography of the coatings greatly influence the roughness and wettability of coatings. Figure 4 compares the water contact angle (WCA) and arithmetic average surface roughness parameter (Ra) of the different coatings. The WCA for ENP1, ENP2, ENP3 are $94.1° \pm 0.89$, $102.6° \pm 0.70$, and $93.9° \pm 2.49$, and the Ra values are 1.24 ± 0.11 µm, 1.72 ± 0.08 µm, and 2.16 ± 0.21 µm, respectively. The Ra of the ENP+PTFE duplex coatings increased with higher PTFE content and large grain size. ENP3 recorded the highest Ra and highest surface energy (wettability), while ENP2 demonstrated the least wettability at $102.6°$ with water. Therefore, it could be said that the Ra was not only influenced by pre-treatment of the surface but also the globular grain size with PTFE particle addition. In contrast, the effective distribution of the nanoparticles in the matrix was significant for the hydrophobicity of the coatings.
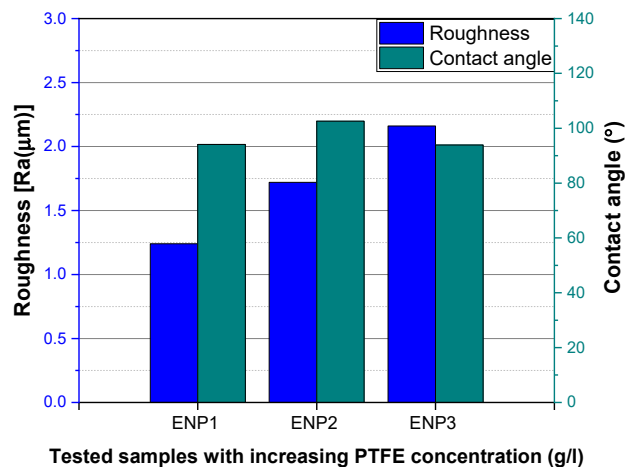
Figure 4. The water contact angle (WCA) and arithmetic average surface roughness parameter (Ra) of the deposited electroless ENP duplex coatings.

3.4. Microhardness Analysis of the Coatings

Generally, friction and wear have been attributed and influenced by properties such as surface roughness, stiffness, and hardness of two materials in relative motion. The microhardness of the coatings was determined since microstructural changes were observed in the XRD analysis with PTFE addition. Figure 5 shows the obtained hardness of the coatings after 12 indentations, with increased hardness measured for the ENP+PTFE coatings compared to the mild steel substrate measured as 163.1 ± 0.2 HV. The mean microhardness was 300.7 ± 37, 301.8 ± 27 and 480.8 ± 51.8 HV. The hardness of the coatings increased with increasing PTFE content, contrary to other literature [25,27], which defined PTFE as a softer polymer.

Further examination of the EDS findings (in Table 1) reveals that ENP1 represented the least amount of F (3.1 wt%) but had a hardness value comparable to ENP2 (9.2 wt% F). This suggests the variation in hardness of the duplex coating was dependent on PTFE dispersion in the Ni-P matrix. Accordingly, the microhardness of as-plated ENP coating is reported between 500 and 550 HV for Ni-P alloy with no PTFE fillers [25,28,29]. Similar to the non-uniformly distributed PTFE coating (i.e., ENP3 in this work), the coating with free spots in the Ni-P matrix (due to PTFE particle agglomeration) yielded the highest hardness value (i.e., 400–550 HV) with a broad standard deviation. This explains the disparity in increasing hardness between this work and other literature.
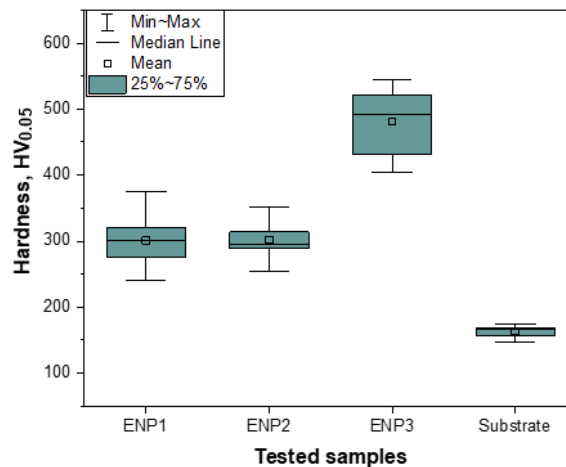
Figure 5. The effect of PTFE content on microhardness of the deposited ENP+PTFE: ENP1, ENP2 and ENP3 duplex coatings.

3.5. Tribological Properties

For optimizing the individual tribological performances, a dry wear test was carried out with coefficient of friction (CoF) and wear rate as the performances' index. Figure 6 shows friction evolution with sliding time for the different duplex coatings against a 100Cr6 steel ball under the different loads. The shape of the curves exhibits some stages, which depicts the overall friction-time behavior. The stages are associated with running-in (i.e., the onset of the sliding period before steady-state) and stick-slips (see Figure 6a), which observed a series of steps in the steady region in the curves. The higher the load, the shorter the running-in time. Higher shear motion and multiple occurrences of friction spikes in the plots at such loads (as seen in Figure 6b—0.5 h test) indicate stick-slip behavior dependent on the physical or chemical nature of the surface [30], which was most visible in ENP1 and ENP3.

Meanwhile, the CoF of the ENP2 coatings was smooth, low and steady. This behavior suggests a well-lubricated tribosystem maintaining a balance in each test condition of the average kinetic friction, wear rates, lubrication debris concentration, and surface roughness. The friction-related transitions for the other coatings, on the other hand, were discontinuous and triggered by test parameters, PTFE nanoparticles' lubrication effect, Ni-P undercoat interfacial processes, and substrate stresses. For instance, the PTFE nanoparticles and Ni-P matrix's friction contribution are apparent in the 2 N-1 h curves (Figure 6c), showing two regions with continuous increase in friction coefficient of the coatings after the onset of sliding even for the ENP2. This is because the softer PTFE is removed first where a film formation in the contact controls lubrication. The corresponding mean values of CoF at the 2 N-1 h test were 0.37, 0.47 and 0.58 for ENP1, ENP2 and ENP3, respectively. In comparison, the friction value for Ni-P alloy with no fillers was reported to be 0.68 [23]. In ENP1, the interfacial Ni-P (undercoat) with moderate friction effect was visible after the film loss (i.e., the transfer seen in the 5N curve in Figure 6b). However, in the 10 N-1 h test, higher friction evolved when the substrate was locally reached (with the pull-outs seen in Figure 6a). In this study, ENP2 produced a decreased friction coefficient of 79% at the highest load and sliding cycles corresponding to the value 0.17 compared to 0.81 for the 304 L reference material. This suggests that the ENP2 duplex coatings can potentially be a candidate as coating material to reduce wear in components used in geothermal power plants.
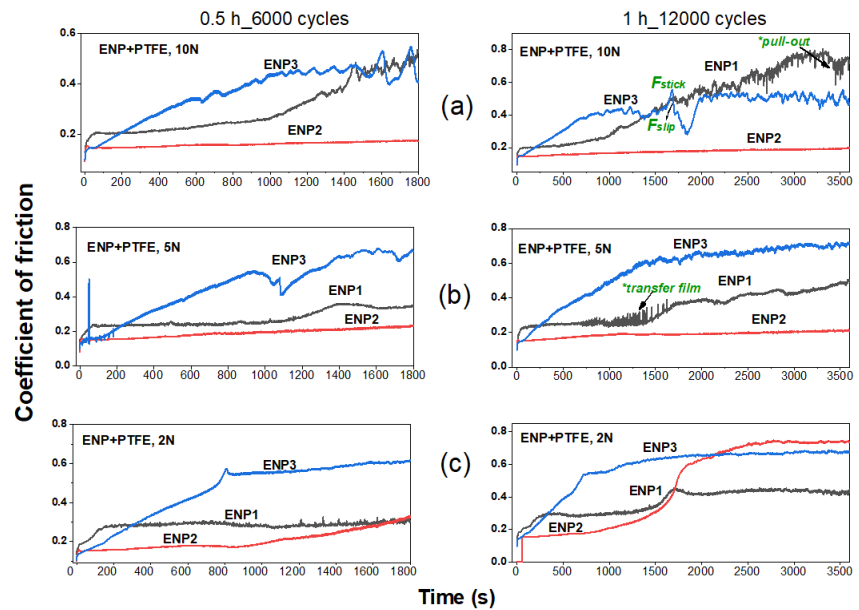
Figure 6. The evolution of coefficient of friction as a function of time at various loads and sliding cycles of the ENP+PTFE: ENP1, ENP2 and ENP3 duplex coatings.

Figure 7 presents the average coefficient of friction values of the different coatings under the various test loads. Although ENP1 contained lower PTFE content, better friction performance was recorded compared to ENP3, suggesting film formation in the tribo-contacts for ENP1. The film acts as a transfer, so-called tribolayer, formed from the mixed fluorine and oxygen debris (from initial wear of the coating) that cushions the surface at increasing load and repetitive cycles. The film loss can confirm this at the 10 N-1 h test, where ENP3 outperformed ENP1. From the friction curves, the film loss in the ENP1 contact resulted in surface galling and pull-outs down to the sub-surface while a steady-state was finally reached for the ENP3 coating.
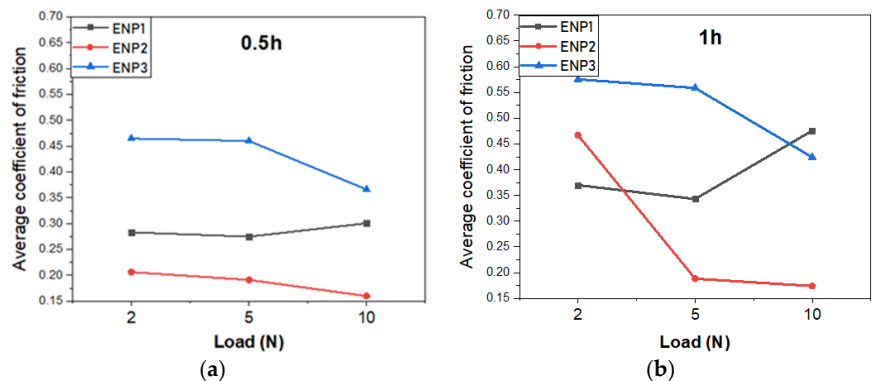
Figure 7. Influence of PTFE content on the average CoF values of the deposited electroless ENP+PTFE: ENP1, ENP2 and ENP3 duplex coatings at different loads.

Comparing the wear results obtained under the different loads, the wear coefficient of the duplex coatings was of the same order of magnitude (i.e., 10^{-5}). The obtained material loss and specific wear rates after testing are plotted in Figure 8a,b, respectively. The wear volume was normalized with the different test loads and sliding distance; thus, the highest

value was observed at 2N load. No measurable material removal was observed for ENP2 and ENP3 at the lowest loads, signifying maximum wear protection by the coating. This suggested that the microstructure, preferably to the hardness of the ENP3 coating, had a major impact on the friction and wear properties. Furthermore, this hypothesis is confirmed by the sparing values between the wear-resistance (see Figure 9), considering the similar hardness of the ENP1 and ENP2 coatings. The highest volume loss was recorded for increasing load and sliding time as expected. The surfaces of the ENP1 coatings had the highest material removal and wear rates.

ENP3 had the lowest wear volume and wear rates at higher sliding cycles and loads, in contrast to the friction results. Under the test loads, the wear performance of the finer-grained ENP1 coating was approximately 4–5 times that of the reference steel, 14–30 times for ENP2, and 15–27 times for ENP3. The incorporation of PTFE in the Ni-P+PTFE composite coating has been reported to produce similar results in other studies [12,15,20] but reports of lower wear rates exhibited larger sub-surface scuffing (i.e., the substrate of single layer deposit) [31]. Comparatively, the wear rate of a single layer deposit reported by Rahmati and Mahboobi [15] with similar PTFE composition as the duplex analyzed in this paper was reduced to 43% and 66% for ENP2 (10 g/L) and ENP3 (15 g/L), respectively. The authors attributed increased wear rate of the single layer ENP3 (15 g/L) to adhesive failure at the substrate and cohesive failure within the ENP+PTFE composite. As a result, the Ni-P interlayer could have been significant for the observed wear performance of the ENP3 duplex coating, which was influenced by the improved adhesion and between the substrate and composite coating, as well as the inherent increase in thickness associated with double layer deposition.

Figure 9 compares the wear-resistance (1/wear rate) [32] as a function of hardness of the ENP+PTFE duplex coatings compared to reference 304 L stainless steel at the highest test load of 10N. The wear-resistance is independent of the load; thus, the worn volumes with the sliding conditions were used. The developed coatings had outstanding performance compared to the 304 L SS. The best performance was observed for the electroless-nickel coating ENP3 with increasing grain size and improved Ni-P coating structures. Therefore, for wear-resistive properties, the preferable concentration of the PTFE reinforcement must be greater than 5 g/L in the electroless plating solution with efficient dispersion.
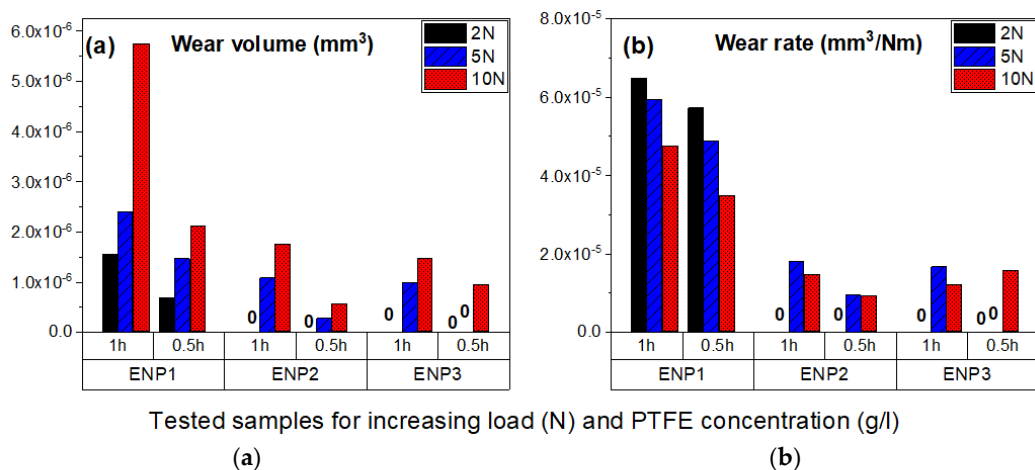
Figure 8. Volume loss from worn tracks (**a**) and wear rates (**b**) of the deposited electroless ENP+PTFE: ENP1, ENP2 and ENP3 duplex coatings at the different loads.
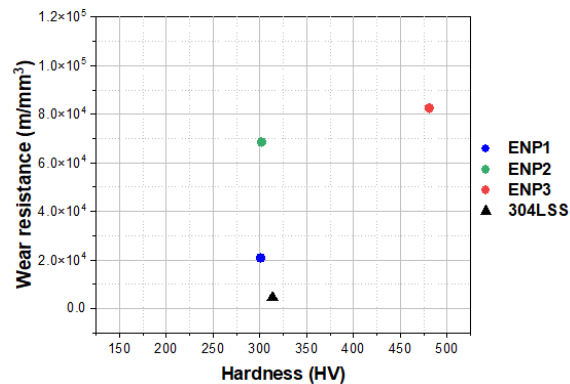
Figure 9. Wear-resistance versus hardness of the ENP duplex coatings and 304 L SS reference material at 10N load after 12,000 cycles.

4. Discussion

Lubrication and Wear Mechanism

Overall, the mechanism was supported by the running-in evolution of friction co-efficient that produced increased wear in the contact, forming a mixed oxide-PTFE film from the wear debris. After few cycles of lower friction ($\approx$0.15–0.6), progressive increment occurs with damage or total removal of the transfer film. Figure 10 shows schematics of the proposed hypothesis on the effects of the fabrication process, with introduction of compressive stresses from the deposition parameters of Ni and microstructural alteration with the increase in PTFE content on increased wear-resistance duplex coatings. The schematics in Figure 11 explain our hypothesis on the transition of wear occurring for the coatings during the tests. The wear behavior can be explained partially by the film behavior and the contact conditions at the ball interface. The friction remained stable for higher amounts of PTFE (ENP2 and ENP3) and showed no significant reduction, whereas for low amounts (ENP1), friction rapidly increased. However, the SEM micrographs and profilometry images from Figures 11–13 show variation in surface appearance (surface irregularities) as a function of PTFE. This suggests that the film formation and duration on the surfaces did not follow the same behavior. The transfer film is smooth and continuous; thus, these conditions reduce the time to achieve stability seen in the ENP2 duplex coatings. Therefore, irrespective of the coating composition and microstructure, the transfer film complicates material loss within the tribo-contact arising from surface irregularities. Thus, after surface analysis, an intermediate state of wear could be described under mild to higher loading and sliding conditions, explaining the higher friction values at such loads.
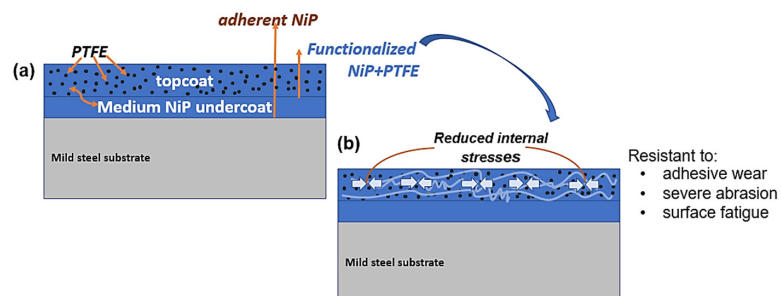
Figure 10. Schematics of (**a**) the structure of the proposed duplex coating and (**b**) the effect of the plating process and optimized PTFE content on improved properties of the coatings for effective wear control.

In a continuous sequence from Figure 11a,b, if PTFE particles removed from the bulk did not attach to the steel counter body but were lost from the system, a clean surface is observed, and wear is minimal. However, in Figure 11c, the counter face experiences abrasive-adhesive wear, producing mixed metal oxide material when the debris is entrapped/picked up, increasing friction and wear. For instance, the deposited layer in ENP3 in Figure 13c (5 N-1 h test) gave rise to wear regions in the profilometry image in Figure 12f with a deeper wear depth of 6.51 μm compared to 2.44 μm for the ENP2 coating. The least worn surfaces had a shallow depth of wear and relatively smooth average roughness with the contrast shown in Figure 11. ENP1 showed the highest material loss from the surface, while the lowest rate was found in ENP3. The microstructure and hardness of the ENP3 coating had a major impact on the friction and wear properties. This is because, despite the non-uniform dispersion of the PTFE in the matrix, the hardness of the Ni-P matrix confers high abrasion resistance to the coatings.
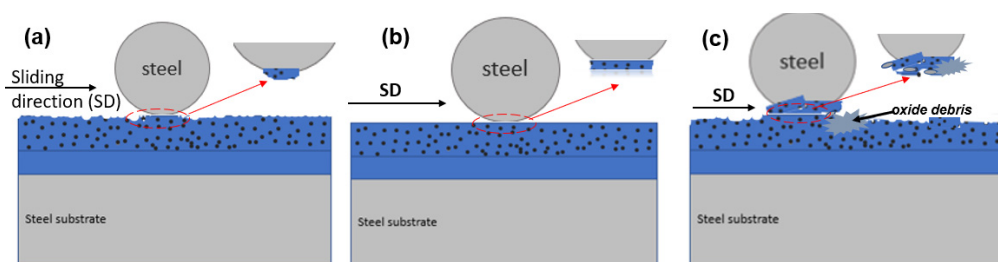
Figure 11. The transition in wear is proposed to have occurred by (**a**) high loss rate as the film formed with high friction (Figure 6: running-in friction of ENP1, ENP2 and ENP3), (**b**) much lower loss rate after the film formed where the tribo-system remained steady (i.e., constant friction and wear conditions; Figure 13b,e: ENP2 and Figure 13f: ENP3), and (**c**) higher loss rate from the film due to fragments (Figure 13a: ENP1) or total film loss due to cyclic sliding (Figure 13d: ENP1) and material gain on the hard coating from abrasive-adhesive wear of the steel counter body (Figure 13c: ENP3).
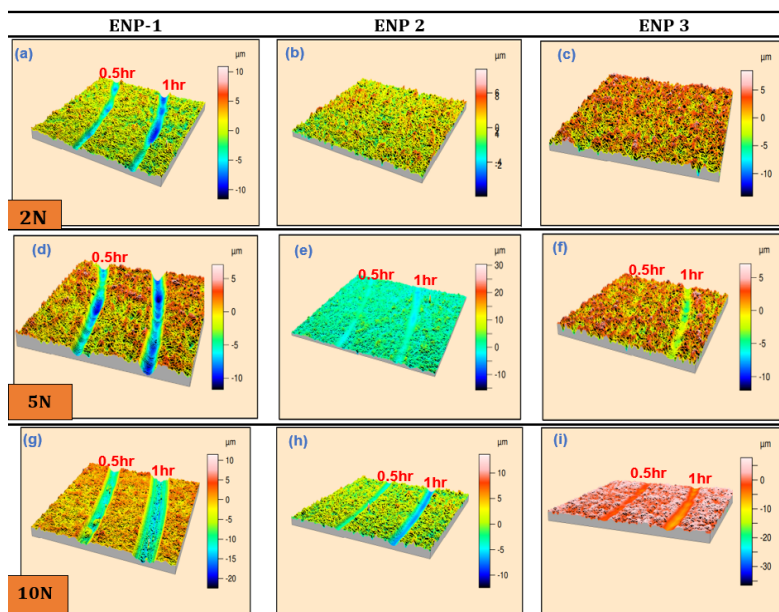
Figure 12. 3D optical profilometry images of the worn tracks on the developed ENP+PTFE: ENP1, ENP2 and ENP3 duplex coatings at various loads and sliding cycles.

The SEM results of ENP2 and ENP3 show fine scratches and third body effects (picked-up oxide layer) visible on all the coating surfaces. To provide valuable wear information, Figure 13 was beneficial in determining the two-failure mechanisms present:

(1)   the smoothing by plastic deformation from gradual abrasion of the Ni-P+PTFE top layer and

(2)   the fatigue wear of only ENP1 due to high internal stresses via spalling [31].

The amorphous and multiple fine grains of the ENP1 coatings explain the already strained state of the Ni-P+PTFE duplex coating. Whereas the lower P content, microcrystalline Ni peak in the XRD and coarsened grains from entrapment of the PTFE particles may have been a source of compressive stress reducing the stresses in the ENP2 and ENP3 duplex, resulting in an improved microstructure (depicted in Figure 11). Furthermore, with the intrinsic stresses in ENP1, the expectations of a soft and ductile FCC matrix and the deformation mechanism of the amorphous structure (i.e., with no grain boundaries), the pull-outs and spalling in Figure 14 can easily be explained.

Moreover, increased addition of PTFE in ENP2 and ENP3 with the effect of low phosphorus produced a robust friction film hindering tip penetration since low phosphorus coatings have been reported with good frictional properties [33]. Thus, the absence of cracks, spalls, and debris in the ENP2 and ENP3 micrographs (Figure 13b,c,e,f). Further observation of the damages in ENP1 by SEM displayed significant delamination in the mid-regions and smooth/adhesive traces at the edge (Figure 14a,b). This is because of the high contact pressure in the center of the counterbody (steel ball), which falls to zero at the end. At lower cycles (0.5 h), the surface analysis showed picked-up oxide layers that cracked and spalled off (Figure 14a) due to its brittleness (hence it acted as the fatigue crack nucleation sites during sliding), producing the craters on the worn surface. With such delamination in central regions, the surfaces stick, whereas, around the annular areas, slip occurred, contributing to the mixed stick-slip condition for the ENP1 coating. On the other hand, in the friction curves of ENP3, the stick-slip phenomenon was related to thicker oxide patches with high-stress concentrations during sliding.
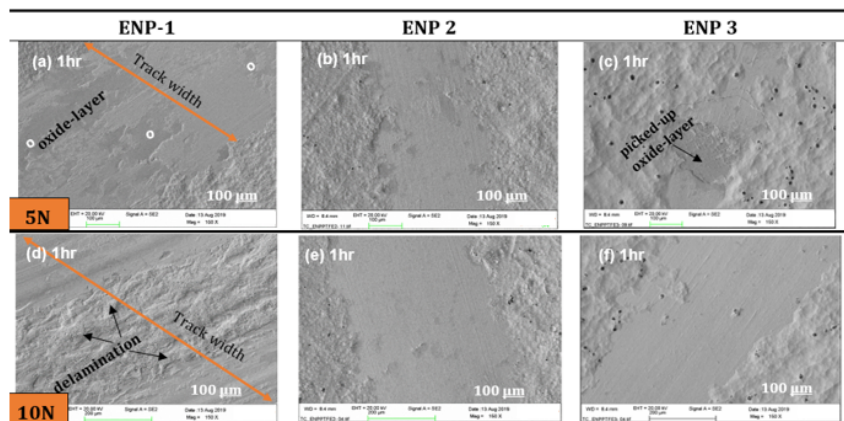
Figure 13. SEM surface micrographs of the worn tracks from 5 N and 10 N test loads on the ENP+PTFE: ENP1, ENP2 and ENP3 duplex coatings at 12,000 sliding cycles.

Figure 15 compares the surface chemistry of ENP1 and ENP3 coatings at the 10 N-1 h testing conditions. The SEM/EDS area spectrum 1, 2, 3, corresponds to less worn, highly worn and unworn areas of the test surface, respectively. The result shows a decrease in Ni in the wear tracks at locations 1 and 2 with increasing Fe (56.6 wt%) and O (7.7 wt%) content in the mid-track of ENP1 (scanned area 2). This is attributed to substrate wear and oxidation of the wear debris in the atmosphere. In ENP3, mild wear features were visible, showing only areas 1 and 3 in Figure 15b. Moreover, the concentration of F decreased by 9%

compared to the initial composition of ENP3 before the wear test, suggesting a significant contribution of P and C_2F_4 to the enhanced tribological performance. The rim or edges of ENP1 (i.e., area 1) demonstrated similar wear features where minor wear occurred. The high Ni to low Fe content was complemented with higher C, F and P weight fractions at such spots. Comparatively to the center, wear was enhanced by the Ni-P topcoat and undercoat running against the steel ball apparent in the decreased (82.3 wt%) Ni- (5.4 wt%) P content in area 3 to (27.9 wt%) Ni- (0.84 wt%) P in area 2 of Figure 15a.
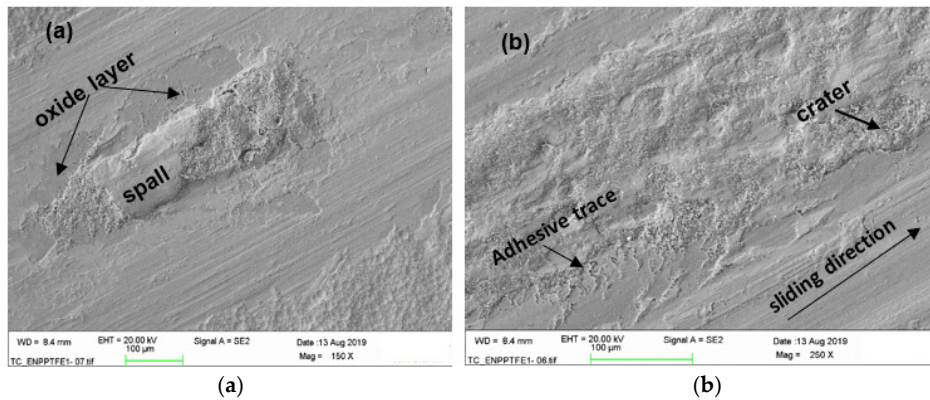
Figure 14. SEM morphology of worn zones of the developed ENP1 duplex coating at 10N load for duration of: (**a**) 6000 cycles-0.5 h and (**b**) 12,000 cycles-1 h.

Area	Ni	P	F	C	Fe	O
1	81.0	4.4	2.0	8.0	2.1	2.6
2	27.9	0.84	0.8	5.7	56.6	7.7
3	82.3	5.4	3.0	9.0	0.4	
Map	71.1	3.4	1.8	7.4	10.8	5.5

(**a**)

Area	Ni	P	F	C	Fe	O
1	84.8	2.8	3.1	9.0	0.2	
2						
3	77.4	3.3	7.1	12.2		
Map	80.7	3.0	4.5	10.6	0.2	1.0

(**b**)
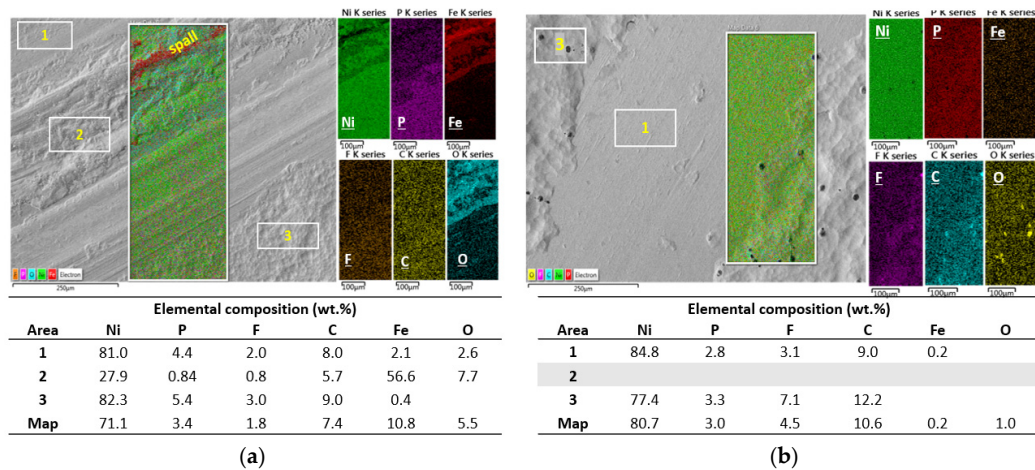
Figure 15. SEM morphology of wear surfaces and EDS maps of the worn zones of the developed ENP+PTFE: (**a**) ENP1 and (**b**) ENP3 duplex coatings at 10 N load for a duration of 1 h-12,000 cycles.

5. Conclusions

Duplex electroless nickel-phosphorus composite (ENP thin adhesive layer and ENP+PTFE top functional layer) coatings were developed from the dispersion of PTFE nanoparticles in different ENP baths. All the developed coatings outperformed the reference 304 L SS material with good wear-resistance at the applied load based on the following conclusions:

1. SEM/EDS and XRD analyses demonstrated the presence of PTFE particles. Significant changes in the coatings' morphology and microstructure were observed to improve grain size, hydrophobicity, arithmetic average surface roughness, and hardness with

PTFE addition. In the ENP solution, the ideal amount for PTFE homogenization was 10 g/L in this work.

2. In the tribological testing, the PTFE was responsible for the lubricating properties of the coatings. Independent of the coating composition and structure, PTFE positively influenced the formation of a robust transfer film eliminating stick-slip, high volume loss and adhesion in the tribo-contact. However, this property is a function of PTFE dispersion. In comparison to the reference 304 L SS, the ENP2 found a steady friction value of 0.17 with a 79% increase in lubricity at the highest test load and cycles.

3. The sporadic hardness values measured in the ENP3 coating confirmed the clustering effect of PTFE particles and affected steady-state friction-wear conditions. The cycles to steady-state friction occurred at the highest load and sliding cycles.

4. The worn zones of the coatings displayed smooth surfaces from fine abrasion or scratching, however, at higher loads and sliding cycles, ENP1 coating failed by galling and fatigue wear.

5. Finally, the coating with dispersed PTFE reduced surface energy by more than 100% compared to the substrate. Thus, the combination of low friction and low hydrophobicity suggests that the duplex coatings present good candidacy for drag, scaling and corrosion mitigation in heating and cooling units (e.g., heat exchangers) used in geothermal power plants. Furthermore, ENP2 (10 g/L PTFE) is optimum for both low friction and wear applications at low contact load, while ENP3 (15 g/L PTFE) has desirable wear resistances but compromised lubrication under dry contact sliding (due to non-uniform dispersion and agglomeration of PTFE in the matrix).

References

1. Buchtík, M.; Kosár, P.; Wasserbauer, J.; Tkacz, J.; Doležal, P. Characterization of Electroless Ni–P Coating Prepared on a Wrought ZE10 Magnesium Alloy. *Coatings* **2018**, *8*, 96. [CrossRef]
2. Sudagar, J.; Lian, J.; Sha, W. Electroless nickel, alloy, composite and nano coatings—A critical review. *J. Alloy. Compd.* **2013**, *571*, 183–204. [CrossRef]
3. Balaraju, J.N.; Narayanan, T.S.N.S.; Seshadri, S.K. Electroless Ni–P composite coatings. *J. Appl. Electrochem.* **2003**, *33*, 807–816. [CrossRef]
4. Krick, B.A.; Ewin, J.J.; Blackman, G.S.; Junk, C.P.; Sawyer, W.G. Environmental dependence of ultra-low wear behavior of polytetrafluoroethylene (PTFE) and alumina composites suggests tribochemical mechanisms. *Tribol. Int.* **2012**, *51*, 42–46. [CrossRef]
5. Sahoo, P.; Das, S.K. Tribology of electroless nickel coatings—A review. *Mater. Des.* **2011**, *32*, 1760–1775. [CrossRef]
6. Gutsev, D.; Antonov, M.; Hussainova, I.; Grigoriev, A.Y. Effect of SiO_2 and PTFE additives on dry sliding of NiP electroless coating. *Tribol. Int.* **2013**, *65*, 295–302. [CrossRef]
7. Karthikeyan, S.; Ramamoorthy, B. Effect of reducing agent and nano Al_2O_3 particles on the properties of electroless Ni–P coating. *Appl. Surf. Sci.* **2014**, *307*, 654–660. [CrossRef]
8. Tang, A.; Wang, M.; Huang, W.; Wang, X. Composition design of Ni–nano-Al_2O_3–PTFE coatings and their tribological characteristics. *Surf. Coatings Technol.* **2015**, *282*, 121–128. [CrossRef]

9.   Mukhopadhyay, A.; Barman, T.K.; Sahoo, P.; Davim, J.P. Comparative study of tribological behavior of electroless Ni-B, Ni-B-Mo, and Ni-B-W coatings at room and high temperatures. *Lubricants* **2018**, *6*, 67. [CrossRef]

10. Zhou, Y.-R.; Zhang, S.; Nie, L.-L.; Zhu, Z.-J.; Zhang, J.-Q.; Cao, F.-H.; Zhang, J.-X. Electrodeposition and corrosion resistance of Ni–P–TiN composite coating on AZ91D magnesium alloy. *Trans. Nonferrous Met. Soc. China* **2016**, *26*, 2976–2987. [CrossRef]

11. Balaraju, J.N.; Seshadri, S.K. Synthesis and corrosion behavior of electroless Ni-P-Si$_3$N$_4$ composite coatings. *J. Mater. Sci. Lett.* **1998**, *17*, 1297–1299. [CrossRef]

12. Mohammadi, M.R.; Ghorbani, M. Wear and corrosion properties of electroless nickel composite coatings with PTFE and/or MoS$_2$ particles. *J. Coat. Technol. Res.* **2011**, *8*, 527–533. [CrossRef]

13. Zhang, S. State-of-the-art of polymer tribology. *Tribol. Int.* **1998**, *31*, 49–60. [CrossRef]

14. Keogh, W.; Boakye, G.O.; Neville, A.; Olsen, J.H.; Charpentier, T. Lead Sulfide (PbS) Scale Behavior and Deposition as a Function of Polymeric Sulfide Inhibitor Concentration in Multiphase. In Proceedings of the International Corrosion Conference and Expo Series 2018, Phoenix, ZA, USA, 15–19 April 2018.

15. Rahmati, H.; Mahboobi, F. Studying the Effect of the Concentration of PTFE Nanoparticles on the Tribological Behavior of Ni-P-PTFE Composite Coatings. *Iran. J. Oil Gas Sci. Technol.* **2015**, *4*, 67–75.

16. Tajbakhsh, M.; Yaghobizadeh, O.; Nia, M.F. Investigation of the physical and mechanical properties of Ni-P and Ni–P–PTFE nanocomposite coatings deposited on aluminum alloy 7023. *Proc. Inst. Mech. Eng. Part E J. Process Mech. Eng.* **2019**, *233*, 94–103. [CrossRef]

17. Kinoshita, H.; Yonezawa, S.; Kim, J.; Kawai, M.; Takashima, M.; Tsukatani, T. Electroless Nickel-plating on PTFE fine particles. *J. Fluor. Chem.* **2008**, *129*, 416–423. [CrossRef]

18. Balaji, R.; Pushpavanam, M.; Kumar, K.Y.; Subramanian, K. Electrodeposition of bronze–PTFE composite coatings and study on their tribological characteristics. *Surf. Coat. Technol.* **2006**, *201*, 3205–3211. [CrossRef]

19. Sahoo, P. Tribological performance of electroless Ni-P coatings composite. In *Materials and Surface Engineering*; Woodhead Publishing: Swanston Cambridge, UK, 2012; pp. 163–205.

20. Sheu, H.H.; Jian, S.Y.; Lin, M.H.; Hsu, C.I.; Hou, K.H.; der Ger, M. Electroless Ni-P/PTFE self-lubricating composite thin films applied for medium-carbon steel substrate. *Int. J. Electrochem. Sci.* **2017**, *12*, 5464–5482. [CrossRef]

21. Huang, Y.; Zeng, X.; Hu, X.; Liu, F. Corrosion resistance properties of electroless nickel composite coatings. *Electrochimica Acta* **2004**, *49*, 4313–4319. [CrossRef]

22. Sharma, A.; Singh, A.K. Electroless Ni-P-PTFE-Al$_2$O$_3$ dispersion nanocomposite coating for corrosion and wear resistance. *J. Mater. Eng. Perform.* **2014**, *23*, 142–151. [CrossRef]

23. Sharma, A.; Singh, A.K. Corrosion and wear resistance study of Ni-P and Ni-P-PTFE nanocomposite coatings. *Cent. Eur. J. Eng.* **2011**, *1*, 234–243.

24. American Society for Testing and Materials. *ASTM G99-05, Standard Test Method for Wear Testing with a Pin-on-Disk Apparatus*; American Society for Testing and Materials: Philadelphia, PA, USA, 2010.

25. Liu, Y.; Zhao, Q. Study of PTFE content and anti-corrosion properties of electroless Ni-P-PTFE coatings. *Plat. Surf. Finish.* **2004**, *91*, 48–51.

26. Srinivasan, K.N.; John, S. Studies on electroless nickel–PTFE composite coatings. *Surf. Eng.* **2005**, *21*, 156–160. [CrossRef]

27. Fayyad, E.M.; Abdullah, A.M.; Hassan, M.K.; Mohamed, A.M.; Wang, C.; Jarjoura, G.; Farhat, Z. Synthesis, Characterization, and Application of Novel Ni-P-Carbon Nitride Nanocomposites. *Coatings* **2018**, *8*, 37. [CrossRef]

28. Chen, S.Y.; Shi, Y.; Fan, H.; Liang, J.; Liu, C.S.; Sun, K. Synthesis of Ni-P-PTFE-nano-Al$_2$O$_3$ composite plating coating on 45 steel by electroless plating. *J. Compos. Mater.* **2012**, *46*, 1405–1416.

29. Jiang, W.; Shen, L.; Wang, Z.; Wang, K.; Xu, M.; Tian, Z. Wear resistance of a Ni-PTFE composite coating strengthened with nano-SiC particles. *Mater. Res. Express* **2019**, *6*, 096443. [CrossRef]

30. Blau, P. Effects of Tribosystem Variables on Friction. In *Nondestructive Evaluation*; CRC Press: Boca Raton, FL, USA, 2008; pp. 269–313.

31. Ramalho, A.; Miranda, J. Friction and wear of electroless NiP and NiP+PTFE coatings. *Wear* **2005**, *259*, 828–834. [CrossRef]

32. Hutchings, I.; Gee, M.; Santner, E. Friction and Wear. In *Springer Handbook of Materials Measurement Methods*, 1st ed.; Springer: Berlin/Heidelberg, Germany, 2006; pp. 685–710.

33. Taheri, R.; Oguocha, I.; Yannacopoulos, S. The tribological characteristics of electroless NiP coatings. *Wear* **2001**, *249*, 389–396. [CrossRef]

Journal Paper 2

G. Oppong Boakye, L.E. Geambazu, A.M. Ormsdottir, B.G. Gunnarsson, I. Csaki, F. Fanicchia, D. Kovalov, S.N. Karlsdottir,

Microstructural Properties and Wear Resistance of Fe-Cr-Co-Ni-Mo-Based High Entropy Alloy Coatings Deposited with Different Coating Techniques,

Article

Microstructural Properties and Wear Resistance of Fe-Cr-Co-Ni-Mo-Based High Entropy Alloy Coatings Deposited with Different Coating Techniques

Gifty Oppong Boakye [1], **Laura E. Geambazu** [2,3], **Arna M. Ormsdottir** [1], **Baldur G. Gunnarsson** [1], **Ioana Csaki** [2], **Francesco Fanicchia** [4,5], **Danyil Kovalov** [1,6] and **Sigrun N. Karlsdottir** [1,*]

[1] Faculty of Industrial Engineering, Mechanical Engineering, and Computer Science, University of Iceland, Hjardarhagi 2-6, 107 Reykjavík, Iceland; gob13@hi.is (G.O.B.); arnamaria@hi.is (A.M.O.); bgg8@hi.is (B.G.G.); dankov@hi.is (D.K.)

[2] Material Science and Engineering Faculty, University Politehnica Bucharest, Splaiul Independentei 313, 060042 Bucharest, Romania; laura.geambazu@icpe-ca.ro (L.E.G.); ioana.apostolescu@upb.ro (I.C.)

[3] National Institute for R&D in Electrical Engineering ICPE-CA Bucharest, Splaiul Unirii 313, 030138 Bucharest, Romania

[4] TWI Ltd., Granta Park, Cambridge CB21 6AL, UK; francesco.fanicchia@cranfield.ac.uk

[5] Surface Engineering and Precision Centre, School of Aerospace Transport and Manufacturing, Cranfield University, Bedford MK43 0AL, UK

[6] Department of Materials Science and Engineering, University of Virginia, Charlottesville, VA 22904, USA

* Correspondence: snk@hi.is

Abstract: Materials can be subjected to severe wear and corrosion due to high temperature, high pressure and mechanical loads when used in components for the production of geothermal power. In an effort to increase the lifetime of these components and thus decrease cost due to maintenance High-Entropy Alloy Coatings (HEACs) were developed with different coating techniques for anti-wear properties. The microstructure, mechanical and tribological properties of $CoCrFeNiMo_x$ (at% x = 20, 27) HEACs deposited by three different technologies—high-velocity oxygen fuel (HVOF), laser cladding (LC) and electro-spark deposition (ESD)—are presented in this study. The relationship between surface morphology and microstructural properties of the as-deposited coatings and their friction and wear behavior is assessed to evaluate their candidacy as coatings for the geothermal environment. The wear rates were lower for the HVOF coatings compared to LC and ESD-produced coatings. Similarly, a higher hardness (445 ± 51 HV) was observed for the HVOF HEACs. The mixed FCC, BCC structure and the extent of $\sigma + \mu$ nano precipitates are considered responsible for the increased hardness and improved tribological performance of the HEACs. The findings from the study are valuable for the development of wear-resistant HEAC for geothermal energy industry applications where high wear is encountered.

1. Introduction

In past developments, wear resistance has been linked to the intrinsic hardness directly related to a raw material property (e.g., diamond, cubic boron nitride). Subsequently, extrinsic hard coatings from a combination of elements, phases, structures, gradient layer and multilayers have been evolved through the implementation of binary, ternary and quaternary alloying [1]. Mainly nitrides, carbides, carbon-based oxide and the borides of a single base element or metal are the materials used in coating technologies.

New possibilities have arisen recently for developing multi-principal element coatings based on bulk materials known as high entropy alloys (HEAs) and compositional complex alloys (CCAs) [2–6] which have shown to achieve high hardness by at least quinary-based alloys. Recently, differences have been made between high-entropy single-phase alloys and

compositionally complex multi-phase alloys (CCAs), both of which meet the defined requirements for high-entropy alloys containing at least 5% to 35% of the near-or-equiatomic elemental concentration blends. Several classes of CCAs have been proposed over the years including CCAs with a large number of components in equal or near-equal proportions dependent on their alloying method, the constituent species, the manufacturing process and the micro-and-phase structures that arise [2–6]. The synthesis of these CCAs has the propensity to form definite solid solution matrices, whereas nano-sized dispersed particles or intermetallic compounds have also been shown to improve mechanical properties. However, such intermediate phases reported in the literature [5–8] had structures of intermetallic compounds such as B2, L12, sigma and laves phases, in some cases leading to performance issues [6,9] such as the decrease in corrosion resistance in corrosive environments [9].

Currently reported HEAs and CCAs include those based on 3D transition metals and those based on refractory elements (Co, Cr, Cu, Fe, Mn, Ni, Ti, W, Zr, Nb, Ta and V) [5]. Due to the extreme melting temperature (>1000 °C) of these elements and consolidation capabilities, research and development have introduced a relatively short list of HEA/CCA thin films or coating layers on substrates while extensive research has been dedicated and reported on developing bulk HEAs and CCAs. The majority of related research focused on mechanical properties, deformation and strengthening mechanisms derived from crystallized phases, grain refinement, lattice distortion, precipitation and solution hardening [8,10–13]. A review of high entropy bulk alloy, HEA films and HEA coatings (HEACs) [14–17] revealed that the fabrication is identical to conventional coating techniques. The authors emphasized this growing field via deposition techniques such as vapor deposition (e.g., vacuum arc, sputtering), laser-based methods (e.g., laser cladding (LC)), cold/plasma/thermal spraying (e.g., high-velocity oxygen fuel (HVOF)) and electro-spark deposition (ESD). The functionality of the produced coatings depends on the microstructure, adhesion, thickness, ductility, hardness, oxide levels and stress state developed from the fabrication techniques mentioned above. Thus, microstructural, chemical compositional, mechanical and tribological analyses of novel HEACs from different fabrication processes are important for exploring their potential usage in intended engineering and structural applications, for example, as durable and cost-effective solutions for components in geothermal power production, where corrosion, erosion and wear are experienced due to mechanical loads and the corrosive nature of geothermal fluid [18].

A widely researched equiatomic HEA alloy is the single-phase-$Co_{20}Cr_{20}Fe_{20}Ni_{20}Mn_{20}$ alloy with excellent fracture toughness and ductility but low yield strength [10] reported by Cantor and his team [11]. Meanwhile, several related variants of the Cantor alloy compositions have been developed, including non-equimolar and multi-phase derivatives. Research by Miao et al. [12] in optimizing such alloys' mechanical properties found that the plasticity was attributed to the inherent FCC slip system of all the series of CoCrFeNi quaternary, CrCoNi ternary and other binary sub-unit alloys. Per such explorations and the simplest design of HEAs, the highly soluble–ductile CoCrFeNi alloy is retained as a quaternary stem (QS) [19–21] and further exploited for their mechanical/tribological properties (influenced by a balance in strength and ductility). An atomic size ratio (ASR) study of the QS + X alloys by Tsai et al. [19] concluded that X is replaceable or added on by similar-sized elements. As such, group 3B to 4B elements have contributed to the secondary-phase strengthening of HEAs and hence coating performance [13–19].

Xiao et al. [21] studied the tribological properties of plasma-sprayed CoCrFeNi alloy against WC-Co ball in dry sliding conditions. The as-sprayed and annealed HEAC demonstrated good wear resistance, which doubled with optimized process parameters. Similarly, Cui et al. [22] added fractions of Al to the cantor alloy and evaluated the wear resistance against 4Cr5MoSiV die steels. The HEAC with Al fraction at 0.75 demonstrated the existence of two dual phases (FCC+BCC), yielding the least worn volume at room temperature. Lin et al. [23] also reported improved properties, i.e., increasing hardness for as-cast and aged Al0.5CoCrFeNi due to the FCC to BCC matrix transition formation of segregated Al-Ni phases. Lin and other researchers [7,24] deduced Al as a BCC former. The

BCC structures' appearance with increased elemental concentration and associated lattice distortion confirmed the hypothesis. Zhang et al. [25] affirmed an excellent compromise between strength and ductility for the Ti-Al$_x$ rich + QS alloy, contrary to the non-ductile failure captured for the alloy with no Al. Wu et al. [26] reported a low wear coefficient with increasing Al-rich phases in Al$_x$Cu + QS in a Cu segregated microstructure. In a study to control the segregation, Ni et al. [15] fixed at% Cu and at% Al in Al$_x$Cu$_x$ + QS deposited laser clad on aluminum alloy. This rendered the alloy a micro-hardness of 750 HV, eight times that of the substrate. Therefore, aside from segregation, the matching counter surface undergoes severe wear if softer, detrimental to practical applications. Zhang et al. [16] investigated the addition of Si instead of Cu to the Al$_x$Cu$_x$ + QS alloy deposited by laser cladding. The deposit avoided abrasive wear, although a decrease in hardness was observed to 630.4 HV with Si segregation, while surface oxidation promoted strong wear resistance.

Other researchers have pursued the effect of Mo on the microstructure of the QS. Due to the QS's known properties, other authors achieved self-lubricating and wear resistive coatings in the presence of Mo, MoS$_2$ and graphite powders for tribological applications. Zhang et al. [20] spark plasma sprayed (SPSed) a well dispersed, densified, anti-wear and self-lubricating composite from room temperature to 800 °C of a QS matrix. The wear resistance increased because the composite's yield strength almost doubled by adding the nickel-coated-MoS$_2$ and graphite. CoCrFeNiMo bulk material fabricated by Cui et al. [27] showed a reduction in friction coefficient from 0.61 to 0.15 by treating with ion sulfurization with a similar trend for the wear coefficient. Liu et al. [6] found hard intermetallic phase precipitation and subsequent strengthening with no observed embrittlement by the secondary phases, even with the minor addition of Mo (at x = 0 to 0.3). However, Deng et al. [28] spark plasma sintered (SPS) QS + Mo$_{0.2}$ and Mu et al. [29] arc plasma sprayed (APS) QS + Mo coatings and both reported worn surfaces dominated with combined abrasive and adhesive wear under dry sliding wear conditions. Shun et al. [14] further increased the Mo fraction to 0.85, which showed the hard phases formed improved the mechanical properties. Fanicchia et al. [30] found that the QS + Mo$_{0.85}$ coating deposited with HVOF with FCC and BCC mixed phases had good corrosion resistance in electrochemical tests at room temperature. Improved wear resistance is critical for extending the life of materials used industrial plant components, such as in geothermal power plants, which must withstand high mechanical loads and corrosiveness of such aggressive environments. The development and testing of HEACs with high hardness, wear, corrosion and erosion resistance could be a solution for industrial application. While there is a clear potential for Mo addition to the QS, information on tribological properties is scarce particularly for HEAC coatings; thus, further evaluation of the microstructure and tribological properties of QS-based HEAC coatings in connection to possible fabrication techniques is needed.

The present work investigates starting compositions of two QS + Mo powders, i.e., CoCrFeNiMo$_x$ (at% x = 20, 27), each deposited by three different coating technologies—laser cladding (LC), high-velocity oxygen fuel (HVOF) and electro-spark deposition (ESD)—selected for application potential in the geothermal energy industry with prospects in improving service life of shafts, rotors and oscillating and sliding parts. The resulting morphology, microstructure is investigated with scanning electron microscopy (SEM), energy-dispersive X-ray spectroscopy (EDX) and X-ray diffraction (XRD), and tribological properties with hardness and wear sliding tests. Compared to previous research, the tribological properties of QS + Mo$_x$ are rarely reported, so further study is necessary to enhance their applicability beyond the research level. This work, therefore, allows the assessment of surface conditions and tribological properties of these alloys correlated to the microstructural characteristics obtained for each deposition technique.

2. Materials and Methods

2.1. Materials and Coating Processes

High purity, raw powders of Fe, Cr, Co, Ni and Mo were processed in a planetary ball mono-mill (Pulverisette 6® Fritch, Idar-Oberstein, Germany). Stainless steel vial and balls were used to avoid contamination in a 10:1 ball to powder weight ratio under Argon atmosphere. A wet milling process was selected, with 2% N-Heptane as the process control agent (PCA), increasing the alloying ratio and decreasing the powder's adherent tendency to the balls and vial. From the overall batch of powder produced, $-56 + 20$ μm, $-35 + 10$ μm and $-150 + 63$ μm size distributions for the HVOF, ESD and LC process, respectively, were obtained by using mechanical alloying and composition of the materials employed in the work is reported in Table 1. The powders used for the ESD technique were consolidated by pressing and sintering in a step-by-step approach to achieve the best consolidation degree. Electrodes were then machined from the bulk material obtained from the pressing and sintering (P&S) of powders. Electro-spark deposition (ESD) equipment was used (SparkDepo® Model 300 Shizuoka, Japan) for the ESD depositions by employing a miniature applicator using the process parameters shown in Table 2. The HVOF deposition was conducted at the process parameters in Table 3 by using the (Tafa Model 5220 HP/HVOF®, Praxair Surface Technologies, Indianapolis, IN, USA) gun equipment. A 5.3 kW disc laser system (Trudisk 8002 Trumpf®, Ditzingen, Germany) equipped with a TruControl 1000 controller and Trumpf BEO D70 processing optics with motor collimation was used to prepare the LC coatings. The process parameters used for the depositions are summarized in Table 4. The parameters were optimized in the design phase of the research project to minimize defects such as pores and micro-cracks in the coatings which were then tested in this study. The 304 stainless steel (SS) substrates were cut into 30 mm disc with 5 mm thickness and prepared by grit finishing to a 60 size and degreasing with acetone before deposition.

Table 1. Summary table of the powder composition, properties and techniques used for the different deposition techniques.

Coating Type	Nominal Powder Composition (at.%)		Experimental ID
$Co_{19}Cr_{17}Fe_{19}Ni_{18}Mo_{27}$	19.0% Co, 17.0% Cr, 19.0% Fe, 18.0% Ni, 27.0% Mo		HEA_Mo$_{27}$
$Co_{20}Cr_{20}Fe_{20}Ni_{20}Mo_{20}$	20.0% Co, 20.0% Cr, 20.0% Fe, 20.0% Ni, 20.0% Mo		HEA_Mo$_{20}$
Powder processing	Powder size distribution [μm]	Coating process ID	Experimental ID
Mechanical alloying (MA)	20–56	HVOF	HVOF-HEA_Mo$_{27}$ HVOF-HEA_Mo$_{20}$
	63–125	LC	LC-HEA_Mo$_{27}$ LC-HEA_Mo$_{20}$
MA + Pressing and sintering	16–45	ESD	ESD-HEA_Mo$_{27}$ ESD-HEA_Mo$_{20}$

Table 2. Electro-spark deposition (ESD) process parameters employed to deposit high entropy alloy powders.

Capacitance	Voltage (V)	Frequency (Hz)	Atmosphere
20 μF	100	150	Argon

Table 3. High-velocity oxygen fuel (HVOF) process parameters employed to deposit the high entropy alloys powders.

Process Parameter	Oxygen Flow	Kerosene Flow	Nitrogen Flow	Standoff Distance	Number of Passes
	(slpm)	(slpm)	(slpm)	(mm)	(–)
Value	834	0.33	12.27	360	20

Table 4. Laser Cladding (LC) process parameters employed to deposit the high entropy alloys powders.

Sample	Laser Power	Laser Speed	Overlap Rate	Powder Disk Speed Parameter	Number of Layers	Carrier Gas Flow (Ar)	Shielding Gas Flow (Ar)
	(W)	(mm/s)	(%)	(%)	(–)	(L/min)	(L/min)
HEA_Mo27	550	10	33	9.3	1	4	6
HEA_Mo20	400	10	33	9.3	1	4	6

2.2. Surface Morphology and Microstructural Analysis

Microstructural and chemical analysis was carried out with a field emission-scanning electron microscope (FE-SEM, Zeiss Supra 25® Oberkochen, Germany), fitted with an Energy Dispersive X-ray Spectroscopy Detector (EDX, Oxford Instruments®, Oxford, UK). The X-ray Diffraction (XRD) measured the phase composition on a diffractometer (Empyrean, Panalytical® Malvern, UK) with Cu Kα radiation (λ = 1.54056 Å), 45 kV, 40 mA in the 2θ range of 20–100 degree. A non-contact optical profilometer (NC-OP) (Solarius® California, USA) coupled with the Mountains® software-generated 2D and 3D topographic profiles to investigate the average roughness Ra and other morphological surface features of the HEACs.

2.3. Hardness Test

The hardness of the HEACs was obtained from seven different locations in the cross-section with Vickers micro-hardness tester (VH1202 Wilson®, Esslingen, Germany) using 0.1 kg-f load.

2.4. Tribological: Friction and Wear Testing

The tribological wear tests of the as-sprayed coatings were conducted at ambient temperature with a ball-on-disc configuration using a tribometer (TRB³, Anton Paar® Graz, Austria). The set-up, procedures [31] and measurements followed the ASTM G99 standard [32]. The test involved unidirectional dry sliding of the ball pressed against the 30 mm coated disc at an applied load of 5 N. Based on the Archard elastic model [33] (i.e., H_0/H value should be high; H_0 is the hardness of the abradant, and H is the hardness of the test sample) and the known properties of WC (tungsten carbide) coatings on bearings, seals and turbine blades [34], WC balls were considered as a counter body to the sprayed coatings to produce an appreciable and reliable wear assessment in the laboratory accelerated-wear test. WC ball with 6 mm diameter and higher hardness of 1640 HV was used as a rubbing counterpart. The test duration and motor speed were kept constant at 3600 s and 200 rpm (linear speed: 10.47 cm/s), respectively. In practice, the steam turbines, e.g., geothermal turbines (with targeted units such as bearings, valve stem, shaft, rotor and blades) rotates at 1800–3600 rpm, which is clearly faster than the speeds selected for this work. Here, we simulate startup and shutdown conditions where frequently slower speed runs (100–600 rpm for 1 h) to troubleshoot before normal operational speeds are reached [35]. Furthermore, with no shaft/rotor imbalance, steam turbines run smoothly at inlet pressures ranging from 400 to 4000 kPa and vibration levels less than 2.54 mm/s [36].

The coefficient of friction (CoF) was monitored during rubbing without interruption. The data from the tribometer was processed with Anton Paar® Instrument X software version 8.1.5. The COF (μ) Equation (1) was used to calculate the dimensionless averages values of the stepwise and entire stable stages of the curve and the standard deviation (SD) was used to assess the degree of fluctuation during the tangential friction (F_t) acquisition process. The SD values obtained primarily explain the degree of fluctuation of COF (μ) and geometric contact changes during the test that could reflect the contact interface properties.

$$\mu_{sample} = F_t/F_n[-] \tag{1}$$

The wear rate, w_{sample} (mm^3/Nm), was evaluated according to Equation (2) by measuring the volume of the removed material, v (mm^3), and using the applied load, F_n (N), and the distance covered during testing, L (m). After the wear test, cross-sectional profiles and images were extracted from the worn areas with optical profilometer (NC-OP) (Solarius® California, San Jose, CA, USA). The extracted profiles were from at least three representative locations on the wear tracks and final averages were used to determine the wear volume and calculate the wear rate (w_{sample}). Each sample was subjected to three parallel tests, with the results reported as averages.

$$w_{sample} = v/F_n \cdot L \left[mm^3/Nm \right] \tag{2}$$

3. Results and Discussion

3.1. Surface Morphology, Microstructure and Chemical Composition

The microstructural images and chemical composition of the coatings resulting from the various deposition techniques are presented in Figures 1–6. Figures 1, 3 and 5 show the top surface while Figures 2, 4 and 6 reveal cross section microstructural SEM images and corresponding EDX surface maps of the as-deposited HEACs. The micrographs of the as-sprayed coatings revealed a clear distinction in surface morphology for coatings deposited by different technologies. The surface morphology of the coatings consists of fully melted, semi-melted and un-melted particles. Surface defects observed were generally either or both pores and/or micro-cracks and are typical of such deposits. Dissimilarities between the same deposition technique for the different types of coating (i.e., HEA_Mo$_{27}$ and HEA_Mo$_{20}$) can be difficult to discern only by SEM/EDX analysis of the top surface; thus an XRD analysis was additionally performed as discussed in Section 3.2. From the high content of oxygen detected on all the surfaces, as can be seen from the EDX surface maps in Figures 1, 3 and 5, it can be concluded that particles underwent oxidation during the deposition for all deposition processes. While this is not surprising for the HVOF and ESD coatings deposited in air, the finding also applies to the LC coating where argon was used as shielding gas. The high content of oxygen found with the chemically stable elements (i.e., Ni, Cr, Mo, Fe) can be due to the active formation of surface protective films in contact with the atmosphere.

Apart from oxygen, the result from SEM/EDX reveals that all the precursor elements in the HEA powders (reported in Table 1) were present. However, the composition of the HEACs showed inconsistencies with the nominal (theoretical) powder composition, suggesting the activation of effects during the deposition process [37]. These phenomena can be linked to chemical-physical properties of the substrate and materials to be deposited and deposition technique-specific thermodynamic effects (such as convective motion and substrate/coating interdiffusion in laser metal deposition, etc.). The relevant substrate and coating material properties that are relevant in the final composition of the coating include melting temperatures, solubility, volatility and mixing enthalpy. Due to the mechanical alloying process of the powder production used for the HVOF and LC deposition techniques, fractions of single elements are likely to be still present in the powder prior to deposition for this alloy composition [27]. The melting points of Fe, Co, Ni, Cr and Mo elements at ambient pressure are 1538, 1495, 1455, 1907 and 2623 °C, respectively. For the coatings from the LC and ESD processes, less amount of the highest melting point element (Mo) was observed in the elemental maps of the surfaces compared to the powder starting composition. This could be because of the non-homogenous distribution of Mo and/or substrate melting and dilution, which both affect the composition in the melt pool [18,27]. Furthermore, each element was of 5% to 35% atomic concentration, which falls within the rigorous HEA definitions and satisfies the overall goal of exploring the central regions of complex phase space.
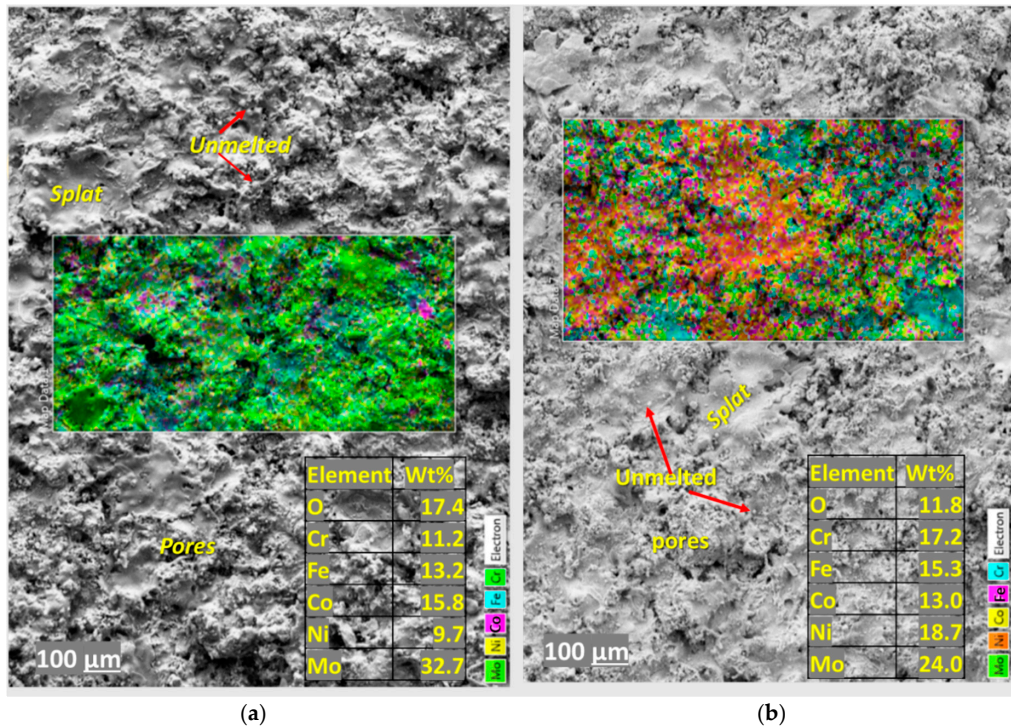
Figure 1. Top surface morphologies, elemental concentration and surface maps of the as-sprayed (**a**) HVOF-HEA_Mo$_{27}$, and (**b**) HVOF-HEA_Mo$_{20}$ coatings.

3.1.1. Morphological and Microstructural Characterization of HVOF HEACs

The HVOF process produced features characteristic of thermally sprayed coatings (see Figures 1 and 2), such as splats (full-melted particles) and semi-molten particles, which were also seen in other articles [29,30]. The mixed powder grain size and thermal process ensured good adherence and spread of molten lamellar deposits to achieve cohesive splats within the coating bulk. Thus, no line cracks were present in the coatings' cross-section (Figure 2a–f). The observed porosity, a common feature in such coating systems, is due to the overlap between unmelted and melted particles during splats overlap.

Figure 2a–d show the cross-section micrographs with line scans by SEM/EDX for the HVOF coating compositions. The results indicated a lamellar structure, all elements present and a higher oxygen content compared to the top surface across the thickness. The HVOF-coating process ensured good adherence maintaining coating thickness of 418.7 ± 20 μm and 313.8 ± 24 μm for HEA_Mo$_{27}$ and HEA_Mo$_{20}$, respectively. Both had a good mechanical interlayer interface but with some Al$_2$O$_3$ grit retention from surface preparation of sample before spraying. Distinctive variation in phase distribution was observed along the cross-section of the HVOF HEACs. The cross-sections of both HVOF HEACs in Figure 2b,d had similar features; the only difference is that a brighter phase (Mo rich) is more visible and involves a greater amount for the HEA_Mo$_{20}$ compared to dark gray phases in the HEA_Mo$_{27}$. The coating has three variations in the splats with different compositions resulting from the impingement and high oxidation related to the coating process. The EDX mapping (see Figure 2e,f) showed the two soft grey regions in the microscopic images (see BSE Figure 2b,d) to be of either Co-Mo/Fe-Mo or FeCoNi matrix with traces of Mo and Cr for the HEA_Mo$_{27}$. A darker grey region visible in the microscopic images exhibited higher Cr content, while a bright grey region is rich in Mo. The line profiles show that the average composition across the thickness

contains higher Mo and O than the other elements for both the HVOF HEACs, but an increase in Cr was observed for the HVOF-HEA_Mo$_{20}$ (see Tables in Figure 2 and EDX maps in Figure 2e,f for the comparison). In correlation to backscattered images shown in Figure 2c,d, the Cr-splats were rich in O. The high melting and boiling points (i.e., 2623 °C and 4639 °C, respectively) can potentially explain the Mo content. During the HVOF process, in-flight particle temperature is estimated as 3000–3300 °C, significantly lower than the boiling point and approximately close to pure Mo melting temperature. Moreover, Mo volatility is the lowest in the CoCrFeNiMox molten alloy due to its higher molecular weight. Fanicchia et al. [30] identified similar bright Mo-rich phases uniformly distributed in MA-QS + Mo$_{0.85}$ coating and the appearance of oxides related to the HVOF spray process.
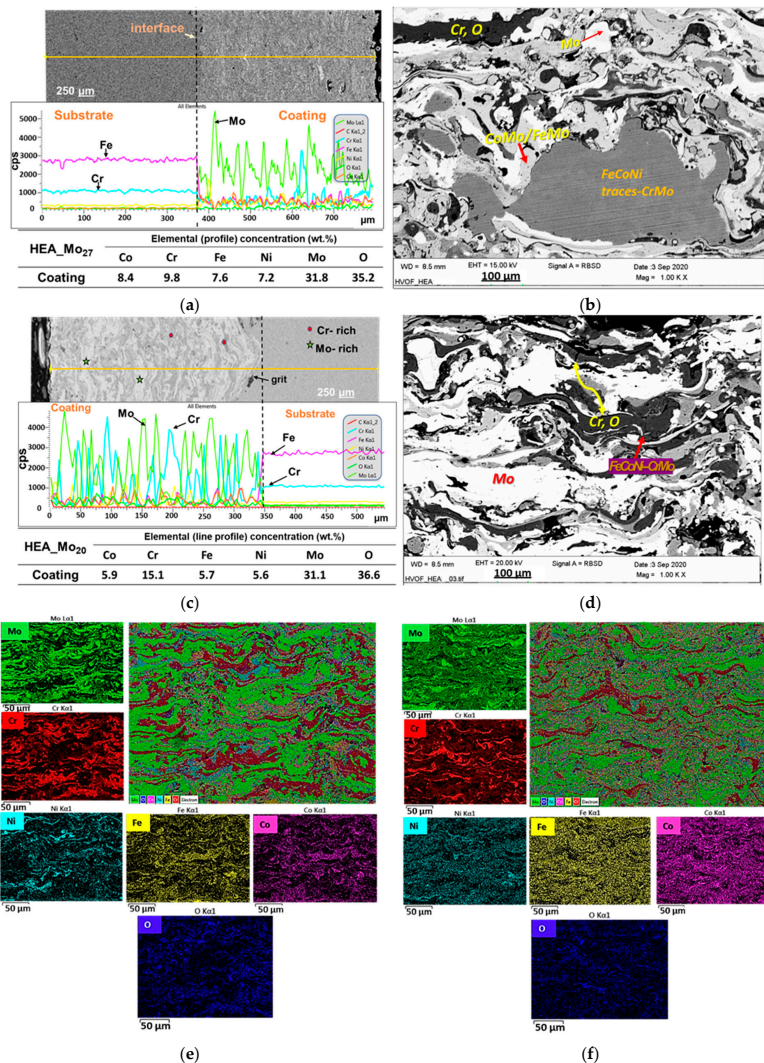
Figure 2. SEM (**a**,**c**) and BSE micrographs (**b**,**d**) of the cross-sections of the as-sprayed HVOF-HEA_Mo$_{27}$ (**a**,**b**,**e**) and HVOF-HEA_Mo$_{20}$ coatings (**c**,**d**,**f**) and the corresponding EDX line scans (**a**,**c**) and maps (**e**,**f**).
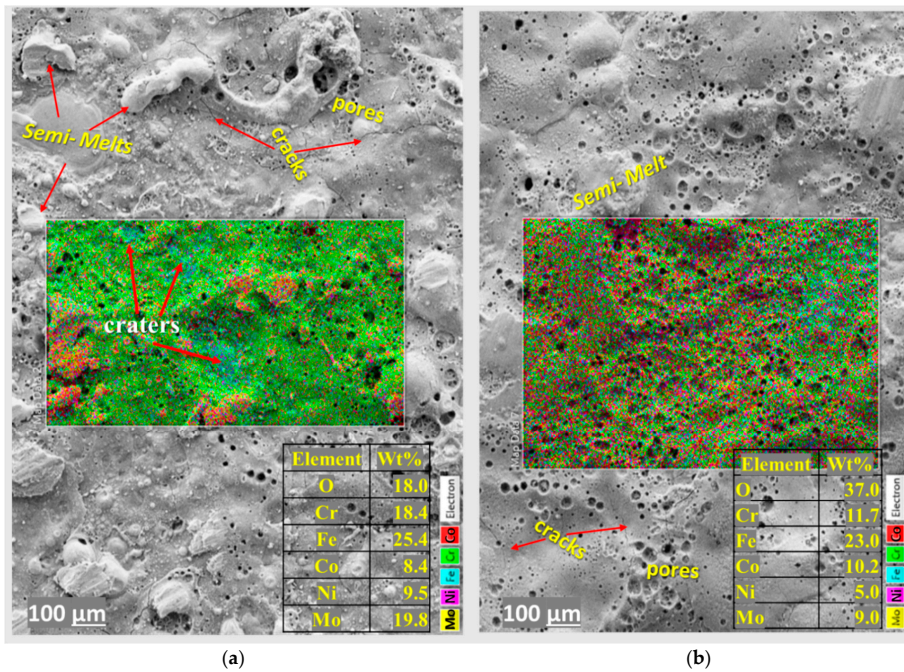
Figure 3. Top surface morphologies, elemental concentration and surface maps of the as-sprayed (**a**) ESD-HEA_Mo$_{27}$, (**b**) ESD-HEA_Mo$_{20}$ coatings.
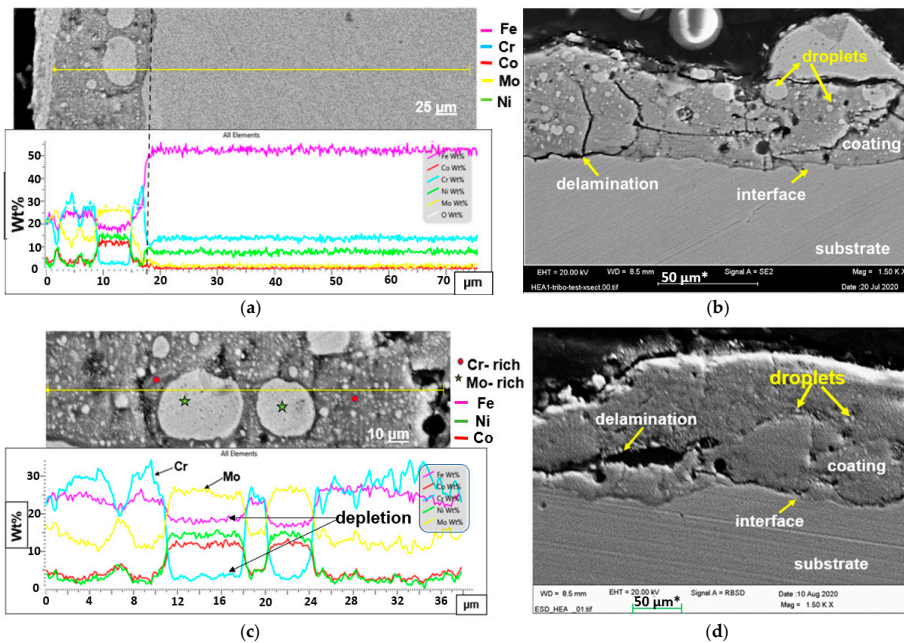
Figure 4. SEM and BSE micrographs of the cross-section and EDX line scans, revealing of the as-sprayed (**a**,**b**) ESD-HEA_Mo$_{27}$ and (**c**,**d**) ESD-HEA_Mo$_{20}$ coatings.
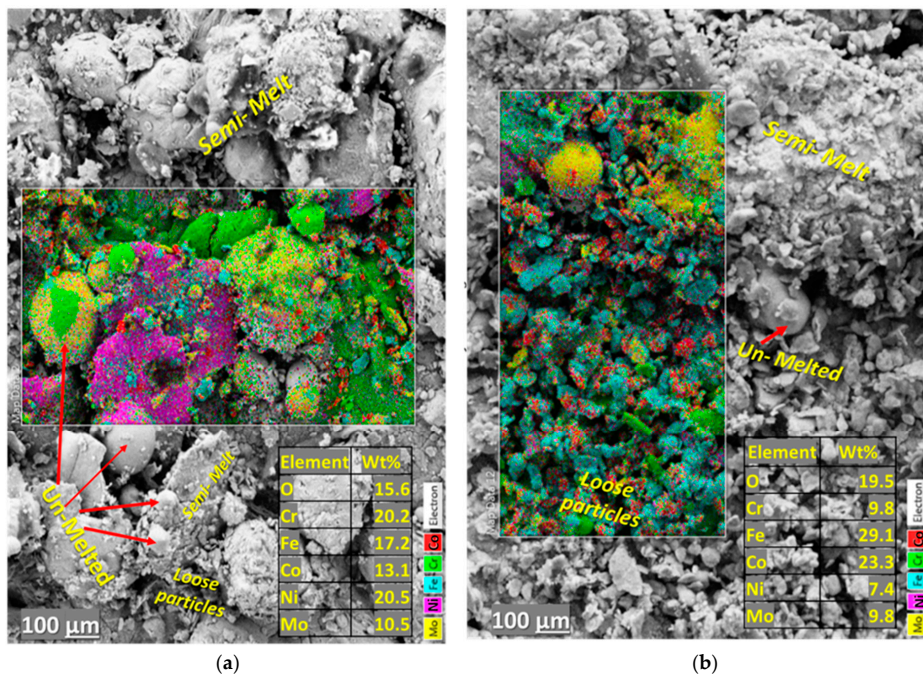
Figure 5. Top surface morphologies, elemental concentration and combined EDX surface map of the as-sprayed (**a**) LC-HEA_Mo$_{27}$ and (**b**) LC-HEA_Mo$_{20}$ coatings.

3.1.2. Morphological and Microstructural Characterization of ESD HEACs

Figures 3 and 4 show the top surface and cross-sectional views of the ESD-HEACs as analyzed via SEM/EDX. The top surfaces of the coatings show more micro-cracks and pores compared to the coatings prepared by the HVOF and LC techniques. However, the SEM images and the corresponding EDX maps in Figure 3a,b revealed a uniform, smooth and continuous coating. The top morphology appeared bubbly on a 1 mm scale but expanded into pinholes and soft bulges overlapping with craters, as seen in Figure 3a,b. These craters are likely formed from the shrinkage of the hot liquid pool thrusting around semi-melted or unmelted droplets from the solidifying molten pool. The surface maps show a relatively homogeneous elemental distribution of Co, Cr, Fe, Ni, Mo and O in the HEACs. However, the EDX mapped surface of the HEA_Mo$_{27}$ reveals an area with increased Fe concentration in the craters and higher Co content in the droplets compared to the HEA_Mo$_{20}$ (see Figure 3a,b).

Cross-section micrographs in Figure 4 show the microstructure of the ESD HEACs. The two-phase microstructure was characterized by a single-phase dark grey matrix and a significant amount of spherical droplet particles, as shown in Figure 4. The dark grey matrix was highly oxygenated with no secondary phases present. A pulsed-arc welding process is used to build multi-pass ESD HEA layers on the substrate from individual splats of the material from the electrode. A single spot deposit using this technique has a typical 'splash appearance' [38]; therefore, droplet particles were likely trapped if uneven heating and electric field oscillations occurs during the manual application. The obvious difference between the coatings HEA_Mo$_{20}$ compared to HEA_Mo$_{27}$ (SEM micrographs of Figure 4d over Figure 4b) is the increased thickness and consolidated microstructure without the large globules indicating spraying of fine molten droplets along the discharge arc during argon shielding deposition. A homogeneously dense and adherent two-phase microstructure with no pores was reported by Karlsdottir et al. [39] for the same deposition technique as for the HEA_Mo$_{20}$ (QS + Mo) coating. However, the HEA electrode was prepared by vacuum

arc melting with multiple passes (3–4) in that study and thus thicker and more uniform coating was obtained. The ESD process produced a coating thickness of 23.5 ± 5 µm and 28.8 ± 6 µm for HEA_Mo$_{27}$ and HEA_Mo$_{20}$, respectively, which the approximated value is comparable to already reported single deposit thickness [38]. The droplet particles appear light grey in SEM/EDX analysis and are rich in Mo, although traces of Cr and O are also found. The maps and line profiles from Figure 4a,c confirmed a considerable amount of Cr, Fe and Mo in the HEACs. The Fe and Cr content increased from substrate melting and mixing in the liquid pool, which explained the craters' high Fe content from the surface analysis (see Figure 3). The ESD process has been reported to promote Cr segregation in FeCrMo type alloys with CrxOy formation [39]. There is also evidence of this in this work, as clearly shown in the composition profile scans in Figure 4a,c, showing depletion of Fe and Cr indicated by lower wt% in the un-melted regions. The entrapped powder particles contributed to coating layer-to-layer (L/L) fusion and defects in substrate-coating interfacial (S/C). As seen in Figure 4b, spherical voids in the coating could also be generated by entrapped gas during deposition.
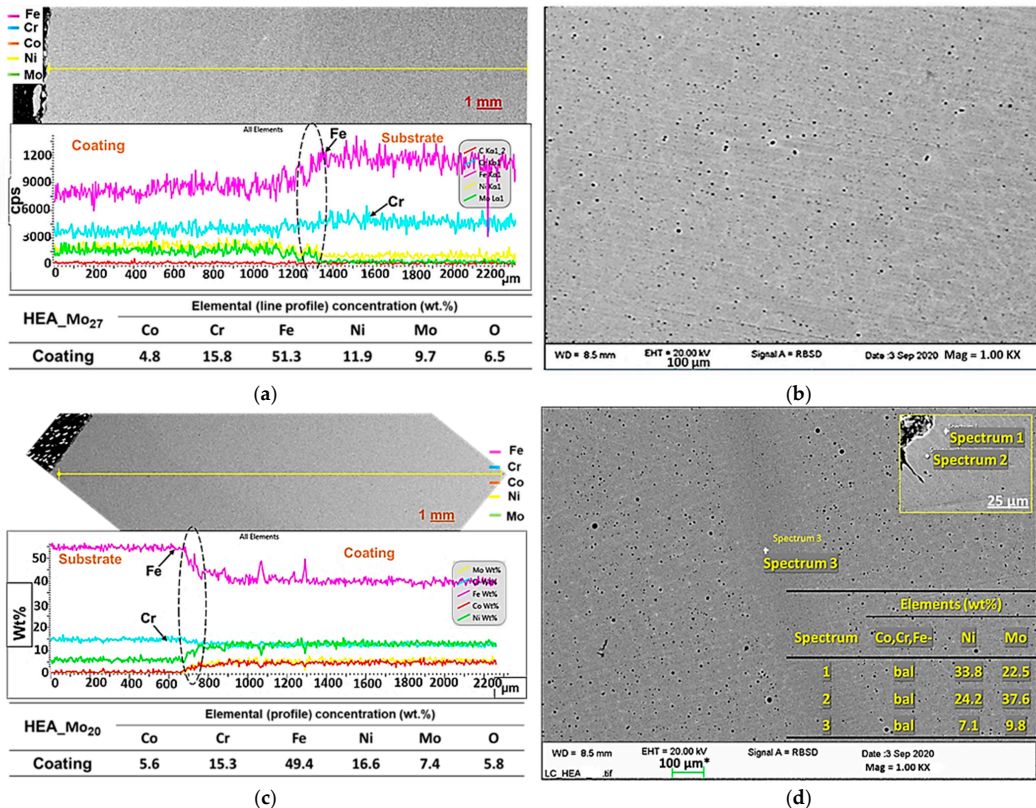
Figure 6. SEM and BSE micrographs of the cross-sections, and EDX line scans, point and area analysis of the as-sprayed (**a**,**b**) LC-HEA_Mo$_{27}$ and (**c**,**d**) LC-HEA_Mo$_{20}$ coatings.

Furthermore, branched cracks originated from the bridging of the voids during solidification. Residual thermal effects and stresses most likely propagated other cracks, either parallel or perpendicular to the surface. The L/L stresses created within the coating during L/L fusion promoted the formation of cracks, which propagated vertically (see Figure 4b). Additionally, delamination cracks also formed in a direction parallel to the surface (see Figure 4b,d). Hence, delamination resulted in a weak metallurgical interlayer at the S/C interface.

3.1.3. Morphological and Microstructural Characterization of the LC HEACs

The top surface morphology showed spherical granules and loose particles lightly bonded to large lumps of semi-melted structures. The mixed coarse powder distribution and rapid solidification of the LC process may have led to uneven heating of the particles promoting an uneven surface where the particles were partially melted or maintained their shape. However, finer granules were observed on the HEA_Mo$_{20}$ coatings compared to HA_Mo$_{27}$ (see Figure 5) due to high melting capabilities needed with the increase in Mo. Thus, the alloy elements are not homogeneously spread on the surfaces, as seen from the EDX surface maps in Figure 5a,b.

Figure 6 shows the microstructures of the cross-sectional area of the LC HEACs. The LC technique is known to develop thicker coatings, where the measured thickness was 1200 ± 0.1 μm and 1300 ± 0.1 μm for HEA_Mo$_{27}$ and HEA_Mo$_{20}$, respectively. The L/L build in the micrograph was homogeneous, dense and compact with no entrapped particles, only nano-scale pores (seen in Figure 6b,d) likely caused by the residual shielding gas. Compared to the HVOF and ESD coatings, the dense and homogenous structure is due to the higher temperatures reached by the process, leading to the development of a melting pool. At high magnification, the LC process was seen to have generated a dense cross-section and substantial substrate interdiffusion zone. The effect of volume fraction between the different molten phases resulted in the final morphology of a two-phase microstructure produced by spinodal decomposition, which was previously reported for the same alloy [40]. The compositional profiles in Figure 6a,c show the S/C metallic bond is enhanced with substrate melting and dilution, indicated with the increasing wt.% of Fe, %Cr and %Ni at the interface verified by the EDX line scan results, which then decreased across the coating thickness. Moreover, in Figure 6b,d, light grey phases are obvious in both alloys. The features and preferred orientation of the segregated phases were different in the matrices. The darkest phase (see Spectrum 3 in Figure 6d) was (Fe, Cr)-rich, while the brightest phase (see Spectrum 2 in Figure 6d) was Mo-rich. The solidification rate and temperature gradient during the multiple pass process in laser cladding can influence the crystal formation, transformation and final microstructure across the coating thickness due to the dependence of the ratio of both phenomena on crystal growth along a plane or the fastest direction of heat dissipation [41,42].

3.2. X-ray Diffraction (XRD) Analysis

Figure 7 shows XRD patterns of CoCrFeNiMox coatings fabricated from the MA powders. It shows three major phases: A mixture of FCC and BCC, as well as a residual Mo phase linked to the Mo element present in both alloys. The valence electron concentration (VEC) is a parameter that predicts FCC and BCC phase content present in a structure. The VEC number of the equiatomic CoCrFeNiMo alloy suggests that FCC phases should form in more significant quantities than BCC [43], the diffraction patterns reported here support this hypothesis, see Figure 7. The VEC of the CoCrFeNiMox decreases by 1.4% by increasing at% x from 20 to 27. Thus, HEA_Mo$_{27}$ has a lower calculated VEC, 7.69, compared to HEA_Mo$_{20}$ which has a VEC of 7.8, which would suggest more dominance of the FCC and less BCC for the HEA_Mo$_{20}$. The XRD patterns support that, particularly for the LC-HEA_Mo$_{20}$ coating as shown in Figure 7b where the FCC peaks are sharper and more pronounced than the BCC. Additionally, σ phase was detected in the HEA_Mo$_{27}$ patterns. The established σ phase of a tetragonal structure was Fe-Cr or Cr-Mo rich and Ni deficient [37,38,43], while the Mo compound-based phase was a Fe-Mo or Co-Mo rich phases of a rhombohedral structure (presumably an μ phase) with Ni traces as reported in [39,43,44]. The Fe-Mo phase was present in the ESD and LC developed coating explained by high Fe content in the microstructure from SEM/EDX results whereas Co-Mo phase was found in the HVOF HEACs. Research on the CoCrFeNiMox alloy revealed the same crystal structures for these two intermetallics and that the σ phase + μ phase could co-exist [6,16] or undergo a transformation in the same matrix [44–46]. Thus, this confirms some segregation, as indicated as an example with: (1) The Co-Mo and Cr-Mo soft grey

phases predicted in Figure 2b,d; (2) the Fe-rich FCC matrix depleted in Mo (see EDX results of LC-HEA_Mo$_{20}$ in table in Figure 6d), while the bright region is a Mo rich -Ni phase, according to Figure 6d. The droplet phases in the ESD-HEA_Mo$_{27}$ in Figure 4 show a similar trend in composition related to the BCC structures. The element distribution is in line with the literature [29,37,41–44] and has been attributed to sluggish Mo diffusion, which tends to be divided into dendritic and interdendritic regions during solidification. While research on Mo-containing HEA systems (cast or coated) is limited, our results are comparable to those of other studies with HEA alloys where similar VEC values are prone to the formation of σ intermetallic phase and FCC + BCC structures [13].
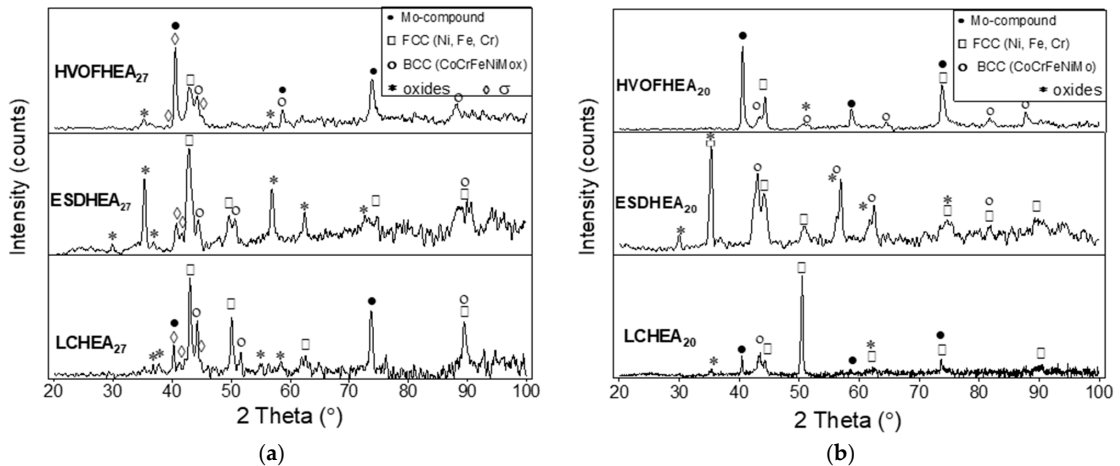
Figure 7. XRD scan of the as-sprayed (**a**) HEA_Mo$_{27}$ and (**b**) HEA_Mo$_{20}$ coatings with the different deposition techniques.

All the coatings show the appearance of oxide phases generated during all the deposition processes; this is in line with what has been reported for HEA coatings produced with thermal spray processes due to the oxygenated atmosphere. The oxides identified in the diffraction pattern were composed of the following elements: Ni, Cr, Mo and Fe. This is consistent with the microstructure analysis of CoCrFeNiMox coatings developed by [30] by LC and [39] by ESD deposition who reported the formation of both FCC and BCC phases in the structure. Both researchers related the FCC structures to a binary constituent of Fe, Ni and Co while BCC to Mo compounds. Liu et al. [6] attributed the strength of CoCrFeNiMox bulk material to the formation of BCC phase and hard σ + μ intermetallic structures.

3.3. Micro-Hardness of the HEACs

The averages of micro-hardness results taken are reported from the cross-section of the coatings. The substrate's hardness was improved from 164 HV$_{0.1}$ to an average of 444.5 HV$_{0.1}$ for the HEA_Mo$_{27}$ and 304.2 HV$_{0.1}$ for the HEA_Mo$_{20}$ coatings produced by the HVOF technique. The HVOF coatings were recorded with the highest hardness among the ones tested in this work, likely due to the additional hard phases such as the Cr$_2$O$_3$ phases shown in Figure 2c,d. In addition, grain boundaries are visible around splats from the HVOF technique, which may increase the resistance to the deformation mechanism during indentation. The LC-HEACs had the thickest coatings and defect-free interface, suggesting a good metallurgical bond. The LC-HEA_Mo$_{27}$ samples had a hardness value of 276 HV$_{0.1}$. However, a lower value was obtained for LC-HEA_Mo$_{20}$ at 209.3 HV$_{0.1}$. Thus, using the LC instead of HVOF technique, the hardness of HEA_Mo$_{27}$ decreased by 38%, while HEA_Mo$_{20}$ by 31%. This is the same trend as for the HVOF, i.e., HEA_Mo$_{27}$ outperformed the HEA_Mo$_{20}$ in the hardness testing. This can likely be attributed to localized hardening due to the microstructural strengthening of each precipitated phase, the σ phase that

was only detected in the XRD analysis for the HEA_Mo$_{27}$ and not for the HEA_Mo$_{20}$. Additionally, based on the backscattered images in Figure 6b,d, the solution matrix is undoubtedly made up of Fe, Cr and Ni elements. Further examination of the XRD results in Figure 7 reveals a higher intensity of the prevalent double-diffraction peaks from 42° to 45° in HEA_Mo$_{27}$ than in HEA_Mo$_{20}$, implying that the mass fractions of Fe, Cr and Ni in phase formation also affect the hardness. The Fe, Cr, Ni fractions are 51.3 wt%, 15.8 wt%, 11.9 wt% for HEA_Mo$_{27}$ and 49.4 wt%, 15.3 wt%, 16.6 wt% for HEA_Mo$_{20}$, respectively. Because wt% of Fe accounts for roughly half of the mass fraction, it can be assumed that the hardness was influenced by Fe compositional variations in the microstructure. Moreover, Zhang et al. [16] found the formation of martensitic structures (i.e., FCC Fe to BCC Fe compounds) in lower regions via 304 stainless steel substrate dilution as a contributing factor to the overall hardness of LC produced coatings [8].

Thus, by comparing the microstructures explains the higher hardness of the HEA_Mo$_{27}$ over HEA_Mo$_{20}$ alloy since: (1) BCC and tetragonal phases were dominant for HEA_Mo$_{27}$, which promoted hardness; and (2) the decrease in hardness in HEA_Mo$_{20}$ was confirmed as the tetragonal-σ phase disappeared or transformed into a rhombohedral-phase structure shown in the patterns (compare Figure 7a,b), as observed and supported by relevant literature [31,34]. The formation of the Cr, Mo-based -σ phase in the matrix improves the alloy hardness as has been also reported by Shun et al. for age hardened CoCrFeNiMo$_{0.85}$ high-entropy alloy [45], as lattice distortion associated with Mo increase is noticeable in the solid solution strengthening for the CoCrFeNiMo$_x$.

The thinnest coatings were produced by the ESD technique, measured with 23.5 ± 4.6 μm and 28.8 ± 5.0 μm for HEA_Mo$_{27}$ and HEA_Mo$_{20}$, respectively. For these coatings, Vickers micro-hardness could not be determined in the cross-section due to their thin nature.

3.4. Surface Roughness of the HEA Coatings (HEACs)

A critical factor in defining tribological properties is the surface interaction of two moving parts. In practice, the arithmetic average roughness, Ra, or its root mean square, Rq, are the engineering parameters that determine the load-bearing capacity of surfaces. The results from the surface roughness analysis for the HEACs showed a similar increasing trend in roughness for both compositions of the as-sprayed HEACs in the order: ESD < HVOF < LC as reported in Table 6. This low roughness could be related: The lower the process speed, the smaller the precursor particle size and post treatment (pressing and sintering of the MA powder) to consolidate the electrode for the ESD process. The surface features of HEA_Mo$_{27}$ and HEA_Mo$_{20}$ had similar features defined by each coating process' inherent characteristics; thus, in this case, only information on HEA_Mo$_{27}$ is presented. The Ra for both coating types was evaluated and compared in Table 6.

Figure 8 is a pictorial display of 3D topographic images of the surfaces from the LC, ESD and HVOF deposition techniques. The images show rough bulges on all the surfaces. The surface roughness parameters with the initial *S* were investigated with other height distribution parameters such as skewness (Ssk) and kurtosis (Sku). The obtained average and root mean square surface roughness (Sa, Sq) values of the HVOF and ESD coating were approximately half that of the LC coatings. The correlation between Ssk and Sku converged for height distribution near-symmetry in all the coatings except the HVOF.

The as-sprayed LC and HVOF HEACs had low valleys and sharp peaks (from the rule of thumb: Sku ≥ 3). However, the HVOF surfaces were characterized with the highest and sharpest peak ratio (Figure 8a), where the value of Ssk was unity. The ESD developed coatings were somewhat sensitive to low valley formation to symmetric broader peaks (hills in Figure 8), where Ssk was negative. The LC HEACs depicted a similar distribution, but the features of a more compact and spiky surface asperities (peaks) were seen. The plateau-like microdomain structures showed close symmetry in peak sharpness and height distribution (Sku ≈ 3, Ssk ≈ 0, see Figure 8c). This localized macro to nano-scale structures on LC HEACs contributed to the large statistical roughness parameters in line with the coarse granular morphology seen from the top surface SEM micrographs in Figure 5a,b. Thus,

though all the coatings contained similar precursor elemental content, the highest Sa was recorded for the LC coating deposition process, which is consistent with the microstructural SEM analysis of the coating surfaces.
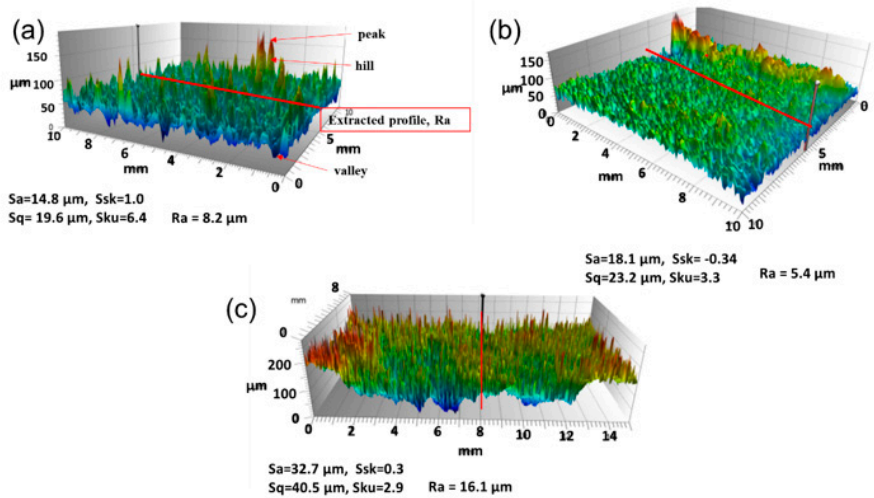
Figure 8. Three-dimensional topographic images and selected surface parameter of the as-sprayed (**a**) HVOF-HEA_Mo27 (**b**) ESD-HEA_Mo27 and (**c**) LC-HEA_Mo27 coatings.

3.5. Sliding Friction Coefficient and Wear Behavior

The representative coefficient of friction (CoF) curves of each as-sprayed HEAC with its deposition process as a function of time under the dry sliding is shown in Figure 9a–c. Figure 9d compares the CoF traces for all the HEACs and 304 SS substrate. Two time-dependent regimes characterized the fluctuations. From Tables 5 and 6, the average values in these regions and that of the entire curves were compared with the value of stainless steel of 304 SS (0.80). On contact between the tribo-pairs under the applied load, an initial force is needed to alter the morphology of the contact zone for a continuous motion. The initial sliding period corresponded to breaking-in or running-in with the highest CoF value (μ_{pk}) shown on the friction curves. The running-in is related to the surface structures or morphology of the coating and the 304SS. The running-in was severe for all the HEACs and the steady-state was harder to achieve in the HEA_Mo$_{27}$ than HEA_Mo$_{20}$ coatings before coating run-through (μ_c). Figure 9a,b show a very short running-in stage for both the HVOF and ESD techniques with the least Ra values (i.e., 8.2 and 5.4) but recorded the highest μ_{pk} values (see Table 5). This may be attributed to a higher nominal/apparent contact area since, at the initial contact pressure, the area to load ratio is low during sliding (i.e., there is a low volume of material/asperity peaks above). However, this effect did not guarantee a high overall mean CoF value, implying an opposite general trend in which frictional response was controlled by the wear behavior of the coatings. Figure 9a–c shows these transitions (μ_{pk}, μ_c, μ_s) according to the friction behavior indicated lines (and arrows, only for Mo$_{27}$ due to clarity).
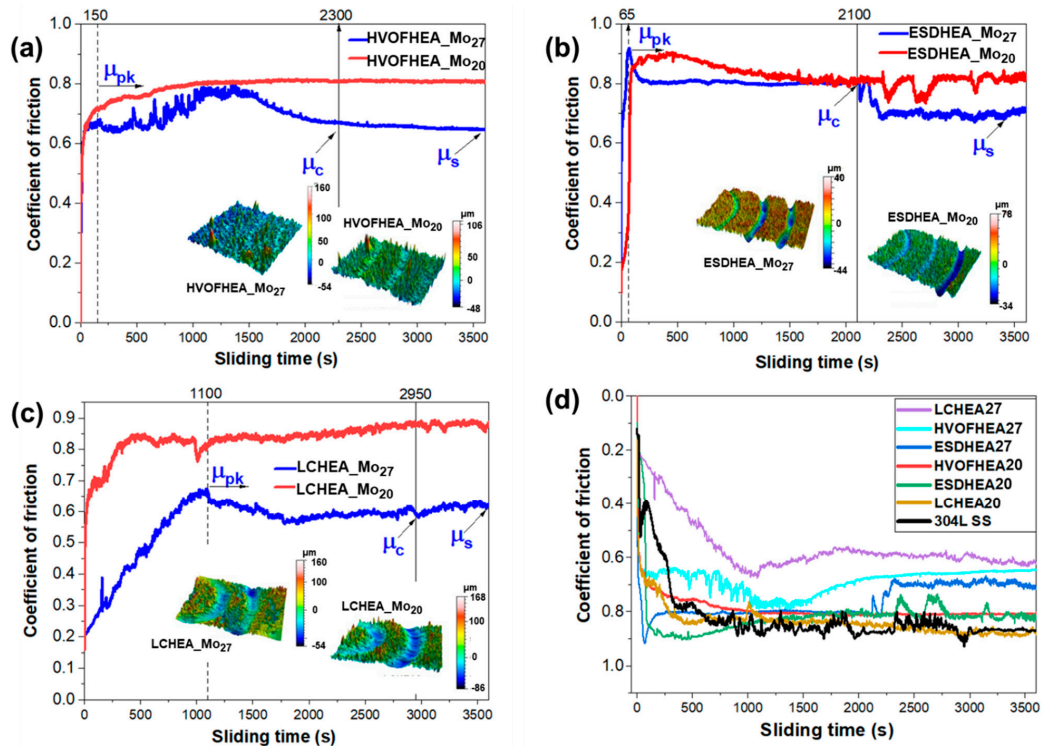
Figure 9. Evolution of coefficient of friction (CoF) versus sliding time after 12,000 wear cycles under dry test condition for the as-sprayed (**a**) HVOF, (**b**) ESD, (**c**) LC -HEA coatings and (**d**) 304L SS and HEACs with the different deposition techniques.

Table 5. Averaged transition stages in the friction traces of HEA_Mo$_{27}$ coatings from the different deposition techniques assigned as: Break-in peak value—μ_{pk}; coating run-through—μ_c; sub-stresses from substrate—μ_s.

Coating ID	μ_{pk}	μ_c	μ_s	μ_{mean} (CoF$_{mean}$) 12,000 Cycles	Wear Rate (mm^3/Nm)
HVOF-HEA_Mo$_{27}$	0.82	0.71 ± 0.05	0.70 ± 0.17	0.69 ± 0.04	1.34 × 10^{-5}
ESD-HEA_Mo$_{27}$	0.92	0.80 ± 0.02	0.70 ± 0.02	0.76 ± 0.06	2.24 × 10^{-4}
LC-HEA_Mo$_{27}$	0.71	0.59 ± 0.03	0.63 ± 0.03	0.56 ± 0.99	4.41 × 10^{-4}

Table 6. Summary table of the surface characterization results obtained for each HEAC deposited with the different coating techniques and results from the hardness and dry sliding wear test.

Experimental ID	Av. Roughness	Vickers Hardness	Coating Thickness	CoF	Wear Depth	Wear Rate
	(R$_a$)	(HV)	(μm)	(–)	(μm)	(mm^3/Nm)
304 SS – Reference steel	0.12 ± 0.04	189 ± 24	-	0.80 ± 0.11	20.4–26.6	2.56 × 10^{-4}
HVOF-HEA_Mo$_{27}$	8.2 ± 0.3	445 ± 51	418.7 ± 43	0.68 ± 0.12	9.50–13.9	1.34 × 10^{-5}
ESD-HEA_Mo$_{27}$	5.4 ± 0.3	. . . [1]	23.5 ± 5	0.79 ± 0.03	22.4–39.4	2.24 × 10^{-4}
LC-HEA_Mo$_{27}$	16.1 ± 0.6	276 ± 19	1200 ± 0.1	0.56 ± 0.20	29.1–59.0	4.41 × 10^{-4}
HVOF-HEA_Mo$_{20}$	8.6 ± 0.4	414 ± 83	313.8 ± 24	0.81 ± 0.09	12.0–21.6	7.17 × 10^{-5}
ESD-HEA_Mo$_{20}$	5.5 ± 0.4	. . . [1]	28.8 ± 6	0.81 ± 0.08	25.8–44.1	3.16 × 10^{-4}
LC-HEA_Mo$_{20}$	17.2 ± 0.4	209 ± 7	1300 ± 0.1	0.83 ± 0.15	39.5–111	6.79 × 10^{-4}

[1] The ESD_Mo$_{27}$ and ESD_Mo$_{20}$ coatings were too thin for indents of HV$_{0.1}$ scale.

The HEACs with the lowest mean CoFs values (between 0.5–0.8) were the HEA_Mo$_{27}$ with LC, HVOF and ESD deposition techniques which were similar or slightly smoother than HEA_Mo$_{20}$ (Figure 9). While the roughness effect was difficult to clarify, the influence was reflected in the surface conformance indicated by fluctuations of the CoF curves. For instance, the LC-HEA_Mo$_{27}$ with the highest fluctuations (SD = 0.2, indicating the least friction stability) had a low and comparable average roughness parameter (Ra = 16.1) to LC-HEA_Mo$_{20}$ (Ra = 17.2) but experienced the largest CoF reduction of about 30% when compared to the 304SS substrate. Moreover, although high Ra influenced maximum contact of the sliding pair, which was critical for developing real contact zones and lowering CoF [47], other mechanical processes were unavoidable in the unlubricated contact (such as plastic deformation depicted in very large deviation in CoF with sliding time to achieve the steady-state conditions). This is illustrated in the pronounced elastic shakedown or the gradual accumulation of plastic strains in the LC-HEA_Mo$_{27}$, HVOF-HEA_Mo$_{27}$ and ESD-HEA_Mo$_{27}$ friction curves (see Figure 9a–c) in the initial stages, which persisted until the steady state or coating wear-through (μ_c).

In the present study, all the HEACs showed a general decrease in the steady-state friction coefficient compared to the 304 SS bulk material (Figure 9d). The mean CoF values (μ_{mean}) are reported in both Tables 5 and 6. The largest CoF reduction of the LC-HEA_Mo$_{27}$, HVOF-HEA_Mo$_{27}$, ESD- HEA_Mo$_{27}$ coatings compared to 304 SS was about 30%, 14% and 5%, respectively, whilst a 1% to 3% rise was observed for the HEA_Mo$_{20}$ coatings. It should be noted that these HEA coatings investigated in this work have heterogeneity in surface morphology, microstructure, phases and oxides (before the sliding test) as discussed in earlier sections. Therefore, the transitions and progressive evolution of friction were mainly attributed not only to the microstructure but alterations in the surface condition with repetitive sliding (i.e., wear debris, adhesive shear, films and local roughening of the subsurface). For instance, the sharp friction rises (0.7–0.9) in the curves of HEA_Mo$_{27}$, then the monotonic decrease in the curves until coating wear-through (μ_c) around the 40th min or changes due to sub-surface stresses (μ_s) (see Figure 9). Under the same loading conditions, the CoF of the lower hardness HEA_Mo$_{20}$ coatings increased rapidly after the running-in and continued to the steady-state. At maximum contact, when the pressures exceed the elastic limit of the HEACs, large tangential forces, strong adhesion, extensive plastic deformation and/or material loss occur. While such transitions are gradual and difficult to assign definite values, the recorded averages are given in Table 5 for the HEA_Mo$_{27}$ coatings which showed the best lubrication and wear-performance. As can be seen in Table 5, the μ_{pk} decreased by 13% for HVOF-HEA_Mo$_{27}$, ESD-HEA_Mo$_{27}$ and 17% for LC-HEA_Mo$_{27}$ coatings before a steady state coating run through (μ_c) was achieved. Likewise, other transition (μ_c to μ_s) showed a further decrease in the CoF values at about 1%, 13% and 7% for HVOF, ESD and LC obtained with slight variance except in the HVOF technique (SD = 0.17).

The wear rate estimated from measurable material loss or wear volume was calculated with Equation (2) as previously described to evaluate the wear resistance of each HEAC for the corresponding deposition technique. Figure 9 has the 3D surface maps of the worn surfaces of the coatings observed by an optical profilometer where profiles were extracted as shown in Figure 10. The results of the wear depth and wear rates are given in Table 6.

Surfaces with higher material removal showed large and broad wear tracks with a deeper depth of wear track at maximum contact between the WC ball and the coatings. It was found that the LC HEACs had the roughest and deepest profile (see Figure 10). Since the coatings were over 1 mm thickness, the average width and maximum depth were about 938 μm and 110 μm (Figure 10b), which was observed in the HEA_Mo$_{20}$ coatings. Among the HEA_Mo$_{20}$ coatings, track width and a complete coating depth wear-through approximately 864 μm and 44 μm, respectively, was observed for the thin ESD-HEA_Mo$_{20}$ coating (initial average thickness of 28.8 μm). The least depth was observed for the HVOF-HEA_Mo$_{20}$ coatings at about 20 μm corresponding to 5% decrease in the original thickness of the coating. Similarly, the wear rate from this removed volume corresponded to 72%

improvement in wear resistance compared to 304 SS. The estimated average track width was rather wider (1.32 mm), which complements the excessive WC ball wear diameter (1.71 mm see Figure 11a). In Figure 11b, the local roughening of the WC ball can be seen that occurred due to repeated wear of the LC-HEA_Mo_{20} with a consistently lower micro-hardness (209 $\pm$ 7 HV) throughout the cross-section.
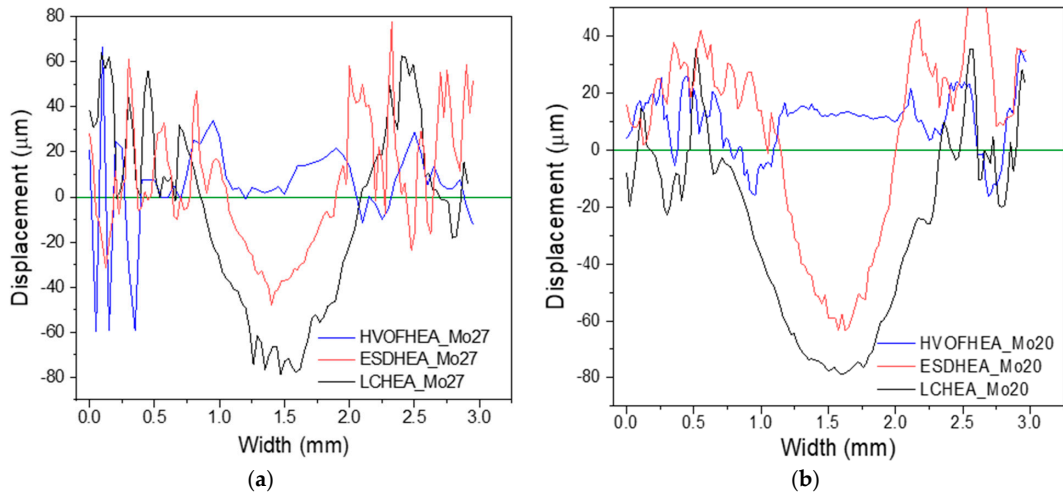
Figure 10. The topography profiles of the HEA coatings with the different deposition techniques after 12,000 wear cycles under dry test condition (**a**) HEA_Mo_{27} and (**b**) HEA_Mo_{20}.

In accordance with the CoF results, the HEA_Mo_{27} coatings exhibited the highest wear resistance, since higher CoF and wear rate values were measured for the HEA_Mo_{20} coating. It was found that both for HEA_Mo_{27} and HEA_Mo_{20}, the wear reduction from using HVOF over LC deposition techniques were 81% and 35%, respectively, and that the ≈420 μm thick HVOF-HEA_{0.85} decreased wear rate by 95% compared to the 304SS.
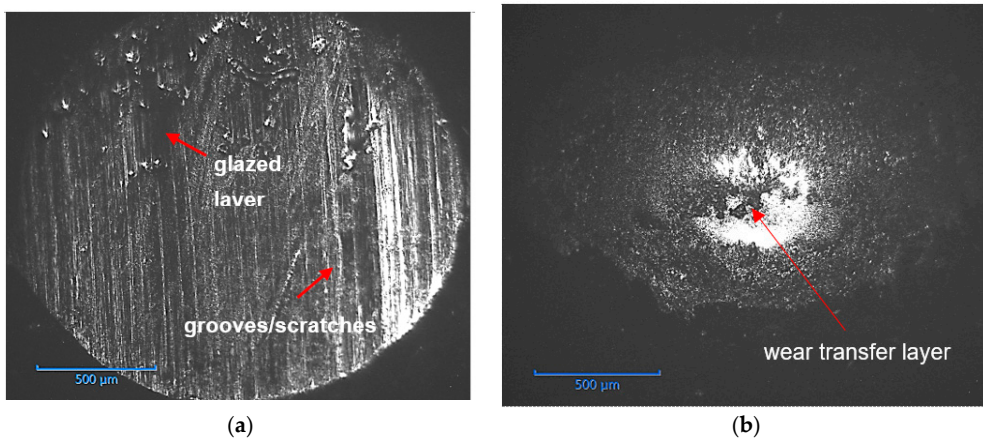
Figure 11. Optical micrographs of worn scars morphology of WC ball sliding against (**a**) HVOF-HEA_Mo_{20} and (**b**) LC-HEA_Mo_{20} coatings after 12,000 wear cycles under dry test condition.

A similar room-temperature dry sliding frictional behaviour was reported for dual-phase and equimolar HEA alloys: CoCrFeNiMnAl_x (x = 0, 0.25, 0.5, 0.75) [19], CoCrFeMnNi and CoCrFeNiAl_x (x = 0.3, 0.6, 1) [48]. The study reported the highest fluctuations and

CoF value for the equimolar CoCrFeNiAl alloy at 0.73. Though the CoF values obtained in the present study differ from values of AlCoCrFeNi, similar high CoF values have also been reported for CoCrFeNiMn [21] and CoCrFeNiMo [26]. Xiao has shown that the plasma sprayed coating's cohesive strength and hardness were adversely affected by the Mn_2O_3. Concurrently, oxides of both Mn_2O_3 and Cr_2O_3 formed a protective layer that enhanced wear resistance [21]. Thus, the debris oxidation-related HEA materials compared to 304 SS under dry wear conditions significantly influence the wear process. Wear rates for the different deposition methods decreased in the following order: LC, ESD and HVOF coatings, from highest to lowest. This was the case for both coating types: The HEA_Mo$_{27}$ and the HEA_Mo$_{20}$. However, wear depth results obtained from cross-section profiles, on the other hand, showed complete coating wear through in ESD coatings. Meanwhile, in the LC HEACs, the largest penetration depth was less than 10% of the nominal coating thickness. Thus, it is worth mentioning that the depth of wear was not visible in cross-section SEM images of both the LC and HVOF sprayed coatings after the dry sliding test. It was observed that the wear rate of the HVOF coatings was of the order of 1×10^{-5} mm^3/Nm, indicating shear resistance from sliding ranges to a magnitude higher than ESD and LC (1×10^{-4} mm^3/Nm). The results show that the wear resistance of the CoCrFeNiMo$_x$ alloys were sensitive to the resulting microstructure (FCC, BCC, σ + μ) after deposition, which can be linked to the hardness and deformation resistance of the alloys [46] discussed in the next section.

3.6. Worn Scar Morphology and Wear Mechanism

The surface SEM micrographs from the wear tracks are shown in Figures 12 and 13, where wear characteristics for the two coating systems and three different deposition techniques can be seen. The red arrows indicate discontinuous regions in the tracks that were either minimally abraded (with oxide debris) or had no wear-forming abrasion pits. The white arrows point out the areas that experienced continuous smearing or scratching from the repetitive sliding of the coatings. The arbitrary track features on the coating surfaces were promoted by the high surface irregularities (Sa) and large thickness in LC HEAC. From the wear trace morphology in Figure 12(a1,a2), obvious oxide film was observed (indicated with white arrows) on the HVOF HEACs in the direction of sliding at room temperature, with HEA_Mo$_{20}$ having the best film continuity. In comparison to the coatings prepared by the LC and ESD techniques, the micrographs revealed severe plastic deformation, glazed (adhesive) layer and oxide debris for the LC and ESD samples, as shown in Figure 12(b1–c2). Moreover, localized damage close to the contact area and a transfer film was observed on the counter body (see WC ball in Figure 11b).

In Figure 13, the localized microscopic surface damages were revealed in higher magnification SEM micrographs. Based on images in Figure 13(a1,a2), it can be inferred that the primary mechanism of the HVOF HEACs was mild abrasive to oxidative wear. While lower Ssk values tend to minimize friction [47], no correlation is observed here. This is because, while the steady state CoF does not change with surface roughness, the plowing and adhesion components of friction do [49]. The results from surface topography showed the HVOF technique were found to produce coatings of the many high peak-to-low valley ratio (Ssk≈unity), significantly influencing a non-conforming contact between the polished WC ball and the as-sprayed coatings reducing real contact areas. Thus, during the wear process, high peaks (asperities) wore off and the valleys filled up with the debris from the plastic deformation of the previous peaks. The truncated peaks then bore the load through oxidation of the exposed plateau and the debris (oxide layer) generated during smearing or scratching. It should be noted that both types of HVOF HEACs have FCC and BCC phases where the differences were from the additional tetragonal -σ, rhombohedral -μ and extrinsic oxide compositions. EDX map of the micrographs of the oxide layer in Figure 13(a1,a2) and the elemental composition are presented in Figure 14. It has been reported by many studies that the oxidized debris has a crucial role as a protective interlayer preventing metal to metal contact [28]. Therefore, the wear resistance of the HVOF HEACs can be attributed to

the microstructures in contact under severe plastic deformation and the tribo-layer formed on the surface during sliding. The chemical composition of Figure 13(a1,a2) was determined using EDX analysis. The results show the oxide layers of both HEACs rich in O and Mo and similar concentrations of Co, Cr, Fe, Ni from the EDX table in Figure 14. It is evident that the wear mechanism at the early stage of sliding is typical abrasion (dominant) and the steady-state sliding is characterized by continuous plastic deformation and oxidation of the produce debris flakes to form a tribo-layer separating the contact pairs.
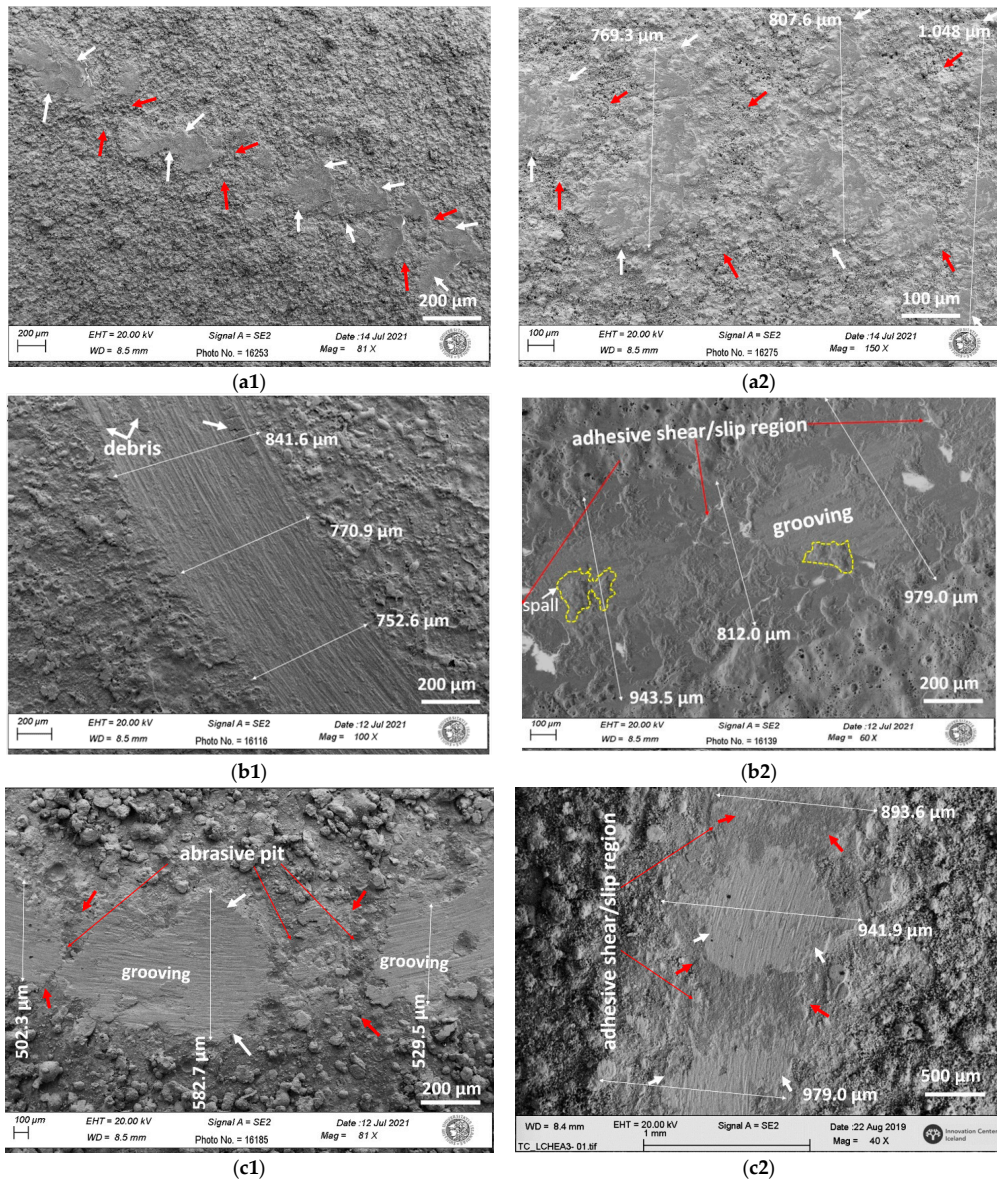
Figure 12. SEM micrographs of morphology of the wear tracks of the (**a1**) HVOF-HEA_Mo$_{27}$, (**b1**) ESD-HEA_Mo$_{27}$, (**c1**) LC-HEA_Mo$_{27}$ and (**a2**) HVOF-HEA_Mo$_{20}$, (**b2**) ESD-HEA_Mo$_{20}$, (**c2**) LC-HEA_Mo$_{20}$—CoCrFeNiMo coatings with the different coating techniques after 12,000 wear cycles under dry test condition.
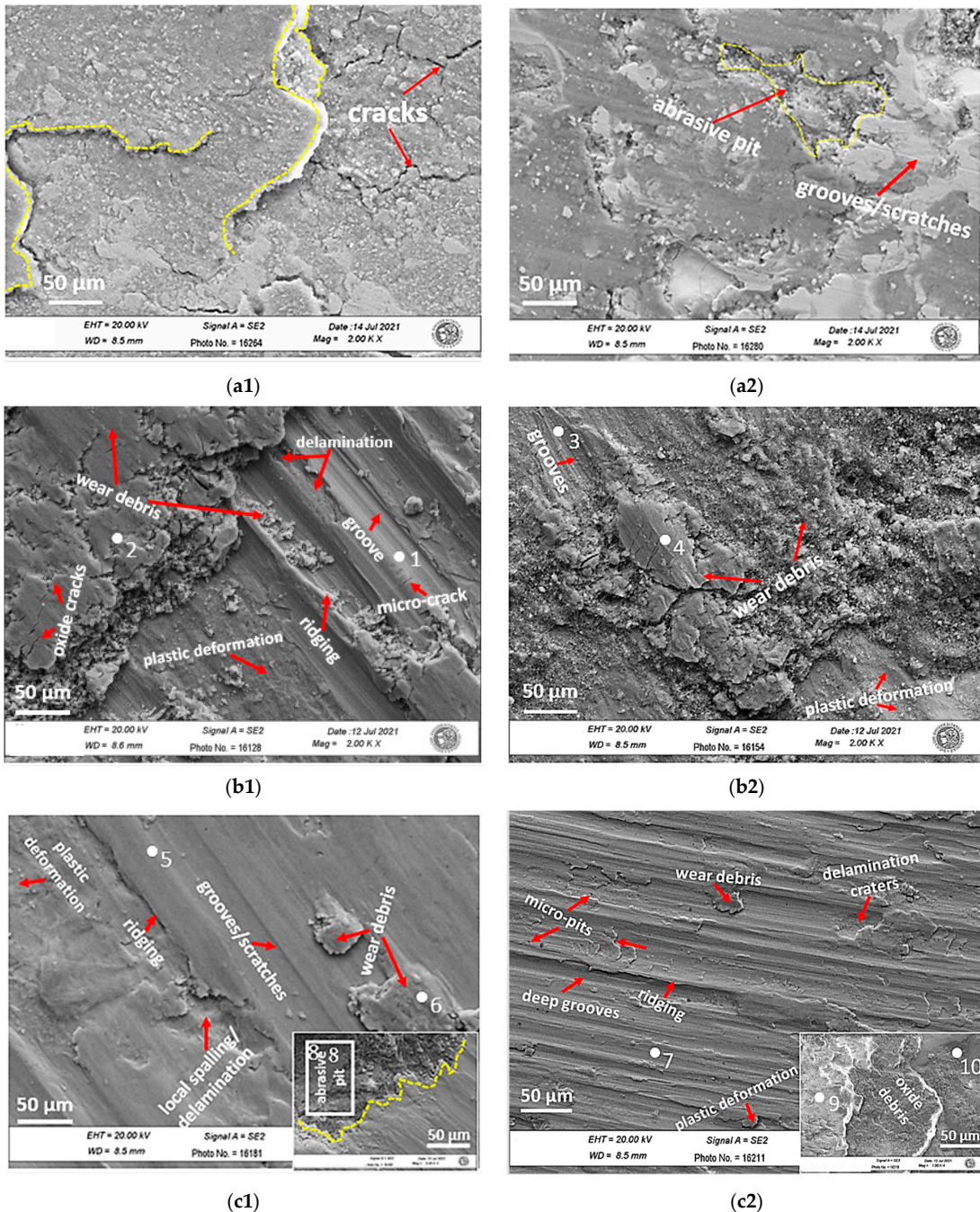
Figure 13. SEM micrographs of morphology of the wear scars and debris of the (**a1**) HVOF-HEA_Mo$_{27}$, (**b1**) ESD-HEA_Mo$_{27}$, (**c1**) LC-HEA_Mo$_{27}$ and (**a2**) HVOF-HEA_Mo$_{20}$, (**b2**) ESD-HEA_Mo$_{20}$, (**c2**) LC-HEA_Mo$_{20}$ coatings with the different deposition techniques after 12,000 wear cycles under dry test condition.

a(1)　　　　　　　　　　　　　　　　　　　a(2)

50 µm　　　　　　　　　　　　　　　　　　50 µm

Element	O	Cr	Fe	Co	Ni	Mo
wt%	22.9	9.3	10.1	10.7	10.4	36.6

Element	O	Cr	Fe	Co	Ni	Mo
wt%	24.2	11.1	12.3	7.0	8.1	37.3
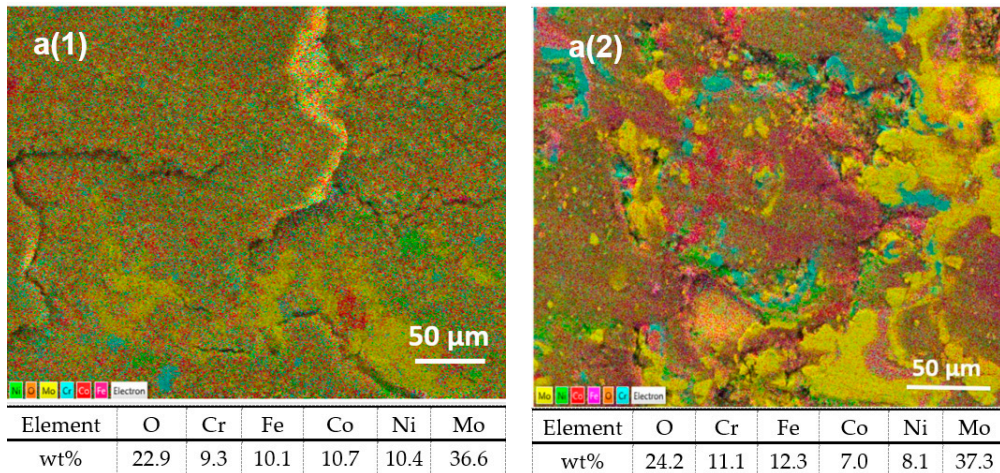
Figure 14. EDX mapping results (**a**) of the layer formed on the (**a1**) HVOF-HEA_Mo$_{27}$ and (**a2**) HVOF-HEA_Mo$_{20}$ as-sprayed coatings after 12,000 wear cycles under dry test condition.

This phenomenon was evident in the friction curve of HVOF-HEA_Mo$_{27}$, where a hump in the friction trace (see Figure 9a) indicates the debris accumulation within the coatings during the coating wear-through (μ_c). In addition, the FCC+BCC matrix which permitted extensive plastic deformation additional identified secondary σ and μ structures reinforced the HEA_Mo$_{27}$ coating [6,13]. Moreover, the work hardening effect on the surface increase the shear strength of the HVOF produced hard HEA_Mo$_{27}$ coatings, reducing yield and tangential forces (≈lower CoF values) while increasing brittleness when the contact pressure exceeded the strain limit. This means that while the harder surface partially covered with oxide layers can reduce wear, the wear phenomenon can also intensify associated with the abrasive action of the debris. While MoOx particles are lamellar flaking in shape, MoO$_3$, which is easily produced from decomposition of the Mo-based coatings during sliding, lacks intrinsic shear properties (unlike amorphous C and MoS$_2$) [20,27] because of its sharp edge crystalline structure. The SEM/EDX image in Figure 14(a1)) shows the lamellar debris generated from wear of the surface which undergoes micro-cracking either parallel or at an angle to the surface to sustain the repetitive sliding stress. As the crack appears in the plastically deformed surface oxide layers, the flaky debris generated, if not refined to build up the lamellar layer, acts as an abrasive, causing (three-body) wear. Because the VEC number suggested a more dominant BCC phase, the cracking on the HEA_Mo$_{27}$ (Figure 14(a1)) coating is reasonable; nonetheless, prior research revealed that the σ and μ strengthening phases that existed in the matrix were hard but also brittle [6]. Thus, if the FCC matrix sustains the rather high deformation by extreme work hardening, micro-cracking is suppressed as seen in the HVOF-HEA_Mo$_{20}$. Furthermore, the grain and inter-splats boundaries (with local compositional variation) in the near-surface layer minimize the propagation of plastic deformation under the abrasive wear to prevent subsurface fracture. Thus, the friction curves fluctuate and the CoF value increases significantly (Figure 9a), which was typically observed in the HEA_Mo$_{20}$.

The energy dissipation in the contact and low wear rates of the HVOF HEACs were compensated by material loss from the WC counter ball by abrasion (see Figure 11a), where a glazed layer reduces the continuous wear of the ball. The oxidized worn surfaces and debris were composed of high contents of Mo and Cr, as well as traces of Ni, Co and Fe observed as constituents of the BCC phase (with load-bearing properties) [24,28] from the XRD results. These phases have been linked to the wear resistance of HEA alloys [50]. Moreover, Zhao found Al$_{0.8}$CrCoFeNi, less frictitious and more wear resistive compared to equiatomic AlCrCoFeNi; however, the surfaces had severe abrasive peeling explained by

the FCC+BCC dual-phased matrix reported [50]. The BCC phases were reported harder compared to the highly plastic FCC phases. Due to the high wear resistance, removing softer FCC phases produces a higher CoF, while removing the same amount of hard BCC and σ phases require more energy, explaining the lower CoF. From the EDX result of the tribo-oxide layer, the oxygen content reached 31.6% for HEA_Mo$_{27}$ and doubled for HEA_Mo$_{20}$ coatings after the dry sliding signifying a large number of atmospheric oxidation processes and mechanical mixing. In conclusion, groove or scratch marks constituted the wear features, a sub-mechanism of abrasion, but wear resistance was dependent on the formation and growth of tribo-oxide layer within the contact and their strain rate response during plastic deformation. Therefore, the HVOF HEAC surface having a dense and adherent oxide film resulted in the lowest wear.

The LC HEACs and ESD HEACs (Figures 12(b1–c2) and 13(b1–c2)) experienced higher wear rates compared to the HVOF HEACs. The surfaces were severely grooved in the direction of sliding along with wear debris either flaky or fragmented. Accordingly, severe run-in occurred for both HEA_Mo$_{27}$ and HEA_Mo$_{20}$ ESD coatings within the shortest time compared to HVOF and LC coatings by rapid truncation of the asperities It can be inferred that the coatings from both techniques experienced abrasive wear. Large strain rates have been associated with material removed from the sides of the grooves (ridges) during microploughing and microcutting [30]. Moreover, microcracking, chipping and delamination (shown in Figure 13(b1–c2)) cause wear volumes greater than the grooving or scratching in the coatings. The SEM images in the LC-HEA_Mo$_{27}$ coating (Figure 13(c1)) showed rather fine striations on the powdery debris remnants from previously worn asperities and pull-outs from local spalls. Thus, ploughing and cutting of micro-asperities during the friction test are primarily responsible for the extent of wear in LC-HEA_Mo$_{27}$. From the surface wear morphology, the debris was generated and most pits that appeared were by abrasive wear rather than spalls. The debris (tribolayer) is mostly oxidized at the maximum contact pressures, but is metallic at intermediate loads. This occurs when the debris is non-adherent or lost within the contact. The transition from oxidative to severe adhesive wear (metallic) causes a rapid increase in wear rate seen in LC-HEA_Mo$_{20}$ and ESD HEACs.

After testing, the EDX analysis results in the grooves (marked at points 1, 3, 5 and 7) on worn areas of both coating compositions given in Table 7 revealed almost no oxide formed and higher wt% Fe (possibly from the steel substrate). The mass fraction of Fe in the region for ESD and LC are 69.1 wt%, 43.5 wt% (HEA_Mo$_{27}$) and 68.3 wt%, 50.3 wt% (HEA_Mo$_{20}$) demonstrating the severe wear conditions for the ESD technique and typically for the HEA_Mo$_{20}$. However, in LC HEAs, the increase in mass fractions in the worn depth compared to nominal composition were 55.4%, 19.6%, 76.4% (HEA_Mo$_{27}$) and 12.7%, 6.2%, 11.5% (HEA_Mo$_{20}$) for Co, Ni, Mo. This shows little-to-no contribution of the substrate to the wear rate. In Figure 13(b1,b2) (ESD HEACs) and Figure 13(c1,c2) (LC HEACs) it can be seen that the oxidized wear debris was constantly consumed and regenerated. If consumed, the particles are fragmented, forming a multilayer or clump shaped as a result of continuous oxidation after peeling (see Figure 13(b1–c1)). From the EDX results, the elemental debris composition (points 2, 4 and 6) shows the high wt% of Fe, O. For instance, confirming the complete coating wear-through, Fe and O increased over 60% in the ESD-HEA_Mo$_{27}$ but a 12.5% reduction in wear rate was observed compared to the 304 SS. In the ESD-HEA_Mo$_{20}$ coating, the oxygen content in the debris increased by 51.9%, where the easiest oxide to form under this system is Fe$_2$O$_3$.

Table 7. Chemical composition of the HEA_Mo$_{20}$ and HEA_Mo$_{27}$ coatings deposited with the different coating techniques from EDX analysis after the dry sliding wear test. The EDX point and area spectra 1–10 are marked in the SEM images in Figure 13.

Location	Elemental Concentration (wt%)					
	O	Cr	Fe	Co	Ni	Mo
point 1	0.4	17.8	69.1	0.4	10.4	1.9
point 2	11.9	15.5	61.1	0.4	9.1	2.0
point 3	0.8	17.7	68.3	0.4	10.9	1.9
point 4	23.5	13.9	52.7	0.4	8.0	1.5
point 5	1.4	14.6	43.5	8.1	14.6	17.8
point 6	13.4	13.9	31.1	8.6	14.9	18.1
point 7	1.7	15.8	50.3	6.3	17.6	8.3
area 8	29.2	60.4	5.9	1.1	1.6	1.8
point 9	28.6	13.0	35.3	4.0	13.5	5.6
point 10	22.0	70.7	4.4	1.2	0.8	0.9

Points 1–7 compare grooves and the wear debris. Points 8–10 compares the slip regions.

Besides the grooves/scratches, oxides could be seen on the mid-junctions and edges (red arrows) of the worn surfaces of the HEACs, as can be seen in Figure 12(b2–c2). Thus, the initial wear process of the ESD coatings was due to abrasion wear within the contact zone followed by oxidative wear. Here, abrasive pits with oxidized debris were observed for abrasive resistant coating (i.e., LC-HEA_Mo$_{27}$ in the bottom image in Figure 13(c1)). Furthermore, the continuous grooving process co-occurred with delamination related to near-surface damage during the repeated sliding cycles. In lower wear-resistant coatings, the lamellar oxides are hoarded to the surface forming adhesive junctions. The hoarded lamellar mixed oxide film in the ESD HEACs reduced friction and wear by acting as slip regions, contrary to the flake debris in LC HEACs. The discontinuous smooth glazed layer suggested that adhesive and oxidative wear occurred confirmed in EDX results of points 9 and 10 in Table 7, while in the other regions, the debris sloughed, aggravating the abrasive wear as in the bottom image in Figure 13(c2). Additional debris formed was propelled by localized spallation and delamination (forming micropits, craters) developed from repeated plastic deformations apparent as fractured ridges or adhesive traces (Figure 13(b1–c2)). Firstly, this is the result of the cutting-type mechanism attributed to the ductile microstructure which causes materials to deformation plastically in the direction of sliding. Secondly, in both ESD and LC techniques, the coating and the substrate were well combined, with no visible grain boundaries in the microstructure of the coating that was metallurgically bonded due to the dilution effect of Fe (from the substrate). Furthermore, the coating possessed a mixed FCC (Fe-Cr-Ni) and Mo-based BCC phase with intermetallic compounds or secondary phases. This effectively allows spalling during the dry-sliding wear process which originates from deformation of the hard particles [6,8,22]. Lastly, the coatings exhibited the lowest hardness and thus lowest strength, which can resist plastic deformation and delamination. However, extensive plastic deformation was compromised by the mid-junction adherent-oxidized debris layers (see Figure 12(b2–c2)).

Besides, studies indicate a proportionality of debris volume to load and sliding distance with further research employed by Archard [33] to characterize sliding wear volume (w) depicted in Equation (3) where hardness (H) of the contacting surface approximated with the workdone by friction forces (i.e., Load (F_n) ∗ sliding distance (L)).

$$v_{sample} = K \cdot F_n * L / H \left[mm^3 / Nm \right] \tag{3}$$

The value of dimensionless K is constant in a stable wear situation, experimentally related to surface quality, chemical affinity, etc. A thorough wear test under constant conditions, on the other hand, indicated that the wear rate is variable where Archard [33] defined K factor as 'mild' wear (10^{-8}) ≥ K ≥ 'severe' wear (10^{-2}).

At higher magnification images in Figure 13(c1,c2), the HEA_Mo$_{27}$ had sufficient wear performance, owing to the long-term lubrication of the phases in the oxides layer that formed and lack of surface adhesion. Figure 11b shows an optical micrograph of LC-HEA_Mo$_{20}$ coating heavily glazed with debris due to material transfer. In the EDX results, of the 50 μm images of Figure 13(c1,c2) given in Table 7, the loose wear debris in abrasive pits (area spectrum 8) are mainly Cr, O content reaching 60.4 wt%, 29.2 wt%, respectively.

Similarly, in the EDX results of the hoarded oxides (i.e., adhesive-oxidized debris layer), the lamellar oxide layer underneath had wt% Cr and wt% O as 70.7 and 22.0 (point 10) compared to the top layer 13.0 and 28.6 (see point 9). The Fe content in the top layer reached 35.3%, with O at 28.6%. Thus, the contact pressures were supported by both oxide films. Therefore, under these composition systems and the selected test conditions, the main atmospheric oxides that could form are MoO, MoCrO (see SEM/EDX of HVOF HEACs), NiO, Cr$_2$O$_3$ and Fe$_2$O$_3$. From EDX maps, all the oxides appeared denser except Fe$_2$O$_3$, which was obviously loose and peeled easily in the contact and functioned as third body abrasive.

Meanwhile, to confirm the wear behavior from the cross-section results from the optical profilometer, SEM/EDX analysis was performed on the grooved regions in Figure 13. The EDX results of two HEACs deposited by ESD and LC technique is presented in Table 8 to support the high magnification images generated in Figure 13(b1–c2). It was found that the surfaces (grooved/excessively abraded regions) are predominantly composed of Fe, Cr and Ni with little-to-no O (reaching the maximum value of 6.07 wt% in ESD-HEA_Mo$_{20}$). This confirms complete coating wear-through for the ESD HEACs. In the LC and HVOF technique, the worn regions from the abrasion zone were observed with higher weight concentrations of Co, Ni and Mo. The increase in mass fractions on the surfaces with these elements from the EDX data, like HVOF HEACs, confirm that such highest constituent phase in enhancing wear performance are primarily found in the oxidized intermetallic phases reported with good mechanical properties and wear resistance by XRD [6].

Table 8. Chemical composition of the HEA_Mo$_{20}$ deposited with ESD and LC techniques from EDX analysis after the dry sliding wear test. The EDX map spectrum from worn regions with parallel grooves in the SEM images in Figure 13.

Experimental ID	Elemental Concentration (wt%)					
	O	Cr	Fe	Co	Ni	Mo
ESD-HEA_Mo$_{27}$	3.65	17.12	66.29	0.54	10.3	2.11
LC-HEA_Mo$_{27}$	3.49	15.08	42.63	7.46	14.23	17.11
ESD-HEA_Mo$_{20}$	6.07	16.73	64.4	0.99	9.83	1.96
LC-HEA_Mo$_{20}$	1.7	15.81	50.3	6.31	17.63	8.25

Figure 15 shows the schematic of the proposed wear mechanisms based on the surface characterization of the HEA coating compositions by the different deposition techniques. The identified wear behavior was an abrasion-mixed mechanism with plastic deformation to an extent for all the tested coatings. However, depending on the coatings' inherent surface, mechanical and microstructural properties, the wear mechanism transitioned into oxidative (i.e., in the HVOF HEACs) and adhesive wear (i.e., in the ESD HEACs and LC HEACs), affecting the debris generation and surface damage. In summary, owing to the good mechanical properties and compatibility with the substrates, the microstructure and phases formed by the HVOF and LC techniques provided sufficient hardness, which increased the resistance to excessive plastic deformation under the dry sliding test. Based on the results of the experiments conducted in this study, it seems evident that adjusting the spray parameters is needed to achieve a thicker and dense coating for the ESD technique to improve the microstructure and minimize defects. An excellent mechanical and wear performance was observed for the HVOF sprayed coatings as a dense tribo-oxidation

layer was formed from the generated debris from the dominant abrasive wear mechanism preventing near-and sub-surface damages, schematically shown in Figure 15b. On the other hand, the oxidation of the wear debris associated with the two HEA coatings changes in morphology and composition in the overall sliding period causing transitions in the friction and wear modes. The HEA_Mo$_{27}$'s tribological properties are excellent evident by the hardness and wear resistance. This affords the possibility to employ HEA_Mo$_{27}$ on components that are subject to wear and erosion-corrosion in challenging environment as in geothermal power plants and well components such as valves, turbine rotors and shaft.
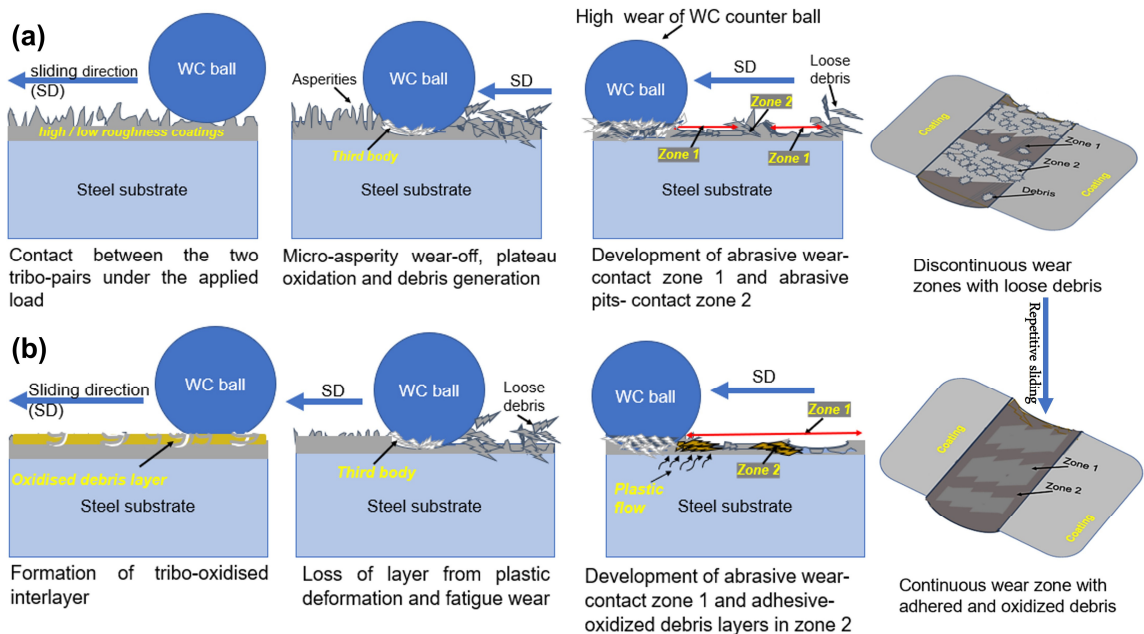
Figure 15. A schematic of the wear evolution proposed for the produced HEACs: (**a**) abrasive wear mode with plastic deformation and debris generation at the onset of sliding and (**b**) third body influence with subsequent decrease in the wear. Wear transition from mode (**a**) to (**b**) due to oxidation and repetitive sliding.

4. Conclusions

In summary, the study investigated the microstructural, mechanical and tribological properties of Co$_{19}$Cr$_{17}$Fe$_{19}$Ni$_{18}$Mo$_{27}$ and Co$_{20}$Cr$_{20}$Fe$_{20}$Ni$_{20}$Mo$_{20}$ deposited by HVOF, ESD and LC techniques. As expected, the coatings' topography, microstructure, hardness, friction and wear properties were depended on the coating composition and deposition technique. The main following conclusions from the study are:

- The results indicate that the HVOF and LC were more efficient deposition techniques than ESD in the powder melting of all elements, producing a relatively even surface and cross-section microstructure for both HEA compositions (Co$_{19}$Cr$_{17}$Fe$_{19}$Ni$_{18}$Mo$_{27}$ and Co$_{20}$Cr$_{20}$Fe$_{20}$Ni$_{20}$Mo$_{20}$). The surface morphology correlated with the topographic features. Accordingly, the surface roughness was very large in all cases, representing a potential concern during running-in for practical applications.
- The results showed that Co$_{19}$Cr$_{17}$Fe$_{19}$Ni$_{18}$Mo$_{27}$ had better mechanical and tribological performance than Co$_{20}$Cr$_{20}$Fe$_{20}$Ni$_{20}$Mo$_{20}$. The Co$_{19}$Cr$_{17}$Fe$_{19}$Ni$_{18}$Mo$_{27}$ had lower roughness, coefficient of friction and wear rates compared to the equiatomic Co$_{20}$Cr$_{20}$Fe$_{20}$Ni$_{20}$Mo$_{20}$ HEA coating.

- Three major phases: A mixture of FCC and BCC and a residual BCC phase linked to the Mo element were detected in both HEAC compositions, and additionally two intermetallics (σ phase and Mo-rich phase concluded as μ phase). In $Co_{19}Cr_{17}Fe_{19}Ni_{18}Mo_{27}$, a mixture of σ and μ phase precipitation occurred, while the μ phase was only observed in $Co_{20}Cr_{20}Fe_{20}Ni_{20}Mo_{20}$.
- The variation in microstructure and hardness of each coating was explained by the difference in Mo content in the coatings, which contributed to improved resistance to deformation through the formation of BCC, σ and presumably the μ phases.
- The coatings wore out by a mixed-abrasive and oxidative wear mechanism for the HVOF HEACs. For ESD HEACs and LC HEACs, delamination occurred in areas where abrasive wear was severe and transitioned into adhesive wear, but the adhesive oxidative layers compromised excessive surface damage.
- Despite $Co_{19}Cr_{17}Fe_{19}Ni_{18}Mo_{27}$ coating producing better results than $Co_{20}Cr_{20}Fe_{20}Ni_{20}Mo_{20}$ from this study, more research on the coating properties would be beneficial before usage in a geothermal environment, such as corrosion resistance, due to the complex microstructure produced from mechanical alloying and the powder deposition, which plays a crucial role in the performance of the alloys.

References

1. Hoornaert, T.; Hua, Z.K.; Zhang, J.H. Hard Wear-Resistant Coatings: A Review. In *Advanced Tribology*; Springer: Berlin/Heidelberg, Germany, 2009; pp. 774–779. [CrossRef]
2. Yeh, J.-W.; Chen, S.K.; Lin, S.-J.; Gan, J.-Y.; Chin, T.-S.; Shun, T.-T.; Tsau, C.-H.; Chang, S.-Y. Nanostructured High-Entropy Alloys with Multiple Principal Elements: Novel Alloy Design Concepts and Outcomes. *Adv. Eng. Mater.* **2004**, *6*, 299–303. [CrossRef]
3. Ye, Y.; Wang, Q.; Lu, J.; Liu, C.; Yang, Y. High-entropy alloy: Challenges and prospects. *Mater. Today* **2016**, *19*, 349–362. [CrossRef]
4. Miracle, D.B.; Miller, J.D.; Senkov, O.N.; Woodward, C.; Uchic, M.D.; Tiley, J. Exploration and Development of High Entropy Alloys for Structural Applications. *Entropy* **2014**, *16*, 494–525. [CrossRef]
5. Senkov, O.N.; Miracle, D.B.; Chaput, K.J.; Couzinie, J.-P. Development and exploration of refractory high entropy alloys—A review. *J. Mater. Res.* **2018**, *33*, 3092–3128. [CrossRef]
6. Liu, W.; Lu, Z.; He, J.; Luan, J.; Wang, Z.; Liu, B.; Liu, Y.; Chen, M.; Liu, C. Ductile CoCrFeNiMox high entropy alloys strengthened by hard intermetallic phases. *Acta Mater.* **2016**, *116*, 332–342. [CrossRef]
7. Senkov, O.; Senkova, S.; Woodward, C.; Miracle, D. Low-density, refractory multi-principal element alloys of the Cr–Nb–Ti–V–Zr system: Microstructure and phase analysis. *Acta Mater.* **2013**, *61*, 1545–1557. [CrossRef]
8. Shu, F.; Yang, B.; Dong, S.; Zhao, H.; Xu, B.; Xu, F.; Liu, B.; He, P.; Feng, J. Effects of Fe-to-Co ratio on microstructure and mechanical properties of laser cladded FeCoCrBNiSi high-entropy alloy coatings. *Appl. Surf. Sci.* **2018**, *450*, 538–544. [CrossRef]
9. Niu, Z.; Wang, Y.; Geng, C.; Xu, J.; Wang, Y. Microstructural evolution, mechanical and corrosion behaviors of as-annealed CoCrFeNiMox (x = 0, 0.2, 0.5, 0.8, 1) high entropy alloys. *J. Alloys Compd.* **2020**, *820*, 153273. [CrossRef]
10. Lehtonen, J.; Koivuluoto, H.; Ge, Y.; Juselius, A.; Hannula, S.-P. Cold Gas Spraying of a High-Entropy CrFeNiMn Equiatomic Alloy. *Coatings* **2020**, *10*, 53. [CrossRef]

11. Cantor, B.; Chang, I.T.H.; Knight, P.; Vincent, A.J.B. Microstructural development in equiatomic multicomponent alloys. *Mater. Sci. Eng. A* **2004**, *375–377*, 213–218. [CrossRef]

12. Miao, J.; Guo, T.; Ren, J.; Zhang, A.; Su, B.; Meng, J. Optimization of mechanical and tribological properties of FCC CrCoNi multi-principal element alloy with Mo addition. *Vacuum* **2018**, *149*, 324–330. [CrossRef]

13. Tsai, M.-H.; Tsai, R.-C.; Chang, T.; Huang, W.-F. Intermetallic Phases in High-Entropy Alloys: Statistical Analysis of their Prevalence and Structural Inheritance. *Metals* **2019**, *9*, 247. [CrossRef]

14. Shun, T.-T.; Chang, L.-Y.; Shiu, M.-H. Microstructure and mechanical properties of multiprincipal component CoCrFeNiMo$_x$ alloys. *Mater. Charact.* **2012**, *70*, 63–67. [CrossRef]

15. Ni, C.; Shi, Y.; Liu, J.; Huang, G. Characterization of Al$_{0.5}$FeCu$_{0.7}$NiCoCr high-entropy alloy coating on aluminum alloy by laser cladding. *Opt. Laser Technol.* **2018**, *105*, 257–263. [CrossRef]

16. Zhang, G.; Liu, H.; Tian, X.; Chen, P.; Yang, H.; Hao, J. Microstructure and Properties of AlCoCrFeNiSi High-Entropy Alloy Coating on AISI 304 Stainless Steel by Laser Cladding. *J. Mater. Eng. Perform.* **2020**, *29*, 278–288. [CrossRef]

17. Sharma, A. High Entropy Alloy Coatings and Technology. *Coatings* **2021**, *11*, 372. [CrossRef]

18. Karlsdóttir, S. Corrosion, Scaling and Material Selection in Geothermal Power Production. In *Comprehensive Renewable Energy*; Elsevier: Amsterdam, The Netherlands, 2012; pp. 241–259. [CrossRef]

19. Tsai, M.-H.; Fan, A.-C.; Wang, H.-A. Effect of atomic size difference on the type of major intermetallic phase in arc-melted CoCrFeNiX high-entropy alloys. *J. Alloy. Compd.* **2017**, *695*, 1479–1487. [CrossRef]

20. Zhang, A.; Han, J.; Su, B.; Li, P.; Meng, J. Microstructure, mechanical properties and tribological performance of CoCrFeNi high entropy alloy matrix self-lubricating composite. *Mater. Des.* **2017**, *114*, 253–263. [CrossRef]

21. Xiao, J.-K.; Tan, H.; Wu, Y.-Q.; Chen, J.; Zhang, C. Microstructure and wear behavior of FeCoNiCrMn high entropy alloy coating deposited by plasma spraying. *Surf. Coat. Technol.* **2020**, *385*, 125430. [CrossRef]

22. Cui, Y.; Shen, J.; Manladan, S.M.; Geng, K.; Hu, S. Wear resistance of FeCoCrNiMnAl$_x$ high-entropy alloy coatings at high temperature. *Appl. Surf. Sci.* **2020**, *512*, 145736. [CrossRef]

23. Lin, C.-M.; Tsai, H.-L. Evolution of microstructure, hardness, and corrosion properties of high-entropy Al$_{0.5}$CoCrFeNi alloy. *Intermetallics* **2011**, *19*, 288–294. [CrossRef]

24. Wang, W.-R.; Wang, W.-L.; Wang, S.-C.; Tsai, Y.-C.; Lai, C.-H.; Yeh, J.-W. Effects of Al addition on the microstructure and mechanical property of AlxCoCrFeNi high-entropy alloys. *Intermetallics* **2012**, *26*, 44–51. [CrossRef]

25. Zhang, K.; Fu, Z.; Zhang, J.; Wang, W.; Wang, H.; Wang, Y.; Zhang, Q.; Shi, J. Microstructure and mechanical properties of CoCrFeNiTiAlx high-entropy alloys. *Mater. Sci. Eng. A* **2009**, *508*, 214–219. [CrossRef]

26. Wu, J.-M.; Lin, S.-J.; Yeh, J.-W.; Chen, S.-K.; Huang, Y.-S.; Chen, H.-C. Adhesive wear behavior of Al$_x$CoCrCuFeNi high-entropy alloys as a function of aluminum content. *Wear* **2006**, *261*, 513–519. [CrossRef]

27. Cui, G.; Han, B.; Yang, Y.; Wang, Y.; Chunyang, H. Microstructure and tribological property of CoCrFeMoNi High entropy alloy treated by ion sulfurization. *J. Mater. Res. Technol.* **2020**, *9*, 2598–2609. [CrossRef]

28. Deng, G.; Tieu, A.K.; Lan, X.; Su, L.; Wang, L.; Zhu, Q.; Zhu, H. Effects of normal load and velocity on the dry sliding tribological behaviour of CoCrFeNiMo$_{0.2}$ high entropy alloy. *Tribol. Int.* **2019**, *144*, 106116. [CrossRef]

29. Mu, Y.; Jia, Y.; Xu, L.; Tan, X.; Yi, J.; Wang, G.; Liaw, P. Nano oxides reinforced high-entropy alloy coatings synthesized by atmospheric plasma spraying. *Mater. Res. Lett.* **2019**, *7*, 312–319. [CrossRef]

30. Fanicchia, F.; Csaki, I.; Geambazu, L.E.; Begg, H.; Paul, S. Effect of Microstructural Modifications on the Corrosion Resistance of CoCrFeMo$_{0.85}$Ni Compositionally Complex Alloy Coatings. *Coatings* **2019**, *9*, 695. [CrossRef]

31. Boakye, G.O.; Kovalov, D.; Thórhallsson, A.Í.; Karlsdóttir, S.N.; Motoiu, V. Friction and Wear Behaviour of Surface Coatings for Geothermal Applications. In Proceedings of the World Geothermal Congress 2020 + 1, Reykjavik, Iceland, 24–27 October 2021; pp. 1–9.

32. *ASTM, G99*; Standard Test Method for Wear Testing with a Pin-on-Disk Apparatus. ASTM Int.: West Conshohocken, PA, USA, 2016; Volume G99, 1–5. [CrossRef]

33. Archard, J.F. Contact and Rubbing of Flat Surfaces. *J. Appl. Phys.* **1953**, *24*, 981–988. [CrossRef]

34. Mannem, U.D.; Anand, K.; Gray, D.M.; Ghasripoor, F. Protective Coatings Which Provide Wear Resistance and Low Friction Characteristics, and Related Articles and Methods, 11/610,826. 2008. Available online: https://patents.google.com/patent/US20080145649A1/en (accessed on 16 July 2019).

35. Perez, R.X.; Lawhon, D.W. Installation, Commissioning and First Solo Run. In *Operator's Guide to General Purpose Steam Turbines: An Overview of Operating Principles, Construction, Best Practices, and Troubleshooting*, 1st ed.; John Wiley & Sons, Inc.: Salem, MA, USA, 2016; pp. 147–186.

36. Perez, R.X.; Lawhon, D.W. Operator's Guide to General Purpose Steam Turbines. In *Operator's Guide to General Purpose Steam Turbines: An Overview of Operating Principles, Construction, Best Practices, and Troubleshooting*; Wiley: Salem, MA, USA, 2016. [CrossRef]

37. Hsu, U.; Hung, U.; Yeh, J.; Chen, S.; Huang, Y.; Yang, C. Alloying behavior of iron, gold and silver in AlCoCrCuNi-based equimolar high-entropy alloys. *Mater. Sci. Eng. A* **2007**, *460–461*, 403–408. [CrossRef]

38. Xie, Y.-J.; Wang, M.-C. Microstructural morphology of electrospark deposition layer of a high gamma prime superalloy. *Surf. Coat. Technol.* **2006**, *201*, 691–698. [CrossRef]

39. Karlsdottir, S.N.; Geambazu, L.E.; Csaki, I.; Thorhallsson, A.I.; Stefanoiu, R.; Magnus, F.; Cotrut, C. Phase Evolution and Microstructure Analysis of CoCrFeNiMo High-Entropy Alloy for Electro-Spark-Deposited Coatings for Geothermal Environment. *Coatings* **2019**, *9*, 406. [CrossRef]

40. Dong, Z.; Sergeev, D.; Dodge, M.F.; Fanicchia, F.; Müller, M.; Paul, S. Microstructure and Thermal Analysis of Metastable Intermetallic Phases in High-Entropy Alloy CoCrFeMo$_{0.85}$Ni. *Materials* **2021**, *14*, 1073. [CrossRef] [PubMed]

41. Niemann, R.; Backen, A.; Kauffmann-Weiss, S.; Behler, C.; Rößler, U.; Seiner, H.; Heczko, O.; Nielsch, K.; Schultz, L.; Fähler, S. Nucleation and growth of hierarchical martensite in epitaxial shape memory films. *Acta Mater.* **2017**, *132*, 327–334. [CrossRef]

42. Yang, J.; Li, X.; Li, F.; Wang, W.; Li, Z.; Li, G.; Xie, H. Effect of Cooling Method on Formability of Laser Cladding IN718 Alloy. *Materials* **2021**, *14*, 3734. [CrossRef]

43. Chen, R.; Qin, G.; Zheng, H.; Wang, L.; Su, Y.; Chiu, Y.L.; Ding, H.; Guo, J.; Fu, H. Composition design of high entropy alloys using the valence electron concentration to balance strength and ductility. *Acta Mater.* **2018**, *144*, 129–137. [CrossRef]

44. Su, S.-Y.; Fan, Y.-T.; Su, Y.-J.; Huang, C.-W.; Tsai, M.-H.; Lu, M.-Y. Lattice distortion and atomic ordering of the sigma precipitates in CoCrFeNiMo high-entropy alloy. *J. Alloys Compd.* **2021**, *851*, 156909. [CrossRef]

45. Shun, T.-T.; Chang, L.-Y.; Shiu, M.-H. Age-hardening of the CoCrFeNiMo0.85 high-entropy alloy. *Mater. Charact.* **2013**, *81*, 92–96. [CrossRef]

46. Wu, Q.; Wang, Z.; He, F.; Li, J.; Wang, J. Revealing the Selection of σ and μ Phases in CoCrFeNiMo$_x$ High Entropy Alloys by CALPHAD. *J. Phase Equilibria Diffus.* **2018**, *39*, 446–453. [CrossRef]

47. Joseph, J.; Haghdadi, N.; Shamlaye, K.; Hodgson, P.; Barnett, M.; Fabijanic, D. The sliding wear behaviour of CoCrFeMnNi and AlxCoCrFeNi high entropy alloys at elevated temperatures. *Wear* **2019**, *428–429*, 32–44. [CrossRef]

48. Sedlaček, M.; Podgornik, B.; Vižintin, J. Correlation between standard roughness parameters skewness and kurtosis and tribological behaviour of contact surfaces. *Tribol. Int.* **2012**, *48*, 102–112. [CrossRef]

49. Menezes, P.L.; Kishore; Kailas, S.V. Influence of surface texture on coefficient of friction and transfer layer formation during sliding of pure magnesium pin on 080 M40 (EN8) steel plate. *Wear* **2006**, *261*, 578–591. [CrossRef]

50. Zhao, D.; Yamaguchi, T.; Wang, W. Fabrication and wear performance of Al$_{0.8}$FeCrCoNi high entropy alloy coating on magnesium alloy by resistance seam welding. *Mater. Lett.* **2020**, *265*, 127250. [CrossRef]

Journal Paper 3

Corrosion Behaviour of HVOF developed Mo-based High Entropy Alloy coating and selected Hard coatings for High Temperature Geothermal Applications

Gifty Oppong Boakye[1], Erlend Oddvin Straume[1], Baldur Geir Gunnarsson[1,2], Danyil Kovalov[1], Sigrun Nanna Karlsdottir[1*]

[1]University of Iceland, Faculty of Industrial Eng., Mechanical Eng., and Computer Science, Hjardarhagi 2-6, Reykjavík, Iceland

[2]Tæknisetur ehf, Árleynir 2-8, 112 Reykjavík, Iceland

gob13@hi.is, erlend@hi.is, baldur@taeknisetur.is, dankov@hi.is, snk@hi.is

Abstract

The corrosion behaviour of High Entropy Alloy (HEA) and wear-resistant cermets, self-fluxing Ni alloy, Fe-based amorphous alloy coatings were investigated in simulated high temperature geothermal environments with/without H_2S and CO_2 gases for geothermal applications. Phase density of the corrosive fluid (liquid/vapor) influenced the corrosion behaviour in the test environments. The NiCrSiBFe self-fluxing coating formed a continuous corrosion surface film while the FeCrMoWMnBCSi amorphous coating was prone to localized corrosion in the liquid phase. The cermet coatings had pores and cracks that led to localized penetration. The $CoCrFeNiMo_{0.85}$ HEA showed the highest corrosion resistance in all test environments.

Keywords: CO_2/H_2S; High temperature; HEA; Wear resistant coatings; Geo-Drill

1. Introduction

In the utilization of geothermal energy, corrosion, erosion, and wear challenges are met due to the corrosive and often abrasive nature of geothermal fluids often with suspended solids. The extent of corrosion in geothermal operational systems can be categorized based on material-dependent and solution-dependent factors. Alloy composition, surface condition and heat treatments are all factors that can influence the susceptibility of materials to corrosion [1]. The solution-dependent factors include physical properties (pressure, temperature, pH) and chemical properties (electrochemical potential, corrosive ions, and gases such as CO_2 and H_2S) in the hot fluid systems [1,2].

Most geothermal fields are utilized to be flashed systems under pre-exploitation conditions of two-phase flow from medium (100 °C – 180 °C), high enthalpy (>180 °C) [3,4] or superheated (>350 °C) [5] systems with drilled wells down to 5 km depth [3–5]. When a fluid boils at such depth, CO_2 and H_2S gases escape into the vapor/steam phase and travel toward the surface. Moreover, CO_2 and H_2S could both dissolve in the fluid, thus, producing several cathodic reactions by hydration and dissociation (Equations 1 to 4) forming sulfides, bicarbonate, carbonate, and hydrogen (H^+) ions the in aqueous media.

$$H_2S_{(g)} + H_2O_{(l)} \quad \leftrightarrow \quad H_2S_{(aq)} \tag{1}$$

$$H_2S_{(aq)} \quad \leftrightarrow \quad H^+ + HS^-_{(aq)} \quad \leftrightarrow \quad H_{2(g)} + S_{(s)} \tag{2}$$

$$CO_{2(g)} + H_2O_{(l)} \quad \leftrightarrow \quad H_2CO_{3(aq)} \tag{3}$$

$$H_2CO_{3(aq)} \quad \leftrightarrow \quad H^+ + HCO_3^-{}_{(aq)} \leftrightarrow \quad H^+ + CO_3^{2-}{}_{(aq)} \tag{4}$$
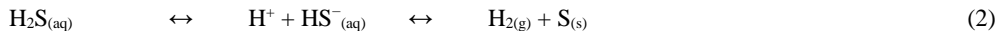
Iron sulfides are known to form when commonly used ferrous steels react ($Fe_{(s)} \rightarrow Fe^{2+}{}_{(aq)}$) in H_2S-containing environments (Equation 5) [2]. However, it is important to note that the corrosion process

consists of a series of anodic and cathodic reactions. Subsequent oxidation of Fe^{2+} to Fe^{3+} (Equations 6 and 7) can occur with cathodic reactions involving the generation and consumption of the various intermediate products. Nonetheless, alloy materials used in such systems can form a protective surface film that can slow down corrosion rates (CRs) when exposed to the high temperature geothermal fluid (liquid/steam) [2].

$$Fe + H_2S \rightarrow FeS + H_2 \tag{5}$$

$$2\ Fe \rightarrow 2\ Fe^{2+} \rightarrow 2\ Fe^{3+} \rightarrow Fe_2O_3 + 3\ H_2O \tag{6}$$

$$Fe_2O_3 + 2H_2S + CO_2 \rightarrow FeS_2 + FeCO_3 + 2H_2O \tag{7}$$

These corrosion effects, along with drilling-related cyclic loads and abrasive formation significantly impact the performance and reliability of the materials used during geothermal exploitation. Carbon and low alloy steels (Cr-Mo) [6,7] are commonly used for geothermal drilling equipment. These steels are not corrosion resistant and can fail due to fatigue and corrosion fatigue during exposure to the geothermal environment, whereas high-strength corrosion resistant alloys (CRAs) have demonstrated the risk of SSCC (sulphide stress corrosion cracking) and HIC (hydrogen induced cracking) [7,8]. This raises the question of whether hard-wear resistant coatings could be used for this environment.

Previous studies of various alloys in hot geothermal brine showed acceptable uniform CRs but detrimental localized attacks [9–11]. The authors showed that at higher temperatures, Ni-based alloys are preferable to duplex and austenitic steels [9] but were not considered suitable when tested in artificial geothermal fluids above 200°C [10]. Robust coatings are widely utilized in the other energy industries to protect metallic components from these impacts. Turbine blades, rotors, shafts, drill stabilizers, fasteners, and valves have long been protected against high stresses, wear, and corrosion by high-strength corrosion-resistant composite coatings (such as cermets) [12]. However, currently available products and methods may not be suitable for the high temperature and pressures encountered in the geothermal environment. Moreover, coating engineering has primarily focused on solutions for corrosion of surface equipment, with little attention paid to downhole corrosion. Because down-hole conditions in geothermal wells are more extreme in terms of temperature and pressure, thus, selecting appropriate materials for equipment used over the short-term drilling or long-term casing of a well is technologically and economically demanding. Furthermore, the balance of the power plant is dependent on the successful steam separation of the high-density fluid [3] from down-the-hole to the production systems. Steam transmission lines convey the vapor phase (>200 °C-flashed steam) to operate the generator turbine for electric power. As a result, a comprehensive analysis of corrosion behaviour of existing and/or new coatings on a low-cost substrate in both liquid and steam phases is important in the evaluation of wear and corrosion resistant coatings for geothermal drilling and well components. Furthermore, a successful outcome from the selected coating materials may offer prospective use to surface equipment exposed to corrosive geothermal steam hosting non condensable gases (NCGs).

Thermal spray procedures typically high-velocity oxygen fuel (HVOF) is often a preferred option to produce high-quality coatings on plant equipment [13–15]. Tungsten and chromium carbides (WC/CrC) ceramic materials well known for their high hardness have been employed with metal matrices including cobalt (Co), nickel (Ni), and chromium (Cr) for high wear components. The WC-CoCr and CrC-NiCr coatings are customary to application temperatures up to 500 °C and 800 °C, respectively [14]. Co is reported to contribute to hardness properties, and in terms of corrosion, the Ni and/or Cr-rich matrix allows for passivation, which reduces the reported corrosion of the matrix and carbide particles in harsh conditions [16]. In an exposure test in steam from a deep production well at 150 °C and 0.5MPa, a CR of 0.007 mm/yr was measured for a Cr_3C_2-NiCr coating [12]. The author reported that corrosion on the base metal was seen due to coating cracking [12], suggesting alternate or combined degradation mechanisms.

Meanwhile, passive alloys have been shown to improve the stability of surface oxidized protective layers, with Ni usually recommended for high-temperature service. The compromise between wear and corrosion has been the subject of several studies, with most of the work focusing on the hard-passive alloy (Cr, Mo, and Ni) coatings [17]. Studies on coatings of passive alloys at various higher temperature environments ranging from 200 °C to 730 °C showed high-temperature corrosion resistance compared to carbon steels and CRAs [18–21]. Corrosion test of Ni-based (NiCrBSiFe) coating showed good corrosion resistance at 725 °C in a boiler environment [19] but a similar coating was reported to have cracked and delaminated when exposed to geothermal steam at 210 °C [21]. Another research demonstrated that the addition of minor amounts of Co, silicon (Si), aluminium (Al), and iron (Fe) to passive elements forming composites coatings improved the high-temperature corrosion performance [20]. The investigated microstructure and properties of a FeSi-WC composite mixed with NiCr showed the coatings retain their Fe-based amorphous features after spraying and demonstrated good abrasion and corrosion resistance [20].

Another promising candidate coating material group that has drawn attention over conventional alloys recently is high entropy alloys (HEAs). Recent studies have reported that HEA alloys with Co, Ni, Mo, and Cr composition have shown promising results for the development of corrosion and wear resistant coatings for the geothermal environment [22–26]. Low CR was reported for an equiatomic CoCrFeNiMo alloy tested in-situ in two-phase geothermal steam containing corrosive H_2S and CO_2 gases at 200 °C [25]. Similarly, microscopic analysis of an equiatomic CoCrNiFeMo alloy showed no corrosion damage after testing in a simulated superheated geothermal steam environment containing HCl at 350 °C [23]. In another research, electrochemical testing revealed that a CoCrFeNiMo alloy had a CR of less than 0.1 mm/yr at room temperature in a brine environment [22]. The results also showed the CoCrFeNiMo bulk material had high hardness (593 HV) [22] and higher wear resistance compared to $CoCrFeNiMo_{0.85}$ when produced as coatings [27]. However, Fanicchia et al. reported localized corrosion damage of $CoCrFeNiMo_{0.85}$ coating, when tested electrochemically at 25 °C in 3.5 wt.% NaCl solution [26]. Based on these studies, it can be concluded that the corrosion behaviour of HEA coating materials in different high temperature geothermal environments is still not fully understood necessitating further research.

The goal of this study is to evaluate the corrosion behaviour of HVOF-developed coatings; WC-CoCr, CrC-NiCr, WC-CrCNi, NiCrFeBSi, FeCrMoWMnBCSi and $CoCrFeNiMo_{0.85}$ tested in simulated geothermal drilling environment. A high temperature and high pressure (HTHP) autoclave laboratory was used with a controlled selection of testing parameters to mimic the conditions found in the field. This study expands on previously reported work on wear-resistant coatings in dry sliding contact [27,28] and other selected anti-abrasion coatings available commercially. The HVOF composite and metallic coatings were tested in liquid phase or vapor phase conditions to evaluate the corrosion resistance for the possible application as wear and corrosion resistant coatings for components in geothermal environments. The performance of the HVOF coatings was studied with chemical and microstructural analysis to determine how the integrity of the coatings was affected by the liquid and vapor phase corrosion conditions. The study is expected to provide new insights into the application of such coatings in environments relevant to the geothermal industry.

2. Materials and Experimental method

2.1. Test conditions

The HTHP autoclave system used for the tests can create conditions to simulate geothermal fluids with physical and geochemical properties such as temperature, pressure, and geochemical composition in a single phase (liquid) or two-phase (liquid-vapor) condition at a selected pressure of 50 bar and temperatures

of 120 °C and 250 °C. Corrosion tests were carried out to simulate three conditions: (i) in drilling fluid (i.e., liquid phase test) in geothermal well conditions at high temperature, and (ii, iii) when drilling fluid circulation ceases but high temperature corrosive geothermal fluid leaks into the well (i.e., liquid/vapor phase test) as shown in Table 1.

In geothermal drilling, the cooling fluid used is usually water-based or alkaline to avoid corrosion [29], sometimes achieved with added viscous polymers which also allow easier transport of cuttings. Based on the stated, Icelandic tap water of pH 9 was used to simulate geothermal drilling fluid at 120 °C in the corrosion tests. After the solution had been filled and samples installed, the autoclave lid was lowered to seal the autoclave vessel with 250 Nm torque. In the autoclave, the temperature was raised by 25 °C/h and stabilized at 120 °C for 14 days by pressurizing to 50 bar. The rotation speed of the stirrer was set to 60 RPM. For test conditions (ii-iii) (Table 1) CO_2 and H_2S corrosive gases were used to simulate the geothermal fluid. The 3 L reaction chamber was half-filled with deionized water containing dissolved 0.60 g of NaOH and 0.44 g of NaCl for testing in the liquid and vapor phase at 250 °C. For this test, lower pH was desired to represent geothermal fluid with the ingress of gasses thus pH in the range of 5-7 was desired thus dissolved NaOH and NaCl were added to the deionized water according to the geochemical modelling to obtain the desired conditions in the autoclave during testing. For safety reasons, the autoclave is pressurized to 50 bar with nitrogen (N_2) at 25 °C for a day to check for gas leakage. After successful completion of the test, the pressure was reduced to 0 bar before filling with the H_2S, and CO_2 gases. The autoclave vessel was filled with 1.07 g of H_2S, 11.05 g of CO_2, and 7.04 g of N_2. The H_2S, CO_2, and N_2 gases used in the experiment were all of 99.5% purity. The filling was controlled and measured by Brooks mass flow controllers, and the values were recorded by the data logging program. After each experiment, the autoclave was cooled at a rate of 25 °C/h. The autoclave was then flushed with N_2 and depressurized to trap H_2S gases, if present, in an 11g Zinc acetate in a 0.5 L water solution. This ensured that all remaining sulfur dissolved in the water was precipitated as ZnS. A set of modelling was performed to predict the changes in pH from RT to 120 °C and 250 °C, these values are given in Table 1. The composition of the vapor and liquid phases at the experimental pressure and temperature for the conditions at 250 °C with the corrosive gases were calculated by using the Peng-Robinson chemical model in Phreeqc® and are given in Table 2 and Table 3.

Table 1: Test conditions for autoclave corrosion experiments and calculated pH at either 120 °C or 250 °C and 50 bar by using the Peng-Robinson chemical model in Phreeqc®.

Test type	Temperature T(°C)	Pressure (bar)	Test environment fluid composition	Test condition phases	Solution pH @25°C	Solution pH @T(°C)	Test time (hours)
i	120	50	Tap water and N_2	liquid	8.9	7.2	336
ii	250	50	NaCl, NaOH, H_2S, CO_2, and N_2	liquid	5.7	6.8	168
iii				Vapor			

Table 2: Chemical components of the water-based solution (mg/kg) at 250 °C and 50 bar calculated by using the Peng-Robinson chemical model in Phreeqc®.

CO_2	HCO_3^-	H_2S	HS^-	N_2	Na^+	Cl^-

(mg/kg)	1981	393	472	99	292	350	181

Table 3: Chemical composition of vapor phase (mol%) calculated by Peng-Robinson calculation using a chemical model in Phreeqc®.

	H_2O	CO_2	H_2S	N_2
(mol%)	79.8	8.5	0.3	11.4

2.2. Experimental setup for autoclave–corrosion testing

The test facility and experimental setup are displayed in Figures 1(a) to 1(c). The autoclave corrosion setup is illustrated in Figure 1a. The reactor is filled with the fluid and pressured with N_2, H_2S, and CO_2 via the gas inlet lines from the bottom of the reaction (autoclave) chamber (Figures 1(a) and 1(b)). The gas components were fed through a gas filling panel (Figure 1(c)), with the filling rate regulated by Brooks mass flow controllers. The custom-made sample holder was installed in the lid, and during the experiment, the test samples were installed between the vertical sample holder supports (Figure 1(b)). The geometry of the test sample (50 mm x 25 mm x 3 mm) was designed to fit onto a threaded metallic sample holder with 6 mm diameter Polytetrafluoroethylene (PTFE) insulators to avoid galvanic corrosion (Figure 1d). In Figure 1d, PTFE separators were fit between each adjacent test sample to prevent the easy transfer of corrosion deposits. The use of PTFE separators may create a micro-gap; however, the discussion of the results explores the possibility of crevice corrosion at the PTFE/coating interface. A preliminary 7-day corrosion test was successfully carried out at 250 °C and 50 bar gauge to establish and demonstrate the interface and the positions A and B (seen in Figure 1(b)) for testing the sample sets in the simulated liquid and vapor phase test conditions. Followed by the experiments designed to simulate geothermal drilling and aggressive corrosion conditions which are reported in the result section. A 14-day (336 hours) exposure of the coatings simulated geothermal well drilling conditions at 120 °C, in tap water (no corrosive gases) pressurized to 50 bar with N_2: test (i) in Table 1. A 7-day (168 hours) corrosion test was performed at 250 °C in liquid/vapor phase conditions with CO_2 and H_2S corrosive gases pressurized to 50 bar with N_2 to mimic HTHP geothermal environment exposure of the coatings: tests (ii) and (iii) in Table 1.
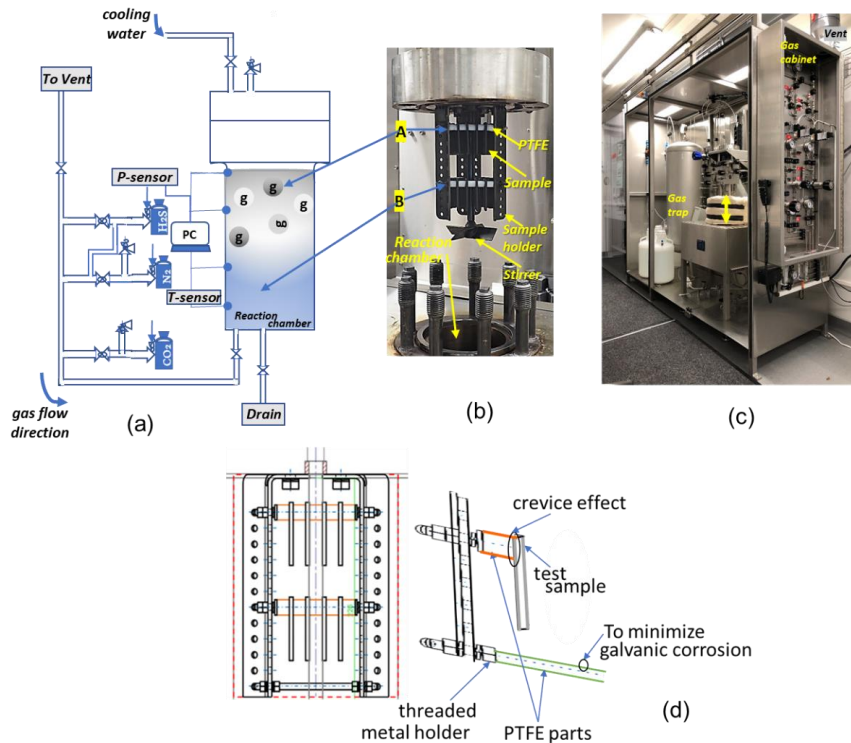
Figure 1. The HTHP autoclave and setup used for the corrosion testing; (a) the flow-through process to the autoclave reaction chamber (b) image of the sample holder with sample positions; vapor phase – A, and the liquid phase – B and (c) cross section of sample holder showing the PTFE separators. The yellow arrow in (c) shows the insulation of the sealed autoclave to eliminate heat loss.

2.3. Materials

The targeted application areas (components) considered for the coating materials evaluated in this study generally have a smooth surface finish, complex geometry, and close tolerances, such as geothermal drill pipes, stabilizers, turbine rotors, blades, shafts, valve systems, and housings. HVOF coating technology has shown to produce relatively smooth coatings, even without post-treatment, that improve lubricity and sliding wear resistance [28]. Based on this, five coating compositions that are available and known commercially were chosen for the HVOF-spray technique. The sprayed materials include: three cermets ($WC_{10}Co_4Cr$, $75Cr_3C_2$-$25NiCr$, WC-$20C_3rC_2$-$7Ni$), a self-fluxing Ni-based ($Cr_{14}Fe_5Si_5B_3Ni_{bal}$) and an Fe-based amorphous/nanocrystalline ($Cr_3C_2Mo_{20}W_{10}Mn_5B_5Si_2Fe_{bal}$) powders. Additionally, a novel High Entropy Alloy ($CoCrFeNi$-$Mo_{0.85}$) coating composition was selected to assess the corrosion resistance, particularly for the CO_2/H_2S conditions. TWI limited Cambridge – UK provided samples coated with the six different types of the HVOF coatings, which were deposited on a through-hardened low alloy steel type 817M40. Table 4 reports the chemical composition of the steel. The samples were tested for the 2 different

simulated environments and 3 conditions in the autoclave (i.e., 120 °C water, 250 °C liquid and 250 °C vapor phase tests), including the reference alloy steel substrate.

Table 4: Chemical composition of the 817M40 low alloy steel material.

Element	C	Cr	Ni	Mo	Mn	Si	B	O
Content (wt.%)	0.4	1.2	1.4	0.2	0.3	0.6	0.01	0.03

2.4. Characterization of coatings

Microstructural analysis was conducted with field emission scanning electron microscopy (FE-SEM, Zeiss Supra 25®). The SEM was equipped with an energy dispersive X-ray spectrometer (EDS, Oxford Instruments®) used for the elemental and compositional analysis of the coatings reported in weight percent (wt.%). The SEM equipment also estimated the thickness of the coatings. Using a Taylor Hobson Ametek® stylus profilometer, ten measurements were taken to determine the average surface roughness parameter (Ra). The coating's porosity assessed from microstructural images of polished cross-section surfaces was captured using optical microscopy. Averaged porosity was measured using ImageJ® software using area fraction analysis and thresholding at least twenty micrographs. The microhardness of the HVOF sprayed coatings was determined by the Vickers hardness test. Indentation loads of approximately 300 gf recorded hardness values in the cross-section of the coatings using the Buehler VH1202 Wilson® hardness tester. The resulted averaged values and standard deviations for all coating properties are shown in Table 6. X-ray diffraction (XRD) was conducted in an X-Pert Pro Empyrean from PANalytical® with CuKα radiation (λ = 1.5406 Å). The data was collected after sample alignment at 45 kV, 40 mA in the 2θ range of 5–100 degrees depending on the coating type and analysed with High Score software. Crystal structure analysis of corrosion products was carried out with XRD while localized corrosion damages on the samples were analysed further in SEM/EDS by cross-sectioning, mounting, and casting the samples in a conducting polymer (Bakelite) at elevated temperature under pressure. SEM/EDS analysis was performed in selected regions of the coatings before and after the autoclave corrosion testing.

3. Results

3.1. Pre-exposure analysis and coating properties

The microstructure of coatings deposited from the HVOF process is shown in Figure 2. All the HVOF coatings in the study had no bond defects such as delamination, and a smooth surface finish. The microstructure of the coatings inherently showed a dense laminar microstructure (i.e., layered with splat boundaries). Horizontal microcracks are observed at the edges and corners of the coated samples. A few cracks were detected on the coating top surfaces and some pores, in the Flux and Amor cross-section of the coatings. The microstructural analysis shows WC, Flux and Amor have homogeneously mixed phases (Figures 2(a), 2(d), 2(e)); however, Cr/Mo seems to segregate at splat boundaries in the CrC, WC-CrCNi, Amor and HEA coatings (Figures 2(b), 2(c), 2(e) and 2(f)) which was verified by EDS analysis. The CrC is comprised of a metallic binder -NiCr region (bright areas) with carbide C_3rC_2 phases (dark areas) shown in Figure 2(b). A similar microstructural heterogeneity in the layered structure is seen in the HEA coating. Aside from the well-alloyed zones, minor bright and dark portions in the splats were observed as Mo-rich and Cr -rich regions, respectively (see Figure 2(f)). Oxides were observed in all coatings where the highest content was detected in the HEA (3.6 wt.%) as can be seen in the results from the EDS analysis given in

Table 5. Table 5 presents the chemical composition analysis of six as-sprayed HVOF coatings analysed in the cross-section with SEM/EDS. Table 6 reports the results from the surface characterization and coating properties after deposition, where the cermet coatings showed the highest hardness (HV) and least surface averaged roughness (Ra). The difference in hardness is likely influenced by the alloy composition, metallic binders (Co, Ni, and Cr) and percentage of porosity in the coating. Higher hardness was obtained with harder ceramic phases and/or metallic binder. Among the non-cermet, the HEA was measured with the lowest porosity (<2%) but the lowest hardness; this may be attributed to the reported heterogenous mixed-phase solid solution and intermetallic phases [30]. Although, the porosity results demonstrate that the deposited coatings were generally dense, retaining 99.0 to 96.0 % of the precursor (powder) which can be attributed to the good flowability of the powders and a high deposition efficiency of the HVOF process.
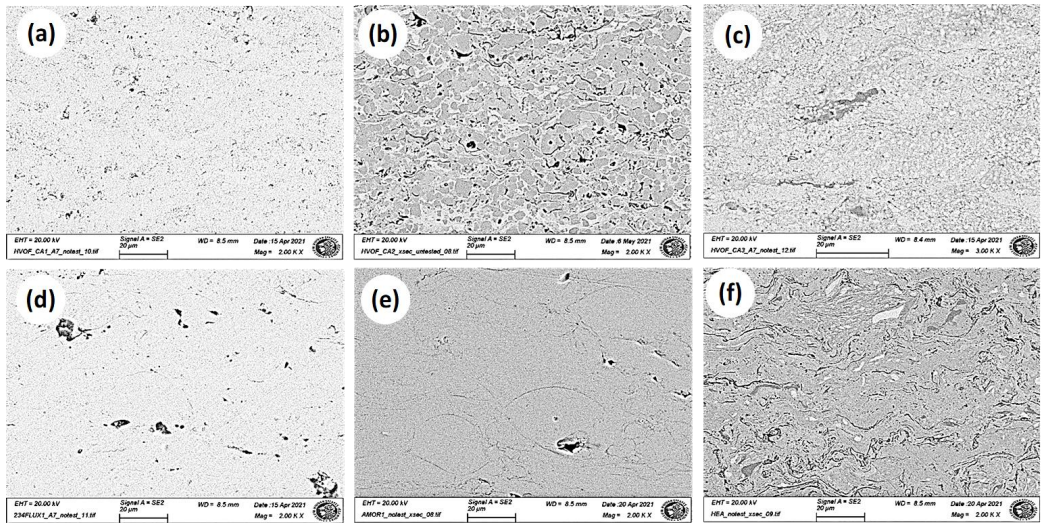
Figure 2. SEM cross-section images showing the microstructure of the untested HVOF coatings; (a) WC, (b) CrC, (c) WC-CrCNi, (d) Flux, (e) Amor and (f) HEA.

Table 5: Chemical composition of the HVOF-deposited coatings analysed with EDS analysis.

Material	Test ID	Nominal composition (wt.%)											
		O	C	W	Cr	Ni	Fe	Mo	Co	Al	Mn	Si	B
WC-CoCr	WC	0.8	9.2	75.1	3.8	-	-	-	9.5	1.6	-	-	-
CrC-NiCr	CrC	3.6	11.2	-	61.7	23.1	-	-	-	0.5	-	-	-
WC-CrC-Ni	WC-CrCNi	1.5	-	68.4	22.1	8.0	-	-	-	-	-	-	-
NiCrFeBSi	Flux	0.3	8.9	-	14.2	65.1	3.5	-	-	-	-	3.7	4.3
FeCrMoWMnBCSi	Amor	0.9	6.8	5.9	18.8	-	51.1	13.5	-	-	1.8	1.0	0.2
CoCrFeNiMo$_{0.85}$	HEA	3.6	0.7	-	15.1	17.7	17.2	21.6	18.0	6.1	-	-	-

Table 6: Average values of the coating properties of the HVOF-deposited coatings.

Coatings	Roughness [Ra(μm)]	Porosity [31] (%)	Thickness (m)	Hardness (HV$_{0.3}$)

WC	3.7±0.2	1.9±0.4	0.40±0.02	1199.5±163
CrC	3.8±0.1	1.1±0.1	0.25±0.01	868.7±49
WC-CrCNi	5.3±1.0	1.6±0.3	0.21±0.03	1069.8±49
Flux	6.2±0.5	2.4±0.3	0.25±0.02	800.0±74
Amor	6.3±0.5	3.6±0.7	0.31±0.02	747.2±68
HEA	5.0±0.2	1.6±0.3	0.27±0.02	586.7±55

3.2. Post-exposure analysis: Microstructure and chemical composition analysis

3.2.1. Simulated drilling condition at 120 °C

Microstructural and chemical compositional analyses were performed using SEM/EDS analysis of the samples after 14 days of corrosion testing in the simulated drilling condition at 120 °C. Negligible corrosion was observed in all the tested samples after exposure to the 120 °C in tap water with no corrosive gases. The surface SEM images of the HVOF coatings did not show extensive corrosion products, i.e., the surfaces were not covered with thick corrosion film or scale. A small number of particles were observed on the surfaces and identified as oxides of Mo, Cr, Ni and Al but were not easily detected in the further cross-sectional analysis (see Figure 3). The results showed porosities typically in the Amor and Flux, but no indication of delamination or localized damage at the coating/substrate interface (Figures 3(a) – 3(f)). From the porosity assessment of the coatings (1 – 4 %), the voids may not be interconnected, therefore, minimum permeation of the electrolyte or ingress of corrosive species occurred during the 14 days of water testing. All the coatings were corrosion resistant under the 120 °C simulated drilling operation.
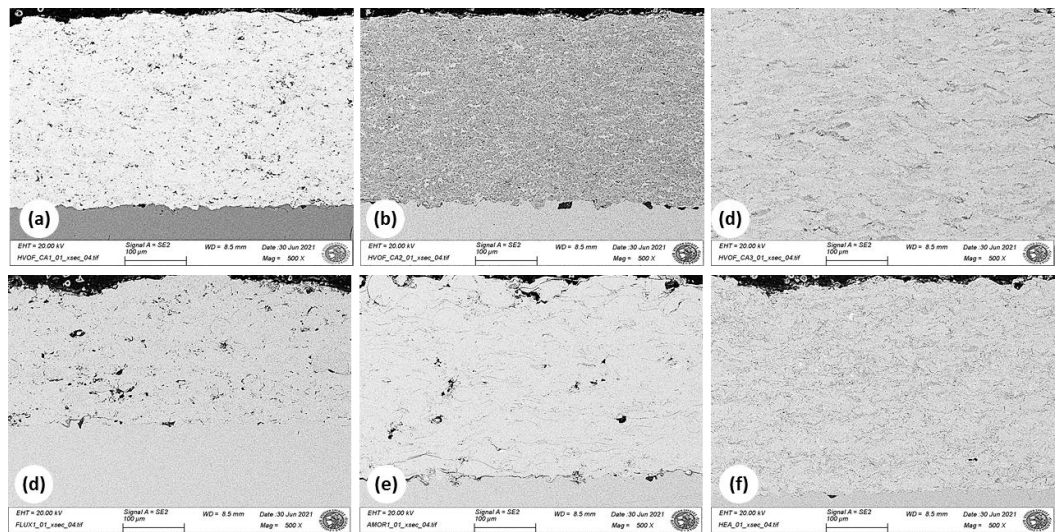
Figure 3. SEM cross-section images of (a) WC, (b) CrC, (c) WC-CrCNi, (d) Flux, (e) Amor and (f) HEA - HVOF developed coatings – after 120 °C water corrosion test.

Regarding the uncoated low alloy steel exposed to 120 °C water, SEM/EDS analysis reveals a Fe, O-rich film and minor traces of Cr formed with surface pits after the test. EDS line mapping of the surface showed

an O deficiency in the pits (Figure 4(a)) suggesting the alloy experienced general corrosion and is susceptible to pitting corrosion in the HTHP tap water environment. This point seems critical where coating coverage is limited or peels off at the edges. Figure 4b shows localized corrosion of the low alloy steel in the cross-section found at corners and edges of the substrate coated with hard and brittle WC-CrCNi (HV~1100) coating. The image shows an under-deposit film (66.3%Fe-20.2%O) filling the corrosion pit, see area 2 in Fig. 4(b) analysed with EDS.
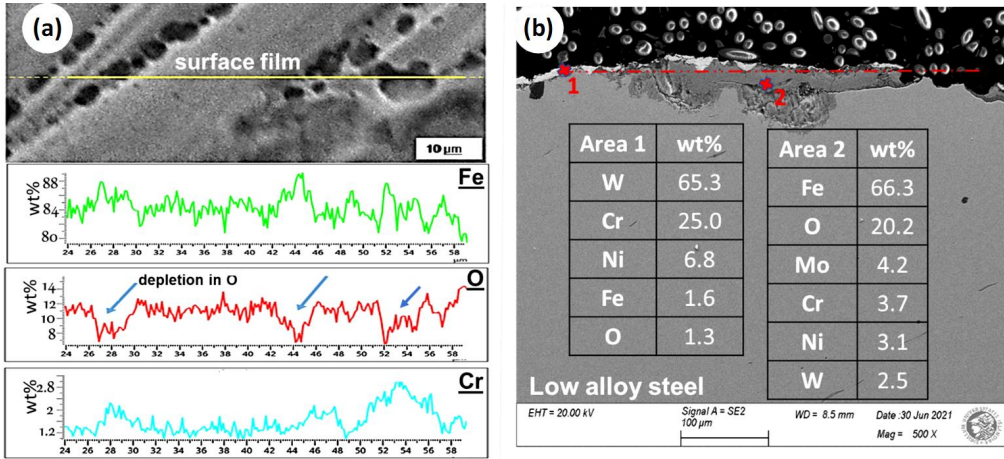
Figure 4. SEM/EDS of corrosion layer (a) with line mapping on the surface of the low alloy steel substrate and (b) in the cross-section showing localized damage of substrate steel at uncoated regions of the WC-CrNi coating after 120 °C water corrosion test. The blue arrows point out a decrease in O at pits in (a).

3.2.2. HTHP liquid/vapor phase test with CO_2/H_2S at 250 °C

After one week of testing with CO_2/H_2S at 250 °C, microstructural and chemical composition analyses of the surface (Figures 5(a), 5(b), 5(c)) and cross-section (Figures 5(d), 5(e)) of the low alloy sample revealed the presence of corrosion products. This could be due to alloy constituent dissolution, apparent in the elemental iron (Fe), molybdenum (Mo), and chromium (Cr) on the surface. The surface shows different crystals from the corrosion reactions, primarily S and Fe-rich. The cross-section image in Figure 5(a) shows no corrosion products or film and minimum corrosion effects on the low alloy sample after liquid phase exposure. However, Figures 5(b) and 5(c) depict SEM micrographs of the surface revealing the deposited material, demonstrating easy spall off the Fe, S- rich corrosion products. In Figure 5(c), three distinctive corrosion products are identified (locations a, b, c) with obvious dissimilarities in the chemistry where contributions of Mo (locations a, b) and Cr, O (location c) are reported in the SEM/EDS mapping. Comparable to the vapor phase exposure (Figures 5(d), 5(e)), two different morphologies were observed in Figure 5(e), in which the difference in chemistry from the SEM/EDS results was due to the presence of carbon (C) and traces of Ni, O. The result of cross-sections analysis showed material loss but had no evidence of localized corrosion damage. Nevertheless, the initiation of localized corrosion is possible to have occurred as shown in Figures 5(a) and 5(d), pointed out by the red arrows in the magnified images.
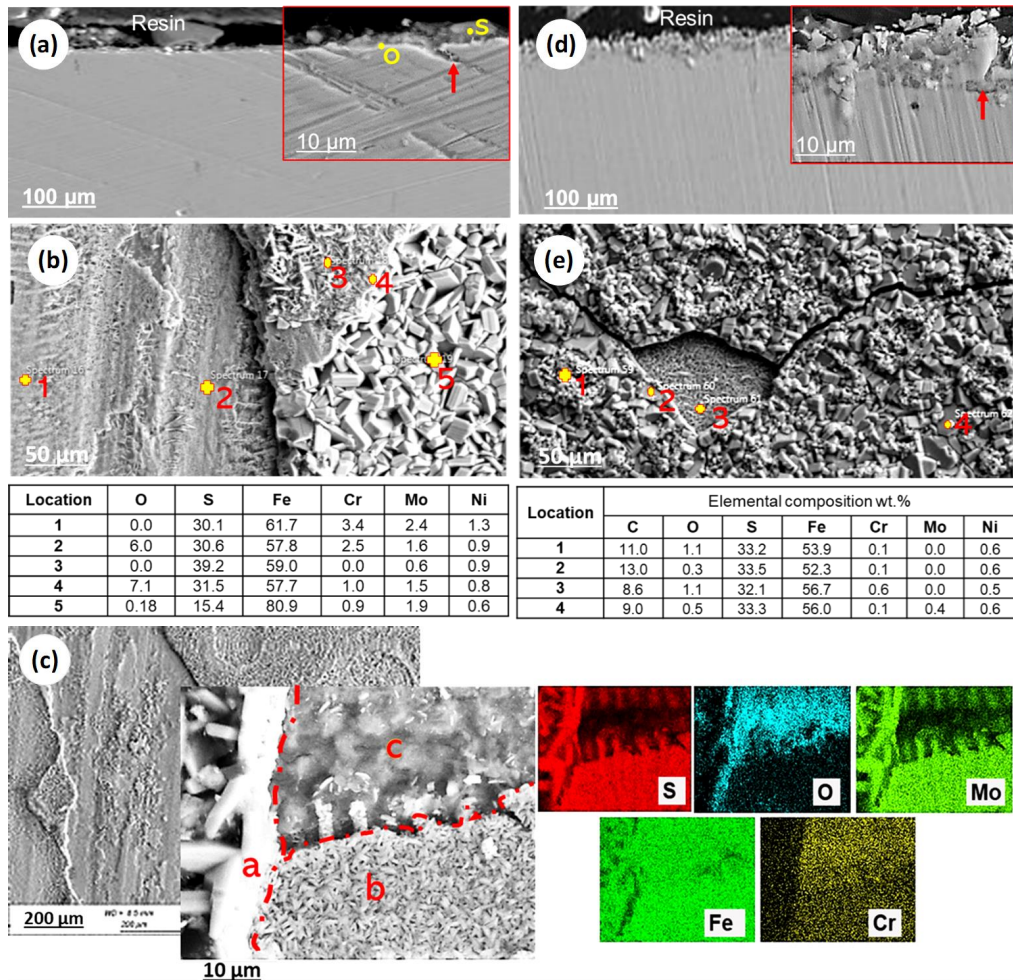
Figure 5. SEM surface images of low alloy steel tested in – (a, b, c) liquid phase and (d, e) vapor phase, in the 250 °C, CO_2/H_2S corrosion test.

The surfaces of the coated samples were examined by the SEM/EDS for all the coatings from both liquid and vapor exposure to study the surface morphology and elemental distribution after the 7-day test with CO_2/H_2S at 250 °C. Figure 6 shows an overview of the surface morphologies of the coatings after testing in the liquid phase and vapor phase. After exposure to the simulated liquid phase geothermal environment at 250 °C with CO_2/H_2S, a minor amount of corrosion products was found on the surfaces of all coatings except for the Flux which had extensive corrosion products formed (Figure 6). The corrosion products observed indicate the surface reaction of the coatings to the corrosive environment. A comparison to the microstructure of the untested coatings revealed that there is a visible change in the morphology of the coatings after testing and more pronounced effects from the vapor phase test for some samples due to the presence of the non-condensable gases (the H_2S and CO_2) in the vapor phase. In addition, crevices, edges, and corners (seen in Figure 6(g)) showed larger-sized corrosion products compared to the other exposed

areas. This shows the potential for crevice corrosion. The observed crevice attack is related to the presence of sub-millimetric interstices (gaps, craters, deposits) altering the environmental conditions on the coating surface or at the coating/PTFE-separator interface. Sulphur, carbon, and oxygen-based rich crystals precipitated on the surface due to reaction with the base elements employed in the coating synthesis. The red arrows in the micro-graphs in Figure 6 point out visible products that formed on the coating surface. The formation of corrosion products on the surfaces may imply that the coatings prevent the substrate from dissolution; nonetheless, it is evident that the coatings were ineffective in protecting their matrices from H_2S and CO_2 corrosion at 250 °C. The distribution of elements and the chemical compositional analysis in the SEM with EDS analyser for both surface and the cross section is presented in the following sections.
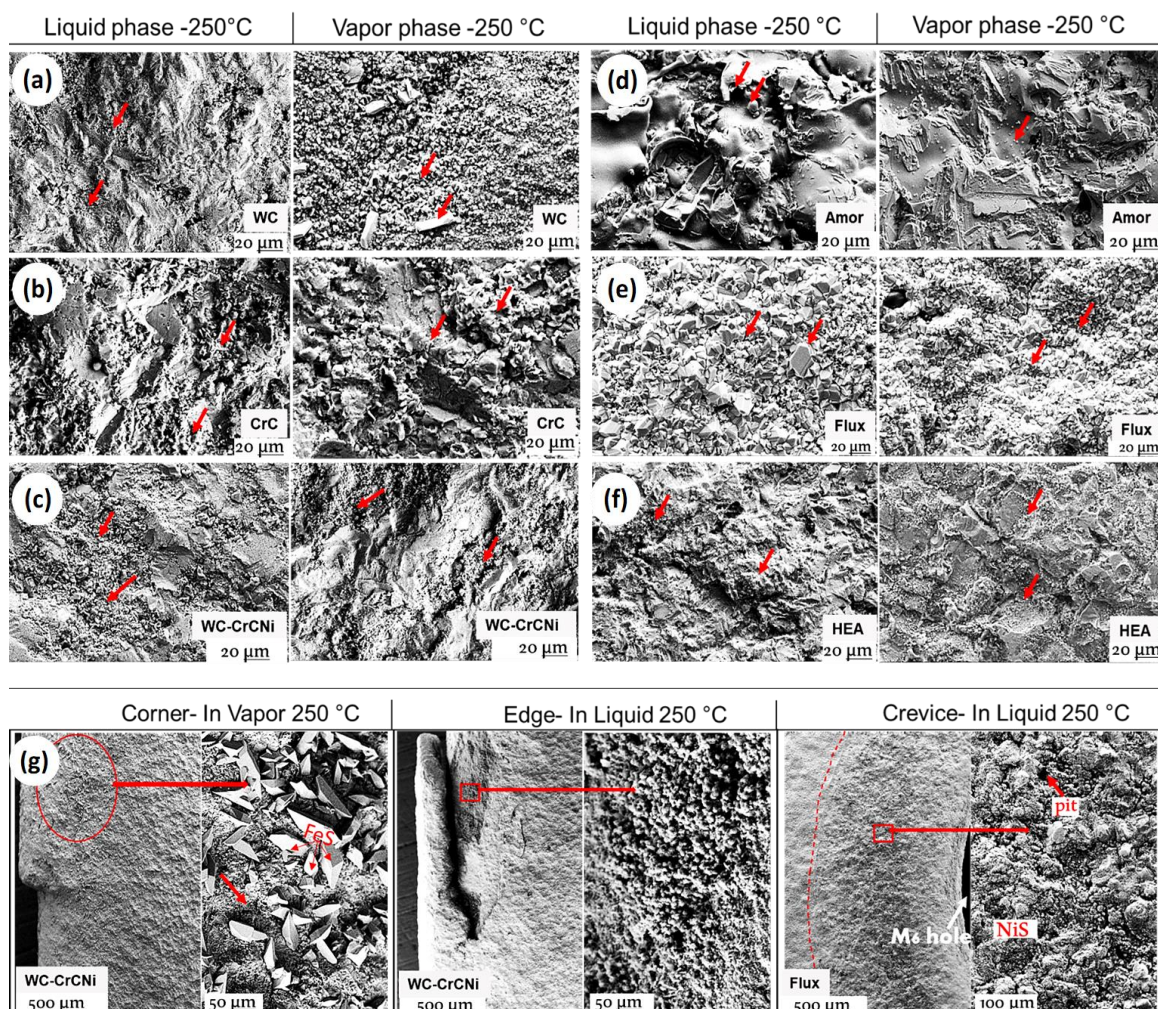
Figure 6. SEM analysis of surface – (a) to (f) corrosion products and (g) edge, corner, and crevice from the liquid and vapor phase exposure. The red arrows point out visible products that formed on the coating surface.

Figure 7 shows SEM images of the cross-sections of the coatings tested in the liquid phase. No delamination or major defects at the interface of the coatings are observed as can be seen in Figures 7 (a) to (f) of the samples in the liquid phase. At higher magnifications, surface cracks and micropores were detected in the SEM analyses. The Amor coating had larger unfilled pores in the cross section with no obvious corrosion film (Figure 7(e)). It is to be noted here that Amor had the highest initial porosities (3.6%) before testing. This may suggest the original pores are not interconnected for ingress the electrolyte into the coating layers confirming the unfilled pores. On the other hand, the pores were many and of random shape and size such that the micropores in the original coating might have become bigger owing to corrosion. However, it is hard to distinguish between the pores from the original coating and corrosion-induced pores. At higher magnification in SEM/EDS results, Mo, Cr and Fe deficiency was found around the large-sized voids in the Amor coating possibly evoked by corrosion reactions in the liquid phase.
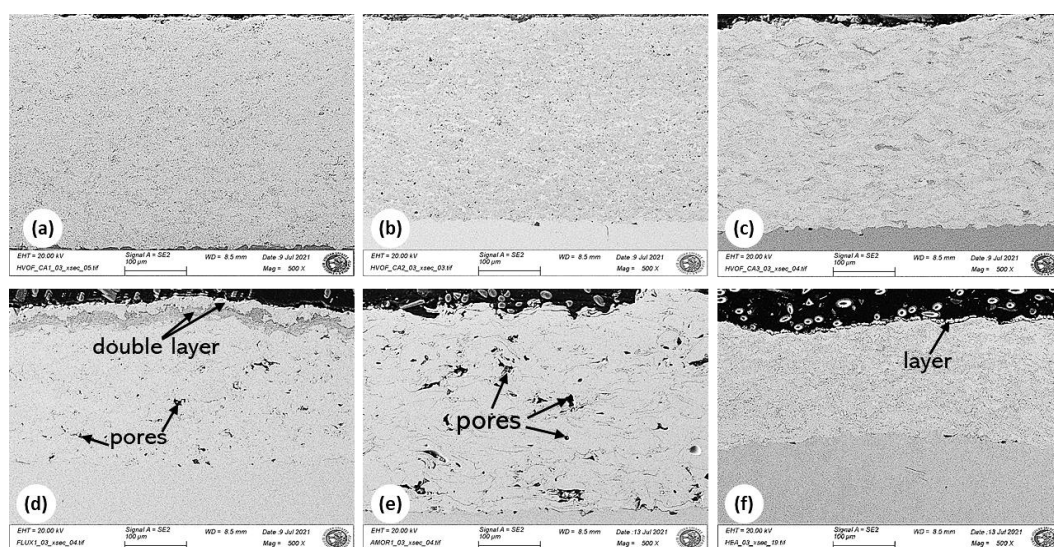
Figure 7. SEM cross-section images showing the coating, coating/substrate interface and substrate of (a) WC, (b) CrC, (c) WC-CrCNi, (d) Flux, (e) Amor and (f) HEA – in the liquid phase; 250 °C, CO_2/H_2S test.

The corrosion surface layers on both the Flux and HEA (shown in Figures 7(d) and 7(f)) were characterized by SEM and EDS analysis at higher magnification, see Figure 8. In Figure 8(a), the SEM image shows mixed-size cube crystals on the Flux surface identified as metal sulphides (19.6 % S) according to the EDS analysis given in the table in Fig. 8(a). A bi-layered corrosion film was identified in the cross-section, each approximately 20 µm thick. EDS elemental mapping showed the outer surface layer is Ni- S rich and the inner layer is rich in Fe, Cr- oxide-based products as shown in Figure 8(b). Figure 8(c) depicts the EDS map of the HEA surface, which showed the presence of S and O indicating the existence of some reaction products. A thin corrosion scale was detected at the rounded edge of the HEA coating. The thin layer was composed of Mo, O, and C- based products as indicated in the EDS analysis in areas 1, 2, and 3 shown in Figure 8(d). The corrosion layer seen in the cross-section was rather flaky and non-adherent. A drastic drop in Mo in the oxide scale was observed with an increase in C in area 3. With the insignificant concentration of the HEA elements; Co, Cr, Ni, Fe, and low S content (~4%) in all three areas (1-3), the oxide film

suggests possible surface oxidation of Mo and Mo oxides in the environment. The SEM analysis of other areas of the HEA coating was comparable to the higher magnification SEM image in Figure 8(d) (i.e., excluding the apparent surface layer), where the coating microstructure was free of pores or cracks and there were no noticeable corrosion pathways.
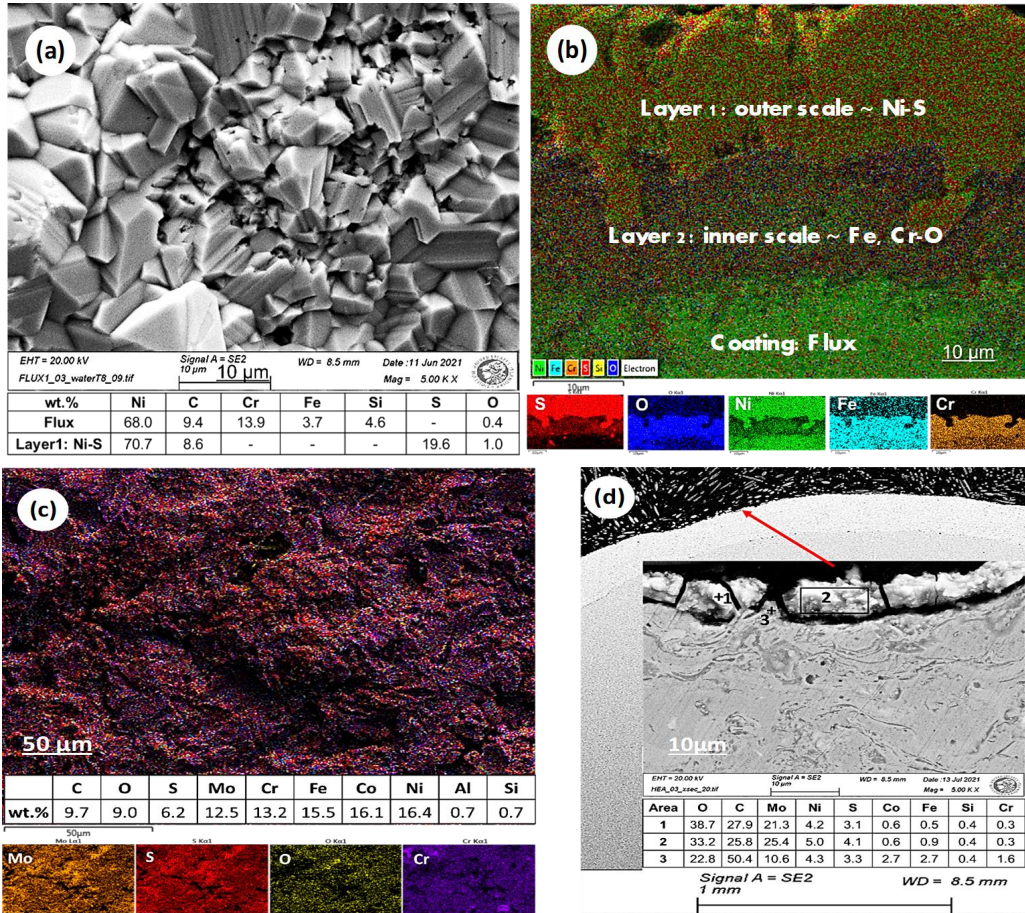
Figure 8. SEM surface and SEM/EDS cross-section images of (a, b) Flux and (c, d) HEA – tested in liquid phase; 250 °C, CO_2/H_2S corrosion test.

A detailed SEM/EDS analysis was also carried out on the samples exposed to the vapor phase environment to verify morphological and compositional changes in the coatings. The surface and the cross-sectional analysis of the WC coating are shown in the images in Figure 9. As can be seen, elemental analysis of WC showed the presence of sulfur and oxygen-based products on the surface and in the matrix of the coating. No localized damage was found at the coating/substrate interface; however, the matrix structure was more porous and had micro internal cracks after the vapor phase exposure. The surface of WC revealed two different shapes and sizes of the corrosion products: W, O- rich larger particles and smaller particles of Co and S, as seen in Figure 9(b). This suggests the dissolution of the Co metal in the binder (CoCr) and ultimate oxidation of the ceramic (WC) hard phases in vapor phase conditions.
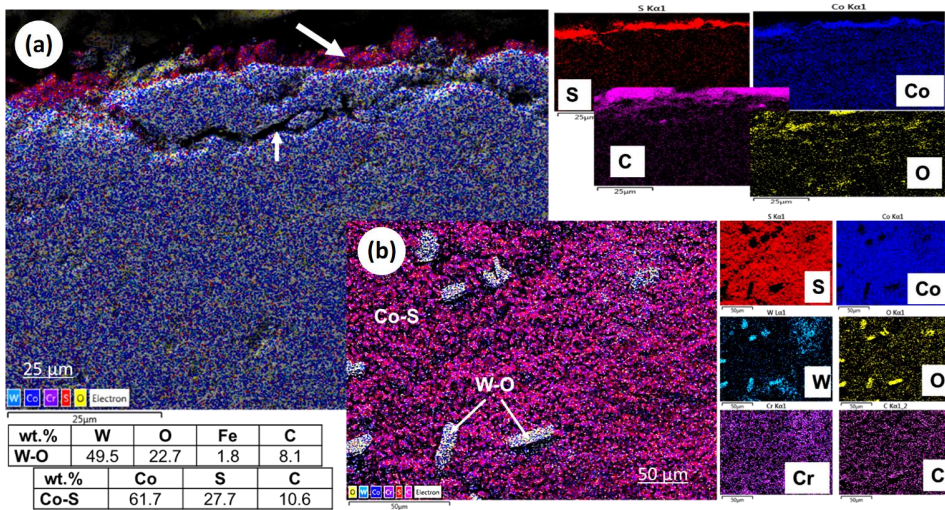
Figure 9. SEM/EDS mapping of WC; (a) cross-section and (b) surface tested in the vapor phase; 250 °C CO_2/H_2S corrosion test. The white arrows point out surface cracks and corrosion products.

SEM/EDS elemental mapping of the cross-sections of the CrC, WC-CrCNi, Flux, and HEA coatings revealed the presence and distribution of the main phases, as seen in Figure 10. For these coatings except the Flux, minor corrosion products in the form of small particles/flakes were found on the surfaces except in the crevices of the samples. Apart from oxidation, segregation in Ni-rich and Cr-rich phases were discovered in the cracked regions of the CrC matrix (Figure 10(a)). This shows that the dis-bonding of the hard ceramic (Cr_3C_2) and metal binder (Ni) phases at 250 °C increases microcracking effect. The cracked matrix had sulphides filling cavities at the detached zones. After the vapor phase exposure, WC-CrCNi, Amor, and HEA displayed a more homogeneous elemental distribution (Figures 10(b) to 10(e)). While no corrosion layer was seen on the top surface of WC-CrCNi or at the rounded edges, S and O were accumulated in the matrix pores and cracks and at the coating/substrate interface (Figure 10(b)). This demonstrates full permeability across the thickness of the coating, yet, with little substrate reaction. After vapor phase exposure, the elemental analysis of the Flux surface showed the presence of similar Ni-S rich crystals earlier discussed in the liquid phase test results. However, the thickness of the bi-layered film (Ni-S and Fe, Cr, O- based products) decreased, as can be seen from the cross-section analysis (Figure 10(d)). The outer and inner layers were approximately 11 µm and 5 µm depicting a 75% and 45% decrease in thickness value compared to the liquid phase corrosion scale. Like WC and CrC, no localized damages were seen at the coating/substrate interface in both the Amor and the HEA as shown in Figures 10(c) and 10(e). The results clearly reveal amorphous phase spot enrichment in the Amor matrix (Figure 10(c)) after the vapor phase exposure. In the HEA, some surface reaction of Mo with S is observed in the elemental map in Figure 10(e). The O present is likely to be from the initial oxidation of elements during the HVOF spray process. This is supported by an EDS investigation performed 50 µm below the top surface, which revealed that the phases in the HEA after corrosion are within 95% with no elemental sulphur present (see Figure 10(e)). Sine Mo and S spectra overlap in the EDS, further analysis of the tested coating surfaces was done with XRD technique.
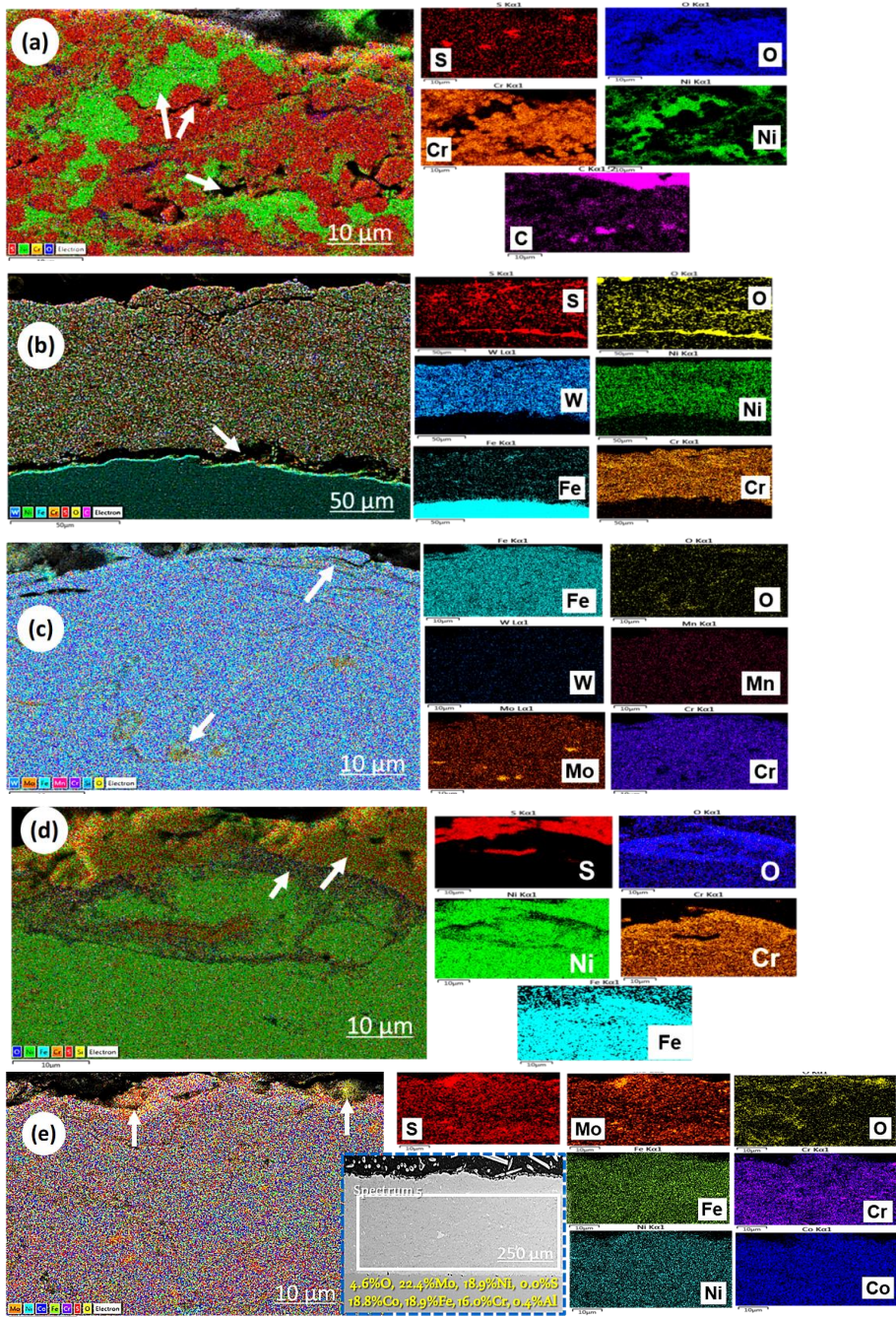
Figure 10. SEM cross-section images showing (a) CrC, (b) WC-CrCNi, (c) Amor, (d) Flux and (e) HEA – tested in the vapor phase, 250 °C, CO_2/H_2S corrosion test. The white arrows point out corrosion damage.

Figure 11 compares the Fe-based Amorphous coating after vapor and liquid phase corrosion. As can be seen in Figures 11(a) and 11(b), the surface of Amor is attacked during corrosion indicated by pitting, spalling, and peeling of the coating layers. Meanwhile, discrete Fe, S- rich corrosion products were identified only after the vapor phase exposure (see Figure 11(b)). An obvious depletion in Fe is observed in the top layer indicated by a 14% and 25% decrease in initial wt.% Fe (from both top surface EDS spectra 1) for the vapor phase and liquid phase corrosion, respectively. However, the results of the cross section showed signs of electrolyte penetration via the porosities present, around non-melted particles, and through splat boundaries. Light grey (S-based) and dark grey (O-based) phases were present in the layered structures of the coating (i.e., between splat boundaries), around clusters of unmelted amorphous particles (island-like), in and around voids/vacancies (see Figures 11(a) and 11(b)). The varying composition is probed in regions, but no obvious compositional patterns were observed. The EDS analysis in Fig. 11 shows three different compositions with varied concentrations of O, S, and reduced metallic content (mainly Fe, Cr, and Mo) with a relatively high C content (locations 1 to 4 shown in SEM images in Fig. 11(a) and (b)) suggesting reaction with the gases present (CO_2/H_2S) in the environment. The internal oxidation and sulfidation are likely the reason for the fewer pores (localized coating damage) in the vapor compared to liquid phase corrosion.

Location (wt.%)	S	O	Fe	Mo	Cr	C	W	Mn	Si
1 (top)	-	3.5	38.2	10.2	13.7	28.2	3.7	1.4	1.2
2 (filled crack)	26.5	4.9	52.7	-	4.2	10.3	0.6	-	-
3 (intersplat)	1.9	8.9	46.9	12.4	15.9	6.5	4.7	1.4	1.4
4 (unfilled pore)	-	3.6	40.2	9.9	15.8	23.9	4.4	1.5	0.7

Location (wt.%)	S	O	Fe	Mo	Cr	C	W	Mn	Si
1 (top)	-	1.6	43.8	10.4	15.7	20.9	5.3	1.5	0.8
2 (filled crack)	-	6.5	23.5	6.6	9.6	48.2	3.6	0.8	0.7
3 (intersplat)	-	13.9	44.5	8.2	11.4	16.1	4.5	0.9	0.6
4 (filled pore)	16.2	3.1	47.3	5.8	8.4	16.2	1.8	0.8	0.4
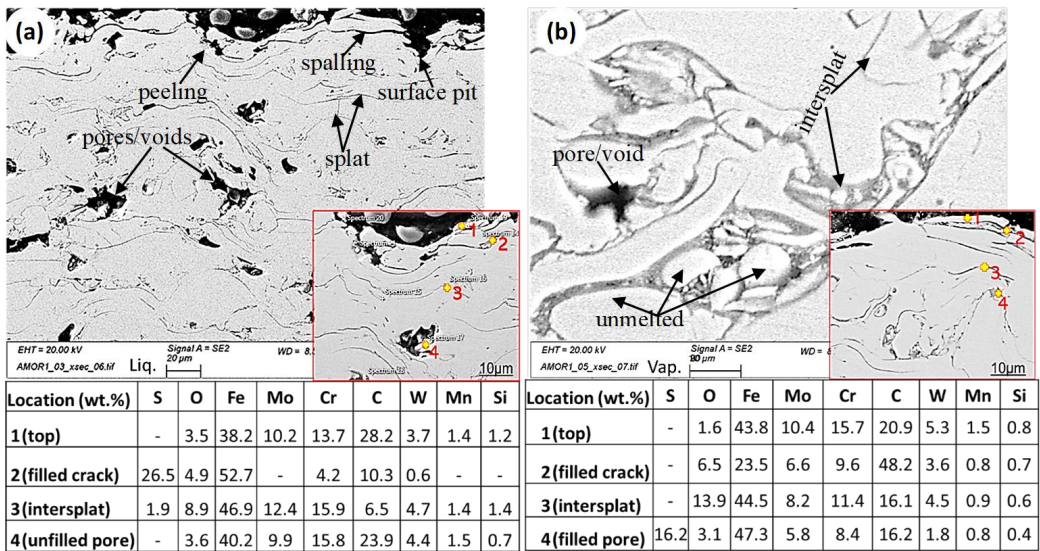
Figure 11. SEM cross-section images showing Amor coating from the 250 °C, CO_2/H_2S corrosion tests; in (a) the liquid phase and (b) the vapor phase, and the EDS analysis of areas marked with numbers in the micrographs.

3.3. X-Ray Diffraction (*XRD*) *analysis*

Due to the difficulty that can arise in distinguishing between the compositions of oxide and sulphide corrosion products because overlapping can occur for the Mo(Lα) and S(Kα) spectra within the energy resolution of EDS systems, further analysis of the tested coating surfaces was done with XRD analysis. XRD was performed on all corroded samples from the liquid and vapor phase tests to analyse the composition and formation of new phases on the surface (see Figure 12). Compositional changes were

detected between corrosion products from the liquid and vapor phase exposure, which is consistent with the EDS analysis. The main corrosion products of WC were Co_3S_4 while additional WO_2 phases were observed after vapor phase exposure (Figure 12(a)). In the XRD results of the coatings with Ni, Cr and Cr_3C_2 particles (i.e., CrC and WC-CrCNi), the corrosion products were dominantly from oxidation and sulfidation of Cr and Ni (Figures 12(b), 12(c)). For the Flux, Ni, S-based products (Ni_3S_2, Ni_9S_8, $FeNi_2S_4$) were detected. However, the less dense Ni_9S_8 and $FeNi_2S_4$ products occurring from reaction with elemental S and cations of H_2S were not detected after the vapor phase corrosion. For both the Amor, HEA and low alloy steel materials, the principal corrosion product was FeS. Meanwhile, a crystalline peak appeared at $2\theta = 26°$ in the Amor and between $35° - 40°$ in the HEA diffractions which were identified by the oxidation of Mo (MoO_2 and MoO_3 in Figures 12(e), 12(f)) after the vapor phase testing. However, Cr sulfidation was not seen with the XRD analysis of the coatings, although the SEM/EDS results identified surface corrosion products with elemental Cr and S. This may be explained by the stability of the iron, nickel, chromium, and molybdenum corrosion products at 250 °C in the CO_2/H_2S environment. Furthermore, Mo is non-homogeneously distributed in most of the original coating composition or segregated at splat boundaries and pores, thus, such corrosion-concentrated sites experience high Mo and potentially compete with the passive Cr metal. In the H_2S containing test conditions, FeS, NiS, Ni_3S_2, Mo_2S_3, and Co_3S_4 / $FeNi-Co_3S_4$ are the stable corrosion products from the XRD data. However, oxides of W, Cr, Ni and Ni-Cr also did form either as particulates or under corrosion products.
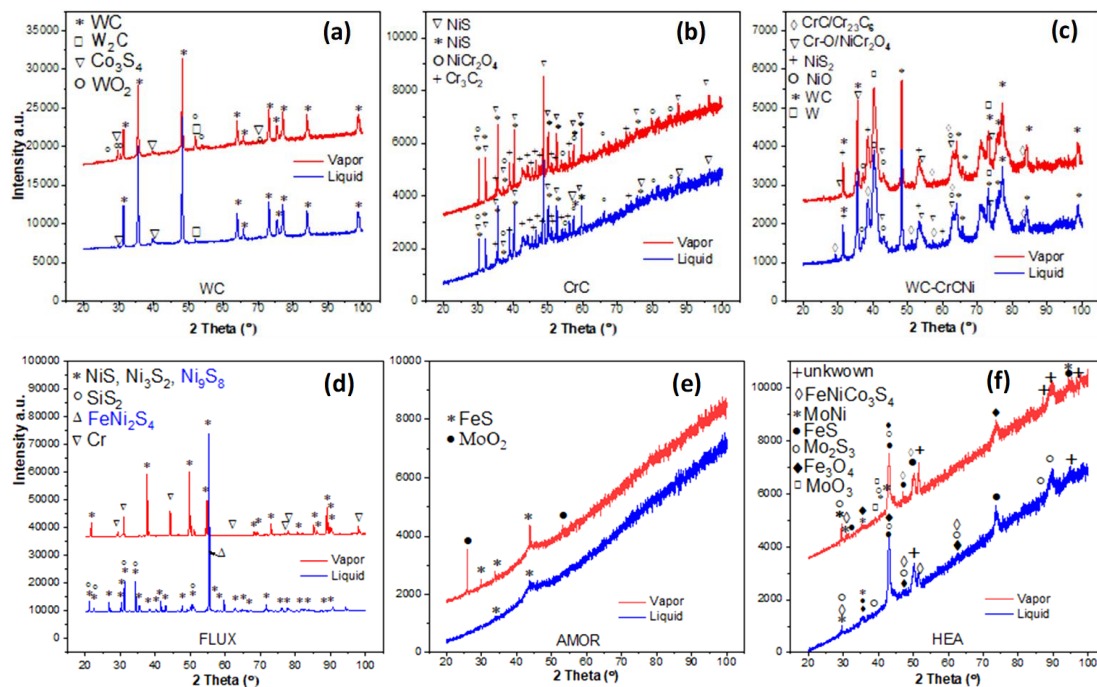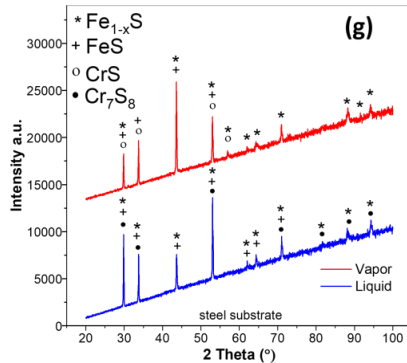
Figure 12. XRD results of tested (a) WC, (b) CrC, (c) WC-CrCNi, (d) Flux (e) Amor, and (f) HEA coatings and (g) substrate in liquid and vapor phase at 250 °C in CO_2/H_2S corrosion test. The top diffractogram is from vapor phase corrosion and the bottom from liquid phase corrosion tests.

4.0. Discussion

4.1. Effect of 120 °C water corrosion.

The corrosion mechanism in the high temperature liquid and vapor environments varied depending on the microstructure, chemistry of the coating and the test condition. Kritzer [29] concluded that high solubility and dissociation of attacking species enhance ionic processes, which accelerate corrosion. Both the solubility and dissociation processes are influenced by the density or ionic product (K_w) of high temperature water. At high densities, water functions as a polar solvent, causing ions to dissociate. However, the corrosion behaviour of all the coatings tested in the 120 °C water in the autoclave indicated no extensive surface reaction products after the testing. Therefore, the coatings protected the substrates from corrosion, acting as a barrier and preventing the substrate dissolution ($Fe \rightarrow Fe^{2+}$) from electrolyte ingress. Moreover, the cathodic reaction in the alkaline solution at 120 °C is predominantly the water reduction ($H_2O \rightarrow OH^- + H_2$) which ionizes more forming hydrogen ions (H^+) through dissociation of H_2, potentially lowering the pH. Here, since the reacting chamber serves as a closed system with no other corrosive species, the decrease in pH value depends solely on the water reactions. Thus, the predicted pH drops to 7.2 from geochemical modelling as reported in Table 1.

In addition, dissociation of the tap water may occur (i.e., if possible) in the N_2 pressurized system. Regardless, the reduction or dissociation of the water-based electrolyte at cathodic sites causes both OH^- and H^+ ionic species) to dominate the adsorption, yielding little-to-no corrosion of the coatings (i.e., at 120 °C, pH + pOH =7 or $[H^+][OH^-]$ =1.0 x 10^{-7} =K_w). Extrapolating the generic understanding of CR (i.e., depth/time or material loss/time) [32], it could be inferred that low CRs within or below the acceptable limit (0.1 mm/yr) occurred in the 120 °C test environment, since no true penetration (µm) of the electrolyte or dissolution of the coatings are observed in SEM/EDS surface and cross-section results after 336 hrs of the water exposure (liquid phase test).

4.2. Effect of 250 °C liquid/vapor corrosion with CO_2 and H_2S

Compared to the 120 °C test, an increase in pH was predicted (from 5.7 to 6.8) for the 250 °C tests. HCO_3^- and CO_3^{2-} (from Equations 3, 4, and Table 2) in the liquid phase create a buffer resulting in a higher pH,

weakening the effect of the carbonic acid (H_2CO_3). This implies the partial pressure of CO_2 was greater than that of H_2S since H_2S has insignificant effect on the solution pH. Furthermore, H_2O makes up more than 80 vol% of total vapor phases (i.e., with H_2S, CO_2 and N_2 in Table 3), and steam pressure is higher at 250 °C (41.6 atm) than at 120 °C (ca 2 atm.) and therefore some water molecules contribute to the pH shift in the respective direction. However, due to the endothermic nature of such a self-ionization reaction ($H_2O \rightarrow OH^- + H$), the equilibrium shifts towards the right side with increasing temperature. CRs in water generally increase with temperature; thus, at the same pressure when liquid temperature increases to 250 °C, the solvency of ionic species increases compared to values above ambient and 120 °C conditions. Tjelta [33] and Thorhallsson [5] reported that the ionic species are the driving force for corrosion in aqueous/steam environments but in pressurized simulated geothermal conditions above 300 °C. Therefore, in this work, the vapor (80% H_2O) and liquid (water-based) phase at 250 °C and 50 bar are under subcritical conditions of polar-like solvent behaviour; thus, the corrosion reactions can be concluded to be electrochemically driven [29]. Thus, pronounced morphological changes in the coatings tested in the 250 °C environments compared to the 120 °C (with no gases) are visible in the SEM and EDS analysis. Meanwhile, higher temperature also decreases the solubility of CO_2 which escapes above the solution into the vapor phase, thus oxidizing the nature of the vapor phase environment. Additionally, a large sulphur atom is more easily polarized than hydrogen or carbon, thus, hydrogen sulphide can interact more strongly with water via a dipole-induced dipole interaction than H_2CO_3 [34]. As a result, the H_2S hydration process is faster, providing an additional cathodic reaction from HS^-, and S^{2-} cations (see Equation 2) for the electrochemical dissolution occurring at the surfaces thus, accelerating the corrosion process.

In the mixed CO_2/H_2S-driven environment with low H_2S the formation of the carbonate scale (e.g., $FeCO_3$) is affected by the sulphides (e.g., FeS, Equations 6 to 7). In the corroded surfaces of reference substrate alloy (low alloyed carbon steel) at 250 °C, and according to EDS analysis, sulphur products and carbonates were deposited in both liquid and vapor phase corrosive environments, respectively. Therefore, the difference between the corrosion behaviour of the liquid phase and vapor phase conditions can be explained by the chemistry of passive film that forms on the tested samples. This is confirmed in the tested samples' surface analysis in Figures 4 and 5. Furthermore, the stated oxygen-based products deposited on the tested steel per SEM/EDS analysis are consistent with such carbonate reacting species (see Figure 5), confirming the preferential oxidation in the vapor phase and the formation of $FeCO_3$ from SEM/EDS analysis. Contrary to the literature, the oxide scales are removed/spalled off from the surfaces more easily than sulphides. This could explain why contrary to the EDS data, the only corrosion product found in the XRD results was pure mackinawite (FeS). But mackinawite likely transformed in other surface sites to pyrrhotite ($Fe_{1-x}S$) of the analysed steel samples (Figure 12(g)). Systematic studies of passive film formation as a function of Cr concentration indicate that alloys containing 10% Cr generate non-protective scales primarily composed of ferric oxide. Above this concentration (minimum growth at 20wt%), the oxide scale is dominated by more protective Cr-rich oxides [19]. The deficiency of chromium and molybdenum reduces the ability to form a protective Cr- oxide layer and maintain passive behaviour and instead forms less protective chromium sulphides.

4.3 Corrosion resistance of the HVOF-deposited coatings

Thermal spray coatings are prone to micro voids and microcracks due to the inter-splat boundaries which are the region for corrosion to start due to the presence of porosities that progresses next to resulting cracks that form (schematically depicted in Figures 13(a) to 13(c)). For the coatings tested in the CO_2/H_2S

corrosive environment, the surfaces generally showed negligible corrosion deposited products after the liquid phase corrosion test. However, opposite effects were found in the vapor phase test of some coatings, but it should be emphasized that the low density of the 'wet steam/vapor phase' relative to the liquid phase most likely influences the reaction rate. Debenedetti [35] demonstrated that the local density of wet steam decreases at higher temperatures and pressures which can be seen in a drop in polarity and catalytic properties of the fluid. However, the author also stated, that in the vapor phase, pressure and solubility can have a significant impact on reaction kinetics substantially influenced by high partial pressure and solubility of gases, resulting in no restrictions in mass transfer (i.e., high particle mobility and reaction rate) [34]. Although the influence of hardness and percent original porosity in HVOF sprayed coatings on corrosion cannot be established, it is found that the distribution of phases and chemical elements (causing oxidation/sulfidation) encouraged localized effects within each coating. A summary of the main findings evaluated from the corrosion testing is presented in Table 7. In table 7, the internal damages reported were analysed at the highest magnification in SEM. The oxide products observed in low magnification surface images of 120 °C liquid corrosion were mainly due to high contamination by Al_2O_3. At 250 °C, sulphide products predominated, with vapor phase corrosion of the cermets showing the most surface corrosion reactions.

4.3.1. WC-CoCr, CrC-NiCr, and WC-CrCNi

In the analyzed liquid and vapor conditions at 250 °C CO_2/H_2S environments, the majority of surface products were limited to 4 – 40 µm of the coating thickness for all tested samples, although WC-CrCNi at the corners reached total penetration >100 µm, according to the cross-section SEM/EDS data. But it should be mentioned that the damage in WC-CrCNi was at the original coated area with defects (i.e., edges) and the negligible effect was found on the underlying substrate. The uniform reaction of the coating surfaces was evaluated as 10% - 20% less of the total averaged coating thicknesses after testing. CrC had negligible corrosion, but localized cracking occurred primarily at either the Cr_3C_2/WC interface or the Cr_3C_2/Ni binder phase explaining the inferior corrosion resistance. CrC and WC coatings had better corrosion resistance compared to the WC-CrCNi coating after exposure to the CO_2/H_2S environment. The coatings' resistance to cracking and substrate corrosion was seen to increase in the following order: WC-CrCNi, WC, and CrC after both liquid and vapor phase exposure. Natural cracking of the hard (1000 – 1200 HV) yet brittle coatings seem to have occurred overtime for the 250 °C tests, and the exposed areas and porosities start corrosion and then rapidly accelerate due to the localized processes, particularly at inter-splat overlaps and at peeled edges as described and stated in the result section. This showed that the possibility of corrosion of the underlying substrate is due to binder separation and/or cracking in the WC/W_2C and Cr_3C_2 phases. Both are significant in the high-density liquid phase (i.e., 120 °C and 250 °C). In the vapor phase, precipitation of Co_3S_4, and WO_2 is visible, which can induce coating disintegration under long-term exposures. Thakare [36] and Cho [37], discussed the formation of tungsten oxides by selective corrosion of W or W_2C phases in strong alkaline and acidic environment, respectively. The authors stated the 4% added Cr positively influenced dissolution however, decarburization of WC in oxygen-dominated aerated solution or the transpassive region caused weak matrix adhesion. This is unfortunate since the W or W_2C phases are reported to improve the friction and wear properties of these coatings [20]. For the WC-CrCNi coating localized corrosion of the low alloy steel substrate, was observed in all three test conditions: water, liquid phase, and vapor phase exposure through the crack-induced effects. Therefore, it can be stated that for the 250 °C with CO_2/H_2S conditions, corrosion of cermets is dependent on the sulfidation of the metal binder

whereas Cr has a major effect on the binder dissolution process [36], but the WC matrix is also vulnerable to cracking and oxidation (where CO_2 acts an oxidizing agent). Moreover, a continuous corrosion protective layer did not form where Ni and Cr both exist in the coating likely due to the strong affinities in the CO_2 and H_2S mixed environment. Cho [29] reported similar corrosion damages and coating failure trends for the similar coatings (i.e., WC-CrCNi, WC-CoCr, CrC-NiCr) tested in 5 wt.% H_2SO_4. The XRD results showed mainly Ni/Cr oxidation and Ni sulfidation forming NiS and Cr-O/$NiCr_2O_4$ on the surfaces suppressing the continuous dissolution of other metallic phases. The corrosion mechanism and damage of the cermets coatings in the CO_2/H_2S high temperature environment are depicted schematically in Figure 13(a).
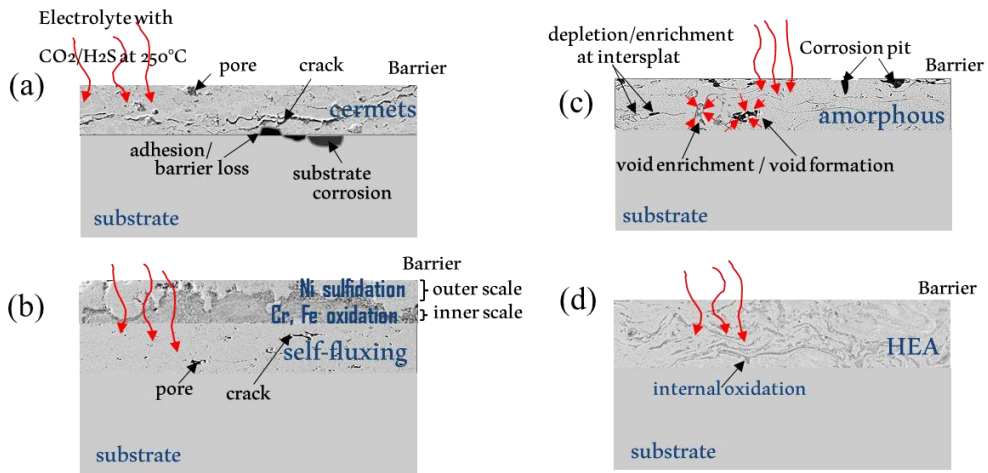
Figure 1313. Schematic description of the proposed corrosion processes resulting in the alteration of the HVOF sprayed coatings (a) WC-CrNi, (b) Flux, (c) Amor, and (d) HEA during the reaction with mixed CO_2/H_2S electrolyte in the 250 °C autoclave corrosion testing.

4.3.2. Ni-based self-fluxing NiCrFeBSi coating

Based on the results from the SEM/EDS and XRD analysis of the Flux coating, the double-layered surface film that formed in a CO_2/H_2S high temperature environment is schematically drawn in Figure 13(b). The Flux coating with 63.4 wt.% Ni and 13.8 wt.% Cr reacts during the exposure to the liquid and vapor phase with the corrosive species, where the Ni with high-temperature properties transfers to the surface reacting with H_2S and its ionic species. The formation of the NiS surface layer seen from XRD results blocks the subsequent formation of Ni oxides; thus, the migration length of oxides and hydroxides increases, and further corrosion proceed through splat boundaries, cracks, point defects and vacancies (see Figure 13(b)). The inhibition property of the NiS dense film influences the formation of the second corrosion layer. Lower density sulphides (such as Ni_3S_2) are likely to have a detrimental effect on the protectiveness, which drives the inherent corrosion of the inner matrix by the reaction of Fe and Cr to the oxides of CO_2/hydroxides of H_2O that migrates into the coating. This is supported by the difference in the double

film thickness after the liquid and the vapor phase corrosion at 250°C. As previously stated, continued corrosion resulted in the accumulation of products, producing a semi-impermeable surface layer that protects the underlying splats according to microscopic observation, typically in the highly porous cross-section morphology found in the 120 °C to 250 °C liquid phase corrosion. The stability and protectiveness of the NiS corrosion scale play a key role in the corrosion resistance of the alloyed coating. However, Paul and Harvey reported that NiCrBSiFe amorphous material showed negligible Ni scale or corrosion products at a temperature above 500 °C in molten salt and gas (O_2, N_2, H_2O, HCl) mixtures indicating a thermodynamically unfavourable environment for forming a fluxing protective layer [19]. Thus, free Ni^{2+} metal ions were the main corrosion products from Ni dissolution in the Ni-based coating in their study which could be inferred for our vapor phase analysis. At temperatures at or near 250 °C, the concentration of S^{2-} and HS^- in liquid phase corrosion is higher at the coating/solution interface where Ni^{2+} and Ni^{3+} co-exists forming the dense corrosion product as NiS, Ni_3S_2, or possibly Ni_9S_8/$FeNi_2S_4$ according to the XRD results. The increase in Ni_xS_y content is beneficial to the formation of the adherent and connected corrosion scale, which reduces mass transfer between at coating/solution interface retarding the corrosion mechanism. A Ni-base alloy with added Cr content was reported to have higher sulfidation protection temperatures (above 635 °C) than unalloyed Ni by the preferential formation of NiS [38]. On the other hand, Chou et al. [38] discovered Cr as a beneficial alloying element for passive sulphide layer protection of metals in an aqueous solution of H_2SO_4 in an ambient environment. Thus, it is concluded in the present study that the inner Fe, Cr-based corrosion product generated from CO_2 oxidation promotes good adhesive capability and thermodynamic stability of the Ni and S compounds formed in the alkaline environment.

4.3.3. Fe-based amorphous- FeCrMoWMnBCSi coating

The surface analysis of the Amor indicated relatively good corrosion resistance in the 120°C liquid test, but increased porosity was identified in the cross-section analysis (see Figure 11 (a)) which affected the corrosion behaviour at the higher temperature test, at 250 °C. Amor exhibited far less surface reactivity to S than to O, this is particularly accurate for liquid phase corrosion (see Figure 6d). According to the SEM/EDS data, the oxygen to sulphur (O:S) ratio was 12.1:0.6% for the liquid phase, 6.3:1.1% for the vapor phase, and 8.3:0.0% for the 120°C water test, respectively. The subsurface porosity was apparent in the liquid phase test whereas, void enrichment (pores filling) was observed in the cross section in the vapor phase test (depicted schematically in Figure 11(b)). Zhang [39] reported pitting corrosion of Fe-based amorphous coatings. It was discovered that atomic diffusion, crystallite precipitation, and Cr depletion caused by oxidation during the spraying process in areas along unmelted particles at metallurgical bond interfaces lead to the onset of pitting. The pitting mechanism is consistent with our findings from Figure 7, which also explains the S and O enrichment around clustered amorphous phases in the vapor phase corrosion. The results indicate that the corrosion initiated from the pores and Mo-rich intersplats. Selective oxidation/sulfidation of passive elements and dissolution of the Fe being more anodic were observed in the Fe-based amorphous matrix. Based on the Kirkendall effect [40], the balance in the selective outward diffusion/oxidation is the inward flux of vacancies. This is apparent by the FeS, MoO_2 surface corrosion product identified in the XRD analysis for the Amor. Furthermore, the original coating is porous and brittle, thus, after the dissolution of the Fe, the matrix falls out leaving more porosities. Based on the XRD results, presumably, the products form on the surface from the corrosion reaction according to:

$$Mo + 2H_2O \rightarrow MoO_2 + 2H_2 \qquad \text{and} \qquad Fe + H_2S \rightarrow FeS + H_2 \qquad (9)$$

As the reaction progresses, the unsteady corrosion film in the alkaline electrolyte likely dissolved explaining the increased porosity of the coating in a higher temperature environment (250 °C). Although the study cannot prove this conclusively, since the growth and/or dissolution of the film is a complex phenomenon, the hypothesis is supported by the 4μm layer observed on the surface after the vapor phase test and local surface pits from the liquid phase corrosion. Moreover, the high C seen in the EDS analysis can possibly be explained by a release of C and CO from the coating from CO_2 gas reactions at sufficient pressures [41]. At the pits, deficiency in Mo/Cr is seen from further oxidation precluding the S corrosion process (depicted schematically in Figure 13(c)). The corrosion attack in the Amor coating occurs at the surface and internal pores and progresses through the growth of pits seen in the cross-section images and schematically illustrated in Figure 13(c). The corrosion path was observed as spalled splats and vertical cracks but increased CO and CO_2 concentration significantly increased sensitivity or worsen pitting. The effect of corrosion on the microstructure and morphology is improved after the vapor phase exposure compared to the liquid phase corrosion. In the vapor phase, the pores and corrosion pits are filled with corrosion products possibly from Mo reaction to CO and CO_2 gases through ingress of the reactive species at defects. Internal oxidation or sulfidation is observed at splat boundaries, around clusters of amorphous particles (island-like) and in porosities. Most likely as MoO_2 since it was detected in the XRD analysis, thus the corrosion products fill the pores reducing the porosity and slowing down material loss in the vapor phase exposure. Bogaerts [10] compared passivity data for non-Mo and Mo-bearing materials, and stated that it was clear that Mo had a considerable inhibitory effect for pitting in 200 °C test conditions. In summary, with the similar Amor composition and exposure duration, the occurrence of subsurface void formation is highly dependent on the ionic species present in the liquid and vapor phase test. It can be concluded that Amor coatings are likely to fail due to peeling off the matrix and spalling the layers of the coating.

4.3.4. High entropy alloy- CoCrFeNiMo$_{0.85}$ coating

The surface reaction of the HEA coating with sulphur species formed Mo_2S_3 and $FeNiCo_3S_4$ during both liquid and vapor phase exposure. No localized corrosion damages could be seen in the morphology of the HEA or at the coating/substrate interface. From SEM/EDS results, internal oxides of Cr, Fe and Mo were detected in the HEA coating, displayed schematically in Figure 13(d), however, this is likely to have occurred during the HVOF deposition [26, 27]. The oxide was identified as MoO_3 from the XRD data. The phases present in the same HEA alloy coating composition have been reported as a mixture of FCC and BCC structures obtained through rapid cooling [27]. The authors showed residual BCC was linked to the Mo σ/μ phases component. The μ phases, with BCC forming binary – FeMo, CoMo, have been reported to form for similar HEA composition, which also improved wear resistance of the coatings and the σ phase associated with FeCr and CoCr alloys [21]. The heterogeneous structure possibly explains the internal Mo nano-phase oxidation and surface sulfidation of the FCC (FeNiCo) matrix seen from SEM/EDS analysis identified in the XRD results. However, according to the results of the current study, the HEA was not susceptible to localized corrosion in the simulated geothermal drilling and H_2S and CO_2 -containing environment at different temperatures and phase conditions. A study of laser-clad-CoCrFeNiMo$_{0.85}$ coatings exposed to an on-site H_2S/CO_2 - chloride-containing geothermal fluid showed acceptable corrosion performance however, the research highlighted that wide manufacturing cracks enhance fluid-induced erosion effect in the vicinity of the cracks [16]. Another test has previously concluded that the CoCrFeNi-Mo$_x$ coating showed localized corrosion damage in an aqueous acidic environment [26], and yet had great resistance in superheated CO_2/H_2S fluid [25]. The author [26] explained the inhomogeneous nature of the coating, with splats of phase composition likely to cause preferential dissolution of more anodic Fe-rich

regions during exposure, degrading the coating structure and forming preferred routes for ingress of corrosive medium. However, a different study reported that the CR of a CoCrFeNiMo HEA bulk material measured from the electrochemical parameters obtained in the corrosion test in the NaCl at room temperature was exceptionally low (0.0072 mm/year) attributed to the passivation of the alloy [14]. In the 120°C water-based corrosion test, a surface MoO_3 layer was observed at the corners and edges which was not uniform and seemed to crack but despite that, overall, the coating showed good corrosion resistance with minimal ingress of corrosion species. A similar flaky product was observed with negligible corrosion reported for HEA samples with different Mo ratios (10 - 30 at%) after a corrosion test in a simulated superheated geothermal environment [23]. Although a passive film was not reported as the corrosion protection mechanism in this study, the possible formation of this layer in a more aggressive environment is possible, since clearly a Mo-O rich film was seen at the coating edge in the liquid phase corrosion. These results encourage testing in various corrosive phase media of different simulated or in-situ geothermal environments. The corrosion behaviour in both the liquid and vapor phase test from this work indicates good corrosion resistance of the HVOF-HEA in the simulated near neutral to alkaline geothermal environment from 120 °C and 250 °C test and thus is encouraging for industrial exploitation in the CO_2/H_2S-containing geothermal environment commonly encountered in geothermal fields.

Table 7: Summary of the corrosion effects of the tested coatings and the main corrosion products detected.

| Material | Corrosion product (surface) | | | 120 °C drilling application | 250 °C CO_2 / H_2S application | | Degradation |
| | 120 °C | 250 °C CO_2/H_2S | | | | | |
	Water	Liquid	Vapor	water	Liquid	Vapor	Internal and/or other damages
WC-CoCr (WC)	12.7%O, Al	4.6 %O, Cr, S	10 %O, Co-S, W-O (locally)	Good	Fair	Not recommended	cracking, few pores, oxidation, crevice corrosion
CrC-NiCr (CrC)	7.5%O, Ni, Cr, Al	5.9 %O, Ni, Cr, S	10.7 %O, Ni, S, Al	Good	Fair	Fair	cracking, phase segregation, crevice corrosion
WC-CrC-Ni (WC-CrCNi)	8.3%O, Ni, Al	6.5 %O, C, Cr, S	16.3 %O, Ni, Cr, S, Al	Not recommended	Not recommended	Not recommended	cracking, pores, crevice corrosion, substrate corrosion
NiCrFeBSi (Flux*)	7.4%O, Al, Si	1.2%O, 40µm Ni-S and Cr, Fe-O uniform layer	0.9%O, Al, 20µm Ni-S (uniform) and Cr, Fe -O layer	Good	Not recommended	Fair	few pores, Ni depletion, Cr oxidation, double layer scale, crevice corrosion
FeCrMoW MnBCSi (Amor)	9.8%O, Mo, Al	12.1 %O, Fe, S, Mo,	6.3%O, Fe, S, Mo, Al,	Good	Not recommended	Fair	pitting, selective Fe dissolution, Splat-Mo, Cr depletion, Mo-pore enrichment
CoCrFeNi-Mo$_{0.85}$ (HEA)	14.8%O, Mo, Al	8.8 %O, Mo, S	9.2%O, Mo, S, Al	Good	Good	Good	No cracks or visible damages, crevice corrosion

5.0 Conclusion

The corrosion behaviour of six wear resistant coatings in high density liquid phase and vapor/steam phase conditions were successfully investigated in an HTHP autoclave. Corrosion damages and microstructural changes due to corrosion were assessed with SEM/EDS and XRD analysis. In summary, all the tested coatings performed better compared to the tested reference materials in the lower temperature (120°C) test with no corrosive gases. In the more challenging environment (i.e., 250°C CO_2/H_2S) the corrosion resistance of the coatings was dependent on their composition, microstructure, and interfacial defects. Their performances are summarized as follows:

- The cermets corroded mainly by binder dissolution and cracking. This was evident in the WC-based coatings where extensive damage by the dissolution of the binder via the inherent porosities and microcracks in the interior of the coating was discovered. These damages became highly profound in WC-CrCNi compared to WC-CoCr (WC) since they form primarily at the Cr_3C_2/WC interface, Cr_3C_2/Ni binder phase, or by decarburization of W/W_2C phases and subsequent oxidation of W explaining the inferior corrosion resistance. For the WC-CoCr coating, Co sulfurizes while W oxidizes in the steam phase at 250 °C with CO_2/H_2S. The Cr_3C_2-NiCr (CrC) showed good general corrosion resistance but was prone to microcracking and internal segregation between the hard Cr_3C_2 phase and metallic binder.
- In the Flux -NiCrBSiFe, a double corrosion layer retarded the corrosion mechanism, which likely acts as a barrier by retarding the corrosion reactions. Subsurface damage was found in coating layers of the Amor -FeCrMoWMnBCSi through dissolution and oxidation of metallic constituents. It was not prone to pitting or any form of local damage when exposed to the liquid phase environment. It is not possible to conclude overall with a tentative performance ranking in the CO_2/H_2S environment, however systematic evaluation of the coatings shows that the integrity of all the coatings except $CoCrFeNiMo_{0.85}$ (HEA) was compromised at the elevated temperatures. The HEA shows the best performance in the test conditions in terms of corrosion resistance.

Data availability

The raw/processed data required to reproduce these findings will be made available on request.

CRediT authorship contribution statement

Gifty Oppong Boakye: Conceptualization, Investigation, Methodology, Data curation, Writing - original draft, Writing - review & editing. Erlend Oddvin Straume: Investigation, Methodology. Baldur Geir Gunnarsson: Investigation, Data curation. Danyil Kovalov: Writing - review & editing, Supervision. Sigrun Nanna Karlsdottir: Conceptualization, Validation, Writing - review & editing, Supervision, Funding acquisition. All authors have read and agreed to the published version of the manuscript.

Declaration of Competing Interest

The authors declare that they have no known competing financial interests or personal relationships that could have appeared to influence the work reported in this paper.

References

[1] P.M. Wright, Geochemistry, in: P.J. Lienau, B.C. Lunis (Eds.), Direct Use Eng. Des. Guideb., 2nd ed., United State Department of Energy, Oregon, 1991: pp. 8–12.

[2] S.N. Karlsdóttir, Corrosion, scaling and material selection in geothermal power production, in: Compr. Renew. Energy, Elsevier Ltd, 2012: pp. 241–259. https://doi.org/10.1016/B978-0-08-087872-0.00706-X.

[3] R. Dipippo, Small Geothermal Power Plants: Design, Performance and Economics, GHC Bull. (1999) 1–8. http://www.geothermalcommunities.eu/assets/elearning/7.10.art1.pdf.

[4] E. Barbier, Geothermal energy technology and current status: an overview, Renew. Sustain. Energy Rev. 6 (2002) 3–65. https://doi.org/10.1016/S1364-0321(02)00002-3.

[5] A.I. Thorhallsson, A. Stefansson, D. Kovalov, S.N. Karlsdottir, Corrosion testing of materials in simulated superheated geothermal environment, Corros. Sci. 168 (2020). https://doi.org/10.1016/j.corsci.2020.108584.

[6] H.S. Klapper, J. Stevens, Challenges for metallic materials facing HTHP geothermal drilling, in: NACE - Int. Corros. Conf. Ser., 2013.

[7] K. Lichti, A. Karstensen, K.A. Lichti, D.M. Firth, A.D. Karstensen, Hydrogen Induced Cracking of Low Strength Steels in Geothermal Fluids, 2005. https://www.researchgate.net/publication/265816823 (accessed June 9, 2022).

[8] R.D. Kane, M.S. Cayard, Roles of H2S in the behavior of engineering alloys: A review of literature and experience, in: NACE - Int. Corros. Conf. Ser., 1998.

[9] R. Bäßler, J. Sobetzki, H.S. Klapper, Corrosion resistance of high-alloyed materials in artificial geothermal water, in: NACE - Int. Corros. Conf. Expo, 2013: p. 2327.

[10] W.F. Bogaerts, I. Winstons, Geothermal corrosion: High-temperature pitting of stainless steels and Ni-alloys, in: NACE - Int. Corros. Conf. Ser., 2017: pp. 2973–2987.

[11] N. Mundhenk, P. Huttenloch, T. Kohl, H. Steger, R. Zorn, Metal corrosion in geothermal brine environments of the Upper Rhine graben - Laboratory and on-site studies, Geothermics. 46 (2013) 14–21. https://doi.org/10.1016/j.geothermics.2012.10.006.

[12] H. Kato, K. Furuya, M. Yamashita, Exposure tests of turbine materials in geothermal steam from a deep production well, in: Proc. World Geotherm. Congr. 2000, 2000: pp. 3193–3198.

[13] M.A. Zavareh, A.A.D.M. Sarhan, B.B. Razak, W.J. Basirun, The tribological and electrochemical behavior of HVOF-sprayed Cr3C2-NiCr ceramic coating on carbon steel, Ceram. Int. 41 (2015) 5387–5396. https://doi.org/10.1016/j.ceramint.2014.12.102.

[14] A.K. Maiti, N. Mukhopadhyay, R. Raman, Effect of adding WC powder to the feedstock of WC-Co-Cr based HVOF coating and its impact on erosion and abrasion resistance, Surf. Coatings Technol. 201 (2007) 7781–7788. https://doi.org/10.1016/J.SURFCOAT.2007.03.014.

[15]   B. Huang, C. Zhang, G. Zhang, H. Liao, Wear and corrosion resistant performance of thermal-sprayed Fe-based amorphous coatings: A review, Surf. Coatings Technol. 377 (2019) 124896. https://doi.org/10.1016/J.SURFCOAT.2019.124896.

[16]   V.A.D. Souza, A. Neville, Mechanisms and kinetics of WC-Co-Cr high velocity oxy-fuel thermal spray coating degradation in corrosive environments, J. Therm. Spray Technol. 15 (2006) 106–117. https://doi.org/10.1361/105996306X92677.

[17]   S.N. Karlsdóttir, T. Jonsson, A. Stefánsson, Corrosion behavior of high alloy austenitic stainless steel in simulated high temperature geothermal environment, in: NACE - Int. Corros. Conf. Ser., 2017: pp. 2988–2999.

[18]   M.A. Uusitalo, P.M.J. Vuoristo, T.A. Mäntylä, High temperature corrosion of coatings and boiler steels in reducing chlorine-containing atmosphere, Surf. Coatings Technol. 161 (2002) 275–285. https://doi.org/10.1016/S0257-8972(02)00472-3.

[19]   S. Paul, M.D.F. Harvey, Corrosion testing of Ni alloy HVOF coatings in high temperature environments for biomass applications, J. Therm. Spray Technol. 22 (2013) 316–327. https://doi.org/10.1007/S11666-012-9820-8/FIGURES/10.

[20]   H.R. Ma, X.Y. Chen, J.W. Li, C.T. Chang, G. Wang, H. Li, X.M. Wang, R.W. Li, Fe-based amorphous coating with high corrosion and wear resistance, Surf. Eng. 33 (2017) 56–62. https://doi.org/10.1080/02670844.2016.1176718.

[21]   K.R. Ragnarsdottir, S.N. Karlsdottir, K. Leosson, A. Arnbjornsson, S. Gudlaugsson, H.O. Haraldsdottir, A. Buzaianu, I. Csaki, G. Popescu, Corrosion testing of coating materials for geothermal turbine application, NACE - Int. Corros. Conf. Ser. 4 (2017) 2949–2962.

[22]   S.N. Karlsdottir, L.E. Geambazu, I. Csaki, A.I. Thorhallsson, R. Stefanoiu, F. Magnus, C. Cotrut, Phase Evolution and Microstructure Analysis of CoCrFeNiMo High-Entropy Alloy for Electro-Spark-Deposited Coatings for Geothermal Environment, Coatings 2019, Vol. 9, Page 406. 9 (2019) 406. https://doi.org/10.3390/COATINGS9060406.

[23]   A.I. Thorhallsson, I. Csáki, L.E. Geambazu, F. Magnus, S.N. Karlsdottir, Effect of alloying ratios and Cu-addition on corrosion behaviour of CoCrFeNiMo high-entropy alloys in superheated steam containing CO_2, H_2S and HCl, Corros. Sci. 178 (2021) 109083. https://doi.org/10.1016/j.corsci.2020.109083.

[24]   A.I. Thorhallsson, F. Fanicchia, E. Davison, S. Paul, S. Davidsdottir, D.I. Olafsson, Erosion and corrosion resistance performance of laser metal deposited high-entropy alloy coatings at Hellisheidi geothermal site, Materials (Basel). 14 (2021). https://doi.org/10.3390/ma14113071.

[25]   I. Csáki, R. Stefanoiu, S.N. Karlsdottir, L.E. Geambazu, Corrosion behavior in geothermal steam of CoCrFeNiMo high entropy alloy, in: NACE - Int. Corros. Conf. Ser., 2018: pp. 1–8.

[26]   F. Fanicchia, I. Csaki, L.E. Geambazu, H. Begg, S. Paul, Effect of microstructural modifications on the corrosion resistance of CoCrFeMo0.85Ni compositionally complex alloy coatings, Coatings. 9 (2019). https://doi.org/10.3390/coatings9110695.

[27]   G. Oppong Boakye, L.E. Geambazu, A.M. Ormsdottir, B.G. Gunnarsson, I. Csaki, F. Fanicchia, D. Kovalov, S.N. Karlsdottir, Microstructural Properties and Wear Resistance of Fe-Cr-Co-Ni-Mo-Based High Entropy Alloy Coatings Deposited with Different Coating Techniques, Appl. Sci. 12 (2022) 3156. https://doi.org/10.3390/app12063156.

[28]   G. Oppong Boakye, D. Kovalov, A.Í. Thórhallsson, S.N. Karlsdóttir, V. Motoiu, Friction and Wear Behaviour of Surface Coatings for Geothermal Applications, in: Proc. World Geotherm.

Congr. 2020, Reykjavik, Iceland, 2020: pp. 1–9.

[29]   NACE MR0175/ ISO 15156-1, Petroleum and natural gas industries. Materials for use in H2S-containing Environments in oil and gas production., 2009. www.iso.org (accessed May 1, 2022).

[30]   Z. Dong, D. Sergeev, M.F. Dodge, F. Fanicchia, M. Müller, S. Paul, Microstructure and Thermal Analysis of Metastable Intermetallic Phases in High - Entropy Alloy CoCrFeMo0.85Ni, Materials (Basel). 14 (2021) 3–16. https://doi.org/10.3390/ ma14051073.

[31]   G. Oppong Boakye, A.M. Ormsdottir, B.G. Gunnarsson, A. Tabecki, F. Zhang, S.N. Karlsdottir, Development of High Velocity Oxygen Fuel Corrosion Resistant Coatings; A Comparison between Novel High Entropy Alloy and Conventional Cermet Coatings for Geothermal Applications, in: NACE Corros. 2018 Conf. Expo, 2022: pp. 1–11.

[32]   Y. Wang, B. Wang, S. He, L. Zhang, X. Xing, H. Li, M. Lu, Unraveling the effect of H2S on the corrosion behavior of high strength sulfur-resistant steel in CO2/H2S/Cl− environments at ultra high temperature and high pressure, J. Nat. Gas Sci. Eng. 100 (2022) 104477. https://doi.org/10.1016/J.JNGSE.2022.104477.

[33]   M. Tjelta, B.C. Krogh, S. Sæther, M. Seiersten, Corrosion, scaling and material selection in deep geothermal wells - Application to IDDP-2, in: NACE - Int. Corros. Conf. Ser., 2019. https://ife.brage.unit.no/ife-xmlui/handle/11250/2608746 (accessed May 1, 2022).

[34]   R. López-Rendón, J. Alejandre, Molecular Dynamics Simulations of the Solubility of H2S and CO2 in Water, J. Mex. Chem. Soc. 52 (2008) 88–92.

[35]   P.G. Debenedetti, Clustering in dilute, binary supercritical mixtures: A fluctuation analysis, Chem. Eng. Sci. 42 (1987) 2203–2212. https://doi.org/10.1016/0009-2509(87)85042-X.

[36]   M.R. Thakare, J.A. Wharton, R.J.K. Wood, C. Menger, Exposure effects of strong alkaline conditions on the microscale abrasion-corrosion of D-gun sprayed WC-10Co-4Cr coating, Tribol. Int. 41 (2008) 629–639. https://doi.org/10.1016/j.triboint.2007.07.012.

[37]   J.E. Cho, S.Y. Hwang, K.Y. Kim, Corrosion behavior of thermal sprayed WC cermet coatings having various metallic binders in strong acidic environment, Surf. Coatings Technol. 200 (2006) 2653–2662. https://doi.org/10.1016/j.surfcoat.2004.10.142.

[38]   J.Z. Albertsen, Ø. Grong, J.C. Walmsley, R.H. Mathiesen, W. Van Beek, A Model for High-Temperature Pitting Corrosion in Nickel-Based Alloys Involving Internal Precipitation of Carbides, Oxides, and Graphite, Metall. Mater. Trans. A. 39 (2008) 1258–1276. https://doi.org/10.1007/s11661-008-9494-5.

[39]   H. Zhang, S. Wang, H. Li, S. Wang, Y. Chen, Effect of Oxidation and Crystallization on Pitting Initiation Behavior of Fe-based Amorphous Coatings, Coatings. 12 (2022) 176. https://doi.org/10.3390/coatings12020176.

[40]   A.D. Smigelskas, E.O. Kirkendall, Zinc Diffusion in Alpha Brass, Trans. AIME. 171 (1947) 130–142.

[41]   M.R. Sievers, P.B. Armentrout, Reactions of CO and CO2 with Gas-Phase Mo+, MoO+, and MoO2+, J. Phys. Chem. A. 102 (1998) 10754–10762. https://doi.org/10.1021/jp983694v.

Journal Paper 4

G. Oppong Boakye, E.O. Straume, D. Kovalov, S.N. Karlsdottir,

Wear-reducing nickel-phosphorus and graphene oxide-based composite coatings: Microstructure and corrosion behavior in high temperature geothermal environment.

Wear-reducing nickel-phosphorus and graphene oxide-based composite coatings: Microstructure and corrosion behavior in high temperature geothermal environment

Gifty Oppong Boakye, Erlend Oddvin Straume, Danyil Kovalov, Sigrun Nanna Karlsdottir [*]

University of Iceland, Faculty of Industrial Eng., Mechanical Eng., and Computer Science, Hjardarhagi 2-6, Reykjavík, Iceland

ARTICLE INFO

ABSTRACT

Polymer coating modified with graphene oxide (GO) and duplex electroless Nickel-Phosphorus (Ni-P) with polytetrafluoroethylene (PTFE) coating were investigated for their corrosion behavior in simulated high-temperature geothermal environments with/without H_2S and CO_2 gases for geothermal applications. The polymer coating with added GO nanosheets demonstrated low wetting ability and suppressed corrosion effects of the substrate at 120 °C. The Ni-P/PTFE duplex coating with the lowest P content was suitable in an H_2O liquid environment at 120 °C while high P was more promising in the two-phase CO_2/H_2S environment. Nevertheless, all the coatings were unprotective and allowed substrate corrosion at 250 °C in the H_2S/CO_2 environment.

1. Introduction

Exploiting geothermal fields and abandoned gas wells are becoming more necessary due to the increased demand for sustainable energy. Friction, abrasion, and corrosion of metal components are issues that affect production and drilling in geothermal formations. Wear resistant materials are desirable during geothermal well drilling because the bottom hole assembly (drill pipes, drill collars, stabilizers, hammer/drill bits) is constantly exposed to and in contact with hard rocks and cuttings transported to the surface. The geothermal well environment commonly has a neutral to alkaline pH (pH 7–10) geothermal fluid but with corrosive H_2S, and/or CO_2 gases [1,2]. Therefore, surface changes from wear and tear, even in highly alloyed materials are likely to cause premature failure owing to accelerated and localized effects of corrosion, erosion, and fouling in the high temperature gaseous environment [1–4]. According to a retrospective study, electroless Ni-P and air/airless sprayed high-performance polymer materials have been employed in the oil and gas industries due to their excellent friction, abrasion, corrosion, and non-wetting properties [5]. Aside from enabling long-term exposure due to higher corrosion resistance, the benefit of such deposition processes in real-world applications is the uniformity and micrometer deposit tolerances for intricate geometries obtained with these techniques [5,6].

Zeng [4] reported the presence of acid fluid in high temperature water-drawn wells resulting in CO_2/H_2S corrosion of steel tubing in an oilfield. The authors stated that pitting and corrosion cracking on the failed tubing occurred at 5086 m owing to high-density fluid or gas-bearing fluid in the bottom. In a liquid-dominated high temperature geothermal well, containing HCl, CO_2, and H_2S, rapid corrosion and hydrogen embrittlement of a downhole steel casing liner occurred at 1600 m during discharge which demonstrates the corrosive conditions that can be met during well drilling and production [7]. Furthermore, due to the presence of abrasive solid particles/scales and highly corrosive gases in most geothermal fluids, corrosion and erosion resistance are required for both downhole and midstream equipment [8,9]. Thus, wear and corrosion resistant coatings on surfaces of inexpensive steel have the potential of achieving a compromise between corrosion prevention and high associated material costs for applications in geothermal well drilling, completion, production, distribution, and powerplant equipment.

Sugama et al. reported fair corrosion performance of high-performance Polyphenylene sulfide (PPS) as a heat exchanger (HX) liner material and on a wellhead component [10–12] exposed to geothermal hot brine at 200 °C and 250 °C [12]. This is because organic coatings are more or less permeable to corrosive agents. When intercalated within MMT (montmorillonite) nanocomposites it led to exfoliation, however, PPS/14 wt% MMT coating applied on primed carbon steel and tested at 300 °C in simulated brine showed maximum

protection of the substrate and no change in coating morphology [13]. Polytetrafluoroethylene (PTFE) has high self-lubricity and is widely used as a lubricant additive in organic coatings [14]. In the HX unit, PTFE added to PPS coating reduced the hydrothermal oxidation reducing scaling with an 80% cost benefit over titanium and steel tubes [10,15]. Furthermore, Nemati et al. [16] discovered the synergistic impacts of graphene nanoplatelets and polytetrafluoroethylene can significantly increase the tribological properties of composite coatings. Graphene oxide (GO), a carbon allotrope, has sparked widespread interest because of its outstanding properties, which include a large specific surface area, exceptional mechanical strength, low chemical reactivity, and high thermal conductivity [17]. Attempts have been carried out to improve the corrosion protection properties using graphene or GO nanosheets. Although graphene films were effective at blocking corrosive particles and were not easily damaged by corrosive media, the metal corroded significantly around wrinkles, cracks, and flaws in the graphene films [17,18].

Meanwhile, the microstructure, mechanical, and corrosion properties of monolayered versus multilayered electroless Ni/low P coatings revealed well-defined interfaces in the multilayered coating, which improved corrosion resistance in NaCl-containing solution by preventing crack propagation and corrosion advancement [19,20]. The P content (i.e., either low or high P) in the electroless Ni plating (ENP) process, eliminating the possibility of combining different P content in the same structure, and the inclusion of nanofillers influenced the properties of the Ni-P layers [19]. Another study by Li et al. demonstrated the time-dependent corrosion behavior of Ni-P coatings in saturated H_2S/Cl^- reporting that Ni-P corroded relatively mildly but under long exposure, the corrosive medium penetrated the coating/substrate interface from inherent defects. Despite the progress in this field, little attention has been paid to the synergistic effects of $Cl^-/CO_2/H_2S$ in hot environments that can be encountered in the geothermal well environment. After 18 months of immersion in CO_2-H_2S, a case study of a slotted liner coated with Ni-P revealed uniform corrosion of the coating but near-substrate local damage from sulfide ions at the coating/substrate [21]. Furthermore, Sun [21] and Sui [22] demonstrated that corrosive ions reached the substrate during Ni-P corrosion in $Cl^-/CO_2/H_2S$ environment. Other works that have been done include electrodeposition of Ni-P and PTFE nanocomposite coatings [23] which report good corrosion and wear resistance [24,25]. These newly developed Ni-P/PTFE coatings were reported to have better corrosion properties than Ni-P in 3.5 wt% NaCl [24]. In these studies, the performance was associated with crystalline or amorphous nature and hard Ni_3P phase precipitation in the matrix was established with annealing. The potential drawback of utilizing Ni-P coatings in geothermal conditions is the possibility of localized corrosion effects at the coating/substrate interface. Therefore, it is expected that adding PTFE to Ni-P layers in high P multilayered coating, after annealing should improve both wear resistance and corrosion in $Cl^-/CO_2/H_2S$ environment. Furthermore, considering the damages demonstrated by Sun et al. [21], attempting to develop and tailor the properties of the coatings can provide anti-corrosion solutions for Ni-P coating. Due to the synergy between geothermal and oil and gas (O&G) well drilling and construction, coatings developed for geothermal applications could also potentially be used for wider applications.

This study expands on previous work on wear-resistant PPS/PTFE-GO [26] and duplex NiP/PTFE [27] coatings from dry sliding contact as tribological studies for geothermal conditions are rarely published. This involves modifying the coatings to develop a top surface functional layer to improve wetting, corrosion, and wear resistance. For the ENP process, additionally, a high P undercoat is deposited forming a duplex to improve adhesion. The coatings that exhibited good friction and wear resistance were selected for testing the corrosion resistance at elevated temperature in an autoclave corrosion test for investigating the potential application in geothermal environments. The autoclave setup in this work replicates two different geothermal application environments: a)

geothermal drilling conditions by simulating water-based drilling fluid at 120 °C and b) two-phase geothermal fluid with CO_2/H_2S gases at 250 °C. The study provides useful insight to determine the coatings' suitability for applications on components for geothermal energy production that need to have a good surface finish, complex geometry, and tight tolerance.

2. Experimental procedures

2.1. Fluid composition and test conditions

Drilling fluids or muds perform a variety of functions, including cooling/lubricating the bit and, perhaps most importantly, maintaining wellbore stability. In Iceland, the drilling fluid is usually tap water due to its high pH which satisfies the requirement of the use of alkaline fluids that prevents corrosion while drilling [28]. The water has a pH of 9 at room temperature because it flows through basaltic rocks, which are rather basic with contents of SiO_2, MgO, and CaO [29]. The corrosion experiments were conducted under two different simulated environments at (i) 120 °C in tap water and (ii) 250 °C with corrosive gases, as shown in Table 1.

The liquid and vapor phase compositions at experimental pressure and temperature for condition 250 °C with corrosive gases were calculated in Phreeqc using the Peng-Robinson chemical model and are shown in Table 2. Table 1 shows the results of an extra set of modeling to identify the changes in pH with temperature over each test duration.

2.2. Experimental setup for autoclave–corrosion testing

The test coupon's shape was designed to be mounted onto the sample holder with 6 mm diameter PTFE insulators to avoid galvanic effects in corrosion testing. The test samples were installed between the vertical sample holder supports illustrated in Fig. 1(a) and the custom-made sample holder was also installed in the lid. The autoclave was filled with electrolytes and purged with N_2, H_2S, and CO_2 through the gas inlet lines from the bottom (Fig. 1b) to maintain the temperature and gas conditions. The gas components are fed through the gas filling panel, with Brooks mass flow controls controlling the filling rate. A detailed analysis of the autoclave setup and procedure has been previously reported [31]. The top row (A) of the sample holder was anticipated to be in the vapor phase during the autoclave test, above the waterline, and the bottom row (C) was in the liquid phase and completely submerged in water. In the simulated liquid and vapor phase test conditions, a preliminary 7-day HTHP corrosion test was successfully carried out at

Table 1
Physiochemical parameters and solution chemistry for autoclave corrosion experiments.

Test parameters	Drilling condition in HT well (14 days test)		Gas conditions in two-phase geothermal fluid at HT (7 days test)	
	tap water		DI water with 10 mmol NaOH and 5 mmol NaCl	
Pressure	50 barg		50 barg	
Temp	25 °C	120 °C	25 °C	250 °C
Gas	PP* (atm)	PP (atm)	PP* (atm)	PP (atm)
CO_2	–	–	4.5	3.8
H_2S	–	–	1	0.2
H_2O	–	–	–	41.6
N_2	ca. 35	ca. 50	5	7
Solution	2 kg	2 kg	1.5 kg	1.5 kg
CO_2	–	–	2199 ppm	1698 ppm
H_2S	–	–	417 ppm	514 ppm
pH	8.9	7.2 *	5.7	6.8 *

*- Partial pressure of gas component before it reacted with the solution and predicted pH values.

Table 2

Chemical components dissolved in the water-based and vapor phase at 250 °C and 50 bar.

	H_2O	CO_2	H_2S	N_2	HS^-	Na^+	Cl^-	HCO_3^{-}
liquid phase (mg/kg)	–	1981	472	292	99	350	181	393
vapor phase (mol%)	79.8	8.5	0.3	11.4	–	–	–	–

250 °C and 50 bar to establish positions A, B, and C (in Fig. 1a) for each sample. Four parallel samples and two sets of test procedures were created to simulate geothermal drilling and aggressive conditions. The coatings were exposed for 14 days at 120 °C in tap water pressured to 50 bar with N_2, simulating standard geothermal well drilling conditions. The second experiment subjected coatings to HTHP corrosion testing for 7 days in a simulated geothermal fluid at 250 °C in liquid/vapor phase conditions compressed to 50 bar with corrosive gases N_2 and CO_2/H_2S. After each experiment, the autoclave is depressurized, and residual H_2S gas is trapped in zinc acetate and NaOH solution to form solid ZnS (Fig. 1c).

2.3. Materials

The design of the experiment involved an autoclave corrosion test for the developed coatings with the best performance from a sliding wear test performed to select the most wear resistant coatings (Table 3). The coatings received were deposited on a through-hardened, 34CrMoNi6 (817M40) low alloy steel. Two coating systems were chosen; air sprayed PPS/PTFE polymer modified Graphene Oxide (GO) coating (PPS-PTFE/GO), and two types of Electroless Nickel-Phosphorus plated PTFE added duplex coatings (ENP/PTFE).

The modified polymer coating is composed of 0.5 wt% GO added to the PPS-PTFE blend. The ENP/PTFE duplex is comprised of a top functional layer (Ni-P/PTFE) plated on a Ni-P adhesion underlayer. The functional top layer is composed of a homogeneous distribution of PTFE in (i) Ni –low P matrix (hp/LPptfe duplex) and (ii) Ni –high P matrix (hp/HPptfe duplex), where the adhesion underlayer is referred to as hp. The chemistry of the bath was designed to improve both corrosion and wear resistance. The preparation chemistry and chemical composition of the four materials selected for the corrosion tests in this study is

presented in Tables 3 and 4. The ENP/PTFE duplex coatings were further heat-treated at 300 °C for 2 h since such post-treatment was reported to increase lubricity and sliding wear resistance of the coatings [27].

2.4. Characterization of coatings

Different characterization methods were employed in determining the structural, physical, and chemical features of the coatings. X-ray diffraction (XRD) was carried out in an X-Pert Pro Empyrean from PANalytical® with CuKα radiation ($\lambda = 1.5406$ Å). The data was collected after sample alignment at 45 kV, 40 mA in the 2θ range of 10–90 degrees depending on the coating type and analyzed with High-Score software. Raman spectroscopy, which is very sensitive to

Table 3

A nomenclature from the preparation chemistry of the composite coatings tested in the autoclave.

Coating	Undercoat	Topcoat		Test ID
polymer	N/A	PPS-PTFE blend		PPS-PTFE
	N/A	PPS-PTFE blend /	0.5 g/L GO	PPS-PTFE/GO
ENP/PTFE	10–13 wt% P	3–5 wt% P /	10 g/L PTFE	hp/LPptfe
	10–13 wt% P	10–13 wt% P /	10 g/L PTFE	hp/HPptfe

*The hp (high P) represents the Ni-P undercoat. LP (low P) and HP (high P) represent Ni-P in the topcoat.

Table 4

Chemical composition of the surfaces of the different composite coatings tested in the autoclave.

Material	Test ID	Nominal composition (wt%)						
		F	C	Si	S	P	Ni	O
unmodified/ modified polymer	PPS-PTFE	11.1	57.0	5.3	17.2	–	–	9.4
	PPS-PTFE/GO	12.4	57.4	2.9	20.3	–	–	6.2
ENP/PTFE	hp/LPptfe	3.4	7.6	–	–	2.9	86.1	–
	hp/HPptfe	6.9	10.5	–	–	10.3	72.4	–
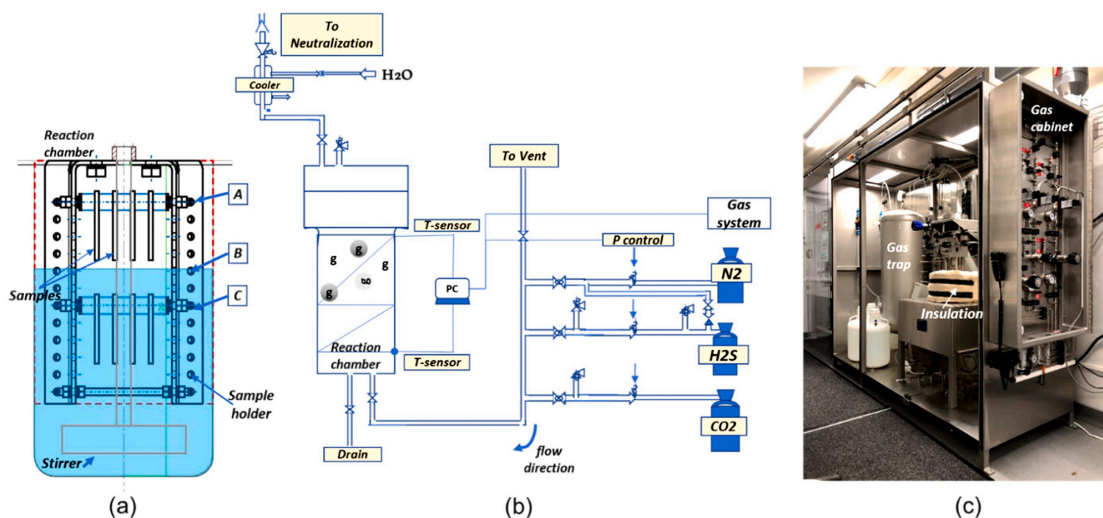
Fig. 1. The experimental design for the HTHP corrosion testing. (a) cross-section of the reaction chamber showing the sample holder with sample positions for A - vapor phase, B - interface, and C - liquid phase (a) flow diagram and (c) the autoclave reactor and H_2S and CO_2 gas system.

symmetric covalent bonds with little or no natural dipole moment, proved a good fit for the structural investigation of GO. A 785 nm line of Ar-ion laser with 5 mW of power and a spot size around 1 μm at the focal point was used to record 5 spectra accumulations on a Horiba Scientific® LabRAM HR Evolution - Raman Spectrometer. Microstructural analysis was conducted with field emission scanning electron microscopy (FE-SEM, Zeiss Supra 25®). The SEM equipment was also used to investigate the thickness of the coatings. Using a Taylor Hobson Ametek stylus profilometer, 10 measurements were taken to determine average surface roughness parameters (Ra). The static contact angles were measured in the DataPhysiscs OCA instrument with a 2 μL drop of water at 20 different locations to evaluate the water contact angle (WCA) of the coatings with PTFE. The microhardness of the coatings was determined using the Vickers method for the polymer coatings and the Knoop method considering the small thickness of the coatings. Indentation test forces of approximately 50 gf were performed in the cross-section of the coatings recording the hardness values. The friction and wear resistance of the developed coatings were assessed using the parameters from Table 5. All coating properties are reported in average values with standard deviations. The SEM was equipped with an energy dispersive X-ray spectrometer (EDS) used for the elemental and compositional analysis of the coatings.

3. Results

3.1. Microstructural characterization and wear properties

Fig. 2(a)–(c) show SEM micrographs of the microstructures of the GO, unmodified polymer, and GO modified polymer coatings. The coating was sprayed on ST37 carbon steel, which is a material commonly used in the construction of geothermal systems. This is why carbon steel was chosen as the substrate, as well as for easy corrosion assessment of the nonconductive PPS-PTFE coating from solution permeability as demonstrated in earlier corrosion studies [26], i.e. the possible localized corrosion damage to the substrate. Similar morphology was seen in the unmodified and modified polymer coatings but with the addition of 0.5 wt% GO, the surfaces appeared more compact. The structures were engulfed in a porous-S rich matrix (inherent to the PPS) with small particles rich in silicon (Si) and oxygen (O) in both coatings as shown in Fig. 2(b)–(d). The flake-like and sheet-like structures were found in the micrographs which are attributed to the semi-crystalline PTFE and GO respectively. Fluorine (F) and O were used as identifiers to estimate the presence and composition of the PTFE (CF_4) and GO nanoparticles. In the higher magnification images, the GO was identified as thin sheets bridging and wrapped around structures (Fig. 2(c), (d)) in the polymer matrix due to their high surface area to volume ratio.

Fig. 3(a)–(c) show the surface morphology and the microstructure of the as-received ENP/PTFE duplex coatings. The coatings were observed with globular particles which are similar to the conventional morphology reported for ENP coatings. Compared to the as-plated state of the coatings, the globules diminished in size and had a finer structure after heat treatment shown in Fig. 3(a) and (c). Nanopores (smaller than 100 μm) were observed on the surfaces of the hp/LPptfe (Fig. 3(c)). The pores were introduced during PTFE incorporation and the hydrogen gas evolution and escape during the plating processes. However, the cross-section appeared dense with no obvious porosity. An indication of a good mechanical bond was also observed between the hp undercoat/substrate and the hp undercoat/HPptfe enhanced top layer. There are no

obvious cracks and pores in the Ni-P adhesion interface. The thickness of the duplexes was approximately 11 ± 0.75 and 20 ± 0.89 μm (Table 6). The undercoat (Ni-P adhesion layer (hp)) had an average thickness of 5–7 μm. From the EDS chemical compositional analysis, it can be seen that the coatings are predominantly Ni and in the coatings with the composition of high phosphorus as both undercoat (hp) and topcoat (HP), high weight fractions of phosphorus are observed in Table 3. However, the PTFE concentration decreases as indicated with the wt% of F in Table 3. The PTFE particles appear as dark spots in the top layer of the cross-sectional SEM image seen in Fig. 3(b) and from the EDS line graph in Fig. 3(d). The EDS line graph of hp/LPptfe in Fig. 3(d), distinctively shows the change in chemical composition from the top functional layer and the hp undercoat to the steel substrate.

The PTFE particle was confirmed in XRD patterns given in Fig. 4(a)–(c). To understand the physical and chemical interaction occurring in the coating layers, an XRD analysis was performed to identify microstructural changes. The results from the XRD patterns of ENP coatings were consistent with the SEM and EDS analyses, where the peaks represented the same elements as detected. The XRD patterns of the PPS-PTFE/GO and ENP/PTFE duplexes are reported compared to the as-plated conditions of the coatings. As can be observed in the XRD patterns, the results are consistent with the EDS analysis of the composite coatings. The diffraction peak of PTFE was diffracted at 18° in all cases. The highest intensity peaks in the duplex coatings were consistent with Ni (111) FCC phase at 44.5°, while the lowest peaks were consistent with BCC Ni. According to the XRD examination, as-plated hp/LPptfe was crystalline, but as-plated hp/HPptfe was amorphous (Fig. 4(a), (b)). Additional Ni_3P phases were found in hp/HPptfe and showed nanocrystalline to some extent after subsequent heat treatment of both duplex coatings for 2 h at 300 °C. The high hardness of this coating is attributed to the amorphous Ni-P matrix and crystalline Ni_3P phase that developed from the annealing of the high P content coating [16]. In summary, the microstructure of the hp/LPptfe is crystalline, whereas that of the hp/HPptfe and PPS-PTFE/GO tend to have a mixed crystalline-amorphous structure. The PPS peak at $2\theta = 20.6°$ (Fig. 4c) is dominant in the PPS-PTFE polymer coating. The PPS and PTFE peaks appeared broader but transitioned to a more crystalline state with the addition of GO nanosheets. In the XRD pattern, a distinct diffraction peaks of GO nanofiller were not seen, although expected at $2\theta = 10.5°$ as reported in the literature. This may be due to the low detection limit for the small concentration of the added GO. However, the peaks intercalated between $2\theta = 10–20°$ of the PPS-PTFE/GO composite demonstrate the contribution of GO to structural alteration which influences the coating properties. From XRD results, the presence of SiO_2 particles was observed in both modified and unmodified investigated polymer coatings. Raman spectroscopy was used to further analyze the polymer coatings to ascertain the presence of the GO nanosheets due to the sensitivity of this technique to carbon-based materials. The coatings showed two quintessential peaks: D (disordered) and G (graphite) in the region of 1310 cm^{-1} and 1582 cm^{-1} respectively (Fig. 4(d)). Schwan et al. [30] assert that the G peak is not always composed of graphite, but also comprises sp2 C=C stretch vibrations (in PTFE), which is also true for all aromatic rings (in the PPS) that exhibit a peak at 1588 cm^{-1}. This could explain the position of the G peak in the neat PPS-PTFE (Fig. 4d) and the crystalline peak found around 26° (Fig. 4c) corresponding to structures aligned in the (002) or (004) planes. The main D peak of sp^3-carbon bonding in graphene oxide at 1310 cm^{-1} matched the spectra for PPS-PTFE/GO which showed higher intensity (I_D/I_G) confirming the structural defect associated with changing graphite to graphene oxide.

Table 5
Parameters used in wear testing of the PPS-PTFE/GO and ENP/PTFE-deposited coatings.

Temperature [°C]	Sliding time [min]	Counter Ball	Load [N]	Radius [mm]	Sliding speed [cm/s]	Sliding distance [m]	Number of cycles [-]
22.5	60	100Cr6	10	7	10.47	377	8572
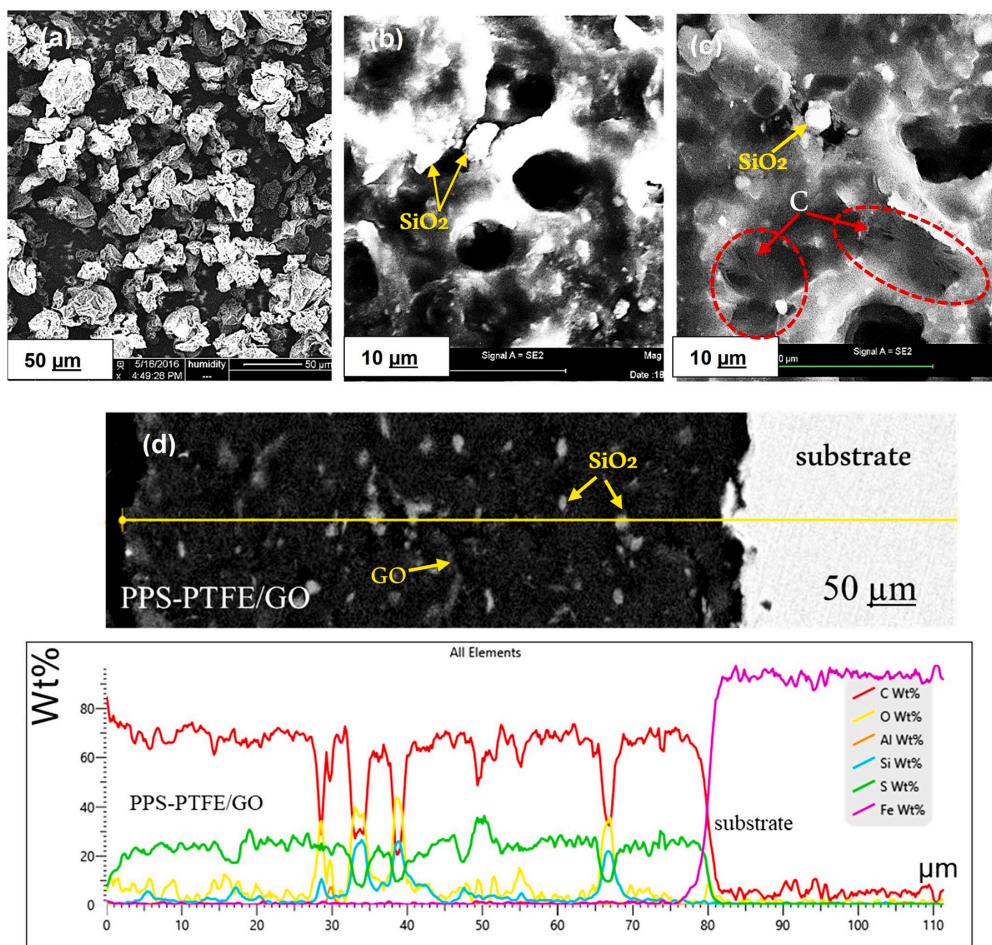
Fig. 2. SEM micrographs of (a) Graphene oxide (GO) (b) PPS-PTFE (c, d) PPS-PTFE/GO – before corrosion testing.

Moreover, the relative intensity for D and G bands was indistinct indicating covalent bonding between GO nanosheets and the PPS-PTFE without significant destruction of the carbon lattice even after oxidation by the hummer's method [31]. The neat PPS-PTFE material showed other bands having a broader distribution of vibrational energy. This is not due to the PPS crystal lamellae but most likely because of the presence of the amorphous phase. Also, the bands disappeared with added GO content compared to the polymer spectra.

Table 6 reports the results from the surface characterization and coating properties of both the air sprayed and electroless plated coatings. The added functional nanoparticles (PTFE, GO) increased the WCA (Water Contact Angle) of the steel substrate (80° ± 0.2) creating a hydrophobic surface. The PPS-PTFE/GO had the lowest hardness value compared to the ENP/PTFE duplex coatings since the coating is over 99 wt% soft polymers. In the ENP/PTFE duplexes, an increase in wt% P increased the amorphous phase content in hp/HPptfe and crystalline Ni_3P phase resulting in higher hardness and WCA values. The roughness was generally low 0.2–2 μm. For the PPS-PTFE/GO the Ra was slightly higher with the addition of GO nanoparticles since the coating became grainy. Additionally, higher angles were found for the as-plated coatings; the average WCA value and the corresponding standard deviation for hp/LPptfe and hp/HPptfe are 116.4° ± 2.9 and 108.1° ± 1.4. This indicates that the heat treatment tends to decrease the non-wetting

properties of the coatings when in contact with water. It can be concluded the results show the coatings demonstrate high hydrophobic properties with WCA above 90°. Thus, the microstructure and the morphology give hydrophobic behavior. The highest hardness was measured for the higher P-containing duplex (i.e., hp/HPptfe) which is consistent with our previous findings [16]. It was asserted that the internal structure was responsible for the hardness; the amorphous nature of the material exhibits atoms in a short-range ordered lattice, making bond dislocation during indentation difficult. In this case, after heat treatment, the Ni_3P crystalline phases additionally disable movement in neighboring atoms preventing the complete breaking of the bond structure.

The CoF (Coefficient of Friction) results correlated with the wear resistance, where the lowest values were measured for the coatings with graphene oxide (PPS-PTFE/GO) showing an 81% reduction compared to the substrate. In the duplex, ENP/PTFE, the low friction coefficient values were consistent with the wear rates after testing. Therefore, the application of the coatings to the steel substrate and further modification with nanoparticles and/or heat treatment improved the dry sliding properties of the coating. The abrasive wear mechanism was identified by grooving and cutting, and the prioritized coatings performed better than the low alloy steel substrate (i.e., wear rate $\sim 3.8 \times 10^{-5}$) indicated in Table 6, a 74%, 91%, and 97% improvement in wear resistance after
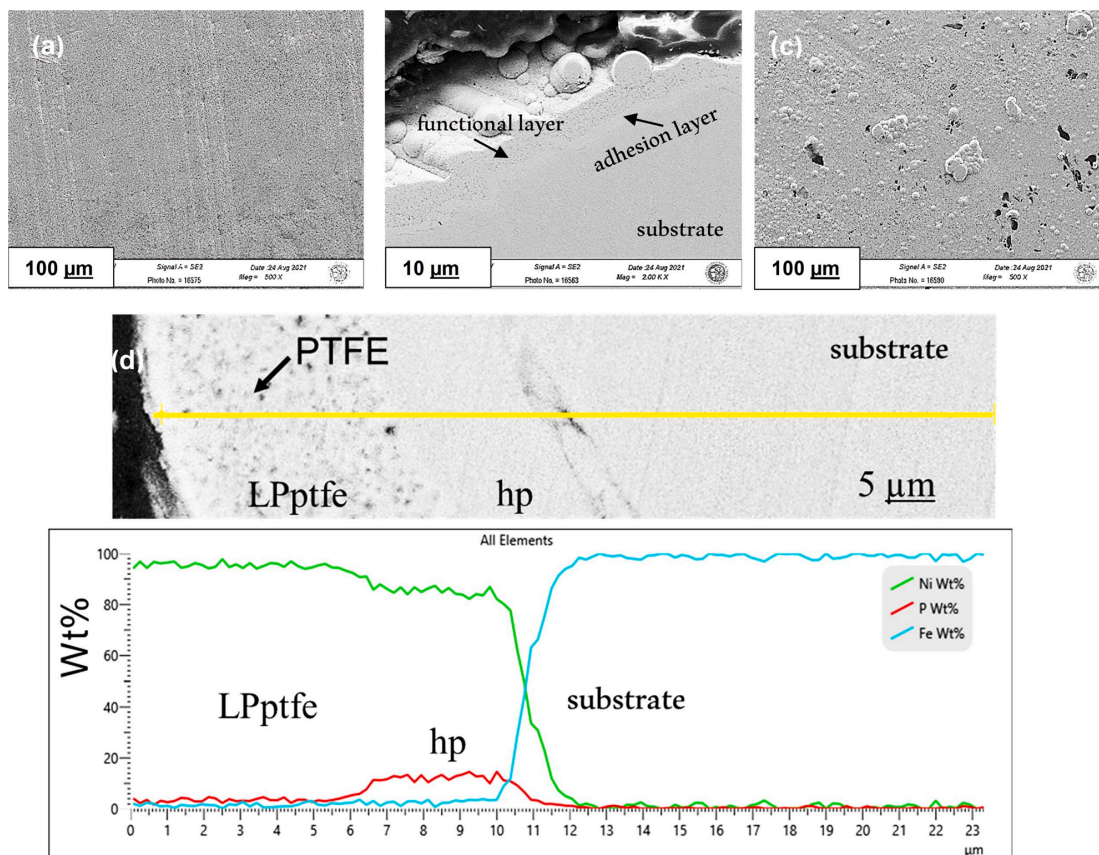
Fig. 3. SEM surface and cross-section micrographs of heat treated (a, b) hp/HPptfe, (c, d) hp/LPptfe – before corrosion testing.

Table 6
Average values of the coating properties of the different coatings tested in the autoclave.

Coatings	Thickness (μm)	Roughness (μm)	WCA (°)	Hardness HK/HV*	CoF (-)	Wear rate (mm³/Nm)
PPS-PTFE	20.1 ± 4.7	1.6 ± 0.1	123 ± 1.8	15.9 ± 1.5	0.18 ± 0.04	1.4×10^{-4}
PPS-PTFE/GO	46.5 ± 9.4	2.0 ± 0.02	122 ± 0.8	14.1 ± 0.9	0.15 ± 0.02	9.8×10^{-5}
hp/LPptfe	20.0 ± 0.9	0.5 ± 0.13	100 ± 9.1	393.8 ± 70.4	0.24 ± 0.05	1.2×10^{-5}
hp/HPptfe	10.9 ± 0.8	0.2 ± 0.03	103.4 ± 3.8	474.1 ± 87.8	0.66 ± 0.03	3.3×10^{-5}

* Hardness reported as $HK_{0.05}$ scale in the ENPs and $HV_{0.01}$ scale in the polymer coatings.

the plating process. The best performance was seen in heat-treated hp/HPptfe, hp/LPPptfe, and PPS-PTFE/GO reported in Table 6. After heat treatment of the hp/HPptfe, the resulting worn surface sliding against the 100Cr6 steel was drastically reduced which is attributed to the increased hardness of these coatings explained by the appearance of the hard Ni_3P phases and the improved adhesion of the films.

3.2. Corrosion test results in simulated drilling condition at 120 °C

Microstructural and chemical compositional analyses were performed using SEM/EDS equipment after 14 days of corrosion testing. Like the surface, cross-sectional SEM images of the PPS-PTFE/GO, tested in the aqueous environment at 120 °C, showed negligible corrosion as seen in Fig. 5(a), (b). In the PPS-PTFE/GO, no localized corrosion damages were observed at the coating/substrate interface as seen in Fig. 5(b). But small pores were detected on the surface, rich in Al and O

(Fig. 5(b) – area spectrum 3), likely a residue from the Al_2O_3 particles used in the surface preparation of the carbon steel substrate before the coating spray process. This indicates good protection for the substrate with these coatings tested in a 120 °C alkaline environment since a good adhesion of the coatings to the substrate was still observed after the test. On the contrary, the coating with no added GO (unmodified PPS-PTFE) observed a considerable amount of deposits rich in Ni, Fe, and O on the coatings surface identified in the EDS analysis as seen in area spectrum 1 in Fig. 5(c) after the 120 °C water test. The Ni-based rich product can possibly be explained by the reaction of the coating layers to traces of Ni available from the Hastelloy autoclave chamber (Fig. 5c). Fe-S deposit on the coating was from the reaction of the substrate through permeation of electrolyte through interconnected pores in the coatings. This is visible in the cross-section image in Fig. 5(d), where substrate oxidation of the steel (area spectrum 3) occurred, showing a remnant (~30 μm) of the chemically inert PPS-PTFE coating layer. At the interface, Fe-O-rich
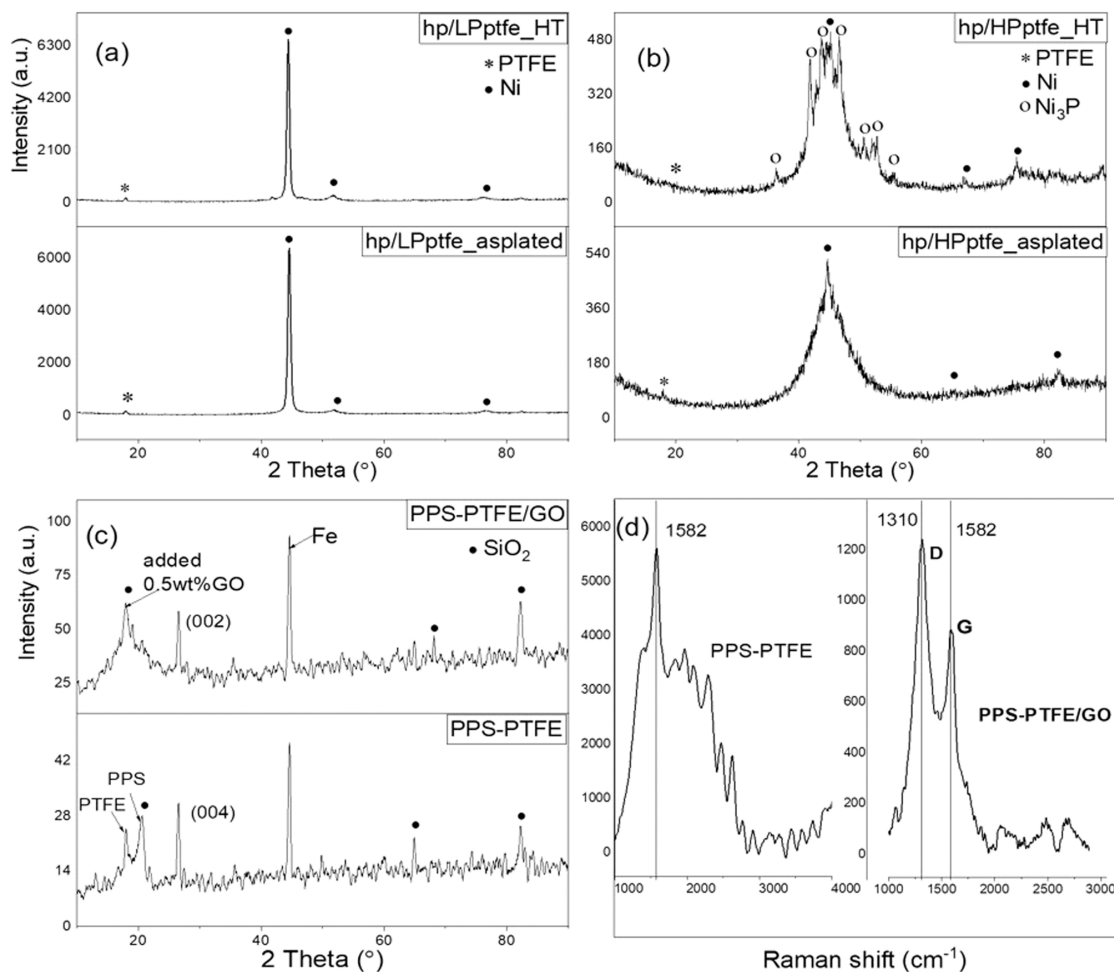
Fig. 4. XRD patterns of (a) hp/LPptfe, (b) hp/HPptfe (c) PPS-PTFE/GO, and (d) Raman analysis of PPS-PTFE and PPS-PTFE/GO.

products filled cavities in the substrate, likewise in the inner portions of the coating.

Negligible corrosion products were observed in all the tested coatings in the 120 °C tap water with no corrosive gases, but the ENP/PTFE coatings were prone to general corrosion. The surfaces of the duplexes were both uniformly covered with a glossy dark deposit and corrosion spots were identified by visual assessment. Porosities were identified in both the surface and cross-section SEM images, mainly in the top functional layer (see Fig. 6(a)–(d)). A thin Ni-O rich surface layer was present on both hp/LPptfe and hp/HPptfe coatings (Fig. 6(a), (c)) with damage under the corrosion film of hp/HPptfe (Fig. 6(b), (d)). This was attributed to the uniform dissolution of Ni in the functional topcoat. The PTFE seems to influence corrosion by blocking porosities from the morphology of the thin sheets in the topcoat (point A in Fig. 6b). When compared to hp/LPptfe, the Ni-O surface corrosion layer in hp/HPptfe (Fig. 6(c) in point B) had a 61%increase in O. Furthermore, in the cross-section of hp/HPptfe, there is clear delamination within the top functional layer (see Fig. 6d), but no apparent separation at the coating/substrate interface. At higher magnifications, the accumulation of pores created a visible corrosion path in the Ni-P matrix. The results indicate that the corrosion mechanism of the high phosphorus hp/HPptfe is associated with Ni dissolution forming Ni-O as indicated from the SEM/EDS map in Fig. 6(d).

3.3. Corrosion test results at high temperature; 250 °C with CO_2/H_2S gases

Figs. 7 and Fig. 8 show surface morphology and compare cross-sectional images of the GO modified and unmodified polymer coatings. The cross-section images show that the coating/substrate interface deteriorated with Fe-S products detected at the interface during the exposure period in all test conditions. On the other hand, the combined SEM/EDS results of the surface of the PPS-PTFE/GO coatings exposed to both liquid and vapor phases (Fig. 7(a)–(c)) showed little or no presence of corrosion products. From the SEM analysis of the PPS-PTFE/GO tested at 250 °C, changes in the surface morphology of the coating after testing (compared to 120 °C and non-tested sample in Fig. 7a) were visible with more blisters and pores but with no extensive changes in the surface chemistry indicating the effect of high temperature on the stability of the coating. The surfaces were found to be rather prone to pore formation and SiO_2 deposition (that readily falls off) suggesting a loss in hydrophobic properties during the vapor phase exposure (see Fig. 7a) [32]. This formation of micropores resulted from local blisters which were visible in both test conditions (Fig. 8(a) and (b)). At the higher magnification, Fe-S rich (25.7 wt%Fe - 54.6 wt%S) corrosion product was seen in the widest hole from the vapor phase corrosion (Fig. 8b) but that of the liquid phase test (Fig. 8a) was free of products. This suggests that

Area	Fe	O	C	S	Ni	Si	F	Al
1	5.8	10.1	46.4	50.4	0.7	1.0	15.5	
2	0.8	5.1	61.6	23.9	-	3.0	5.2	0.2
3	2.4	42.0	5.4	0.3	-	-	-	49.9

Area	Fe	O	C	S	Ni	Si	F
1	14.1	10.7	13.4	13.7	44.0	1.6	2.5
2	46.6	26.1	17.5	4.9	3.7	1.3	-
3	74.8	19.7	4.7	0.3	-	0.6	-
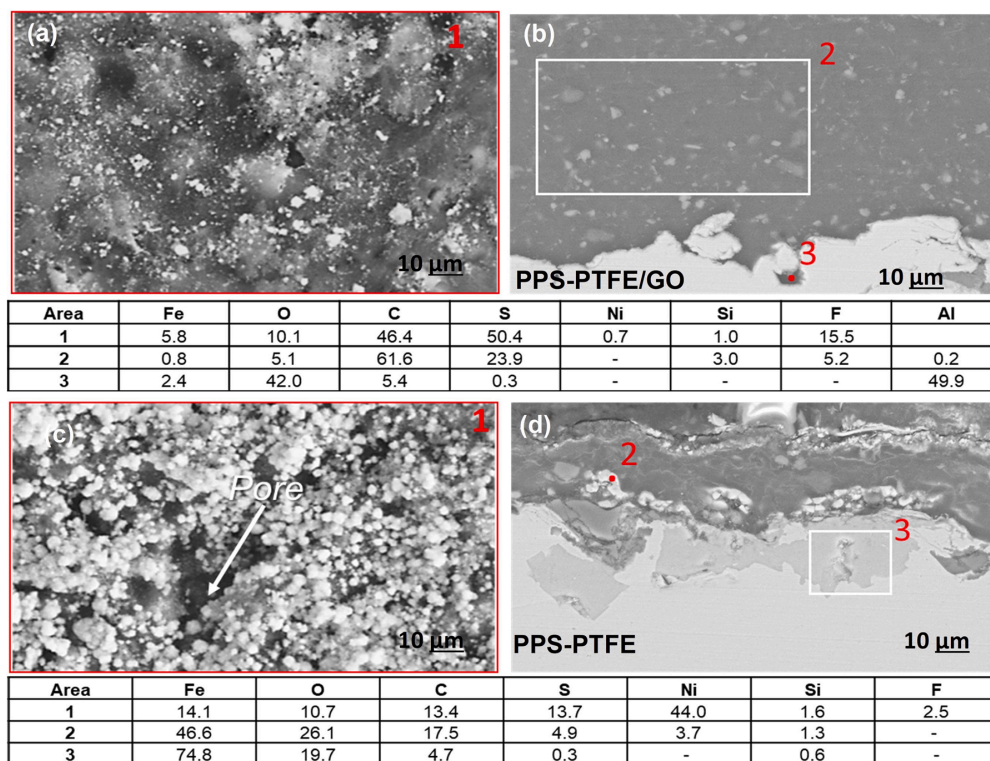
Fig. 5. SEM/EDS micrographs of (a, b) PPS-PTFE/GO and (c, b) unmodified PPS-PTFE – after 120 °C water corrosion test.

although there is a bridging effect from the added GO sheets and PTFE particles, there might be more porous regions within the coating for the GO added coating that promoted permeation of the electrolyte or gaseous species. Zhou reported the impermeable barrier role from GO nanosheets but observed few corrosion products at scratched spots in the composite [33].

Fluorine was found to be reactive in defected regions, such as near or in holes of the PPS/PTFE matrix. Corrosion products were found at the interface of the coating and the underlying substrate. SEM/EDS line analysis was used to examine the composition of the damages seen at the coating interface. The results show the formation of corrosion products at the coating/substrate interface in both the liquid and the vapor phase test. Fig. 8(c) shows a bright Fe, S rich product deposited on a dark dense Fe, O -rich layer at the coating/substrate interface. The thickness of the coatings did not change (~58 µm) since the substrate underwent a dissolution (anodic) process. Apart from morphological changes, no delamination was seen at the interface in the SEM analysis. In conclusion, the unmodified PPS-PTFE exhibits inferior corrosion inhibition according to the cross-section morphology, as seen by a more obvious deterioration of the substrate (see Fig. 7(c)). The coatings appear to be degraded by vapor phase exposure (Fig. 8a) due to inherent micro-defects and the impacts of the close upper limit of 250 °C where the thin liquid layer presumed present in the saturated steam phase reacted with the added gases CO_2/H_2S.

The SEM assessment showed serious corrosion damage on the surface of the ENP/PTFE duplexes coatings presented in Fig. 9 after testing in an H_2S and CO_2 environment at 250 °C. The SEM images revealed a surface scale (A) formation as well as different granular (B, C, I), particulate (E), flaked (F, G), and needle-like (H), corrosion products (Fig. 9(a)–(e)). EDS point analysis was used to determine the chemistry of corrosion products A to G, and a map analysis was used for H. EDS analysis showed

no Fe was found in the investigated dense nickel and sulfur-rich scale in areas 1 and point A (see Fig. 9(a), (d), (e)). However, from continuous corrosion, the thickness of the scale reduced drastically, or completely delaminated in other regions. The delaminated regions provided information on the corrosion mechanism under the surface scales. The morphology of the remnant loose scale is granular with varying concentrations of the major elements: C, Ni, S, and Fe. The particulate and needle-like products indicated the inclusion of O. The needle-like oxides formed on the coating surface after testing in the vapor phase (Fig. 9(a), (c)). The delaminated flakes (point F) were Fe-S-Ni rich. EDS analysis of hp/LPptfe surfaces (points B, C in Fig. 9b), showed mixed corrosion products with all elements in the coating including Fe, O, and mainly S in such delaminated regions. The SEM results show the coatings form blisters on the surface and underneath such blisters localized corrosion occurred leading to cracking and final flakes-off of the coating from the surface forming craters from the delamination process. The under-deposit corrosion likely builds up stresses causing the Ni-S corrosion layer to be non-adherent. As such, the stresses cause the Ni-S rich layer to blister with the subsequent cracking, flaking, and delamination (Fig. 9 (a), and point D in Fig. 10(d)). Blisters were found in defected areas, corners, and next to the M6 hole on the corrosion coupon where there was limited coverage during the electroless plating process.

Additional elemental mapping after the vapor phase test seen in Fig. 9(a) is reported in Fig. 9(e). The resulting map shows the difference in composition, where spectra 2 and 3 revealed high wt% F similar to point G (i.e., 35–50%), indicating clustering of PTFE nanoparticles after the dissolution of the Ni metal in the Ni-P matrix. From the EDS mapping of the delaminated region, a mixture of oxide of phosphorus and sulfide of nickel is seen from SEM/EDS. It can be stated that the nickel sulfide layer is present as an outer scale on the functional LPptfe topcoat and corrosion of the functional layer results in a porous mixed oxide-sulfide
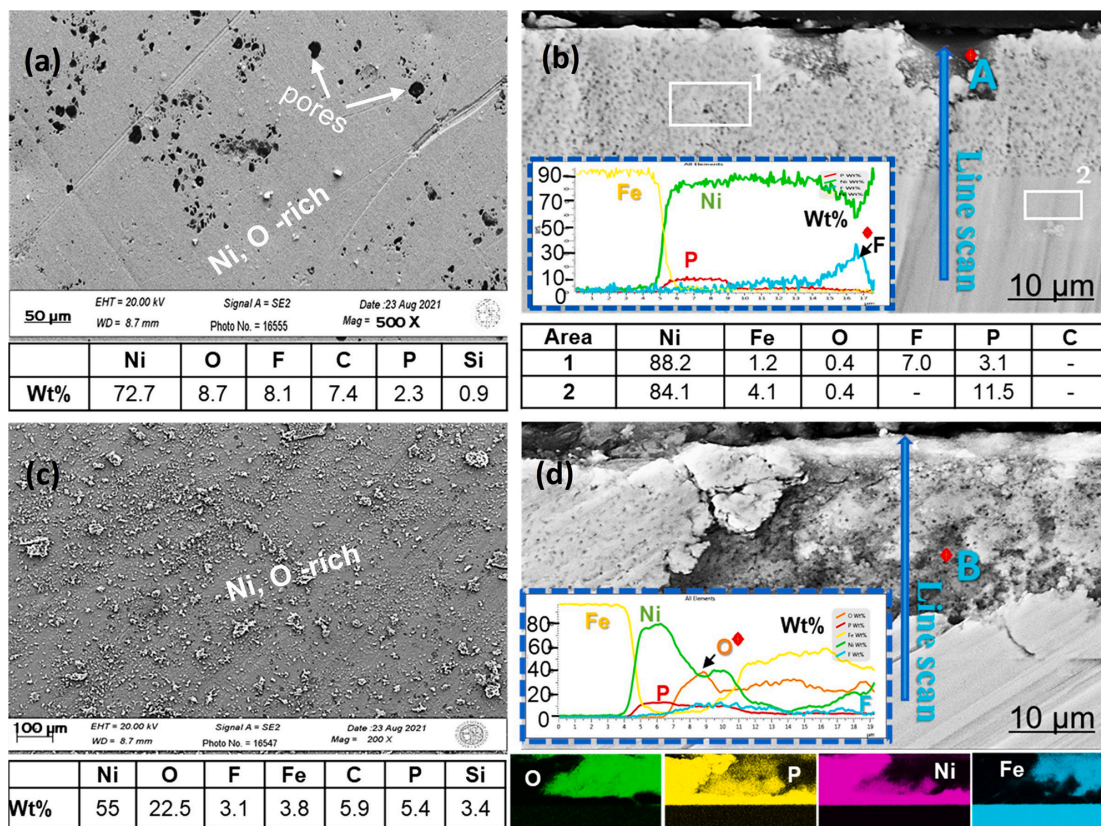
Fig. 6. SEM/EDS surface and cross-section images of (a, b) hp/LPptfe and (c, d) hp/HPptfe duplex coatings – after 120 °C water corrosion test.

product. Whereas from Fig. 9(c) and points A and D, in Fig. 9(d), the Ni-S rich scale seems to replenish but with increased Fe contamination in the outer scale of hp/HPptfe.

3.4. Evaluation of corrosion protection mechanism

The design of the experiment in the autoclave test simulates geothermal waters of relatively high temperatures (120 °C and 250 °C) with/ without CO_2 and H_2S corrosive gases. Fig. 10(a)–(f) compare the cross-section images of the corroded ENP/PTFE duplex coatings after 120 °C and 250 °C tests in the autoclave. The chemical analysis of the external surfaces revealed a Ni reactivity of the coatings with oxygen and sulfur-based aggressive species in the specified environments (Figs. 6 and 9). As a result, after 120 °C and 250 °C corrosion testing, the corrosion layer discovered was Ni-O and Ni-S rich layer, respectively. After 120 °C, no cracks or delamination were seen at the coating/substrate interface in the cross-section. However, porosities in the functional top layer allowed oxidizing corrosive species to permeate and deteriorate the coating top layer, as seen in Fig. 10(a) and (c). The results show the existence of the sulfide film on both hp/HPptfe and the hp/LPptfe samples after the 250 °C CO_2/H_2S corrosion test. Consistent with the results from surface SEM/EDS analyses of hp/LPptfe (Fig. 9(a), (b)), a mixed inner sulfide and oxide layer forms preferentially underneath the outer sulfide corrosion scale whereas a Fe-O rich layer forms at the coating/substrate interface in the cross section after 250 °C corrosion test with CO_2/H_2S (see Fig. 10(b), (c)). The hp/LPptfe duplex coatings were completely delaminated due to significant cracking with the coating layers after exposure to the CO_2/H_2S environment.

The cross-section images in Fig. 10(e)–(f) show a more stable, dense, and adherent sulfide layer forming on the hp/HPptfe in both the liquid and the vapor phase conditions and observed to be protective to some extent. This corrosion layer that adheres to the functional topcoat-HPptfe layer is thicker compared to the liquid phase corrosion. Fig. 10 (e) shows cracks parallel to the substrate in the NiP adhesion layer close to the substrate whereas the top layer was mainly porous, but when exposed to the vapor phase (Fig. 10f) the cracks grow continuously to the NiP+PTFE functional layer. This type of crack is most likely caused by mechanical stresses caused by the growth of corrosion products at the interface. The thin Fe-oxide layer was also present at the coating/substrate interface in both the liquid and vapor phase test (Fig. 10(e), (f)). This suggests the corrosion direction occurred via migration of species from the top functional layer to the substrate which is created from the growth of crack paths traveling through the coating/substrate interface to the top layer of the duplex. However, in the aqueous/liquid phase of corrosion the interconnected pores influence the ingress of corrosion species through the functional layer (i.e., NiP+PTFE) into the coating (Fig. 10(a), (b), (d), (e)). These pores are present in the original coating due to PTFE agglomeration inciting vacancies and the evolution and entrapment of hydrogen gas (H_2) during the plating process.

The cracks presented a travel path for the sulfidizing and oxidizing corrosion species to the Ni-P adhesion layer and from the coating/substrate interface to the functional top layer in both ENP/PTFE duplexes. Further EDS elemental line analysis was carried out in the cross section of the samples from the liquid phase test (Fig. 11) to elucidate the contribution of the elements to corrosion in the duplex coating. The SEM images in Fig. 11(a) and (b) confirm the formation of the outer Ni-S
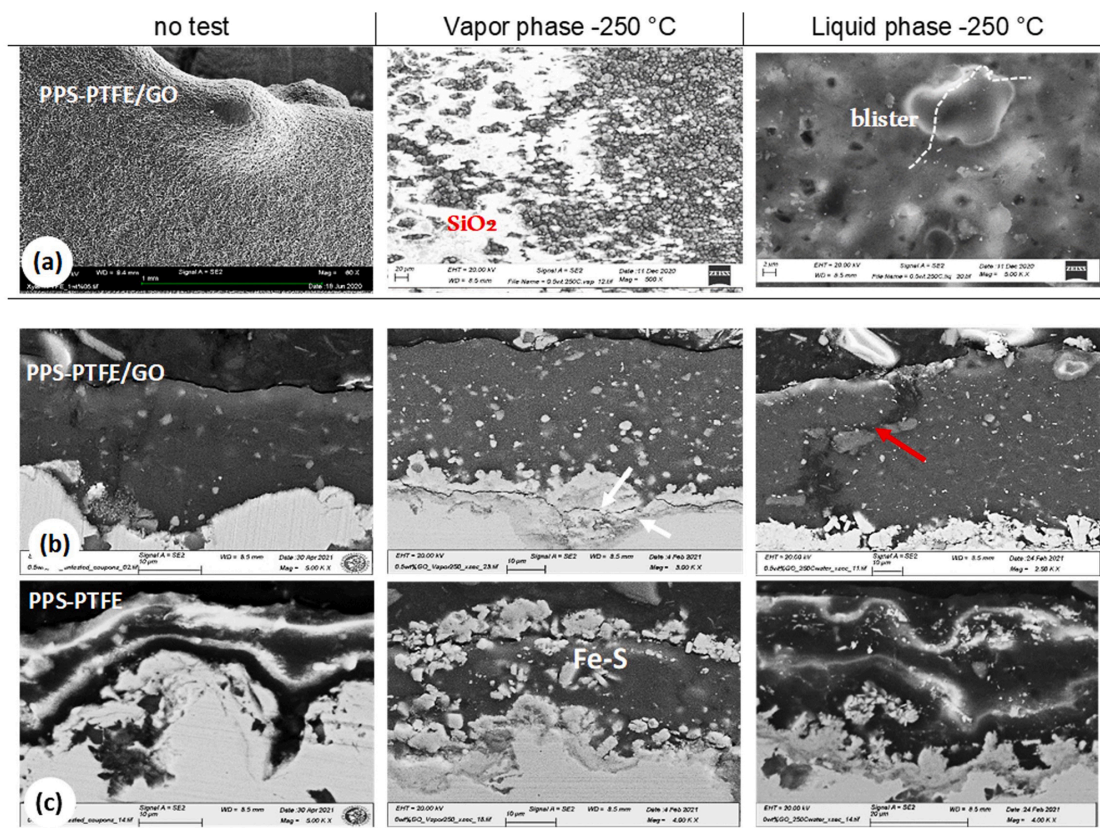
Fig. 7. SEM/EDS image and line mapping of PPS-PTFE/GO in (a) liquid phase (b, c) vapor phase after 250 °C CO$_2$/H$_2$S corrosion test. The red arrow shows the corrosion path and the white arrow's reaction products.

corrosion scale and an inner layer in both the hp/HPptfe and hp/LPptfe coatings. Fig. 11(a) reveals filled-porosities in the functional layer and filled-cracks in the Ni-P adhesion layer from the undetached hp/HPptfe with fairly uniform chemical composition across the duplex (~8–28 μm in thickness). At the coating/substrate interface, the line map shows significant accumulation in O and a steep slope with an increase in Fe, O, and a decrease in Ni, P content. In the significantly cracked hp/LPptfe, the EDS analysis showed a sporadic pattern for the reactivity of the elements present in the duplex and a subsequent increase in O, S, and Fe content.

The chemical analysis of the hp/LPptfe in Fig. 11 (b) shows that in the line map (from 8 μm) the content of the substrate and at the interface shows a decrease in Fe but a subsequent increase in O. The hp/LPptfe contained up to 24% O compared to 5% in hp/HPptfe. After 8 μm, the adhesion layer shows high P wt% and O wt%. The thick non-adherent corrosion product layer (~10 μm) was composed mainly of Ni and S, which suggests that the increased affinity of S blocked successive re-actions of other corrosive anions and species (OH$^-$, CO$_3^{2-}$, H$_2$O) at the surface. Based on the corrosion path, it is likely that an increase in oxidizing ions reaching to the Ni-P undercoat (high %P) occurred resulting in the formation of phosphorus-based oxides. This inner film (Fe-O) can retard to some extent corrosive species of CO$_2$ or H$_2$O dis-solving the substrate as indicated by the results seen in Fig. 11(a) and (b). However, the passive Fe-O layer further degrades locally due to Ni-P reaction to the O - based species and ingress of S - based species near the interface causing extensive localized damage. This is evident in Fig. 11 (b), which depicts cracks and the greatest accumulation of corrosion

products of O in opposing directions to S (see blue arrows) established from the hp/LPptfe corrosion path. This demonstrates O - based corro-sive species from the fluid chemistry have an obvious deterioration ef-fect on the protectiveness of the phosphorus coatings, as also seen in the localized corrosion of hp/HPptfe (see Fig. 10d) at a relatively lower temperature (120 °C).

Further analysis in the cross-section of the hp/LPptfe and hp/HPptfe immersed in the aqueous phase revealed the different damages in the duplex coatings. Partial and complete delamination that occurs in the coating is shown in the SEM images in Fig. 12. In the 250 °C test with CO$_2$/H$_2$S, the coatings tend to blister, crack, flake, and delaminate from the surface according to the SEM analysis (Fig. 9). Debonding occurs at the Ni-S outer scale/coating and the coating/ Fe-O inner scale interfaces (Fig. 12(a) and (b)). Fig. 12(c) and (d) show distinctly oxygen-based corrosion products on the substrate and between the delaminated Ni-S outer scale and the duplex coating. A complete cracking of the duplex coating is reported in Fig. 12(d). The EDS analysis in cross-section was consistent with the discussed chemical composition of corrosion prod-ucts. The detected elements on the top surface and interface were Ni-S and Fe-O rich layers, respectively see Fig. 12(e), and (f). The complete delamination observed allowed CO$_2$/H$_2$S corrosive species to reach the substrate material and a galvanic effect. This shows localized corrosion of the substrate since the Ni-P adhesion layer is more noble contributing to the subsequent passivation of the steel. Nevertheless, it is to be noted here that such local oxidation may destabilize the coating integrity (Fig. 12(d) and (f)) discussed in the next section. The extent of corrosion is demonstrated by the breakdown of the inner film and the increased
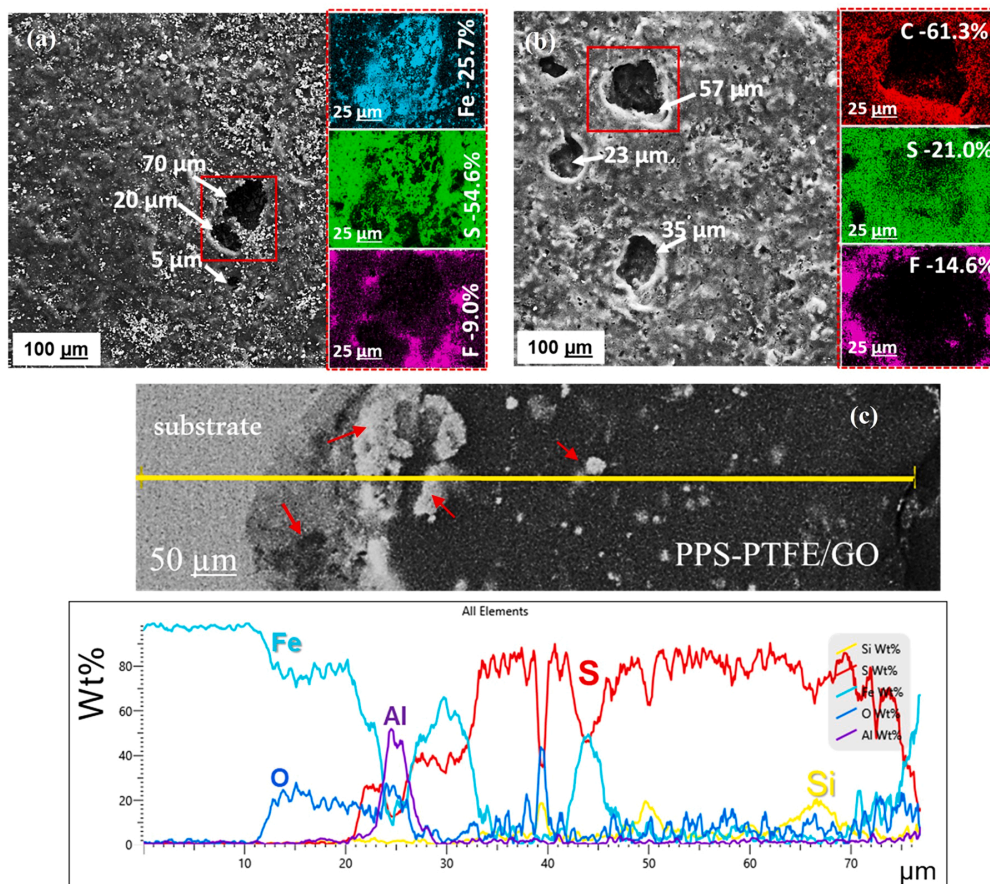
Fig. 8. SEM/EDS image and line mapping of PPS-PTFE/GO in (a, c) vapor phase (b) liquid phase after 250 °C CO_2/H_2S corrosion test. The red arrows show the region of Fe-based corrosion layers at the coating/ substrate interface.

concentration in sulfidizing and oxidizing ions' reaching the coating and the reaction to P and residual Ni. The localized damage to the substrate is demonstrated in the low phosphorus duplex (hp/LPptfe) causing barrier loss from electrochemical galvanic attack (see Fig. 12f). In this case, the metal acts as an anode and the surrounding film as a cathode, resulting in pitting and the diffusion of iron ions (Fe^{2+}) up the cracks/ corrosion path. A Fe, C-oxide based product with traces of Fe-S corrosion products filled the shallow corrosion pits from corrosion of the substrate.

3.5. Corrosion product characterization

Fig. 13 shows the results from the XRD analysis of untested and tested samples after the 120 °C water test and the 250 °C liquid/vapor phase test with CO_2/H_2S. All the corroded hp/LPptfe coatings from the 120 °C water test after 14 days had the highest intensity Ni [FCC] peak ($2\theta = 45°$), indicating no significant changes to the microstructure. This is apparent by comparing the XRD results before and after the test in Fig. 13. However, NiO was identified for the 120 °C samples compared to Fe forming part of the Ni-S structure after exposure in the 250 °C liquid/vapor phase. The XRD pattern of hp/HPptfe showed changes due to the formation of corrosion products. A low-density Ni (Ni_5P_2) and NiO phase were also present in the XRD pattern. However, the dominant Ni_3P phase was still present in the hp/HPptfe coating after corrosion in 120 °C water. In the 250 °C liquid and vapor phase tests, the patterns showed obvious change compared to the untested samples. The main

corrosion product identified after the test was nickel sulfide (NiS) indicating that H_2S dominated in the dissolution of Ni in the duplex coatings. The vapor/steam phase corrosion scale was Ni_3S_2, which is usually regarded to have a negative impact on film protectiveness at high concentrations [22]. Although phosphorus and oxygen were discovered in the duplex after corrosion, the diffraction peaks of the associated products were not visible in the XRD spectra, since Ni-S was thick thus it is not clear if the P-O layer could be detected. In the delaminated region from the vapor phase test, the formation of hematite (Fe_2O_3 in area 'b') from the reaction of Fe and water and subsequent dehydration of iron hydroxide (FeOOH). However, hematite is the most stable layer at ambient temperatures compared to magnetite (Fe_3O_4) in the air is thought to have the higher redox potential to convert to more oxidized hematite phases [34,35]. In a hydrothermal environment, Li [36] demonstrated that oxidation of hematite occurred between 120 °C and 180 °C, above this temperature, slow kinetics occurred due to the growth of hematite on the surface of the magnetite impeding the oxidation of magnetite. Therefore, in Fe^{2+}/Fe^{3+} -rich and O deficient environment, magnetite scale (Fe_3O_4) and hematite that formed were reported to be conductive unlike hematite due to the transformation of weakly magnetic hematite [35,37]. As a result, electric contact between the steel substrate and the partially magnetic Fe based-oxide deposits is possible. This explains why the coating/substrate interface is completely delaminated at the Fe, O-rich layer due to the strong adhesion between the passive layer and the steel (Fig. 12b, d). The Fe based-oxide deposit
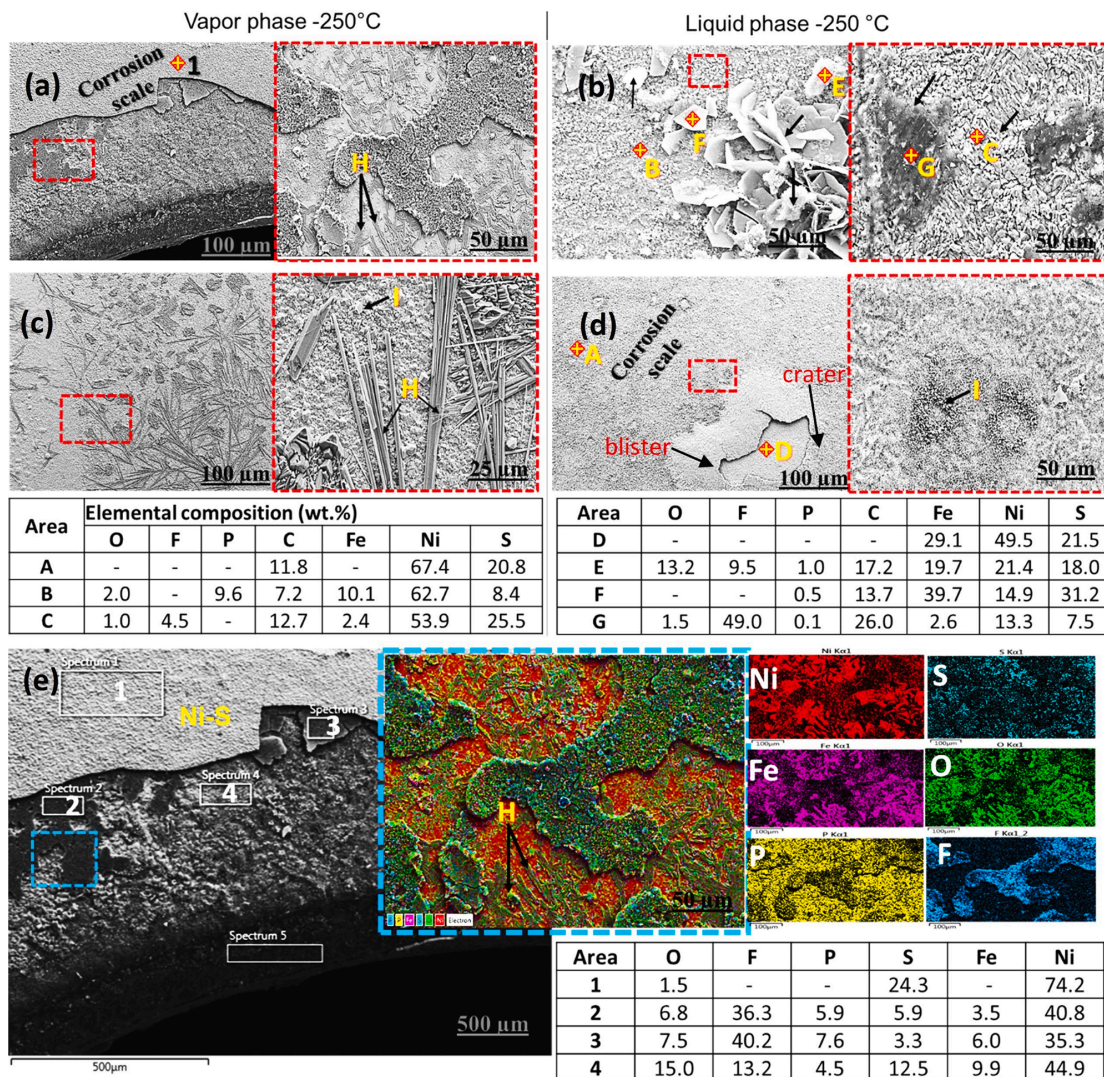
Fig. 9. SEM/EDS surface and cross-section images of (a, b, e) hp/LPptfe, (c, d) hp/HPptfe after 250 °C, CO_2/H_2S corrosion test. Elemental mapping of corrosion product under Ni-S scale in (a) is shown in (e).

has a higher corrosion potential [35], and the steel's corrosion resistance may have increased as their potentials may have shifted in the cathodic direction retarding pitting or under-deposit corrosion in the oxygen starved region. Furthermore, as shown in Fig. 12(a) and (b), a similar mechanism is observed due to a conductivity of the NiS scale [37] because no debris is observed at the scale/coating interface. However, the role of build-up stresses triggering delamination via growth and volume expansion of the corrosion product cannot be disregarded, as shown in Fig. 12(c).

4. Discussion

In the case of uncoated steel ingress and reaction of corrosive species occurs at the exposed surfaces. Therefore, the coatings protected the substrates from corrosion by retarding oxidation reactions. This is explained by the slowed kinetics and rate-determining steps in the reduction of the reactive corrosive species (cathodic reaction) to consume the ions produced from the anodic dissolution. Moreover, OH^- ion discharge at the anode produces water and a lower volume of reactive oxygen gas (i.e., halved O_2, see Eq. (2)). With highly reactive metals, possible oxidation of the matrix or substrate occurs from reaction with the available O_2. However, at 120 °C, water ionizes more, forming hydrogen ions (i.e., the dissociation of H_2 in Eq. (3)), potentially lowering the pH. Here, since the reacting chamber serves as a closed system with no other corrosive species, the change in pH value is dependent on the water reactions. Regardless the electrolyte was an alkaline water-based solution, the water ionizes at 120 °C, causing both hydroxide (OH^-) and hydrogen (H^+) ions to dominate the adsorption creating a balance. The pH value was predicted to shift from 9 to 7.2 according to a geochemical model of the system simulated by using Phreeqc software.

$$2H_2O_{(l)} + 2e^- \rightarrow H_{2(g)} + 2\,OH^-_{(aq)} \tag{1}$$

$$2\,OH^-_{(aq)} \rightarrow 1/2O_{2(g)} + H_2O_{(l)} + 2\,e^- \tag{2}$$
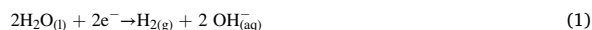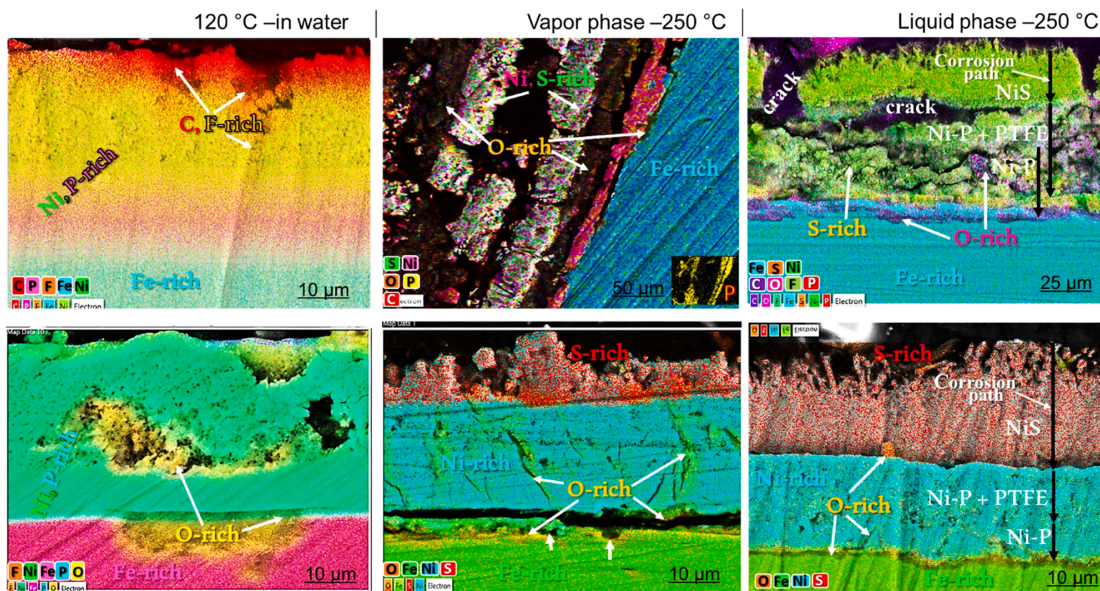
Fig. 10. SEM/EDS cross-section elemental mapping of (a, b, c) hp/LPptfe, (d, e, f) hp/HPptfe after 120 °C water test and 250 °C with CO_2/H_2S corrosion test.
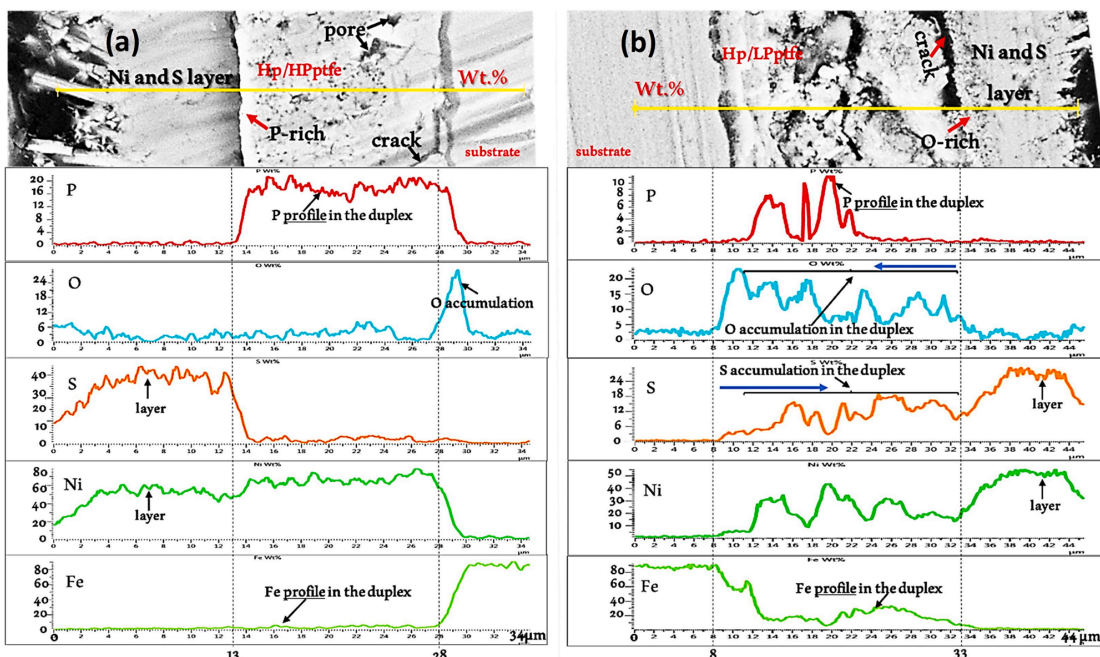
Fig. 11. Cross-section SEM/EDS line mapping of (a) hp/HPptfe and (b) hp/LPptfe after 250 °C, liquid phase with CO_2/H_2S test. The black arrows in the line profiles point to changes in elemental chemistry in the film.

$$H_{2(g)} \rightarrow 2H^+ + 2\,e^- \tag{3}$$

A comparison of unmodified PPS-PTFE tested in the same environment was done to further understand the corrosion mechanism of the PPS-PTFE/GO. According to the results, the unmodified PTFE polymer coating showed limited corrosion resistance (as shown in Fig. 10b)

compared to the coating with 0.5 wt% GO nanosheets (Fig. 10c). The coatings are described to be porous from SEM results, therefore the available oxygen and hydroxyl ions traveled to the underlying substrate. In unmodified PTFE, corrosion products accumulated in the inner layer of the coating and at the substrate interface. This implies the rapid steel dissolution was compensated with hydroxyl and active ions build-up at
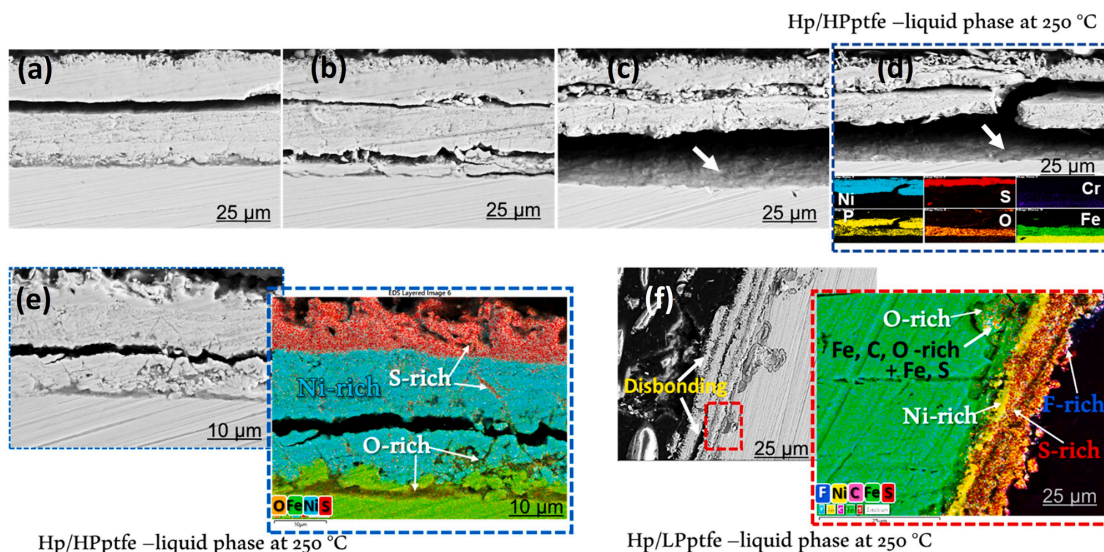
Fig. 12. SEM/EDS cross-section images of hp/HPptfe (a) to (e) and, hp/LPptfe (f) after liquid phase 250 °C, CO_2/H_2S corrosion test. The white arrows indicate Fe-oxide corrosion product.
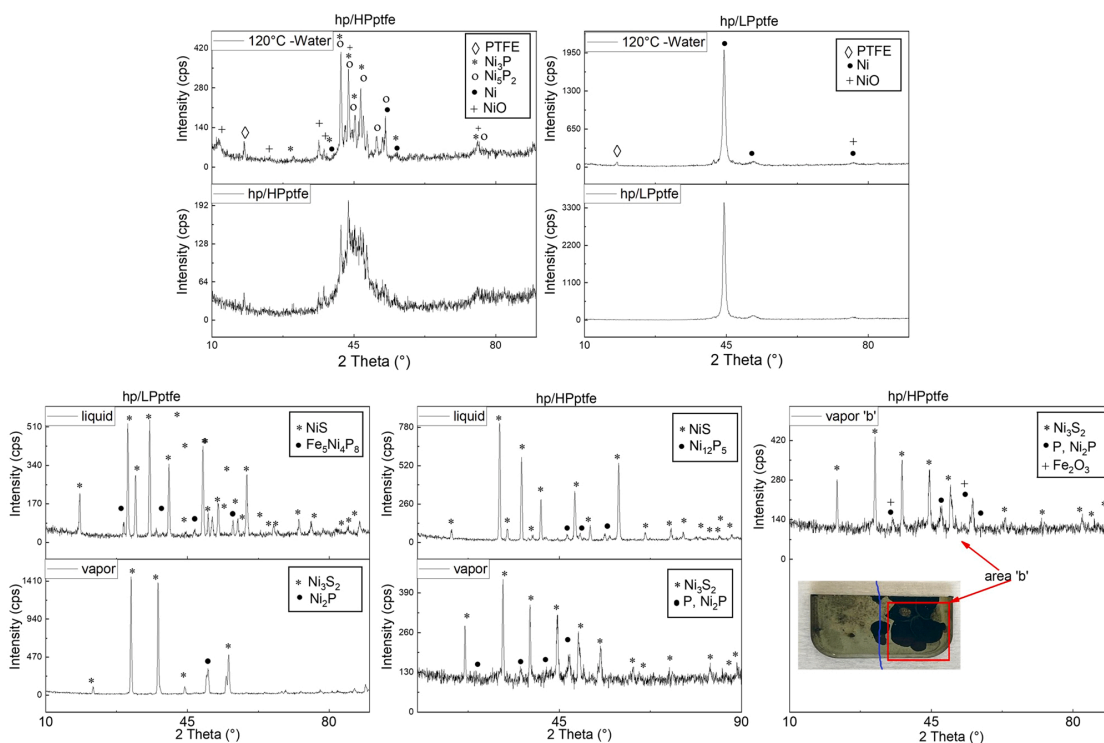
Fig. 13. XRD analysis of corrosion products on the ENP/PTFE duplex coatings after 120 °C water test and 250 °C with CO_2/H_2S corrosion test.

cathodic regions for corrosion to proceed. At the interface, the ferrous substrate oxidizes and Fe^{2+} and Fe^{3+} are released with a cathodic reaction consuming the produced ions forming the products (in Eq. (4)).

$$2\ Fe \rightarrow 2\ Fe^{2+} \rightarrow 2Fe^{3+} + 3H_2O \rightarrow Fe_2O_3 + 6H^+ \tag{4}$$
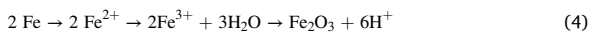
The PTFE flakes and GO nanosheets embedded in the PPS matrix, enhance barrier protection by hampering the diffusion path for the corrosive solution/species shown in Fig. 10(c). In addition, GO bridges gaps in the matrix due to high surface area (see Figs. 2 and 7), which increases the tortuosity of the diffusion paths of the corrosive medium.

Both PTFE and GO contribute to high Ra and WCA, thus initial surface wetting in early corrosion stages is lowered. Furthermore, in the basic environment, nucleophilic attack of GO nanosheets (by reacting with OH⁻) has been reported to leave coatings negatively charged [18] depicted in Fig. 14, reducing the reach of corrosive anions to the coating/substrate interface. The effect of the induced negative charge on corrosion potential is uncertain, however, the surface is said to be cathodically protected, explaining the inherent reaction of S in the unmodified PPS-PTFE to the Hastelloy-Ni over PPS-PTFE/GO (see Fig. 3).

In the ENP/PTFE duplexes, the same tortoise process (in Fig. 10b) was observed during the ingress of the corrosive media through the functional top layer. Also, the Ni- P adhesion layer was semi-permeable and further limited the migration of corrosive species from the functional top layer to the substrate. However, with inherent micro-defects in the topcoat, strong adsorption of oxidizing species into the coating led to the preferential dissolution of Ni formation of Ni-O enriching the coating in P, C, and F. No P-containing oxide products are found on the coating surface from the XRD results. It is hypothesized that the indication of local damage to the HPptfe functional layer is accompanied by further oxidation of P and its products (Eqs. (5) and (6)) from the SEM/EDS elemental maps and line analysis (Fig. 6). According to related studies on corrosion of Ni-P corrosion, hypophosphite (H_2PO_2) formed from water inhibits the anodic dissolution of Ni, but the P-based oxides are unstable and soluble after further oxidation into phosphite and phosphate losing their protectiveness [21,38,39].

$$P + H_2O \rightarrow (H_2PO_2)^- + 2H_2O \rightarrow H^+ + H_3PO_3 + 2e^- \quad (5)$$

$$H_2PO_2 + 2H_2O \rightarrow H_3PO_4 + 3H^+ + 4e^- \quad (6)$$
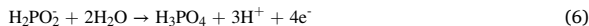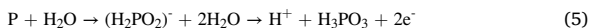
Sun et al. explained that oxidizing alkaline environments favor the hydration of Ni to form $Ni(OH)_2$/NiO through the hydroxoligand mechanism (Eq. (7)) in Ni-P coatings [21]. Accordingly, when the functional layer is exposed to the 120 °C water environment, the dissolution of Ni leads to the fast consumption of H^+ where the uniform corrosion mechanism progresses.

$$Ni + H_2O \rightarrow Ni(OH)_{ads} + H_2O \rightarrow Ni(OH)_2 + H^+ \rightarrow NiO + H_2O \quad (7)$$

The oxide film significantly impedes the transfer of Ni cations from the matrix to the aqueous phase, protecting the metal because any dissolution must occur through this film to satisfy the uniform dissolution kinetics of the passivating oxide shown in Eq. (7). However, because $Ni(OH)_2$ is less protective than NiO, a relatively high concentration of Ni $(OH)_2$ in the $Ni(OH)_2$/NiO layer is reported to reduce the film's protectiveness [39] which could explain the higher corrosion kinetics in hp/HPptfe (Fig. 10d).

The CO_2/H_2S gasses used in the 250 °C test conditions influence the anodic dissolution by changing the solution chemistry. This is quite evident from the results indicated by the clear changes observed on the surface features as well as localized corrosion damage in the cross-section of the coatings in the liquid/vapor test conditions at 250 °C. When the reactor is heated, steam is formed while CO_2 and H_2S are also forced into the vapor phase. Similar to geothermal waters the principal impact is the hydration of CO_2 to produce weak carbonic acid (H_2CO_3)
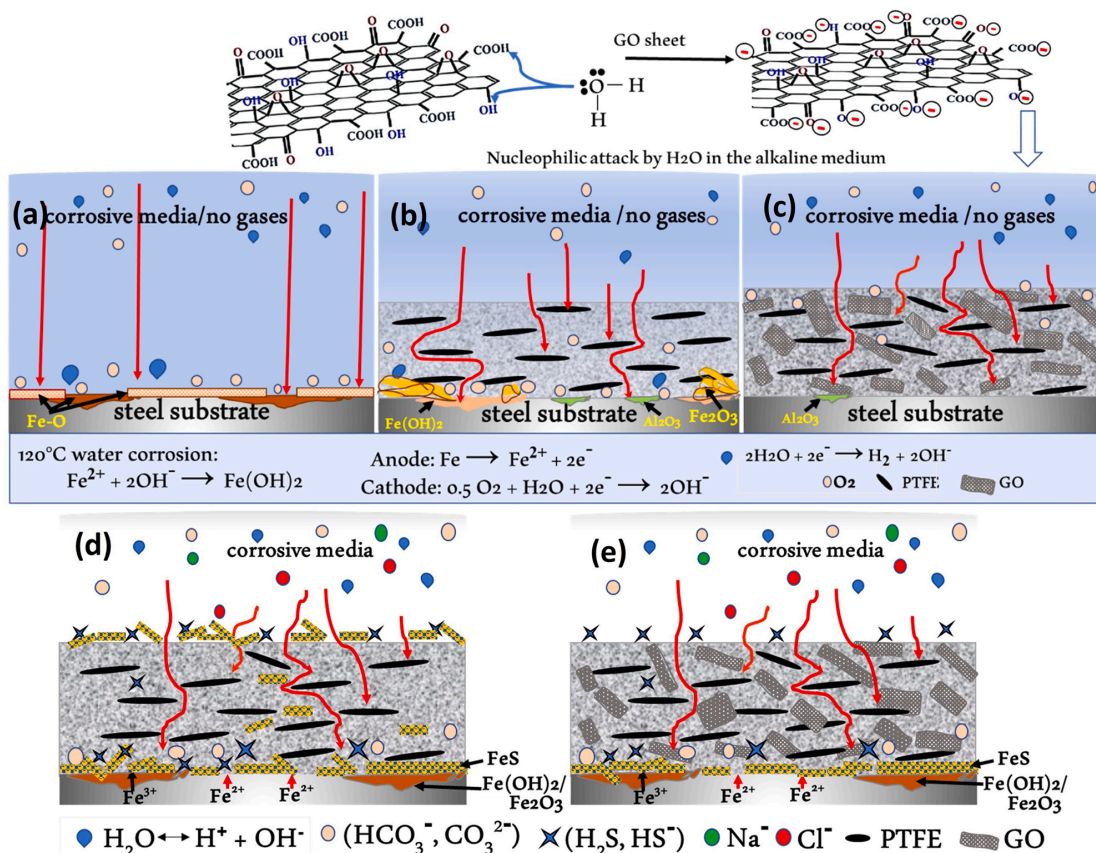
Fig. 14. Schematic of the proposed corrosion mechanism after (a, b, c) 120 °C water and (d, e) 250 °C with CO_2/H_2S illustrated for the:(a) substrate, (b, d) PPS-PTFE, and (c, e) PPS-PTFE/GO in liquid/vapor phase exposure.

and further reduction of bicarbonate species (CO_3^{2-}) which contributed to corrosion in the basic environment. The reaction in the CO_2/H_2S, 250 °C test environment at cathodic sites is proposed to proceed with Eqs (8)–(11). Therefore, the cathodic reactions following the dissolution of metallic components ($M \leftrightarrow M^{n+}$) are relatively complicated processes dominated by the contribution of anionic (HCO_3^-, HS^-) reduction of M. Meanwhile, the predicted increase in pH (from 5.7 to 6.8 at 250 °C) implies the dissociations of both CO_2 and H_2S are inhibited to some extent. Although H^+ content from H_2 ($2 H^+ + 2e^- = H_2$) cannot be neglected, it can be inferred that (from Eqs. (6)–(8) and the pH value) the content of H^+ ions could increase but is lower than the sum of the content in CO_2/H_2S in the mixed environment resulting from synergist corrosion effects.

$$H_2S_{(g)} + H_2O_{(l)} \leftrightarrow H_2S_{(aq)} \tag{8}$$

$$H_2S_{(aq)} \leftrightarrow H^+ + HS_{(aq)}^- \tag{9}$$

$$CO_{2(g)} + H_2O_{(l)} \leftrightarrow H_2CO_{3(aq)} \tag{10}$$

$$H_2CO_{3(aq)} \leftrightarrow H^+ + HCO_{3(aq)}^- \leftrightarrow 2H^+ + CO_{3(aq)}^{2-} \tag{11}$$

It can be concluded that, besides the cathodic reaction (in Eq. (3)), the catalytic process concurrently influenced by the reduction of H_2CO_3 and H_2S (Eqs. (9)–(11)) could affect the corrosion of the coatings (PPS-PTFE/GO and ENP/PTFE duplexes) in the CO_2/H_2S environment as schematically drawn in Figs. 14(d), (e) and 16(i), (ii). During the uniform/local dissolution, further dissociation (HCO_3^- and HS^-) was relevant for the product/scale formation in both the liquid and vapor phase corrosion process. It was observed that spontaneous corrosion is initiated at micro-defects (pores and vacancies) next to the surface of the coatings. This facilitates the penetration of electrolyte and corrosive species to the coating/substrate interface, promoting substrate corrosion.

The synergistic corrosion effect of CO_2/H_2S on the PPS-PTFE and ENP/PTFE composite coatings is mainly dominated by H_2S based on the film characteristics from SEM/EDS analysis. In both coating systems, the localized corrosion at the coating/substrate interface shows simultaneously controlled dissolution of the steel by CO_2 and H_2S cohesively forming $Fe(OH)_2/Fe_2O_3$, $FeCO_3$, and FeS. Uniform dissolution was present only in the metal-based composite (i.e., ENP/PTFE). A relevant study done at temperatures up to 300 °C observed no polymerization of PPS but solution-induced α-form and heat/pressure-induced β-form crystal changes identified in the crystalline sensitive features from Raman and infrared spectroscopy [40]. SEM results of PPS-PTFE/GO showed the formation of holes at 250 °C formed from flared micro-blisters possibly from a direct reaction of the coating in contact with the aqueous/acidic gas (H_2S) and/or the high-temperature effect. In this study, an increase in permeability is evident in the precipitated surface corrosion products in such auxiliary defects. Since there was no complete delamination observed in the PPS-PTFE/GO composite, this suggests the corrosion process was driven by a non-galvanic cell. The results indicate that corrosion has occurred in the less noble substrate forming the FeS corrosion product where the anions could reach the coating/substrate interface. The corrosion then progresses extensively beneath the coating. But minor Fe and O-based corrosion products were possibly also present under the coatings from surface pre-treatment processes before the exposure test. Typically, the reaction was electrochemically assisted at 250 °C, where the Fe reacted with H_2S gases which formed FeS on the Fe_2O_3 layer with fairly homogenous distribution curbing pitting attack. Sugama et al. reported outstanding corrosion resistance of a ZnPh (zinc phosphate) primed and PPS-PTFE composite lined heat exchanger at 200 °C brine [11]. However, found both blistering and delamination in post-test analyses, even at that 80% reduction in capital cost were calculated in comparison to a stainless steel-based heat exchanger. In this research, the individual effect of incorporating SiO_2-PTFE on the properties of polymer coatings with or without GO is unclear. Nevertheless, the results demonstrate that adding 0.5 wt% GO sheets to the matrix did not only increase the barrier effect to corrosive species in the coatings but the higher WCA of the coatings lowered the molecular surface interactions of the coatings in the corrosive environment. If the inherent defects in the modified GO composite could be further reduced, this could improve adherence, compatibility and decrease permeation which will improve the corrosion protection.

In the ENP/PTFE duplex, the initial reaction of H_2S is through the functional topcoat with subsequent formation of the NiS and consequently H_2. The H_2 release can likely incite crack formation and propagation through the Ni-P adhesion layer to the substrate. Here, CO_2, and H_2O being the highest components in both the liquid and vapor phase respectively, acts as a mild oxidizing agent which leads to a complex corrosion path forced by S and/or O corrosive species. The oxidation and sulfidation of Ni are likely determined by the partial pressures of O and S [41] at 250 °C. In the H_2S and S species-controlled corrosion, the process was driven by the rate of dissolution of Ni-P and the maximum solubility of H_2S. Concurrently, the high dissolution rate of Ni is compensated with the additional formation of low-sulfur Ni_3S_2 present after vapor phase CO_2/H_2S corrosion from XRD analysis (in Fig. 13) which modifies the structure of nickel sulfide (NiS) film. The excessive Ni_3S_2 content appears to have a negative influence on the protectiveness of the corrosion film. This is demonstrated by robust adherence and protection of the NiS layer in the ENP/PTFE duplex after liquid phase corrosion. A similar result was observed on a similar ENP/PTFE coating in an in-situ geothermal environment [42]. However, an electrochemical corrosion study revealed lower corrosion resistance caused by co-deposition of PTFE but a lower density and non-uniformity in such composite coatings [25]. It is worth mentioning that LPptfe implies higher Ni (86%)- but lower P (3%) content compared to hp/HPptfe at the coating/solution interface. Therefore, a higher rate of Ni^{2+}, Ni^{3+} dissolution (Eq. (12)) in the rather crystalline FCC material [27] is more likely to occur in the hp/LPptfe and in the 'wet vapor' or fairly aqueous conditions with CO_2/H_2S.

$$Ni + H_2S_{(aq)} \rightarrow NiS + 2H^+ \text{ and } 3Ni + 2H_2S_{(aq)} \rightarrow Ni_3S_2 + 2H^+ \tag{12}$$
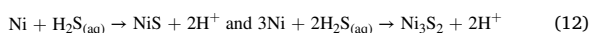
On the other hand, hp/HPptfe is amorphous [27], thus, the reported active absorption of hydrogen causes the Ni-P matrix to be more brittle via volume expansion and crystal deformation [43]. However, defects facilitate corrosion at the interface. Baer investigated the dynamics of hydrogen on a nickel (111) surface and discovered that H has a strong affinity for Ni and provides paths for hydrogen recombination when the metal contains subsurface hydrogen [44]. Moreover, aside from the reactions in Eq. (12), it has been reported the dissolution of P in electroless Ni-P coatings in a CO_2 environment often causes the coating to dissolve and become nonprotective [32,36]. Since the diffusion of the ionic species is not blocked by the adhesion layer due to the dissolution of P, corrosion progressed from the coating/substrate interface to the liquid phase corrosion. Unreacted Fe^{2+} ions from substrate dissolution travel to the top surface forming the Fe-based corrosion products in the ENP/PTFE duplexes. Corrosion and blistering in the hp/LPptfe are, therefore, influenced by significant anodic effects where the further reaction of ferrous ions from corrosion product formation makes the area more anodic, and cathodic reactions at the surrounding perimeter can begin to dis-bond the coating. This is apparent in the Fe, C -oxide based product formed in the corrosion pit.

Also, precipitation of secondary products such as Fe, S rich product is more likely to occur producing the mixed oxide-sulfide product. Chong Sun demonstrated that localized corrosion of the Ni-P coating occurs following cathodic polarization acceleration because the coating defects provide excellent paths for ingress of the electrolyte and active species traveling from the coating to the coating/substrate interface [38].

4.1. Degradation mechanisms

Based on the above analyses, Figs. 14–16 show schematics of the proposed corrosion mechanism produced to clarify the degradation and scale formation of the Polymer and ENP/PTFE duplex coatings in water at 120 °C and 250 °C in CO_2/H_2S (liquid and vapor phase) environment. The results of the PPS-PTFE/GO showed substrate protection in the 120 °C test from the additional impermeable barrier effect of GO nanosheets. The results of Raman, XRD, and SEM analyses revealed the quintessential structure and morphology of PPS-PTFE-GO coating, and as discussed in the 120 °C corrosion test, the GO effectively enhanced the cathodic protection of the coating. However, electrochemically galvanic assisted localized corrosion was observed in both liquid and vapor phase exposure at 250 °C in CO_2/H_2S.

The findings in ENP/PTFE duplexes showed the occurrence of general corrosion and localized corrosion of the substrate. The 120 °C water test (Fig. 15(i)) showed corrosion protection of the substrate occurred by the formation of a thin nickel oxide (NiO) layer (Fig. 15a) on the surface of the coatings. The results indicate that corrosive species infiltrate the coatings through micropores creating a migration path in the coatings. According to the results of the preceding analyses shown in Fig. 15(a) and (b) the following steps are proposed to have occurred in the 120 °C water test:

I. Uniform dissolution of Ni in the topcoat (anodic process) and reaction with oxygen-based anions (cathodic process) form a thin corrosion film on the coatings.
II. Ion migration is hampered by the barrier effect of PTFE particles, which prevents further corrosion of the topcoat and adhesion layer, and
III. Adherence and barrier effect of the high P containing Ni-P undercoat prevents oxidizing corrosive species from further reaching the coating/substrate interface. In the oxidizing (i.e., H_2O) environment, hp/LPptfe (Fig. 15(b)) exhibits no corrosion and no localized damage due to its high crystallinity (Ni-(111)).

Corrosion of the hp/HPptfe was considerable in the 120 °C tap water compared to hp/LPptfe likely because of the higher P content. This suggests the thin NiO film formed on the hp/LPptfe is more crystalline and protective than the non-continuous, and less protective film formed on the hp/HPptfe. The residual P reacts with water in the hp/HPptfe deteriorating the top layer with the PTFE, but no delamination occurred in the adhesion undercoat. Localized corrosion of the substrate occurred due to penetration of oxidizing corrosive species (Fig. 15(b), (c)).

In the CO_2/H_2S environment (Fig. 16), similarly, the aggressive ions permeate the coatings through micropores, but the Ni-P undercoat is subject to cracking due to diffusion of hydrogen forming the 2 major corrosion paths in the coatings. The findings in the 250 °C liquid/vapor test showed corrosion protection of the substrate was similar to the above-stated mechanisms (I, II, III) in the 120 °C water test. However, the complex chemistry of the CO_2/H_2S environment resulted in other associated reactions (Fig. 16(i), (ii)) influencing the corrosion behavior.
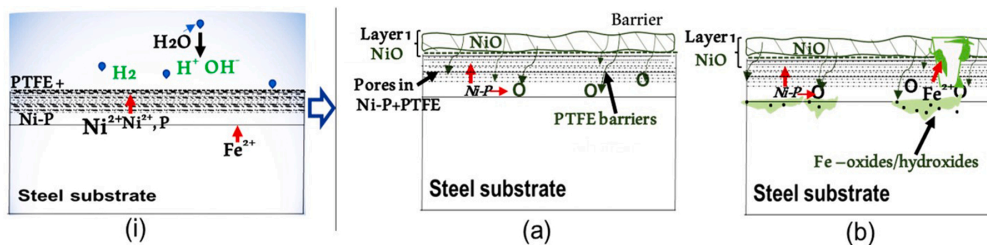
The extent of surface protection was attributed to the nickel sulfide (i.e., NiS or Ni_3S_2) corrosion layer (Fig. 16b). The type of sulfide is facilitated by the H_2S activity, however, NiS was observed to be the more stable phase in the liquid phase test. The strong reaction of Ni to S precludes further reaction to oxidizing species at the surface, therefore non-S species (anions of H_2O/CO_2) migrate into the duplex coating through the pores and crack in the adhesion layer from hydrogen entrapment (Fig. 16b, c). This increases the concentration of sulfides at the surface participating in the corrosion process while stimulating the H_2S effect on the corrosion and increasing the rate of the hydrogen evolution reaction ($H_{2(g)}$ or H^+). This generates more corrosion paths in the coating from the formation of micro-defects and increased crack length which is also associated with H_2S corrosion [45]. The crack path extends to the top layer because the particles and the coating matrix do not have perfect co-adhesion.

Below the NiS scale, P is most abundant in the vicinity of the NiS layer and the adhesion layer in the hp/HPptfe compared to hp/LPptfe. No-to little oxidation occurs in the duplex layers but a major cracking occurs in the amorphous Ni-P adhesion layer, indicating rapid effusion of hydrogen (H^+) compared to O species. The O accrued migrates to the substrate leading to oxidation of the Ni and Fe at the interface (Fig. 16 (c), (d)). Corrosion in hp/LPptfe is severe where deterioration of the coating from O and S species was seen with high content of Fe and Ni (Fig. 16e). Below the crystalline coating, Fe dissolves faster and migrates from the base steel to the surface, due to the galvanic potential difference between Ni (-0.85 V) and Fe (-0.3 V). On the contrary, in hp/HPptfe, stress and volume expansion from scale growth at the adhesion layer and conductivity of the corrosion scale under the adhesion layer results in complete detachment of the coating from the base steel (Fig. 16(f)).

5. Conclusions

Corrosion damages and microstructural changes due to corrosion of PPS-PTFE/GO and duplex ENP-PTFE composite coatings were assessed with SEM/EDS and XRD techniques after testing in simulated high-temperature geothermal environments with/without H_2S and CO_2 gases. The main conclusions of the study are the following:

- In general, the PPS-PTFE/GO coating performed better in the 120 °C test compared to the reference material indicating the hinderance effect of the GO nanofiller. The Ni-based coatings tested in water at 120 °C show preferential dissolution of Ni to generate NiO. The hp/LPptfe demonstrated greater corrosion resistance than hp/HPptfe with the formation of a thin crystalline NiO film and less effect on the coating integrity.
- In the more challenging environment (i.e., 250 °C CO_2/H_2S), the corrosion resistance of the coatings reduced drastically due to higher temperature effects and H_2S/CO2corrosion. This was due to inherent (microporosities) and auxiliary defects (i.e., the cracks in Ni-P and blistering in PPS-PTFE/GO) in the microstructure. Galvanic effects in

Fig. 15. Schematic model of predominant reactions in (i) 120 °C water and localized damages (a, b) in the ENP/PTFE duplex coatings. The typical localized corrosion damage of hp/HPptfe is seen in (b).
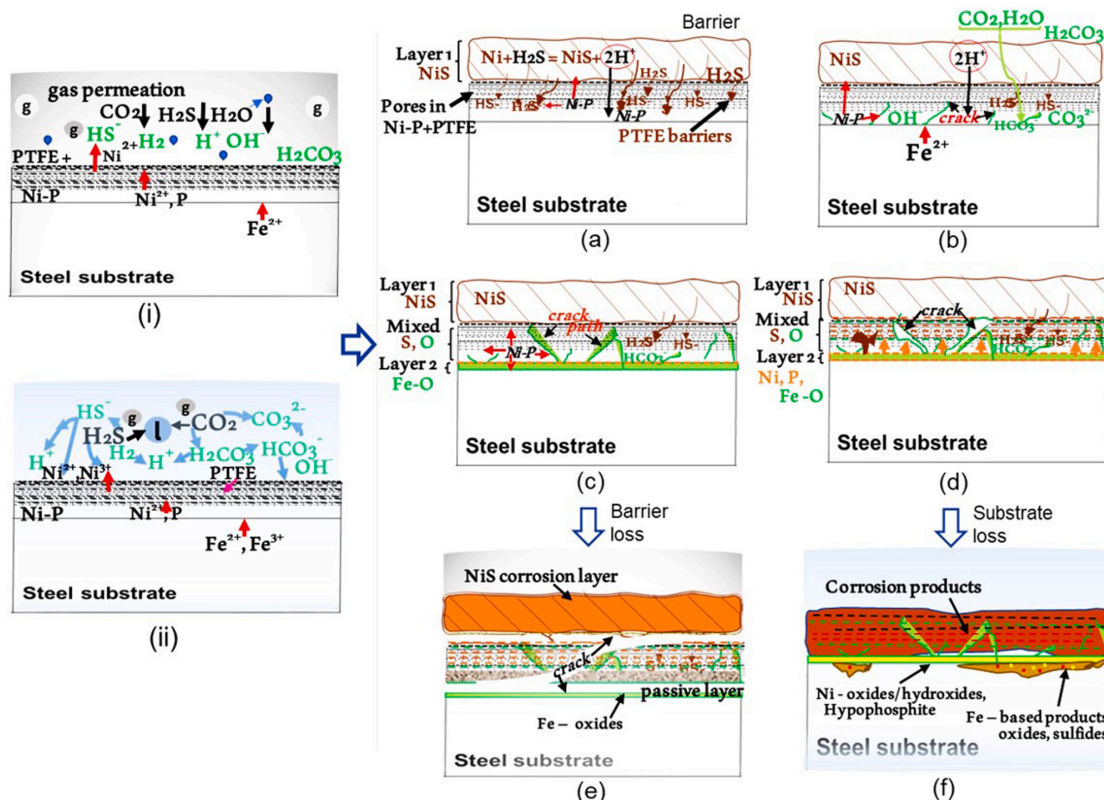
Fig. 16. Schematic model of predominant reactions in the (i) vapor phase, (ii) liquid phase at the 250 °C CO_2/H_2S test conditions, and coating damages (a) to (f). The typical corrosion behavior of hp/HPptfe transitioned from (c) to (e) while hp/LPptfe transitions from (d) to (f).

all coatings raised the possibility of substrate corrosion, despite the formation of a NiS layer on ENP/PTFE duplexes.

- The structural integrity of all coatings was compromised in the simulated high temperature CO_2/H_2S geothermal environment. Improving the PTFE particle adherence in the high phosphorus (HP) matrix could be beneficial for improved corrosion performance in either single-gas H_2S or CO_2 environment and is recommended for further studies.

Funding

Declaration of Competing Interest

The authors declare that they have no known competing financial interests or personal relationships that could have appeared to influence the work reported in this paper.

Data availability

Data will be made available on request.

Acknowledgments

Author statement

References

[1] H.S. Klapper, J. Stevens, Challenges for metallic materials facing HTHP geothermal drilling, in: Proceedings of the NACE – International Corrosion Conference Serie., 2013.

[2] P.F.I. Ellis, M.F. Conover, Materials Selection Guidelines for Geothermal Energy Utilization Systems, 1981. ⟨https://doi.org/10.2172/6664808⟩.

[3] T. Kaya, P. Hoşhan, Corrosion and material selection for geothermal systems, in: Proceedings of the World Geothermal Congress, Antalya, Turkey, 2005, pp. 24–29.

[4] D. Zeng, B. Dong, F. Zeng, Z. Yu, W. Zeng, Y. Guo, Z. Peng, Y. Tao, Analysis of corrosion failure and materials selection for CO2–H2S gas well, J. Nat. Gas Sci. Eng. 86 (2021), 103734, https://doi.org/10.1016/j.jngse.2020.103734.

[5] P. Sahoo, S.K. Das, Tribology of electroless nickel coatings - a review, Mater. Des. 32 (2011) 1760–1775, https://doi.org/10.1016/j.matdes.2010.11.013.

[6] W. ZhongLiu, X. Peng, L. Zhuan, L. Wen, L. Heng, Y. XiaoYu, L. Yang, C. WenBo, Microstructure and oxidation behavior of sol-gel mullite coating on SiC-coated carbon/carbon composites, J. Eur. Ceram. Soc. 35 (2015) 3789–3796, https://doi.org/10.1016/j.jeurceramsoc.2015.06.033.

[7] S.N. Karlsdottir, I.O. Thorbjornsson, Corrosion testing down-hole in sour high temperature geothermal well in Iceland, in: Proceedings of the NACE – International Corrosion Conference Series, 2013.

[8] S.N. Karlsdóttir, Corrosion, scaling and material selection in geothermal power production, in: Comprehensive Renewable Energy, Elsevier Ltd, 2012, pp. 241–259, https://doi.org/10.1016/B978-0-08-087872-0.00706-X.

[9] R. Bäßler, J. Sobetzki, H.S. Klapper, Corrosion resistance of high-alloyed materials in artificial geothermal water, in: Proceedings of the NACE – International Corrosion Conference Expo, 2013, p. 2327.

[10] T. Sugama. High-Performance Coating Materials, Brookhaven National Laboratory, 2015. ⟨www.bnl.gov⟩.

[11] T. Sugama, D. Elling, Poly (phenylenesulfide)-based coatings for carbon steel heat exchanger tubes in geothermal environments, J. Mater. Sci. 37 (2002) 4871–4880.

[12] T. Sugama, Polyethersulfone coating for mitigating corrosion of steel in geothermal, Environment (2005). ⟨https://www.bnl.gov/isd/documents/30855. pdf⟩.

[13] T. Sugama, Polyphenylenesulfied/montomorillonite clay nanocomposite coatings: their efficacy in protecting steel against corrosion, Mater. Lett. 60 (2006) 2700–2706, https://doi.org/10.1016/j.matlet.2006.01.111.

[14] D. Zhang, J.K.L. Ho, G. Dong, H. Zhang, M. Hua, Tribological properties of Tin-based Babbitt bearing alloy with polyurethane coating under dry and starved lubrication conditions, Tribol. Int. 90 (2015) 22–31, https://doi.org/10.1016/j. triboint.2015.03.032.

[15] T. Sugama, S.S. Kelley, K. Gawlik, Hydrothermal degradation study of phenolic polymer coatings by advanced analytical methods, J. Coat. Technol. 73 (2001) 65–71, https://doi.org/10.1007/BF02698399.

[16] N. Nemati, M. Emamy, S. Yau, J. Kim, D. Kim, High temperature friction and wear properties of graphene oxide/polytetrafluoroethylene composite coatings deposited on stainless steel, RSC Adv. 6 (2016) 5977–5987, https://doi.org/ 10.1039/C5RA23509J.

[17] R. Ding, W. Li, X. Wang, T. Gui, B. Li, P. Han, H. Tian, A. Liu, X. Wang, X. Liu, X. Gao, W. Wang, L. Song, A brief review of corrosion protective films and coatings based on graphene and graphene oxide, J. Alloy. Compd. 764 (2018) 1039–1055, https://doi.org/10.1016/j.jallcom.2018.06.133.

[18] B. Ramezanzadeh, E. Ghasemi, M. Mahdavian, E. Changizi, M.H. Mohamadzadeh Moghadam, Covalently-grafted graphene oxide nanosheets to improve barrier and corrosion protection properties of polyurethane coatings, Carbon 93 (2015) 555–573, https://doi.org/10.1016/j.carbon.2015.05.094.

[19] A. Salicio-Paz, H. Grande, E. Pellicer, J. Sort, J. Fornell, R. Offoiach, M. Lekka, E. García-Lecina, Monolayered versus multilayered electroless NiP coatings: Impact of the plating approach on the microstructure, mechanical and corrosion properties of the coatings, Surf. Coat. Technol. 368 (2019) 138–146, https://doi.org/ 10.1016/j.surfcoat.2019.04.013.

[20] T.S.N. Sankara Narayanan, I. Baskaran, K. Krishnaveni, S. Parthiban, Deposition of electroless Ni-P graded coatings and evaluation of their corrosion resistance, Surf. Coat. Technol. 200 (2006) 3438–3445, https://doi.org/10.1016/j. surfcoat.2004.10.014.

[21] C. Sun, H. Zeng, J.-L. Luo, Unraveling the effects of CO2 and H2S on the corrosion behavior of electroless Ni-P coating in CO2/H2S/Cl– environments at high temperature and high pressure, Corros. Sci. 148 (2019) 317–330, https://doi.org/ 10.1016/j.corsci.2018.12.022.

[22] Y. Sui, C. Sun, J. Sun, B. Pu, W. Ren, W. Zhao, Stability of an electrodeposited nanocrystalline Ni-based alloy coating in oil and gaswells with the coexistence of H2S and CO2, Materials 10 (2017), https://doi.org/10.3390/ma10060632.

[23] H. Kinoshita, S. Yonezawa, J. ho Kim, M. Kawai, M. Takashima, T. Tsukatani, Electroless Ni-plating on PTFE fine particles, J. Fluor. Chem. 129 (2008) 416–423, https://doi.org/10.1016/j.jfluchem.2008.02.002.

[24] A. Sharma, A.K. Singh, Corrosion and wear resistance study of Ni-P and Ni-P-PTFE nanocomposite coatings, Cent. Eur. J. Eng. 1 (2011) 234–243, https://doi.org/ 10.2478/s13531-011-0023-8.

[25] Y.S. Huang, X.T. Zeng, X.F. Hu, F.M. Liu, Corrosion resistance properties of electroless nickel composite coatings, Electrochim. Acta 49 (2004) 4313–4319, https://doi.org/10.1016/j.electacta.2004.04.023.

[26] G. Oppong Boakye, O. Straume, B.A. Rodriguez, D. Kovalov, S.N. Karlsdottir, Microstructural characterization, corrosion and wear properties of graphene oxide modified polymer coatings for geothermal drilling applications, in: Proceedings of the NACE – International Corrosion Conference, 2020, pp. 1–9.

[27] G.O. Boakye, A.M. Ormsdóttir, B.G. Gunnarsson, S. Irukuvarghula, R. Khan, S. N. Karlsdóttir, The effect of polytetrafluoroethylene (PTFE) particles on microstructural and tribological properties of electroless Ni-P+PTFE duplex coatings developed for geothermal applications, Geotherm. Appl. Coat. 11 (2021) 670, https://doi.org/10.3390/coatings11060670.

[28] NACE MR0175/ ISO 15156-1, Petroleum and Natural Gas industries. Materials for Use in H2S-Containing Environments in Oil and Gas Production, 2009. ⟨www.iso. org⟩, (Accessed 1 May 2022).

[29] M.J. Gunnarsdottir, S.M. Gardarsson, G.S. Jonsson, J. Bartram, Chemical quality and regulatory compliance of drinking water in Iceland, Int. J. Hyg. Environ. Health 219 (2016) 724–733, https://doi.org/10.1016/j.ijheh.2016.09.011.

[30] J. Schwan, S. Ulrich, V. Batori, H. Ehrhardt, S.R.P. Silva, Raman spectroscopy on amorphous carbon films, J. Appl. Phys. 80 (1996) 440–447, https://doi.org/ 10.1063/1.362745.

[31] N. Nemati, M. Emamy, S. Yau, J.-K. Kim, D.-E. Kim, High temperature friction and wear properties of graphene oxide/polytetrafluoroethylene composite coatings deposited on stainless steel, RSC Adv. 6 (2016) 5977–5987, https://doi.org/ 10.1039/C5RA23509J.

[32] E.O. Straume, G. Oppong Boakye, B. Alonso, S.N. Karlsdóttir, High temperature testing of materials and corrosion resistant coatings for geothermal drilling applications, in: Proceedings of the World Geothermal Congress 2020+1, Reykjavik, 2021, pp. 1–11. ⟨pangea.standard.edu/ERE/db/WGC/papers/WGC/ 2020/27049.pdf⟩, (Accessed 6 May 2022).

[33] S. Zhou, Y. Wu, W. Zhao, J. Yu, F. Jiang, Y. Wu, L. Ma, Designing reduced graphene oxide/zinc rich epoxy composite coatings for improving the anticorrosion performance of carbon steel substrate, Mater. Des. 169 (2019), 107694, https:// doi.org/10.1016/j.matdes.2019.107694.

[34] R.M. Cornell, U. Schwertmann. The Iron Oxides: Structure, Properties, Reactions, Occurences and Uses, second ed., Wiley, 2003 https://doi.org/10.1002/ 3527602097.

[35] S.H. Jeon, G.D. Song, D.H. Hur, Micro-galvanic corrosion of steam generator materials within pores of magnetite flakes in alkaline solutions, Metals 8 (2018) 899, https://doi.org/10.3390/met8110899.

[36] Z. Li, C. Chánéac, G. Berger, S. Delaunay, A. Graff, G. Lefèvre, Mechanism and kinetics of magnetite oxidation under hydrothermal conditions, RSC Adv. 9 (2019) 33633–33642, https://doi.org/10.1039/c9ra03234g.

[37] X. Yong, M.A.A. Schoonen, The absolute energy positions of conduction and valence bands of selected semiconducting minerals, Am. Mineral. 85 (2000) 543–556, https://doi.org/10.2138/am-2000-0416.

[38] C. Sun, J. Li, S. Shuang, H. Zeng, J.-L. Luo, Effect of defect on corrosion behavior of electroless Ni-P coating in CO2-saturated NaCl solution, Corros. Sci. 134 (2018) 23–37, https://doi.org/10.1016/j.corsci.2018.01.041.

[39] R.B. Diegle, N.R. Sorensen, C.R. Clayton, M.A. Helfand, Y.C. Yu, An XPS investigation into the passivity of an amorphous Ni-20P alloy, J. Electrochem. Soc. 135 (1988) 1085–1092, https://doi.org/10.1149/1.2095880.

[40] D.A. Zimmerman, J.L. Koenig, H. Ishida, Infrared and Raman spectroscopy of cyclohexa(p-phenylene sulfide) and the polymer obtained therefrom, Polymer 40 (1999) 4723–4731, https://doi.org/10.1016/S0032-3861(98)00635-1.

[41] J.Z. Albertsen, Ø. Grong, J.C. Walmsley, R.H. Mathiesen, W. Van Beek, A model for high-temperature pitting corrosion in nickel-based alloys involving internal precipitation of carbides, oxides, and graphite, Metall. Mater. Trans. A 39 (2008) 1258–1276, https://doi.org/10.1007/s11661-008-9494-5.

[42] S. Davíðsdóttir, R. Khan, K.R. Ragnarsdóttir, S. Irukuvarghula, S. Guðlaugsson, A.Í. Þórhallsson, In-situ corrosion testing of ENP-PTFE coatings in geothermal environment, Assoc. Mater. Prot. Perform. (2021) 148–162.

[43] A.R.A. Haasz, K.T. Aust, W.T. Shmayda, G. Palumbo, Hydrogen transport in nickel, Fusion Technol. 28 (1995) 1169–1174, https://doi.org/10.13182/FST95-A30566.

[44] R. Baer, Y. Zeiri, R. Kosloff, Hydrogen transport in nickel (111), 10952–10962, Phys. Rev. B 55 (1997), https://doi.org/10.1103/PhysRevB.55.10952.

[45] S.N. Karlsdóttir, S.M. Hjaltason, K.R. Ragnarsdóttir, Corrosion behavior of materials in hydrogen sulfide abatement system at Hellisheiði geothermal power plant, Geothermics 70 (2017) 222–229, https://doi.org/10.1016/j. geothermics.2017.06.010.

Appendix B

Table B.1. An overview of potential failure modes, causes, effects (FMEA) of main and sub-components analysis in the project (Deliverables: Geo-Drill; D1.1 and Geo-Coat; D 1.2)

System	Component	Main part	Potential failure mode	Potential cause	Potent. Failure Effects
Drilling	Drill bit	Anvil/Striking face	Cracking and Breakage of striking face	Overheating of shank, Material quality	Bit shank failure, hammer failure
		Insert	Breakage and Premature wear	Abrasive formation, Improper operation	Reduced RoP, damage to bit matrix/body, loss of hole
	Hammer assembly	Anvil	Overheating, stress fracture, Excessive wear from contaminants	Contamination introduced to hammer (flushing medium), Material quality	Loss of drilling time, tripping out/in
		Chunck nut body and thread	Excessive wear due to erosion of material body, thread root failure	Incorrect torque setting of chuck in hammer body, Erosion of chuck body, high velocity of cuttings in the tight annulus, Material quality	Loss of bit, bit breaking or stucking, possible well loss
		Cylinder (internal sleeve)	Overheating, Excessive wear from contaminants	Contamination introduced to hammer (flushing medium), Material quality	Tripping in/out, loss of drilling time
		Valve	Stress fracture	Material quality, Incorrect torque, Erosion, contamination introduced to hammer	Inefficient drilling, number of usable teeth reduces
		Piston	Overheating, Excessive wear from contaminants, stress fractures	Contamination introduced to hammer (flushing medium), Material quality	Loss of drilling time, tripping out/in
		Body and Back Head	Fracture, cracks, breakage and thread failure	Erosion from cuttings, Material quality	Failure of hammer, Loss of well
	Drill pipe and collars	Pipe and pipe tool joint	Fracture, galling, tool face damage due to wash out, wall thickness reduction, loss of drill string	Fatigue, Erosion, Mechanical wear from formation material, Over or Under torque, SCC	Loss of drill string, Fishing out, External erosion of tooljoints
		Collar pins and box	Cracking leading to fracture	Wear and tear, Cyclic bending stress causing fatigue, Over or Under torque in connections string	Drill strng and component loss, Stucking and Fishing out
	Stabilizer	Blades	Wear and tear from rocks, erosion	Erosion, Mechanical wear from the formation (prominent in directional drilling)	Deviation in drilling direction, Fishing out, Hole loss

System	Component	Main part	Potential failure mode	Potential cause	Potential Failure Effects
Steam production	Well head	Casing below cellar floor	Erosion/corrosion	High velocity fluid, corrosive fluid	Thinning, Leaking
		Flanges	Erosion-corrosion	High velocity fluid, corrosive fluid	Leaking
		master/cotrol/wing valve-seat	Wear, Erosion	particles in fluid, corrosive fluid, maintenance and repair	Leaking, Loss of seal, Difficulty in operation
	surface pipe	Inlet steam pipe	Erosion/corrosion	High velocity fluid, corrosive fluid, silica deposition	High condensate
	Silencer control valve	shaft, disc, seat hard facing	Erosion/corrosion/scaling	High velocity fluid, Corrosive fluid, Poor maintenance	High velocity, Low pH
Steam transmission	Separator	Vessel	Erosion	Particles in fluid	Thining and Reduced strenght
		Steam scrubbing	Erosion	Particles in fluid	Thining and Reduced strenght
	Turbine	Labyrinth seals	Rubbing	friction between parts	Wear, Damage to seals
		Diaphragm	Erosion outer section and blade ends	Particles or droplets in steam,	Wear, Fractures, vibration, Nozzle breakage
		Rotor and rotor blades	Erosion-corrosion, erosion by blate roots	Particles or droplets in steam	Wear, Imbalance/ Vibration, Blade loss
		Casing	Erosion at junctures	Particles or droplets in steam	Steam by-pass
	Valves	Seat, pin	Deposits, Wear/abrasion	Friction between parts	Loss of seal, Sticking
	Working fluid pump	Shaft	Wear/ abrasion	Friction between parts	Clearance/ Vibration
Reinjection	Brine pumps	Impeller	Wear/ pitting	Failure of brine check valve/ Friction in vessel/ Cavitation	Material reduction, Efficiency
	Well head and working pumps	Valves pin, seat and disc	Wear/ erosion/ corrosion	Particles in fluid/ Friction between parts/ Poor maintenance/ Corrosive fluid	Red. Of diameter, No sealing/ Leaking/ Difficult to operate

Table B.2. Common materials used, cost and related chemistry influencing corrosion (Geo-Coat deliverable, D1.1: State-of the-Art).

Materials		Carbon Steels; and low-alloy steels (CS)[a]	Stainless Steels (SS)[a]	Titanium alloys (Ti)[a]	Nickel alloys (Ni)[a]
	Common types	J55, K55, L80, N80, P110 (carbon steel) P91, STBA24, SAE4130, SAE4140 (low-alloy steel)	AISI 304, AISI 316 AISI 403, AISI 410, AISI 430 E-Brite 26-1	Ti Grade 2 Ti Grade 5 Beta-C Ti	Inconel 625 Alloy 20 Hastelloy C-276
	Cost	low	medium	high	high
	Susceptibility	Low pH, Chlorides, H_2S	chlorides	n/a	Chlorides, H_2S

[a]Common materials used (referenced in Table B.2)
n/a: data not avaialable

165

Table B.3. A combined overview of geothermal power generation: Common materials used (State -of-the-Art referenced in Table B.1), stream analysis areas, fluid properties and related degradation mechanisms (Geo-Coat deliverable, D1.1: State-of the-Art).

		Fluid properties					Other		
Stream	**State**	**Temperature** [°C]	**pH** [-]	**Pressure** [high/low]	**NCG** [high/low]	**Bulk velocity** [high/low]	**Used material**[a]	**Degradation mechanisms**[b]	**Equipment affected**[c]
in well equipment	liquid/2-phase	160-300	5.0-8.0	high	high	high	CS, Ti, Ni	S, EC, SCC, UC	P, SC, V
wellhead to 1st separator	2-phase	160-202	5.0-8.0	high	high	high	CS, SS, Ti	EC, S	PS, VS, HX
1st separator to turbine and steam ejector	steam	156-202	n/a	high	high	n/a	CS, SS	UC, EC, S	PS, T
1st separator to 2nd separator (flasher)	liquid	100-154	5.0-6.0	n/a	low	low	CS	EC, UC	PS
2nd separator (flasher) to turbine	steam	101-130	> 6	low	low	n/a	CS	UC	PS, V
2nd separator (flasher) to re-injection	liquid	101-130	> 6	low	low	n/a	CS	S, SCC	P, PS,
turbine to condenser	steam/2-phase	30-130	low	low	high	low	SS	UC	PS
in cooling water systems	Liquid/2-phase	30-60	low	low	high	low	SS	S	SN
from steam ejector	steam	30-60	n/a	low	high	low	SS	n/a	PS

[a]*commonly used materials. Ti is typical for environments with lower pH and NCG such as the Geyser and Salton Sea, California USA.*
[b]*Degradation mechanisms: scaling (S), erosion-corrosion (EC), stress corrosion cracking (SCC), uniform corrosion (UC)*
[c]*Equipment affected: Pump (P), Surface casing (SC), Valves (V), Pipelines (PS), vessel (VS) Heat exchanger tube (HX), Turbine (T), spray nozzles (SN)*
n/a: not applicable or data not available

Table B.4. Overview of average values on characterisation of geothermal fluid at Hellisheiði and Nesjavellir sampling sites in Iceland (Geo-Coat deliverable, D1.3: Fluid Sampling).

Location	*State*	*T [°C]*	*P [bar]*	*pH*	*CO₂*	*H₂S*	*SiO₂*	*Na*	*K*	*Ca*	*Cl*	*SO₄*	*Se*

#		Type	[mg/kg]	[mg/kg]	[mg/kg]	[mg/kg]	[mg/kg]	[mg/kg]	[mg/kg]	[mg/kg]	[mg/kg]	[mg/kg]	[mg/kg]	[mg/kg]
1	Wellhead	**Water**	176-209	16-77	7.12-8.67	4-29.1	7-105	204-1224	9.5-168.7	<4-35	0.32-0.45	5-205	1.5-13.4	0.82-46.9
		NCG	-	-		443-3807	410-1173							
		Cond. steam	-	-	3.95-4.42	-	-	0.172-0.53	<0.1-0.13	<0.4	<0.1	0.08-1.8	0.3-1.6	<0.5-1.43
2	Steam into turbines	**NCG**	172-191	7.4-11.8	-	1268-3470	384-978	-	-	-	-	-	-	-
3	Gas from turbines	**NCG**	-	-	-	37-66 [vol%]	12-34 [vol%]	-	-	-	-	-	-	-
4	Separator water after 2nd flash	**Water**	172-180	8.4-12	8.70-8.94	22-30	50-75	676-758	168-206	33-35	0.30-0.74	155-186	42705	n/a
5	Separator water after 1st flash	**Water**	119	2-10	9.2	20	30	735	203	38	0.85	186	21.5	16
6	Separator water after heat exchangers	**Water**	10.0-8.5	10.0-12.0	8.83-9.2	19.8-23.7	30-82	735-764	159-206	31.6-35.5	0.27-0.78	118-186	18.1-24.4	7.6-15.3
7	Condensate	**Water**	40-60	1	5.1-6.9	2-20.9	1-98.3	<0.06-4.4	<0.1-1.78	<0.4	<0.1-0.86	<0.1-1	1-3.9	<0.5
8	Seal water	**Water**	40-60	1	n/a	365-920	331-560	<0.06	<0.1	<0.4	<0.1	<0.1	7	0.535
9	Sulfix water	**Water**	15.0	7.5	n/a	7100	4000	n/a	n/a	n/a	n/a	n/a	n/a	n/a
10	Cooling water	**Water**	4.0	n/a	7.3	25.7	0	24	6.3	0.9	4.56	5.8	1.4	<0.5
11	Typical ground water	**Water**	-	-	7.72-8.3	-	-	24.1-34.9	6.2-14.8	0.88-1.67	4.8-9.5	7.0-13.2	2.2-10.5	<0.5

Table B.5. The promising candidate (marked 'a') and potential application (highlighted in 'green') for geothermal well drilling tools and powerplant equipment

Materials	Micro-hardness [HV]	Wear rate *10⁻⁵ [mm³/Nm]	CoF (dry)	CoF (80°C wet)	Thickness [um]	Coating Application	Experiment conditions	Blistering	Porosity	Cracking	Permeability	Uniform corrosion	Localized corrosion	Total Delamination	Substrate corrosion
			First stage selection				Liquid (w) 120°c; (L) 250°c, co2/H2s; Steam (S) 250°c, co2/H2s				Second stage selection				
0wt% GO	~15	12.1	~0.2	≥0.2	>100		w	-	+	-	+	-	+	-	+
							L	+	+	-	++	-	++	-	+
						Valves,	S	+	+	-	++	-	+	-	+
0.5wt% GO ᵃ	~15	10.1	≥0.2	≥0.2	>100	Fluidic oscillator,	w	-	-	-	-	-	-	-	-
						Heat	L	+	-	-	++	-	+	-	+
						Exchangers	S	+	+	-	++	-	-	-	+
1wt% GO	~15	20.8	≥0.2	≥0.2	>100		n/a	n/a	n/a	n/a	n/a	n/a	n/a	n/a	n/a
2.5wt% GO	~15	22.6	~0.2	~0.2	>100		n/a	n/a	n/a	n/a	n/a	n/a	n/a	n/a	n/a
5wt% GO	~15	49.3	≥0.2	≥0.2	>100		n/a	n/a	n/a	n/a	n/a	n/a	n/a	n/a	n/a
WC-CoCr	<1000	>10⁻⁶	≥0.6	~0.4	≥400		w	-	+*	-	+	+	+	-	-
							L	-	-	+*	-	+	-	-	-
							S	-	-	+	-	+	-	-	-
CrC-NiCr	~750	>10⁻⁶	≥0.6	n/a	~250-300		w	-	-	+	+	+	-	-	-
							L	-	-	+	+	+	-	-	-
							S	-	-	-	-	+	-	-	-
WC-CrCNi	<1000	>10⁻⁶	≥0.6	~0.4	~250-300	Pipes & Casing,	w	-	-	+	++	+	++	-	+
							L	-	-	+*	++	+	++	-	+
							S	-	-	+	+	+	+	-	-
FLUX ᵃ (NiCrFeBSi)	~800	>10⁻⁵	≥0.6	~0.4	~250-300	Turbine, stabilizers, DTH drill	w	-	+*	-	-	+	-	-	-
							L	-	+*	-	+	+**	-	-	-
						hammer	S	-	-	-	+	+**	-	-	-
AMOR (FeCrMoWMnBCSi)	~750	>10⁻⁵	~0.7	n/a	≥350		w	-	+	-	-	+	-	-	-
							L	-	++,+*	-	++	+	++	-	-
							S	-	++	-	++	+	+	-	-
HEA_Mo0.85 ᵃ (CoCrFeNiMo 0.85)	~600	4.4	~0.8	n/a	~250-300		w	-	-	-	-	+	-	-	-
							L	-	-	-	-	+	-	-	-
							S	-	-	-	-	+	-	-	-
HEA_Mo	≥450	7.1	~0.7	n/a	~300		n/a	n/a	n/a	n/a	n/a	n/a	n/a	n/a	n/a
HEA_Mo1.3	≥450	1.3	~0.7	n/a	~400		n/a	n/a	n/a	n/a	n/a	n/a	n/a	n/a	n/a
PTFE_5g/l_as plated	≥300	3.5	>0.5	n/a	≥20		n/a	n/a	n/a	n/a	n/a	n/a	n/a	n/a	n/a
PTFE_10g/l_asplated	≥300	0.9	>0.2	n/a	≥20		n/a	n/a	n/a	n/a	n/a	n/a	n/a	n/a	n/a
PTFE_15g/l_asplated	>500	1.6	>0.5	n/a	≥20		n/a	n/a	n/a	n/a	n/a	n/a	n/a	n/a	n/a
hp/HPptfe_as plated	~400	27.3	≥0.8	n/a	≥20		n/a	n/a	n/a	n/a	n/a	n/a	n/a	n/a	n/a
hp/Hpptfe ᵃ heat-treated 300 °C	~500	3.3	≥0.7	~0.3	≥20	Valves, Heat Exchangers	w	-	-	-	+	+	+	-	-
							L	+	-	-	++	+**	-	+	-
							S	-	-	+	++	+**	-	+	-
hp/LPptfe_as plated	≥250	2.6	~0.2	n/a	≥20		n/a	n/a	n/a	n/a	n/a	n/a	n/a	n/a	n/a
hp/Lpptfe ᵃ heat-treated 300 °C	~400	1.2	~0.2	~0.3	≥20		w	-	-	-	-	+	++	-	+
							L	+	-	+	++	+	++	-	+
							S	+	-	+	+	+	+	+	+

- : absent. +: present. ++: extensive corrosion damage/ complete permeation from the coating to the substrate. +*: internal porosity/ pitting. +**: adherent corrosion scale/ layer. n/a: not applicable.